The Choreography of Yeast Mating: Modelling Intercellular Communication, Cell Polarity and Morphogenesis

Dissertation

zur Erlangung des akademischen Grades
doctor rerum naturalium
(Dr. rer. nat.)
im Fach Biophysik

eingereicht an der
Lebenswissenschaftlichen Fakultät
der Humboldt-Universität zu Berlin

von Dipl.-Math. Wolfgang Giese

Präsident der Humboldt-Universität zu Berlin
Prof. Dr. Jan-Hendrik Olbertz

Dekan der Lebenswissenschaftlichen Fakultät
Prof. Dr. Richard Lucius

Gutachter/innen:	Prof. Dr. Dr. h. c. Edda Klipp
	Prof. Dr. Martin Falcke
	Prof. Dr. Andreas Schröder
Tag der mündlichen Prüfung:	17.06.2016

Immer dann, wenn man lebendige Organismen als physikalische und chemische Systeme betrachtet, müssen sie sich auch als solche verhalten. Die einzige Frage, von der man etwas über die Richtigkeit dieser Auffassung erfahren kann, lautet, ob die physikalischen und chemischen Begriffe eine vollständige Beschreibung der Organismen ermöglichen. [...] Daher wird es wahrscheinlich für ein Verständnis der Lebensvorgänge notwendig sein, über die Quantentheorie hinauszugehen und ein neues abgeschlossenes Begriffssystem zu konstruieren, zu dem Physik und Chemie vielleicht später als Grenzfälle gehören mögen.

- Werner Heisenberg in *Physik und Philosophie* (Heisenberg, 1990)

Abstract

Research on the yeast *Saccharomyces cerevisiae* – also known as baker's yeast – has been essential not only for fostering basic biological knowledge but even more so for contributing towards understanding diseases such as cancer. In this thesis, general biological phenomena occurring in eukaryotic cells are investigated, exemplified by the mating process of yeast, including intercellular communication, reception of extracellular signals and polarized growth. Cellular functions and processes that occur during yeast mating have been surprisingly well conserved throughout evolution and, therefore, also provide insights into cellular processes in other organisms.

In the haploid phase of their life cycle, yeast cells occur as mating type *MAT***a** or *MAT*$\boldsymbol{\alpha}$, both of which communicate *via* pheromones that are secreted in an extracellular medium and can be sensed by cell-surface receptors of the complementary mating type. In order to mate, yeast cells grow towards a potential mating partner, since they are not able to actively move. The key aspects of the yeast mating process that I examined were **(i)** intercellular communication of cells *via* pheromones, **(ii)** the initial symmetry break and implementation of cell polarity, and **(iii)** subsequent morphogenetic changes. Taking an interdisciplinary approach, concepts from physics and mathematics were used to develop quantitative models and frameworks on the basis of fluorescence and atomic force microscopy (AFM) data. The methods used and findings were as follows:

(i) Pheromone secretion and sensing motifs were modelled using cellular automata models based on reaction-diffusion (RD) equations. My models show that mutual stimulation and increased pheromone secretion between cells improves mating efficiency and unnecessary cell cycle arrest is avoided in cell populations. This outcome was compared with data from mixed cultures of haploid yeast cells.

(ii) To explain yeast mating decisions, two possible model types for cell polarity were tested: a Turing-type and a phase-separation mechanism. Their ability to adapt to spatial perturbations of cell shape and heterogeneities on the membrane and in the cytosol was investigated. Bulk-surface RD equations were investigated analytically and numerically using the finite element method (FEM). Typical cell shapes were reconstructed in 2D and 3D.

(iii) The cell wall was modelled using classical continuum mechanics and a FEM approach that allows for reversible elastic and irreversible plastic cell wall deformation. A mechanism for stress-dependent growth was assumed and tested for different elasticity patterns, as obtained from AFM data, leading to insights regarding the interplay of cell shape and cell mechanics. Mathematical modelling demonstrated that all three processes investigated are precisely orchestrated and interlocked during yeast mating.

Keywords: Mating Yeast, Pheromones, Cell Polarity, Morphogenesis, Cell Wall, Finite Element Method, Reaction-Diffusion Model

Zusammenfassung

Die Forschung an der Hefe *Saccharomyces cerevisiae* – auch als Bäckerhefe bekannt – hat sich für die biologische Grundlagenforschung als unentbehrlich erwiesen und führte zu wichtigen Erkenntnissen in der Erforschung von Krankheiten wie Krebs. Am Beispiel der Paarung von Hefezellen werden in dieser Arbeit wesentliche Aspekte der eukaryotischen Zellbiologie untersucht, wie die Zellkommunikation durch Pheromone, die Verarbeitung von extrazellulären Signalen und das koordinierte Zellwachstum. Diese Prozesse sind im Laufe der Evolution weitestgehend erhalten geblieben und erlauben Rückschlüsse auf andere Organismen.

In der Haplophase des Lebenszyklus der Hefe, treten haploide Zellen als Paarungstyp $MAT\mathbf{a}$ oder $MAT\boldsymbol{\alpha}$ auf. Diese Paarungstypen kommunizieren über Pheromone, die in ein extrazelluläres Medium abgesondert werden und von Zelloberflächenrezeptoren des komplementären Paarungstyps erkannt werden. Hefezellen wachsen in die Richtung eines möglichen Paarungspartners, da sie sich nicht aktiv bewegen können. Die Auswertung von empirischen Daten aus der Fluoreszenzmikroskopie und Rasterkraftmikroskopie (AFM) mit mathematischen Modellen ermöglichte die Rekonstruktion wesentlicher Prozesse der Hefepaarung: **(i)** Interzelluläre Kommunikation über die Sezernierung und Rezeption von Pheromonen, **(ii)** Aufbau der Zellpolarität als Reaktion auf die Pheromonantwort, **(iii)** Induktion und Mechanik der Zellformänderung.

Folgende Modelle wurden für die Rekonstruktion dieser drei aufeinander abgestimmten Prozesse entwickelt: **(i)** Die interzelluläre Kommunikation wurde unter Verwendung von zellulären Automaten mit Hilfe von Reaktions-Diffusions (RD) Gleichungen modelliert. Das Modell zeigte, dass die gegenseitige Stimulierung und erhöhte Pheromonabsonderung zu einer verbesserten Abstimmung in der Paarung in der Zellpopulation führt. Als Basis der Untersuchung dienten Daten von Zellpopulationen aus beiden Paarungstypen.

(ii) Ein Turing- und ein Phasenseparations- Mechanismus wurden als Modelle zum Aufbau der Zellpolarität verwendet. Ihre Fähigkeiten sich an räumliche Störungen und Inhomogenitäten an der Membran und im Zytosol anzupassen wurden getestet. Volumen-Oberflächen gekoppelte RD Gleichungen wurden analytisch als auch numerisch mit der Finite-Elemente-Methode (FEM) untersucht. Typische Zellformen wurden in 2D und 3D rekonstruiert.

(iii) Die Zellwandveränderung wurde mit klassischer Kontinuumsmechanik und der FEM Methode modelliert. Dies ermöglichte eine Beschreibung der reversiblen elastischen und der irreversiblen plastischen Verformungen der Zellwand. Ein Lockhart-Mechanismus für stressabhängiges Wachstum wurde für unterschiedliche Elastizitäts-Muster getestet, welche aus den AFM Daten entstanden sind. Dies führte zu Einsichten in das Zusammenspiel von Zellwachstum und Zellelastizität. Die mathematische Modellierung zeigte, dass alle drei untersuchten Prozesse der Zellkommunikation, der Zellpolarität und der Morphogenese ineinander greifen und präzise choreographiert sind.

Contents

RD	Reaction Diffusion
ODE	Ordinary Differential Equation
PDE	Partial Differential Equation
FEM	Finite Element Method
SFEM	Surface Finite Element Method
GPCR	G-Protein-Coupled Receptor
Cdc42	Cell division control protein 42 homolog, a small Rho GTPase
GEF	Guanine Exchange Factor
GAP	GTPase Activating Protein
GDI	Guanosine Nucleotide Dissociation Inhibitor
$MAT\boldsymbol{\alpha}$	Mating Type $\boldsymbol{\alpha}$
$MAT\mathbf{a}$	Mating Type $\boldsymbol{a}$
MAPK	Mitogen Activated Protein Kinase
AFM	Atomic Force Microscopy
GFP	Green Fluorescent Protein
SBML	Systems Biology Markup Language
GOR	A Turing-type Model for Cell Polarization
WP	Wave-Pinning Model for Cell Polarization
CA	Cellular Automaton

Table 1: List of abbreviations.

1 Introduction

"[Y]east has told us something that is relevant to mankind."

– Leland H. Hartwell, Nobel Lecture, 2001[1]

Cell biology can be enormously complex. Thus, in his Nobel Lecture "Yeast and Cancer" Leland H. Hartwell pointed out how important it is to choose an appropriate model system in order to gain useful insights (Hartwell, 2002). *Saccharomyces cerevisiae* – which is also known as baker's yeast and is focused on in this study – is one of the most powerful eukaryotic model organisms. Due to the tremendous degree of conservation of many biological components during its evolution, *Saccharomyces cerevisiae* has enabled fundamental insights into many biological processes that occur in fungal as well as mammalian cells. Investigating the cell cycle, for example, biologists were able to identify checkpoints in the yeast cell cycle control that were later also identified in other model systems such as *Schizosaccharomyces pombe* and *Xenopus embryos* (Nasmyth, 2001). These checkpoints were found to be essential for precisely coordinating the kind of cell division and malfunction in cell cycle control which also occurs in mammalian tumour cells (Hartwell, 2002). As in this case, research on yeast as a model organism has not only been key for fostering fundamental biological knowledge but even more so for contributing towards understanding diseases such as cancer.

The Model Organism

One of the major advantages of working on yeast as a model organism is that it is easy to manipulate, both genetically as well as biochemically, and has provided great quantities of data during the last decades (Botstein, 2010). The *Saccharomyces* Genome Database[2], for example, provides data for more than 6,000 protein-coding genes and a description of their functions. Since there is a lack of similar data under controlled conditions for mammalian cells, yeast is a favourable model organism for understanding basic principles in cell biology, and such data sets regarding yeast will most certainly contribute to further discoveries in the future (Botstein and Fink, 2011). However, the interactions

[1] Published in: Leland H Hartwell, "Nobel lecture: Yeast and cancer", Bioscience Reports, Vol. 22, Nos. 3 and 4, June and August 2002, p.1

[2] www.yeastgenome.org

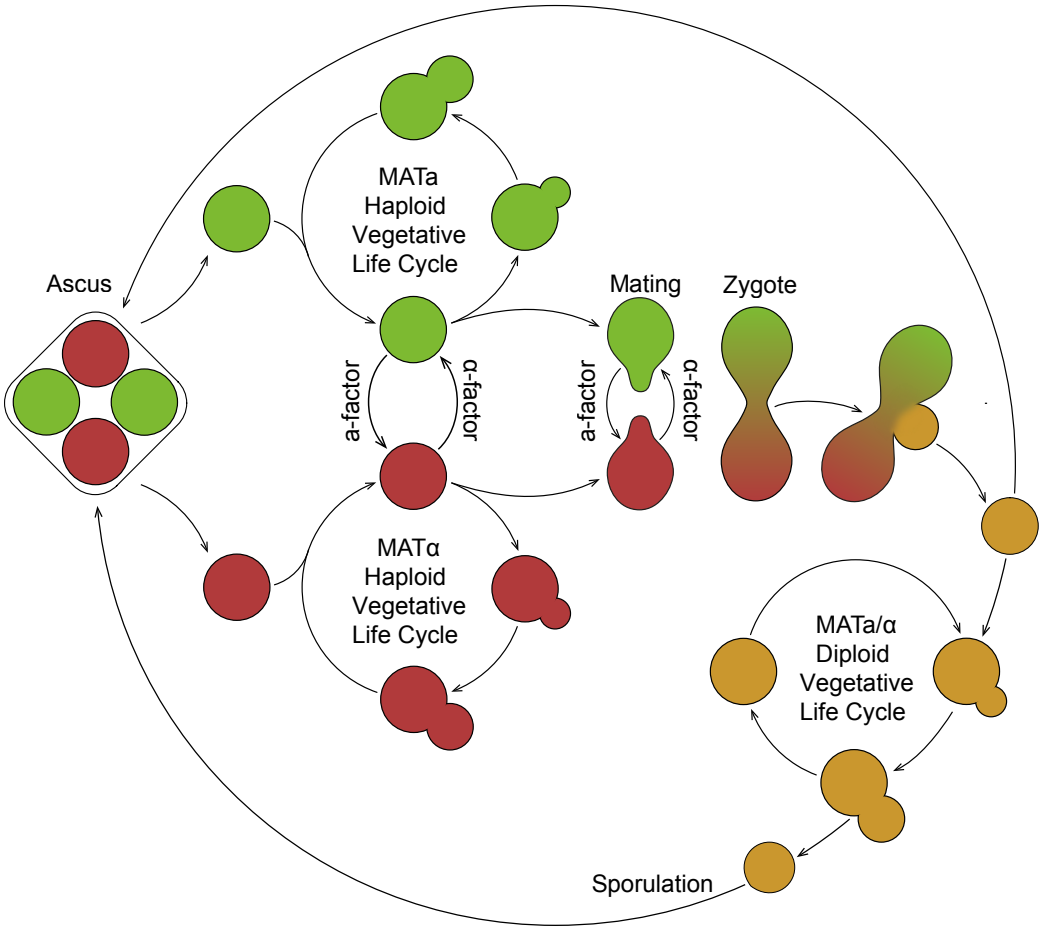

Figure 1.1: **The yeast life cycle.** Yeast can maintain a diploid as well as a haploid life cycle. Usually yeast exists in its diploid form, however, when nutrients are limited, a diploid cell forms four haploid spores by meiosis. These four spores are encased by a solid and protected structure called ascus. The ascus contains two cells of each mating type, $MAT\mathbf{a}$ (green) and two of $MAT\boldsymbol{\alpha}$ (red). Haploid cells can divide or enter the sexual life cycle. Yeast cells are not able to move but grow towards a mating partner. Two mating partners of opposite mating types can form a zygote and their progeny enters the diploid life cycle. The mating process is precisely coordinated and involves elaborated signalling and communication principles that have been conserved throughout the evolution of eukaryotic cells.

between genes and gene products are unimaginably complex, and understanding their functions, even in the smallest eukaryotic model organism, poses a challenge which has not yet been solved. Despite this complexity of even single eukaryotic cells, there have been attempts to structure, analyse and integrate huge quantities of experimental data. This has given rise to the field of systems biology (Klipp, 2011; Klipp et al., 2013; Kitano, 2002), which combines biology with mathematics, physics and computational methods, seeking to answer relevant biological questions. Yet investigations at the systems level of eukaryotic cells can easily push advanced computational approaches to their limits. Consequently, biological models are constantly being developed, changed and adapted, and need to be considered as impermanent and incomplete (Mogilner et al., 2012).

Biological Complexity

Yeast is an ideal model organism to develop and examine computational approaches and modelling methods. As with most eukaryotes, mating is a key process in the life cycle of yeast (see Figure 1.1). Haploid yeast cells occur in the form of two different mating types, $MAT\mathbf{a}$ and $MAT\boldsymbol{\alpha}$, which communicate *via* the diffusible pheromones $\boldsymbol{\alpha}$-factor and **a**-factor, respectively (Duntze et al., 1970). Upon pheromone stimulation, the cell cycle is arrested in G1 phase. Yeast cells cannot actively move and, therefore, need to form a mating projection along a pheromone gradient in order to reach a potential mating partner. The cell shape that occurs during mating is often referred to as a *shmoo*, named after a cartoon character.[3] Perhaps unexpectedly, this asymmetric, and on the surface random-seeming, growth pattern is actually a precisely choreographed process in space and time. When two mating partners of opposite mating types come in contact with each other, the cell fusion process is initiated, resulting in a zygote, which enters the diploid cell cycle. It continues the cell cycle by forming a bud, giving rise to diploid yeast cells *via* mitosis (Cross et al., 1988; Tartakoff, 2015).

Mating Yeast and the Shmoo

The mating of yeast is a well orchestrated process, exhibiting many elements of communication and signal-transmission processes important for both unicellular organisms and cell tissues: better understanding and description of these processes may, therefore, contribute towards solving some fundamental questions of cell biology. In many cases, unicellular and multicellular organisms communicate *via* extracellular signals leading to subsequent cell differentiation, polarized growth and division. G-protein-coupled receptors (GPCRs) that are involved in pheromone sensing are widespread among eukaryotes, from fungi to mammals (McCudden et al., 2005; Jones and Bennett, 2011). During yeast mating, binding of pheromones to GPCRs leads to local G-protein activation, which affects a number of intracellular signalling proteins. For example, the received signal conveyed by the GPCRs is further processed by the cell's polarity machinery, where small GTPases of the Rho family, such as Cdc42 and Rho1, are involved in establishing cell orientation for asymmetric growth which leads to shmoo formation (Etienne-Manneville, 2004). In their evolution, both systems have been highly conserved[4] among eukaryotic cells as in axon guid-

[3] Capp, Al, The Life and Times of the Shmoo (1948), Simon & Schuster

[4] In this context, 'highly conserved' refers to the interacting molecules in the system.

ance of neurons, chemotaxis of fibroblasts toward wounds and the search for a mating partners in yeast to name only a few examples (compare Figure 1.2). In the model organism yeast, initial models of cell polarity during cell division and mating were only first proposed a few years ago (Altschuler et al., 2008; Goryachev and Pokhilko, 2008; Slaughter et al., 2009), and many details still remain controversial. The haploid life cycle of yeast is especially delicate, since bud-site selection and mating behaviour are closely entangled.

In the present thesis, I investigate seemingly three important aspects of the yeast mating process: (i) the intercellular communication of cells, (ii) their initial symmetry break and implementation of cell polarity, and (iii) subsequent morphogenetic changes which lead to shmoo formation. Each of these aspects poses fundamental questions, stated as follows, that are addressed in the subsequent chapters of this thesis. Chapter 2: How does cell communication *via* pheromones in haploid yeast cells work and what are the underlying communication motifs involved? Chapter 3: How do cells orient and respond to often conflicting pheromone signals sent by their potential mating partners, and how can mating as well as budding patterns be explained? Chapter 4: How does the asymmetric growth process unfold, and how is the prominent shmoo shape generated?

Research Questions

To answer these questions, *spatial* data from cell biology needs to be analysed and understood. Data obtained from living cells exhibits high spatial complexity and conventional approaches of cell biology are not sufficient to explain this complexity. To overcome this challenge, the application of unifying quantitative approaches in an interdisciplinary manner has proved to be a fruitful path. Concepts from physics and mathematics are used in this thesis to move beyond temporal modelling of the mating process and, instead, considering time and space as being closely related to investigate not only *when* processes take place but also *where*. In this regard, these concepts are employed to describe spatio-temporal communication, cell polarization and morphogenesis of mating yeast cells. I pursue questions such as Where do pheromone molecules accumulate in the extracellular medium? How does this affects cell communication?, and Where do signalling processes take place within the cell? Are they, for example, situated in the cytosol or on the membrane or along the membrane-cytosolic interface. The geometry of the cytosolic volume and its boundaries with reference to kinetic reactions and signalling processes are important aspects that are investigated here.

An Interdisciplinary Approach

Therefore, I have employed quantitative mathematical and physical approaches towards understanding their regulation in space and time. Namely, the reaction-diffusion model and continuum mechanics are used in order to describe yeast communication and morphogenesis in a quantitative way. Partial differential equations (PDEs) are commonly used to formulate reaction-diffusion processes and continuum mechanical relations in mathematical lan-

These molecules contain protein sequences or are encoded by gene sequences that have only slightly changed during evolution and are very similar or identical in many eukaryotic cells. Often mutations of one of the highly conserved gene sequences that encode for the involved molecules leads to a non-viable life form.

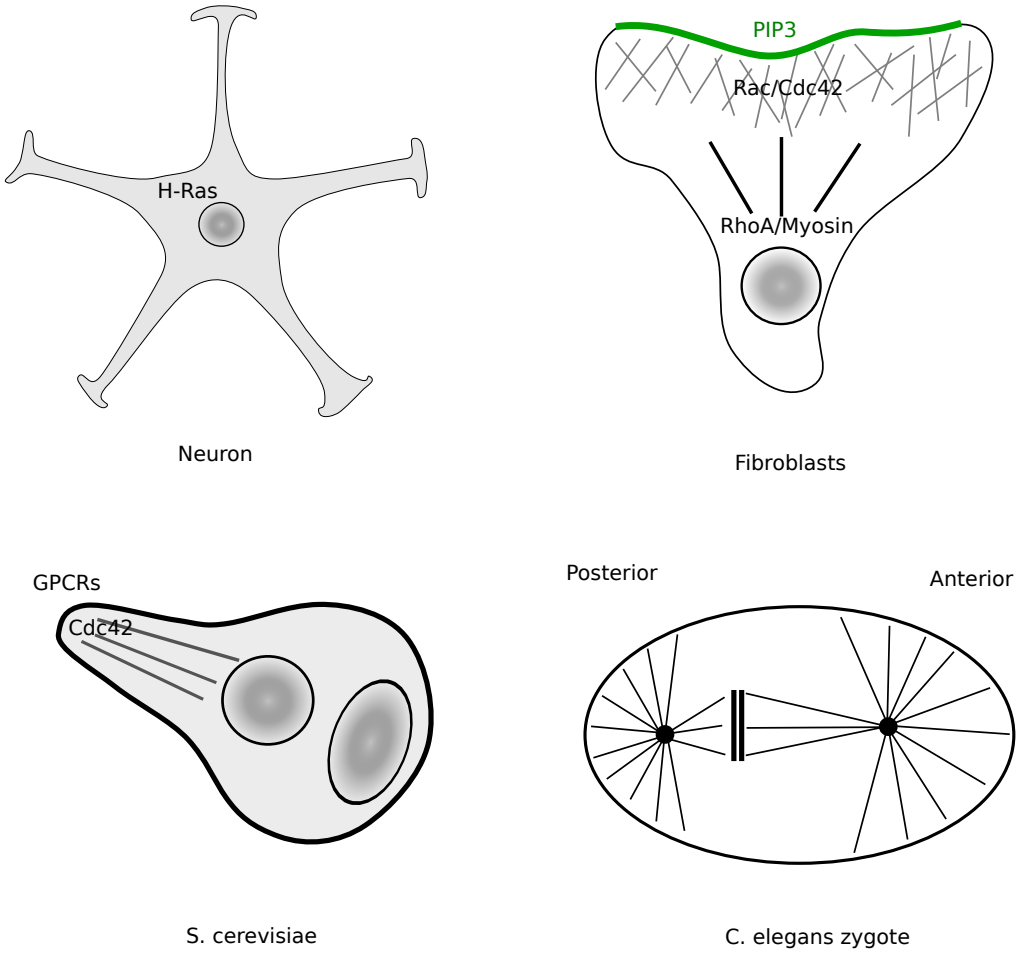

Figure 1.2: **Cell differentiation and morphogenesis in different model organisms.** Cell polarization is a prerequisite for morphogenetic changes. It is frequently carried out by small GTPases such as Cdc42, Rac and Rho and is an overarching principle that occurs in many organisms, including axon guidance of neurons, movement of fibroblasts towards wounds, mating of yeast and development of *C. elegans*. Universal features of polarizing cells and quantitative design principles have been recently revealed by mathematical modelling (Jilkine and Edelstein-Keshet, 2011). Parts of the figure were adapted and modified from Mogilner et al. (2012).

guage. Consequently, to capture the systems behaviour of mating yeast, I have used methods of mathematical analysis as well as from numerical mathematics with an emphasis on the finite element method (FEM). Although, these methods have already been used with some success in computational biology (Holmes and Edelstein-Keshet, 2012; Boudon et al., 2015). However, spatio-temporal modelling approaches are still not used widespread since they are quite technically. Furthermore, spatio-temporal data at the level of a single cell only became available in the last few years.

Spatial Imaging Methods

Experimental techniques as well as analysis methods, have undergone rapid development and have opened up an entirely new perception of cellular processes in space and time. Recent advances in microscopy techniques can provide images with high spatial and temporal resolution of molecular processes (Verveer and Bastiaens, 2008; Smith et al., 2014). In particular, advances in fluorescence microscopy allow determination of movement as well as interaction kinetics for molecules of interest. Among these advances is the total internal reflection microscopy (TIRF) that has been used for observation of a thin region of a sample, mainly the outer membrane (Toomre and Manstein, 2001). Furthermore, fluorescence resonance energy transfer (FRET) (Wouters et al., 2001) and fluorescence lifetime imaging microscopy (FLIM) (Festy et al., 2007) have made it possible to quantify interactions of molecules *in vivo*. For determination of underlying molecular transport processes, fluorescence cross-correlaion spectroscopy (FCCS) (Bacia et al., 2006) has been especially successful.

In a recent study on yeast, for example, the formation of a polarization cap and the dynamics of septins have been dynamically tracked during shmoo formation (Kelley et al., 2015). A whole yeast cell can be reconstructed in three-dimensional space *in vivo* (Spokoini et al., 2012), enabling for instance tracking of changes in organelle shapes and sizes as well as other important structures in space and time (Chan and Marshall, 2014). Other techniques, such as electron microscopy and x-ray tomography, have been used to image yeast cells and their internal structure in astonishing detail (Wei et al., 2012; Larabell and Nugent, 2010). Combining imaging and quantification techniques such as spatio-temporal image correlation spectroscopy (STICS), can now reveal transport properties and kinetics that are useful for spatial modelling (Smith et al., 2014). Furthermore, new computational advances in analysing techniques (Schindelin et al., 2012; Diener et al., 2014; Smith et al., 2015) foster

Spatial Data

the accessibility and evaluation of high-quality spatio-temporal data. Yet to exploit the full potential of high-quality spatio-temporal data and gain further insights into observed cellular processes, these techniques need to be complemented by spatial modelling, which I explain in detail throughout this thesis. Here, I have mainly relied on data from fluorescence and atomic force microscopy (AFM), provided by my lab colleagues. The fluorescence microscopy data was taken from Gabriele Schreiber as well as Christian Diener (also see our collaborative work (Diener et al., 2014)). AFM data from my colleague Björn Goldenbogen was used to gain insights into the evolution of cell shape and material properties of living cells in space and time.

The Yeast Mating Process

A short overview of some biological key aspects relevant for the yeast mating process is given in this section. Yeast cells are unicellular organisms and in their life cycle can occur in haploid or diploid forms (Herskowitz, 1988). Their life cycle comprises two important aspects: proliferation and change of ploidy (compare Figure 1.1). Haploid as well as diploid yeast cells are capable of mitosis, giving rise to two new cells in a process referred to as budding. The smaller cell emerging from the bud is referred to as the 'daughter' cell, while the larger cell is referred to as the 'mother' cell. Both are genetically identical but are asymmetric with respect to aging, since both cells differ in size, number of bud scars, and inheritance of damaged and aggregated proteins (Spokoini et al., 2012; Spiesser et al., 2015). In yeast, diploid cells usually follow a bipolar and haploid cells an axial budding pattern. However, these patterns can be altered in various situations, depending on environmental cues (Erdman and Snyder, 2001). Change of ploidy for diploid cells usually occurs, for example, when nutrients are limited. Diploid cells perform meiosis, which leads to four haploid cells, two of mating type *MAT***a** and two of mating type *MAT*$\boldsymbol{\alpha}$. Cells of opposing mating types can, through a precisely choreographed process, fuse to form a diploid *MAT***a**/$\boldsymbol{\alpha}$ cell (Jackson and Hartwell, 1990a,b). The mating of haploid cells, which includes communication, mating partner selection and directed growth, is addressed in the remainder of this section.

Yeast Life Cycle

Yeast cells communicate *via* pheromones, called $\boldsymbol{\alpha}$-factor and **a**-factor, which are secreted by *MAT***a**- and *MAT*$\boldsymbol{\alpha}$ cells, respectively. Both differ in terms of their structures. Whereas $\boldsymbol{\alpha}$-factor is an unmodified peptide with a length of thirteen amino acids, **a**-factor is a twelve amino acid lipopeptide. The pheromone $\boldsymbol{\alpha}$-factor traverses the secretory pathway and travels in vesicles to the plasma membrane, where it is secreted (Jones and Bennett, 2011). In contrast, **a**-factor is not exported by the classical secretory pathway but is exported by the ABC transporter Ste6 (Michaelis and Barrowman, 2012). Unmodified peptides such as $\boldsymbol{\alpha}$-factor are only found in ascomycetes, while modified peptides such as **a**-factor have been found in ascomycetes and basidiomycetes. In the case of *S. cerevisiae*, pheromones are captured by the GPCRs Ste2 and Ste3 for $\boldsymbol{\alpha}$-factor and **a**-factor, respectively. Furthermore, *MAT***a** cells are capable of producing the aspartylprotease Bar1, which cleaves the $\boldsymbol{\alpha}$-factor. A function of Bar1 is to steepen the $\boldsymbol{\alpha}$-factor gradients produced by *MAT*$\boldsymbol{\alpha}$ cells (Barkai et al., 1998; Jin et al., 2011; Rappaport and Barkai, 2012). Additionally, colleagues and I have also shown that Bar1 promotes higher growth rates in subpopulations of *MAT***a** cells by separating the population into mating and vegetatively growing cells (Diener et al., 2014). Only recently, a complementary protein Afb1 (**a**-factor barrier) has been reported (Huberman and Murray, 2013) and it was hypothesized that Afb1 acts on **a**-factor in a similar manner as Bar1 on $\boldsymbol{\alpha}$-factor. However, its molecular properties are still elusive as well as experimental data on the behaviour of mutants lacking Afb1. Furthermore, data from experiments using **a**-factor are rare, since its hydrophobicity leads to difficulties in the experimental setup.

Intercellular Communication

Therefore, its spatial distribution has not yet been characterized and modelled quantitatively. I address this issue in Chapter 2.

Pathway Activation via GPCRs

Pheromones are captured and recognized by GPCRs on the surface of yeast cells. These receptors have a common structure of seven transmembrane domains and are internalized after stimulation (Schandel and Jenness, 1994; Yi et al., 2003). Both receptors Ste3 (MATα cells) and Ste2 (MATa cells) activate a heterotrimeric G$\alpha\beta\gamma$ complex. This activation causes the heterotrimeric G-protein to dissociate into two sub-units, Gα and the dimer G$\beta\gamma$. The signal is transmitted by the G$\beta\gamma$ sub-unit, which has three main effectors, a Far1/Cdc24 complex, a Ste5/Ste11 complex and the Ste20 protein kinase (Bardwell, 2004). The first complex initiates a mechanism that is crucial for chemotropic growth by activating Cdc42p, a central small GTPase of the Rho family (Butty et al., 1998; Bar et al., 2003; Ventura et al., 2014). The scaffold Ste5 and the Cdc42p-activated signal transducing kinase Ste20 activate the first step of the mitogen-activated protein kinase (MAPK) cascade. From this branch, the signal is processed further *via* a MAPK pathway to nuclear transcription factors and other targets (Bardwell, 2004). A sketch of pheromone signalling is shown in Figure 1.3.

Cell Polarity & Cdc42

The process that determines the direction of yeast cell growth is called the polarization mechanism.[5] A key player in the establishment and maintenance of cell polarity is the small GTPase Cdc42. In the course of polarization, Cdc42 cycles between an active GTP-bound and an inactive GDP-bound state. In its membrane-bound state, Cdc42 is anchored into the membrane *via* a prenyl group and can be removed by its guanosine nucleotide dissociation inhibitor (GDI). Levels of active Cdc42-GTP can be increased by guanine nucleotide exchange factors (GEFs) or reduced by GTPase-activating proteins (GAPs). Upon pheromone stimulation and dissociation of the G$\alpha\beta\gamma$ complex, Far1p binds to the G$\beta\gamma$ sub-unit and recruits Cdc24p to the site of receptor stimulation (Etienne-Manneville, 2004). Then Cdc42 forms a complex with its GEF Cdc24p and the scaffold, Bem1, in the activated membrane-bound state. This complex formation induces a positive feedback on the recruitment of active Cdc42-GTP which leads to a unique polarization cluster at the site of receptor activation and defines the direction of growth. Remarkably, in the absence of a gradient the system also polarizes at a unique site (Etienne-Manneville, 2004), where the orientation of the polarization axis depends on various factors, such as cell shape and former bud sites (Bidlingmaier and Snyder, 2004; Giese et al., 2015). During directed cell growth, the Cdc42 polarization cap is also strongly influenced by septin structures that confine and control the direction of growth (Kelley et al., 2015). Mechanistic models

[5]The word "polarity" is used in many different contexts in the natural sciences, for instance in physics particles or magnets that have two distinct poles are called polar. In a biological context, polarity describes a state of asymmetry rather then having two distinct poles (Wolpert, 2013). In this work "polarity" means the asymmetric distribution of molecules in the cell. Note that Goethe already used the notion of "Polarität" in "Erläuterung zu dem aphoristischen Aufsatz 'Die Natur' " as one of the driving principles of nature (Nakazawa, 1989).

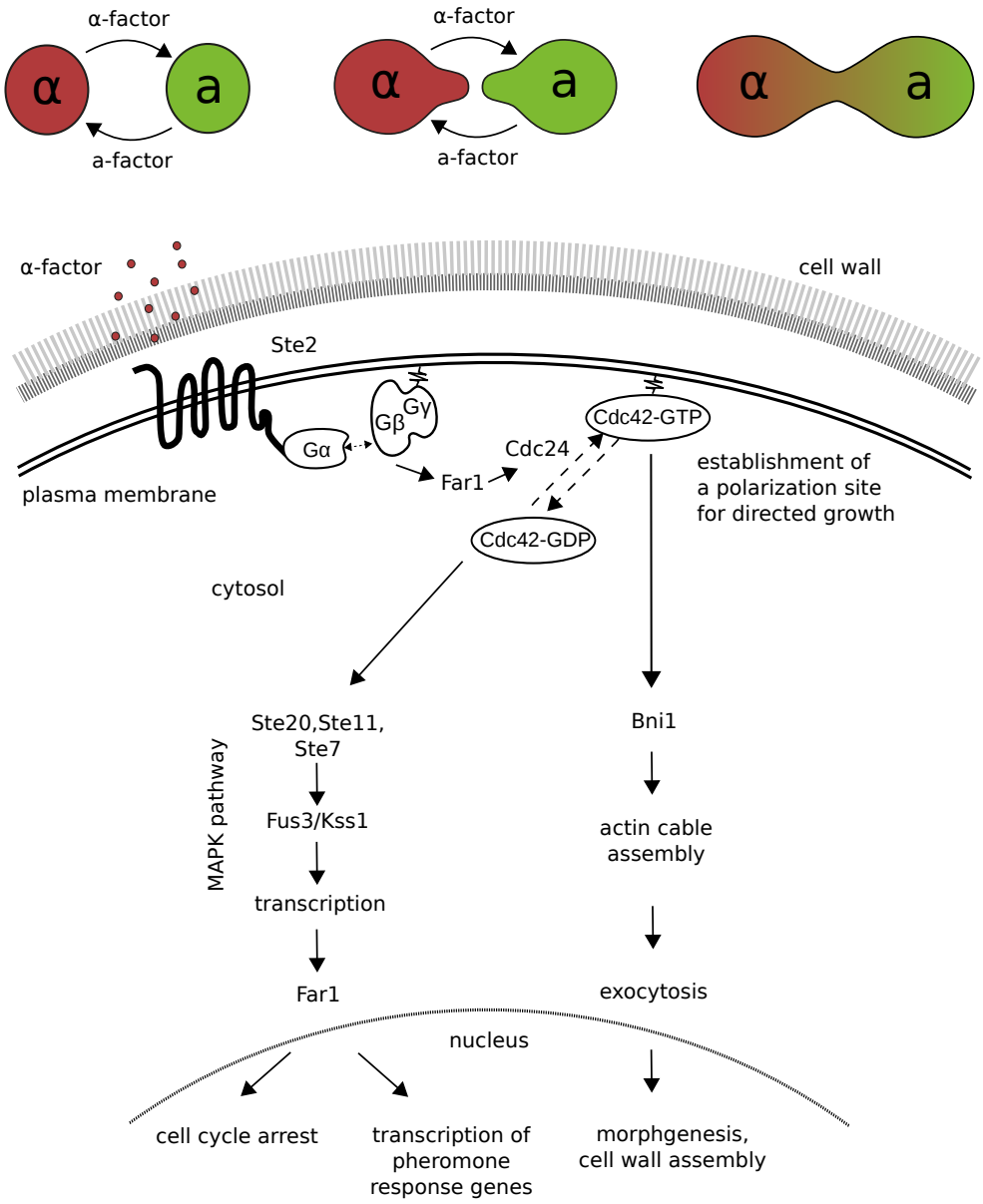

Figure 1.3: **Overview of the yeast pheromone response.** Binding of the pheromone $\boldsymbol{\alpha}$-factor to the Ste2 receptor activates a signalling pathway that produces three responses (i) cell polarization, (ii) cell cycle arrest in G1, and (iii) increasing transcription of pheromone response genes (Bardwell, 2004). (i) Far1p binds to the G$\beta\gamma$ sub-unit and recruits Cdc24p, which interacts with the small GTPase Cdc42. A site of polarity is established, which triggers the subsequent morphogenetic change *via* alteration and growth of the cell wall. (ii) and (iii) The signal is further processed *via* a mitogen activated protein kinase (MAPK) cascade, which results in cell cycle arrest and transcription of pheromone response genes. Note that here only the *MAT***a** side of the signalling process is shown. While the downstream signalling pathway in *MAT*$\boldsymbol{\alpha}$ cells is to a great extent identical, the pheromone **a**-factor is sensed by the receptor Ste3.

for cell polarization are described and tested in Chapter 3.

The pheromone signal is further processed *via* a MAPK cascade, which results in cell cycle arrest and transcription of pheromone response genes. The MAPK cascade contains three sequentially activated protein kinases – MAPK, MAPKK and MAPKKK (Widmann et al., 1999) – with MAPK being the final signal transmitter of the cascade and MAPKKK the first 'domino'. As mentioned above, in yeast pheromone stimulation leads to the activation and dissociation of heterotrimeric G$\alpha\beta\gamma$ proteins. The release of the G$\beta\gamma$ sub-unit, which is attached to the membrane *via* a lipid anchor, activates the MAPK cascade *via* interactions with Ste20 and the scaffold protein Ste5. Ste20, sometimes also referred to as MAPKKKK, and the scaffold protein Ste5, a key player in signal transmission, brings Ste11 (MAPKKK), Ste7 (MAPKK) and Fus3 (MAPK) together (Dohlman and Thorner, 2001). Fus3 has two main phosphorylation sites and transmits the signal to the nucleus, which causes cell cycle arrest and the initiation of polarized growth. A great deal of data, including kinetic information, is available and has been integrated into dynamic ODE models (Kofahl and Klipp, 2004; Thomson et al., 2011) of the signalling process, focused on the temporal order of the processes involved. It has been shown in both theory (Brown and Kholodenko, 1999) as well as experimentally (Maeder et al., 2007) that strong Fus3 gradients are established during the growth of a mating projection. Note that this is only one of five MAPK cascades that occur in yeast, which organize the response to different environmental stimuli. The others four are the HOG (Klipp et al., 2005; Adrover et al., 2011), the cell-wall integrity (Levin, 2011), the filamentous-growth (Roberts and Fink, 1994) and the spore-assembly pathways (Chen and Thorner, 2007). Furthermore, MAPK cascades have been highly conserved in all eukaryotes, where they perform various tasks of signal transmission (Widmann et al., 1999; Bardwell, 2004).

MAPK Pheromone Response

The yeast mating morphogenesis and the formation of the characteristic shmoo shape is mainly determined by the cell wall, which in yeast is a large and rigid structure is built of two layers that mainly contain polysaccharides and mannoproteins. The inner layer is composed of beta-1,3-glucan, beta-1,6-glucan and chitin, while the outer layer is mainly composed of mannoproteins (Cabib and Arroyo, 2013). The cell wall structure is dynamically modulated and adapted during morphogenetic changes and to environmental conditions (Klis et al., 2002). During stress, as for example induced by a heat shock, the synthesis of chitin and glucans increases in order to strengthen and repair the cell wall (Valdivia and Schekman, 2003b). During cytokinesis, enrichment of chitin at the septum has been observed in Cabib and Arroyo (2013). Evidence for chitin enrichment during the formation of a mating projection has been found as well (Schekman and Brawley, 1979). It is also worth mentioning that the cell wall is a structure that is actually outside the cell, meaning outside of the plasma membrane. Consequently, many steps of cell wall synthesis are prepared within the cell, or plasma membrane, and cell wall material is then inserted *via* exocytosis. The break up of crosslinks, the insertion of wall material and the formation of new crosslinks has to be organized within the periplasm,

where common energy sources such as ATP are not present. These complicated cell wall processes are mainly regulated by the cell wall integrity pathway (Chen and Thorner, 2007). During mating, directed growth is initiated and localized *via* Cdc42, which also targets Bni and localizes the polarisome (Bardwell, 2004). Thus, a cell changes its form not only due to local cell wall growth but also because of local changes in the material properties of the cell wall (Goldenbogen et al., 2016). Details of this process will be discussed in more detail in Chapter 4.

As I have outlined here, yeast mating is an elaborate and precisely coordinated process in space and time. Yet, its spatial organization is still elusive, as has been addressed in (Angermann et al., 2012), where the MAPK cascade and morphology changes have been modelled on a coarse-grained lattice grid using hundreds of coupled differential equations to describe the involved species in each compartment. This model does not, however, cover such remaining important aspects as intercellular communication, polarization behaviour and cellular mechanics. In the next section, important developments, aims and concepts of mathematical modelling are discussed that may help to increase our understanding of the challenges that we are confronted with in modelling biological systems.

Physics, Complex Systems and Biology

A focus of this thesis is to identify quantitative principles in cell biology by studying mating yeast using physical laws and computational methods. But why is it so challenging to gain insights into the life and behaviour of even the probably best studied eukaryotic model organisms, that is *S. cerevisiae*? One reason for this lies in the complexity of the aspects of nature that form the objects of study in biology, making it so different from other sciences such as physics or chemistry. This section aims to provide an outline of this problem and a short review on possible solutions to overcome this challenge.

To demonstrate these differences and challenges, the physics of water is a striking example (Newman, 2014). On the molecular level, pure water merely consists of H_2O molecules. Hydrogen bonds that are continually forming and breaking can behave in fascinating ways (Clary, 2016). On a macroscopic level water can take many different forms due to the collective behaviour of its molecules in different environmental conditions. For instance, it can be a liquid, gas or ice, where it can become articulated in a wide variety of snow crystals (Nakaya, 1954; Libbrecht, 2005; Greuel, 2014).[6] Physical treatments of the occurring phenomenological forms of water can be quite complex, but means of understanding them have been developed. For example, three-dimensional growth of snow crystals can be described by PDEs and recapitulated in the computer by using advanced FEM methods (Dziuk, 1990). Another example is heating water in a basin from below, which can cause the occurrence of reg-

[6]For an overview of recent developments in the physical and mathematical descriptions of crystals I refer to (Garcke, 2012).

Snow Crystals, Computations and Living Organisms

ular patterns. These patterns are referred to as Rayleigh-Bénard convection (Rayleigh, 1916). When a critical temperature is reached, a regular pattern of convection cells emerges, which are called Bénard cells. On one side of each Bénard cell warm water rises, while on the other side cool water falls. In each Bénard cell, water convection is directed clockwise, or counter-clockwise, with alternate orientation for neighbouring cells. The Bénard cells have served as a concept to understand self-organizing principles of non-linear system in cell biology and have been extensively studied (Getling and Brausch, 2003; Karsenti, 2008). These two examples show how a substance such as water, which on the surface seems relatively simple on the molecular level, behaves in complex ways. For the description of these physical processes, modelling and simulation techniques, such as PDEs and advanced FEM methods, are used. These techniques are also studied in my thesis.

But in biology, the situation becomes still more complicated. At the molecular level, the number of different molecular species that interact with each other is much larger than with non-living systems (Hopfield, 1994). The yeast genome as well as the human genome was sequenced (Goffeau et al., 1996; Lander et al., 2001) and knowledge of the chemical basis of life has advanced rapidly. However, similar to the case water molecules, many phenomena cannot be understood by looking at their fundamental building blocks alone. For water, the interplay of H_2O molecules plays an important role, whereas in living cells, the next layer of complexity comes from the transcription and translation of genes into a plethora of proteins. Mass spectroscopy has revealed, for example, that the yeast proteome contains more than 6,600 different proteins (Picotti et al., 2013). In addition to this large number, those proteins are folded, change their conformation depending on the environment and interact with other molecules. Examples for these interactions are phosphorylation, dephosphorylation and degradation of proteins (Kitano, 2002). Furthermore, complex macromolecules are formed which behave like molecular machines (Hofmann et al., 2006). The prediction of how these macromolecules fold and behave takes great effort, and simulations even in the millisecond regime, are a computational challenge (Noé, 2015). At the level of single cells, where thousands of different molecule species with different properties interact, the complexity increases dramatically. To understand human diseases, multicellular interactions have to be understood. For example, in organs such as the liver (König et al., 2013), we need to look at collective behaviour of many different cell types. The transcription of genetic information, the translation of proteins, complex interactions and functions of protein motors, the behaviour of single cells and whole tissues comprise several orders of magnitude of time and length. Here, an understanding of diseases such as cancer cannot be restricted to the genes of the organism. Physical descriptions of cellular behaviour and multicellular communication motifs have to be developed.

Another important difference to non-living systems is that biological patterns are created and destroyed in precisely regulated ways. While the snow crystals mentioned above are mainly static, the forming of patterns in biology is often far more dynamic. Since in thermodynamically closed systems entropy

grows and order is destroyed, living systems have to be open systems and can maintain their order only by energy consumption from outside. Theoretical investigations of temporal patterns such as biochemical oscillations go back to the beginning of the last century, when Alfred J. Lotka (Lotka, 1910) suggested in a theoretical investigation that biochemical oscillations might be possible in cases of an autocatalytic reaction. It is an irony of history that this reaction system has not been found to match any reaction system in biochemistry, but his model turned out to be useful in ecology, where it has become known as the Lotka-Voltarra system for describing the dynamics in prey-predator systems (Roth, 2011). In the 1950s, the Russian chemist Boris Pavlovich Belousov tried to create an inorganic chemical oscillator in a closed homogeneous system. Unfortunately, his manuscript describing the first version of the oscillator was rejected, since it was believed to be thermodynamically impossible. He spent six more years in developing a second version of the oscillator, but the corresponding manuscript was again rejected (Roth, 2011). Fortunately, his ideas were picked up again by his colleague Zhabotinsky in the 1960s and the oscillator was named after both researchers. It is nowadays known as the Belousov-Zhabotinsky oscillator. At about the same time, Alan Turing developed his theory of the chemical basis of morphogenesis (Turing, 1952), based on the Michaelis-Menten enzyme kinetics (Michaelis and Menten, 1913), diffusion in membranes and knowledge about genes of the time. Using only diffusion and basic reaction kinetics, Turing was able to show that six different stable patterns can emerge, in a simple two component reaction-diffusion system. Among these patterns are stationary waves, oscillatory waves and homogeneous oscillations (Turing, 1952). Theory and experimentation were consolidated by Progogine and co-workers in Bruessel, where non-equilibrium thermodynamics was further developed and a trimolecular oscillatory system, known as the Bruesselator, was presented as a theoretical example (Prigogine and Lefever, 1968). From then on, many rhythmic oscillations, and their biochemical bases have been identified in cellular systems (Goldbeter, 2002).

Non-linearity

In current biological research, the idea of agents and collective behaviour[7] is becoming increasingly important (Karsenti, 2008). Speaking of molecules and reactions can be considered appropriate at the molecular level, if we are thinking of proteins that have many different binding sites or act as molecular machines. Existing phenomenological macroscopic models might be relatively simple, not necessarily reflecting this microscopic complexity. A good analogy can be found in ecology, where territorial behaviour of intelligent mammals, such as wolves, has been explained with relatively simple PDEs and simple kinetic laws (Lewis and Murray, 1993). In cell biology, a collective behaviour framework has, for example, been used for studying cancer in tissues (Deisboeck and Couzin, 2009; Friedl et al., 2012), where collective behaviour of

Collective Behaviour

[7] The notion comes actually from the social sciences describing human interactions and group dynamics, that cannot be explained by the attitudes of one group member alone (Turner and Killian, 1957). It has also been transferred to the ecology field to describe the self-organization of ant colonies (Camazine et al., 2001) or swarming behaviour of fish (Couzin et al., 2002).

different kinds of cancer cells has been described. This has also been observed for chemotactic cells (Elgeti et al., 2015) and cellular communication in yeast (Youk and Lim, 2014), which will be discussed in Chapter 2. In addition, self-organization of spindle assembly has been investigated in the context of collective behaviour at a single cell level by (Reber and Hyman, 2015).[8] In the yeast mating process, self-organization of signalling molecules is relevant for symmetry break and directed growth, which leads to shmoo formation. The molecular organization during cell polarization is discussed in Chapter 3.

As addressed in the initial part of this section, there are fundamental differences between biology and other sciences such as physics or chemistry. The kinds of self-organized temporal and spatial patterns that can be generated in physical or chemical systems have no function *per se* – they occur as certain conditions are met and vanish again. However, in a biological system they can fulfil a certain function within this system. This leads us to the definition of a functional module of a biological system. The definition by Hartwell is as follows: "A functional module is, by definition, a discrete entity whose function is separable from those of other modules" (Hartwell et al., 1999). The manifestation of such an entity can be "made up of many species of interacting molecules" (Hartwell et al., 1999). Functional modules can occur on a wide range of time and length scales. A functional module in yeast that we have already discussed is the MAPK cascade. In yeast, this sort of signal transduction is, for instance, employed for the regulation of mating, osmotic stress, cell wall integrity, filamentous growth and spore assembly (Chen and Thorner, 2007). These different MAPK cascades in yeast interlock with each other (Schaber et al., 2006) and act context dependent. Many functional modules, such as the MAPK module, are conserved across nature and can be found in mammals, with variations from organism to organism (Bardwell, 2004), where they serve multifarious functions. The idea that a module can only serve a function in a biological system, and that its actual function is dependent on the context in which it exists is closely related to the ideas of systems biology, which I examine in the next section.

Emergence of Functional Modules

An Interdisciplinary Approach: Systems Biology

General principles that governing the behaviour and composition of functional modules have been discovered with the help of close interaction between experiments and theory, and the field of systems biology has provided powerful methods for strengthening this link. Today, researchers have online access to large databases such as the previously mentioned yeast genome project. Systems biology combines biology, mathematics, physics and computer science, in order to investigate biological questions on the basis of such vast amounts of

[8] A lecture series called "Collective behaviour" was held at the IRI in the winter semester 2015/16, which has motivated this paragraph. It contained subjects such as spindle organisation, cell polarity and fish swarms.

experimental data. The field has itself provided large model databases in, for example, the systems biology markup language (SBML) (Klipp et al., 2007), where standards are defined and models for many of the multifarious aspects of life can be found. Many functional models, such as the previously mentioned MAPK cascade are provided in this database and can be tested and extended. In this way functional modules, described with the help of computational models, can be put together and their interaction with other models can be tested. Step by step, this will contribute to the development of a whole-cell model for a eukaryotic cell (Klipp, 2007), that is capable to recapitulate important aspects of cellular behaviour *in silico*. In developing such methods, systems biology has been quite dynamic and has constantly influenced other sciences, from developmental biology (Lander, 2011) to mathematics (Westerhoff et al., 2009), but it has also been influenced *vice versa*.

The purposes of models vary widely, and modelling is important in many different respects as shown in Figure 1.4. Some models are designed to integrate and consolidate large data sets, as for example with metabolic models (Wodke et al., 2013; Tummler et al., 2015). Models can also be used to optimize certain biological processes under certain constraints, such as protein expression levels in E. coli (Dekel and Alon, 2005). While such computational models are built on large data sets and include many parameters, there are also more focused models, that investigate cell polarization (Altschuler et al., 2008) or stochastic processes in signalling (Uschner and Klipp, 2014). Here, the degree of complexity lies less in the integration of large data sets, but more in terms of modelling processes in space and time that are non-linear or stochastic (Mogilner et al., 2012). Furthermore, there are models that are rather abstract, their value lying more in the comprehension of certain dynamics rather than through direct comparison with real experiments. A classic and quite influential example is the work of Alan Turing (Turing, 1952), discussed previously. This was just to name a few examples. For an overview of the field of systems biology I refer to (Klipp et al., 2013).

In my work, as presented in this theses, I want to contribute towards the development of this field and, more particularly, the understanding of functional modules by investigating the yeast mating process at different levels of detail with focus on spatial modelling and spatial data. Below I provide a brief outline of the content of this thesis.

Thesis Outline

In Chapter 2, I investigated communication motifs occurring during yeast mating. Cellular automata (CA) models on the basis of reaction-diffusion (RD) equations are used to describe the communication of yeast cells in mixed cultures of haploid yeast cells of opposite mating type. I begin with a slight modification of the model from Barkai et al. (1998), which describes the impact of Bar1 on $\boldsymbol{\alpha}$-factor distributions in the extracellular medium. Here, I have also added an analysis of time and length scales as well as a parameter study. Then, step by step I extend this model, testing for the trade-off between mating and vegetative growth as observed in Diener et al. (2014). Furthermore, this model is extended to cover the secretion of **a**-factor and the response to the complementary pheromone by increased pheromone production. Different

levels of mutual pheromone induction are tested in varying cell densities and the possibility of an extracellular protein, which degrades **a**-factor.

In Chapter 3, I investigate polarization patterns that occur due to changes in cell geometry and diffusion heterogeneities on the cell membrane, and in the cytosol. I test two different polarization mechanisms and compare them to the polarization behaviour of mating yeast. The first is a Turing-type mechanism proposed in Goryachev and Pokhilko (2008), the second is a phase separation mechanism proposed in Mori et al. (2008). I begin with a simple one-dimensional model to work out differences and similarities of both mechanisms. The one-dimensional model is then extended into higher spatial dimensions in order to investigate the influence of cell shapes and spatial diffusion heterogeneities. The work from Giese et al. (2015) is summarized, compared and extended for the mathematical analysis and simulations in three space dimensions.

In Chapter 4, the morphogenesis of the cell during shmooing is investigated using a continuum mechanical model. First, a simple steady state continuum mechanical model for pressurized shells is introduced to describe essential relations between turgor pressure, cell wall thickness, cell shape and Young's modulus. A finite element (FEM) approach that allows for reversible elastic and irreversible plastic cell wall deformations is then implemented to further investigate dynamic growth. A Lockhart-like model for stress-dependent growth is assumed for cell wall growth and tested for different elasticity patterns, which are based on atomic force microscopy (AFM) data obtained from Goldenbogen et al. (2016).

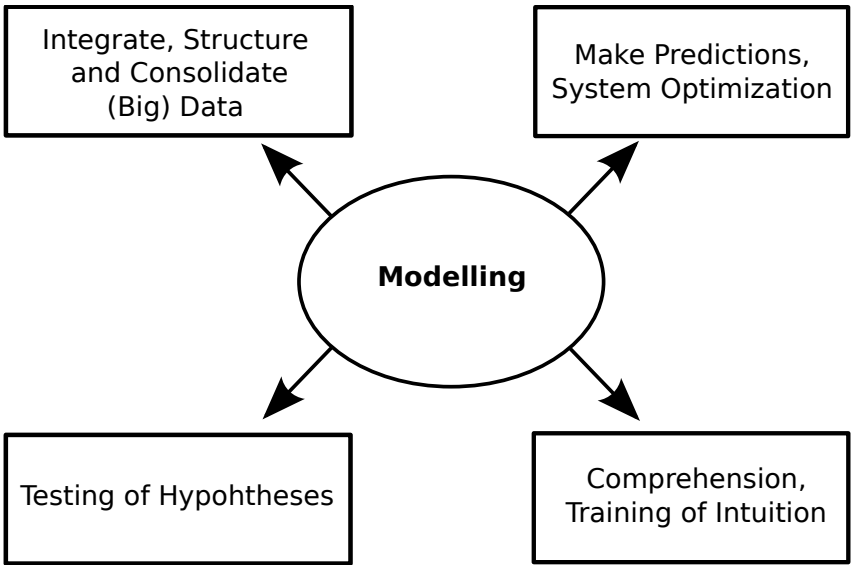

Figure 1.4: **Different purposes of mathematical modelling in biology.** Models can serve one or more purposes as shown in the figure. Models vary in the level of detail and realism. Some models are focused and simple, while others are complex and broad. Since biological systems can be extremely complex, some models integrate large datasets for consolidation and analysis. Given the biological data, relevant parameters can be estimated. Models can also be used to test and validate hypotheses. Purely theoretical or dimensionless models can be helpful for understanding processes such as non-linear dynamics, or the scaling of system properties.

2

Intercellular Communication Motifs and Collective Behaviour in Mating Yeast

Intercellular communication and collective behaviour are a ubiquitous phenomena among microbes as well as multicellular organisms. Examples for these phenomena range from microbial cooperation and competition (Gore et al., 2009), collective behaviour of tumour-immune networks (Wells et al., 2015) to the development of whole organisms (Lander, 2011). Collective behaviour of multicellular systems can emerge from communication motifs of single cells, which secrete and sense signalling molecules with specific molecular properties (Maire and Youk, 2015). In the case of yeast, such motifs are implemented by pheromone sensing and secretion during yeast mating. In Diener et al. (2014), we have shown that in mixed cultures of haploid yeast cells of opposite mating type, an elaborated communication mechanisms is used to sense potential mating partners and to coordinate cell cycle and cell division.[1] The investigation of intercellular communication *via* pheromones in yeast mating mixes is in the focus of this chapter.

Pheromones

Pheromone signalling is used widespread among all kingdoms from bacteria, to fungi, mammals and plants (Jones and Bennett, 2011; Ventura et al., 2014). *Inter alia* fungal species communicate *via* pheromones to coordinate the mating process. Thereby they secrete a mating type specific pheromone, which can be sensed by the complementary mating type. In the case of ascomycetes, the communication is essentially asymmetric, since unmodified peptides as well as lipopeptides are employed for communication between different mating types. In *S. cerevisiae*, cells of mating type $MAT\boldsymbol{\alpha}$ secrete the peptide $\boldsymbol{\alpha}$-factor while cells of mating type $MAT\mathbf{a}$ secrete the lipopeptide **a**-factor. Notably, **a**-factor is a peptide of twelve amino acids length, which is cysteine methylester farnesylated at the C terminus (Anderegg et al., 1988) and, therefore, exhibits a hydrophobic behaviour. Furthermore, in the case of *S. cerevisiae* a protease Bar1 is secreted by $MAT\mathbf{a}$ cells, which degrades $\boldsymbol{\alpha}$-factor (compare Figure 2.1). The basal Bar1 secretion is increased upon $\boldsymbol{\alpha}$-factor sensing. Whether a corresponding protease for **a**-factor also exists is still under debate.

I shall give a short overview on a number of studies, where yeast cells were used to investigate communication principles. In Youk and Lim (2014), $MAT\mathbf{a}$

[1] The system of 'mixed cultures of haploid yeast cells of opposite mating type' is often referred to as mating mixes.

yeast cells were tuned at a molecular level to secrete $\boldsymbol{\alpha}$-factor. Populations of these $MAT\mathbf{a}$ cells were, therefore, able to sense their own pheromone. Yeast cells were tuned to exhibit different strength of feedback. Also stochastic effects in Bar1 expression led to different patterns in collective behaviour. In Gonçalves-Sá and Murray (2011), yeast mating has been tuned in a way that the modified cells of both mating types were able to communicate with two lipopeptides as well as two peptides. Thereby, it was shown that the asymmetric communication could be replaced by a symmetric communication system. The receptors and peptides were introduced from other yeasts such as *Schizophyllum commune*, *Schizosaccharomyces pombe* and *Sordaria macrospora*. Due to its hydrophobic nature, there are only few experimental studies on **a**-factor and the response of $MAT\boldsymbol{\alpha}$ cells to **a**-factor. Only recently, in Huberman and Murray (2013), the existence of a protein that is able to degrade **a**-factor has been reported and was named Afb1 (**a**-factor blocker), hypothesizing that Afb1 fulfils the same function as the protease Bar1. However, for this novel proposed function confirmation is still missing.

Experimental Studies

Computational methods have in addition been extensively used to integrate known quantitative information (Segall, 1993; Barkai et al., 1998; Endres and Wingreen, 2008; Andrews et al., 2010; Jin et al., 2011; Rappaport and Barkai, 2012; Diener et al., 2014). Some of these studies combined computational modelling of pheromone distributions with experiments based on artificially generated gradients (Segall, 1993; Jin et al., 2011). Other studies were merely theoretical (Barkai et al., 1998; Andrews et al., 2010; Rappaport and Barkai, 2012) where potential $\boldsymbol{\alpha}$-factor distributions were computed. In Diener et al. (2014), a combined experimental and computational analysis of $MAT\mathbf{a}$ cell response upon contact with the mating partner as well as synthetic pheromone was performed. In the study, fluorescently labelled $MAT\mathbf{a}$ and $MAT\boldsymbol{\alpha}$ reporter strains were used for microscopic imaging and an extensive quantitative image analysis of pheromone response. Using a computational approach, the level of pheromone response was determined for each individual cell and with the best fit of this model to the microscopic data an estimate of crucial model parameters was achieved. However, the complementary pheromone **a**-factor and generated pheromone landscapes have not been included in the mentioned studies so far.

Existing Models

The localization of Bar1 is controversially discussed. In Barkai et al. (1998); Andrews et al. (2010); Jin et al. (2011), it was assumed to act in the extracellular medium, while Endres and Wingreen (2008); Rappaport and Barkai (2012) assume that Bar1 is only localized in the periplasm. It is generally accepted, that Bar1 has the potential to sharpen gradients and at the same time Bar1 also reduces pheromone levels (Hicks and Herskowitz, 1976; Jones and Bennett, 2011). It is known that Bar1 is secreted into the periplasm, where it is ready to degrade $\boldsymbol{\alpha}$-factor. However, which fraction is diffusing out of the porous cell wall is not known.

In this chapter, I use experimental and computational results from Diener et al. (2014), in which communication patterns in mating mixtures of haploid yeast cells were quantitatively analysed. I extend this study by further analysis

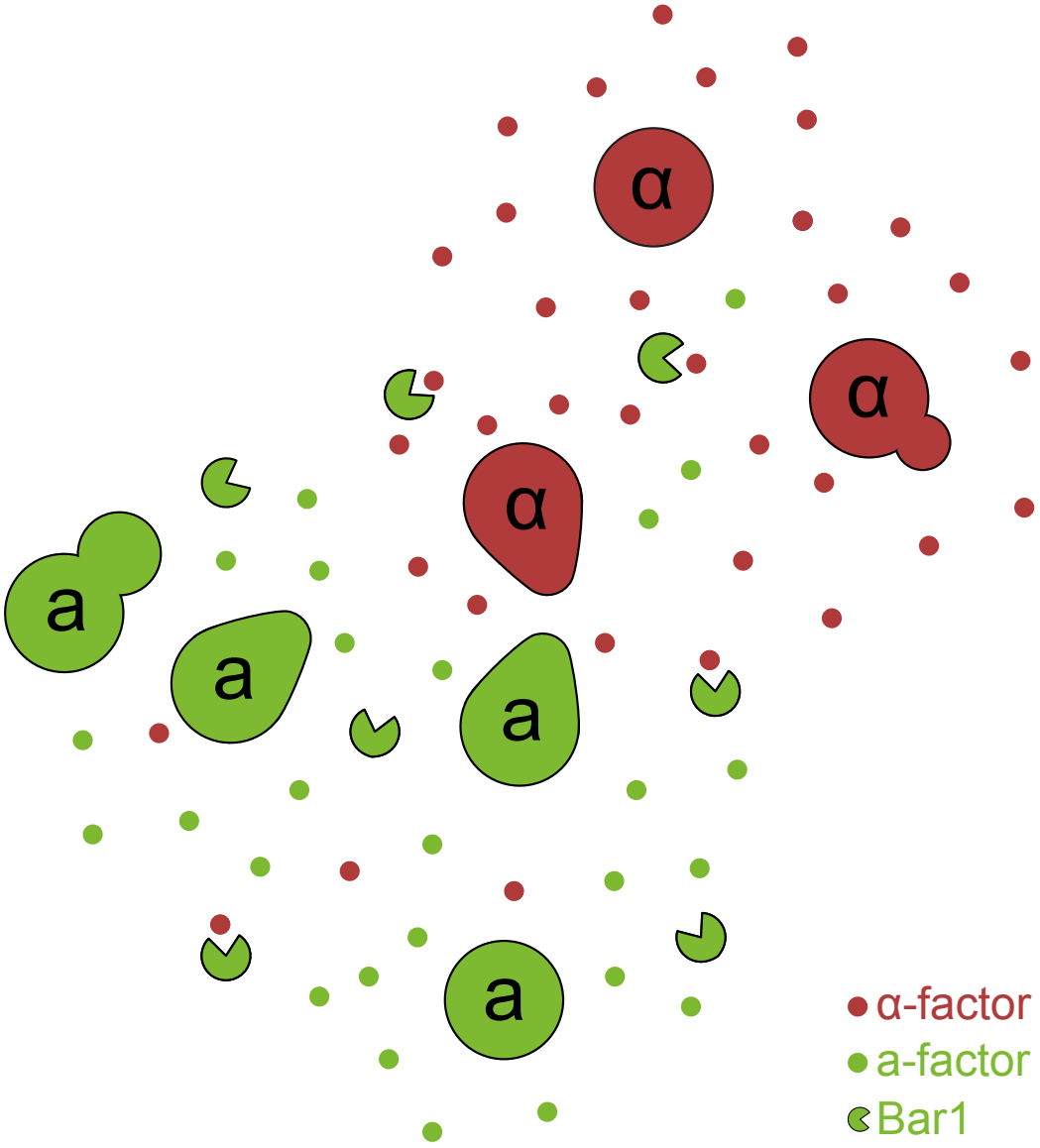

Figure 2.1: **Sketch of the communication of yeast cells in mating mixes**. Cells of mating type *MAT*$\boldsymbol{\alpha}$ secrete the pheromone $\boldsymbol{\alpha}$-factor, which is sensed by *MAT***a** cells. *Vice versa MAT***a** cells secrete **a**-factor, which is sensed by the *MAT*$\boldsymbol{\alpha}$ cells. Additionally, *MAT***a** cells also secrete a protease Bar1 which degrades $\boldsymbol{\alpha}$-factor.

and extension of the model as well as analysis of microscopy data to address questions that remain open: How does the trade-off between gradient sharpening and reduction of pheromone levels by a protease in different cell densities look like? Is there an optimal level of protease activity? Does Afb1 fulfil the same function as Bar1? Which effect does the complementary pheromone **a**-factor and mutual induction of pheromone secretion have on pheromone profiles and cell behaviour? Which mechanisms lead to an asymmetric communication between the two mating types?

In Diener et al. (2014) we used a finite element method (FEM) to solve the reaction-diffusion (RD) equations, which enable high computational accuracy. However, due to the high computational costs we simulated the two-dimensional RD equations for parameter fitting and simulations at the level of a cell population. Here, I shall complement our investigations with an alternative approach based on cellular automata as in Maire and Youk (2015), where large cell communication systems where investigated. In this approach known analytical solutions of the RD equations with simplified boundary conditions were used to keep important system properties while reducing computational cost and complexity. However, the investigations in Maire and Youk (2015) were restricted to one cell type and cellular orientation on the based gradients of signalling molecules was not considered. Here, this modelling approach is extended to two cell types and cellular orientation towards each other in the occurring pheromone gradients. This approach allows equations to be solved fast in 3D and, furthermore, parameter studies can be easily conducted.

Chapter Outline

The model from Barkai et al. (1998) serves as a null hypothesis and is extended step by step by adding more details, to explain observed microscopic data. **(i)** I used the basic model from Barkai et al. (1998) to explore basic features. Additionally, aspects of time and length scales were investigated by using methods known from theoretical developmental biology. **(ii)** The results of this model were discussed in the light of our investigations (Diener et al., 2014) and the activity of Bar1 assumed to be adapted to the overall sensed pheromone level. **(iii)** I investigated the **a**-factor distribution to explore possible asymmetries in the communication and the recently discovered protein Afb1. This model is more hypothetical, but aims to integrate recent experimental findings.

Evaluation of Microscopy Data for Mixed Mating Populations

In this section, I shall give a short overview on experimental results from Diener et al. (2014) for yeast mating mixtures. In this study the behaviour of yeast cells in mating mixtures of $MAT\boldsymbol{\alpha}$/ $MAT\mathbf{a}$ as well as $MAT\boldsymbol{\alpha}/MAT\mathbf{a}$ $bar1\Delta$ was studied using a combined approach of modelling and microscopy. Note, that $MAT\mathbf{a}$ and $MAT\boldsymbol{\alpha}$ refer to the wild type yeast cells, while $MAT\mathbf{a}$ cells with a *BAR1* deletion are referred to as $MAT\mathbf{a}$ $bar1\Delta$ or short $bar1\Delta$ cells. Quantification of the spatial pattern of pheromone distribution is non-trivial

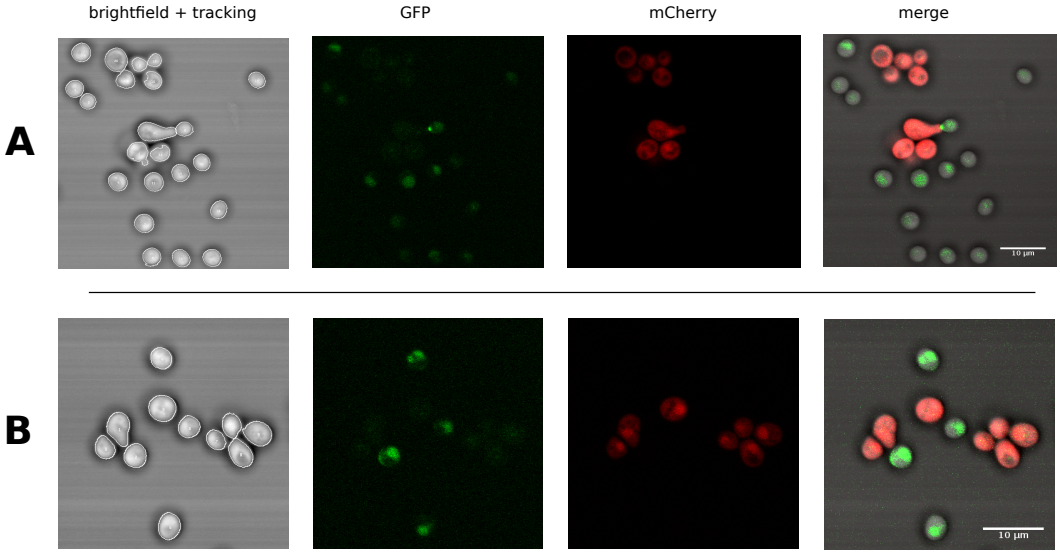

Figure 2.2: **Image segmentation and merging of different channels obtained from confocal microscopy images.** **A**: Mix of wild type cells. **B**: Mix of *MAT*$\boldsymbol{\alpha}$ and *bar*1Δ cells. In **A** and **B** overlays of the bright-field images, Fus1-GFP and mCherry channels allowed recording of the positions of *MAT*$\boldsymbol{\alpha}$ (in red) and *MAT***a** quantitative analysis. Individual cells were identified directly from bright-field images. The GFP channel was used for Fus1-GFP or Rpl9A-GFP fluorescence and the red channel for mCherry fluorescence. Figure from Diener et al. (2014)

since the signalling molecules of interest, the pheromones **a**-factor and $\boldsymbol{\alpha}$-factor, are small peptides that are secreted and diffuse rapidly through the extracellular medium. The pheromone $\boldsymbol{\alpha}$-factor is a peptide of thirteen amino acid residues and **a**-factor is a twelve amino acid lipopeptide (Jones and Bennett, 2011). Since both molecules are very small, labelling them directly with fluorescence markers would change their function as signal transmitters severely. For example, the popular fluorescence marker GFP has a molecular weight of 26.9 kDa, while $\boldsymbol{\alpha}$-factor and **a**-factor have a molecular weight of only 1.684 kDa and 1.808 kDa, respectively. Therefore, marking the pheromones results in a number of yet unsolved difficulties. First, the cell wall is a porous structure (De Nobel and Barnett, 1991), where only small molecules can freely pass and, therefore, modifications such as the attachment of fluorescent markers to the pheromones might limit their secretion into the extracellular medium. Second, the molecules diffuse very fast $> 100\ \frac{\mu m^2}{s}$ (see Appendix A for derivation), facilitating communication over large distances. Thus, altering the diffusion would also lead to a dramatic change in intercellular signalling behaviour. Third, fluorescent markers might limit the activity and recognition by receptors of the opposite mating type. For these reasons, a direct visualization of the pheromone is difficult and has not yet been performed.

To circumvent the technical limitations of direct visualization, we developed an advanced approach combining microscopy and modelling for *in vivo*

quantification of cell communication and reconstruction of pheromone gradients based on a reaction-diffusion model. The method is explained in detail in Diener (2012); Diener et al. (2014). Here, I shall shortly summarize the method and the results. Both mating types $MAT\mathbf{a}$ and $MAT\boldsymbol{\alpha}$ cells were labelled with fluorescent markers, $MAT\mathbf{a}$ cells with Fus1-GFP and $MAT\boldsymbol{\alpha}$ cells with mCherry (see Figure 2.2). Confocal microscopy was used to obtain stacks of bright-field images as well as fluorescence images of the GFP and mCherry channels over the whole time course of mating. Segmentation of the brigh-field images and assignment of measured fluorescence levels of the GFP and mCherry channel allowed the detection of the mating type of each cell.

The fusion protein Fus1 was labelled with GFP in the $MAT\mathbf{a}$ cells and served as a proxy for the response level of the $MAT\mathbf{a}$ cells induced by $\boldsymbol{\alpha}$-factor stimulation. Using this proxy we obtained response curves for wild type $MAT\mathbf{a}$ as well as $bar1\Delta$ cells, which are shown in Figure 2.3. Note, that the response levels were also used as a read-out for the pheromone response of $MAT\mathbf{a}\, bar1\Delta far1\Delta$ cells in Youk and Lim (2014), which lead to a very similar result as obtained for the $MAT\mathbf{a}$ $bar1\Delta$ cells. Since Bar1 degrades $\boldsymbol{\alpha}$-factor and, therefore, controls $\boldsymbol{\alpha}$-factor concentration levels, the response curve is shifted towards higher concentrations compared to $bar1\Delta$ cells not expressing Bar1 (compare Figure 2.3 **A** and **B**). The difference of both response curves was used to estimate the Bar1 activity in the medium, depending on the $\boldsymbol{\alpha}$-factor concentration, since $\boldsymbol{\alpha}$-factor sensing $MAT\mathbf{a}$ cells stimulates their Bar1 production. As a control we also obtained response curves for a pBar1-qVenus reporter strain, where a Venus quatromer was expressed under control of the Bar1 promoter. This constuct served as a direct read out of the Bar1 expression. For semi-automated evaluation of the microscopy images, I implemented an autofocus algorithm in ImageJ (Schneider et al., 2012).

From these experimental observations a relationship of the Bar1 activity and sensed $\boldsymbol{\alpha}$-factor was established. The level of Bar1 actvity was described by a Hill curve, that was fitted to microscopy data (Figure 2.3 **A**). We assumed that this Hill curve describes locally the response for every cell. The response function is given by

$$B_i(t) = k_{0,bar1} + k_{1,bar1} \frac{S(t-\tau)^h_{i,\alpha}}{K_{m,\alpha} + S(t-\tau)^h_{i,\alpha}}, \tag{2.1}$$

where $S_i(t-\tau)$ is the concentration of $\boldsymbol{\alpha}$-factor sensed by the *i-th* $MAT\mathbf{a}$ cell at time $t-\tau$. Note, that all cells were labelled with an identification number and tracked throughout the process.

Diffusion and reaction processes of $\boldsymbol{\alpha}$-factor as well as Bar1 were described by a system of RD equations

$$\begin{aligned} \frac{\partial \alpha(\mathbf{x},t)}{\partial t} &= D_\alpha \Delta\alpha(\mathbf{x},t) - kB(\mathbf{x},t)\alpha(\mathbf{x},t), \\ \frac{\partial B(\mathbf{x},t)}{\partial t} &= D_B \Delta B(\mathbf{x},t). \end{aligned} \tag{2.2}$$

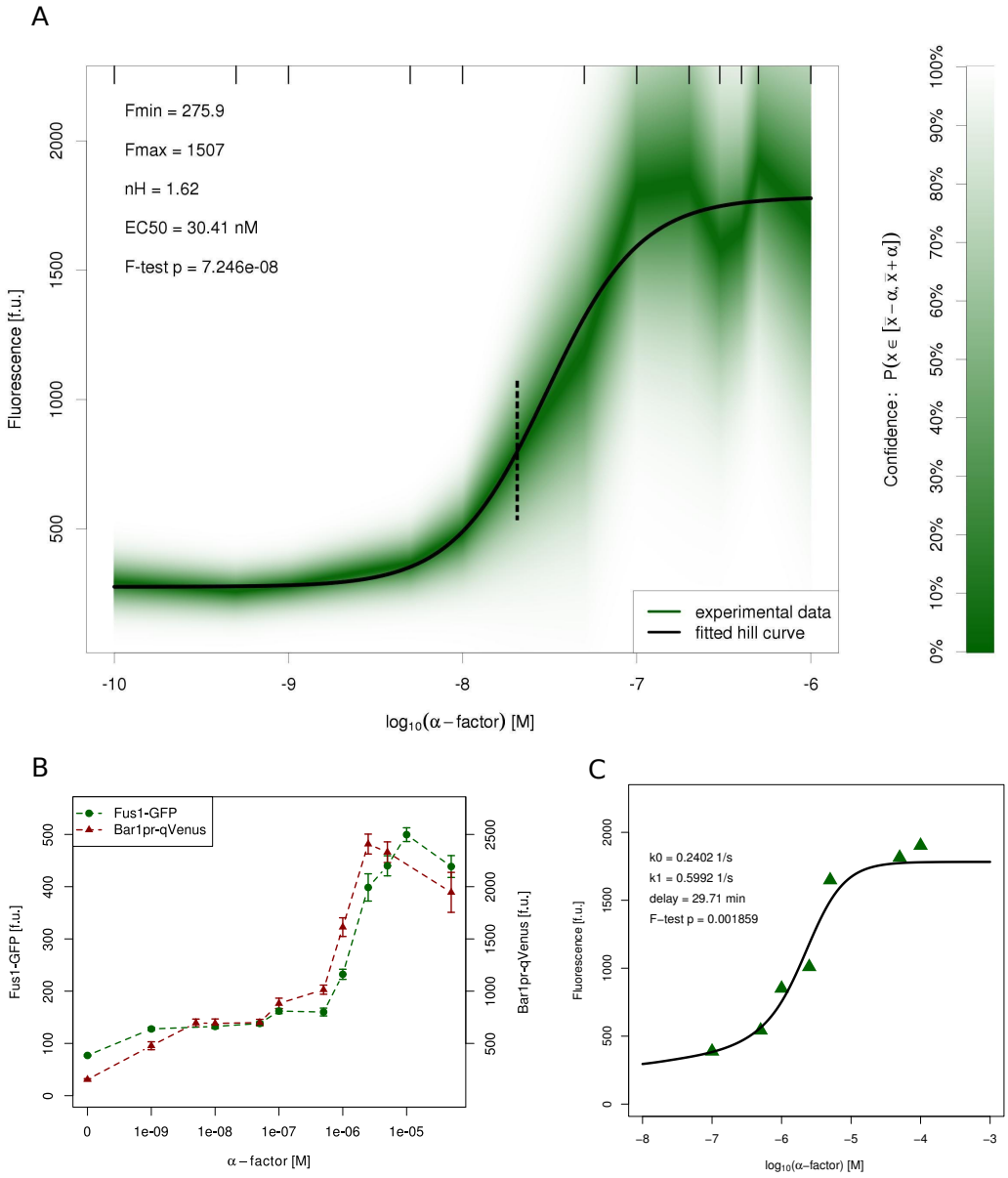

Figure 2.3: **Quantification of the relation between Bar1-activity and Fus1-GFP expression.** **A:** Calibration experiment used to link Fus1-GFP fluorescence to local $\boldsymbol{\alpha}$-factor concentrations for *MAT***a** *bar*1Δ cells. The green band illustrates the distribution of measured fluorescence values from 2965 cells. Relevant $\boldsymbol{\alpha}$-factor concentrations observed in the experiments with wild type mating mixes never exceeded 20 nM (dashed line). **B:** Comparison of the Fus1-GFP expression to the Bar1pr-qVenus expression measured by fluorescence. Error bars denote standard deviation (643 *MAT***a** cells for Fus1-GFP and 578 *MAT***a** cells for Bar1pr-qVenus). **C:** Results of approximating the Bar1 activity kinetics. The green triangles indicate the mean values of measured fluorescence for 2.458 *MAT***a** cells. The Bar1 activitiy was normalized by cell number per volume. Figure from Diener et al. (2014).

This system describes the extracellular dynamics of $\boldsymbol{\alpha}$-factor concentration, $\alpha(\mathbf{x}, t)$, and the activity of Bar1, $B(\mathbf{x}, t)$, at position, $\mathbf{x}$, in space and over time, t. The equations comprise two types of processes: (1) diffusion of both $\boldsymbol{\alpha}$-factor and Bar1, where D_α and D_B are diffusion coefficients (Δ denotes the Laplacian), and (2) degradation of $\boldsymbol{\alpha}$-factor by Bar1. Boundary conditions at the cell surfaces define secretion of $\boldsymbol{\alpha}$-factor by $MAT\boldsymbol{\alpha}$ cells and induced secretion of Bar1 by $MAT\mathbf{a}$ cells.

The secretion of $\boldsymbol{\alpha}$-factor by the $MAT\boldsymbol{\alpha}$ cells was described as a flux boundary condition

$$D_\alpha \nabla \alpha(\mathbf{x}, t) \cdot \mathbf{n} = \begin{cases} -J_\alpha, & \text{on the surface of } MAT\boldsymbol{\alpha} \text{ cells,} \\ 0, & \text{otherwise.} \end{cases} \tag{2.3}$$

The vector $\mathbf{n}$ points towards the cell interior and therefore, the flux $D_\alpha \nabla \alpha(\mathbf{x}, t) \cdot \mathbf{n}$ at the cell boundary takes a negative value for the secretion of molecules. The induction of Bar1 activity at each $MAT\mathbf{a}$ cell is calculated from the average $\boldsymbol{\alpha}$-factor concentration at the surface of the corresponding $MAT\mathbf{a}$ cell. The Bar1 response is described by a Hill-curve as above and modelled as a Dirichlet-Boundary condition for the Bar1 activity

$$B(\mathbf{x}, t) = B_i(t) \text{ on the surface of } MAT\mathbf{a} \text{ cells.} \tag{2.4}$$

For all other boundaries a zero-flux condition was assumed for $B(\mathbf{x}, t)$. In Diener et al. (2014) we used a FEM method to solve the system of RD equations. Details of the numerical scheme and as well as convergence of the time dependent problem can be found in my diploma thesis (Giese, 2010) as well as simulations for a number of cell arrangements. This numerical scheme was revisited again in Diener (2012) with emphasis on the solution of the stationary equation system and parameter optimization methods with respect to the microscopy data. A more concise description can be found in Diener et al. (2014). Simulations on the basis of microscopy data with the fitted parameters are shown in Figure 2.4.

In the following paragraphs, I shall go beyond our investigations from Diener et al. (2014) by developing a complementary computational approach that serves as comparison and confirmation of the published model. Furthermore, the extended model allows for deeper analysis and covers additional aspects of the yeast communication as the response of the $MAT\boldsymbol{\alpha}$ cells to $\mathbf{a}$-factor.

Spatial Modelling of Intercellular Communication Using Cellular Automata Models

In the subsequent sections, main features of cellular communication occurring in mating mixtures are modelled using a cellular automata (CA) model as in Maire and Youk (2015). This approach is based on an analogy to electrodynamics Barkai et al. (1998), to explain the impact of Bar1 on the pheromone

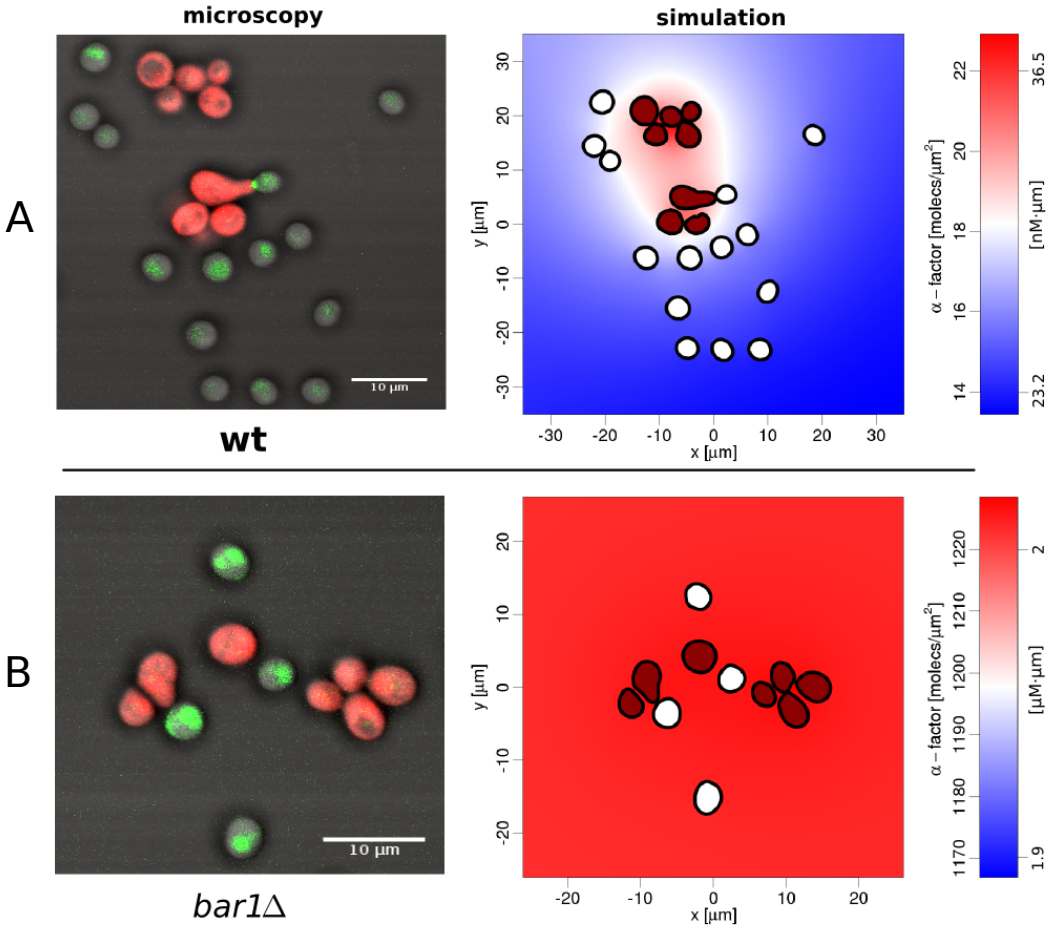

Figure 2.4: **Microscopic images and simulated $\boldsymbol{\alpha}$-factor distributions.** **A**: Mix of wild type cells. **B**: Mix of *MAT*$\boldsymbol{\alpha}$ and *bar*1Δ cells. **A** and **B**: The microscopic images are an overlay of the bright-field, mCherry (for *MAT*$\boldsymbol{\alpha}$) and GFP channels (for Fus1 expression in *MAT***a**) as in Figure 2.2. Computed images (right) show *MAT*$\boldsymbol{\alpha}$ in red and *MAT***a** in white. The extracellular $\boldsymbol{\alpha}$-factor distribution is calculated based on the assumed reaction-diffusion model, the boundary conditions for Bar1 (not shown) at the *MAT***a** cells match the expression Fus1-GFP expression on the bases of experimentally obtained calibration curves. Note the different scales for $\boldsymbol{\alpha}$-factor for wild type (**A**) and *bar*1Δ (**B**). Figure from Diener et al. (2014)

distribution. The Poisson equation for a single point charge at the origin of the coordinate system reads

$$-\epsilon\Delta\phi(\mathbf{x}) = 4\pi\delta(\mathbf{x}) \tag{2.5}$$

Electrodynamics Analogy

with the solution $\phi(\mathbf{x}) = 1/\|\mathbf{x}\|$. The stationary pheromone distribution of a single point source which is secreting pheromone can also be described by a stationary diffusion equation

$$-D_\alpha\Delta\alpha(\mathbf{x}) = 4\pi\delta(\mathbf{x}), \tag{2.6}$$

with a similar solution. Adding a degradation term $-K_B\alpha(\mathbf{x})$, we get the equation

$$-D_\alpha\Delta\alpha(\mathbf{x}) = 4\pi\delta(\mathbf{x}) - K_B\alpha(\mathbf{x}), \tag{2.7}$$

with a solution of the form

$$\alpha(\mathbf{x}) \propto \frac{1}{\|\mathbf{x}\|}\exp(-\|\mathbf{x}\|/\lambda), \tag{2.8}$$

where $\lambda = \sqrt{D_\alpha/K_B}$. Similar analytical solutions of the diffusion equation have been used in Jin et al. (2011); Rappaport and Barkai (2012) to describe the $\boldsymbol{\alpha}$-factor pheromone distribution of a single yeast cell or four yeast cells in an ascus, respectively.

Communication motifs of yeast mating mixes at the level of a cell population with a few hundred cells have not been investigated by this method. Also, cellular responses such as regulation of Bar1 protease levels, induced pheromone secretion and cell cycle arrest were neglected in former models. The approach used in Maire and Youk (2015) demonstrated how communication motifs in abstracted multicellular systems can be explored. Multicellular systems with only one cell type were investigated in that study, which is not appropriate for mating yeast where $MAT\mathbf{a}$ and $MAT\boldsymbol{\alpha}$ cells occur. Therefore, I extended the method from Maire and Youk (2015) to describe the pheromone distribution with the focus of cellular responses that occur in the yeast system.

Model 0: The Effect of Extracellular Bar1 on α-factor Gradients

In the following considerations, the model from Barkai et al. (1998) was taken as null hypothesis. The numerical computation was performed with slight modifications of Barkai et al. (1998), which are explained in the following and finally compared to the original study for validation. For the setup, an arbitrary arrangement $MAT\mathbf{a}$ and $MAT\boldsymbol{\alpha}$ cells was assumed, where N_α denotes the number of cells of mating type $MAT\boldsymbol{\alpha}$ and N_a the number of cells of mating type $MAT\mathbf{a}$. The pheromone concentration in the extracellular space is described by a function $\alpha(\mathbf{x}, t)$, which depends on space, $\mathbf{x}$, and time, t. The

Bar1 concentration is described as well as a function $b(\mathbf{x}, t)$ of space and time. The diffusion and reaction processes of the pheromone in the extracellular medium was modelled using a reaction-diffusion equation of the form

$$\frac{\partial \alpha(\mathbf{x}, t)}{\partial t} = D_\alpha \Delta \alpha(\mathbf{x}, t) - k_B b(\mathbf{x}, t)\alpha(\mathbf{x}, t) - k_\alpha \alpha(\mathbf{x}, t) + p_\alpha(\mathbf{x}, t). \tag{2.9}$$

The constant D_α is the diffusion coefficient, k_B is a bimolecular reaction constant to describe the degradation of $\boldsymbol{\alpha}$-factor by Bar1, k_α is a comparably small auto degradation rate and p_α is a source/production term, which describes the pheromone production by the $MAT\boldsymbol{\alpha}$ cells. An analytical solution of equation (2.9) with some simplifying assumptions regarding the boundary conditions was used to describe the steady state of the pheromone distribution as in Barkai et al. (1998). We assume that all $MAT\boldsymbol{\alpha}$ cells are numbered $1, \ldots, N_\alpha$, and pick the i-th cell, with $i \in \{1, \ldots, N_\alpha\}$. The position of cell i is described by a vector $\mathbf{x}_i$ in 3D space. It was assumed that the pheromone concentration is completely diluted far away from this cell, i.e.

$$\lim_{\|\mathbf{x}-\mathbf{x}_i\|\to\infty} \alpha_i(\mathbf{x}, t) = 0. \tag{2.10}$$

It was assumed that all cells except of this secreting $MAT\boldsymbol{\alpha}$ cell are monitoring cells. Furthermore, the pheromone concentration is calculated at steady state with a homonegeneous Bar1 activity in space and time (meaning $b(\mathbf{x}, t) \equiv \text{const}$ for all $\mathbf{x}$ in the computational domain and times t). The degradation was therefore described as $K_B = k_b b + k_\alpha$. The secreting cells were treated as point sources at positions $\mathbf{x}_i$. Therefore, the source term in equation (2.9) becomes

$$p_\alpha(\mathbf{x}) = \sum_{i=0}^{N_\alpha} p_i \delta(\mathbf{x} - \mathbf{x}_i). \tag{2.11}$$

In Barkai et al. (1998), the equation system was investigated with dimensionless parameters and, therefore, p_i was set equal to an arbitrary constant equal for all cells $i \in \{1, \ldots, N_\alpha\}$. The steady state of the pheromone distribution was then given by

$$\alpha(\mathbf{x}) = \sum_{i=0}^{N_\alpha} \frac{1}{\|\mathbf{x} - \mathbf{x}_i\|} \exp\left(-\|\mathbf{x} - \mathbf{x}_i\|/\lambda\right), \tag{2.12}$$

where $\lambda = \sqrt{D_\alpha / K_B}$.

In the original work it was shown that pheromone gradients get sharper and less ambiguous the more protease is present in the medium. Here, this observation was reproduced with the same model equations, but with the difference that all cells were distributed with midpoints in the x-y-plane and not arbitrarily in 3D space. As in Barkai et al. (1998) cells were assumed to be perfect 'compasses' that orient along the pheromone gradient that is sensed at the respective position. Simulations of 200 randomly distributed cells ($N_a = N_\alpha = 100$) in a square of 100 $\mu m \times 100$ μm were performed for

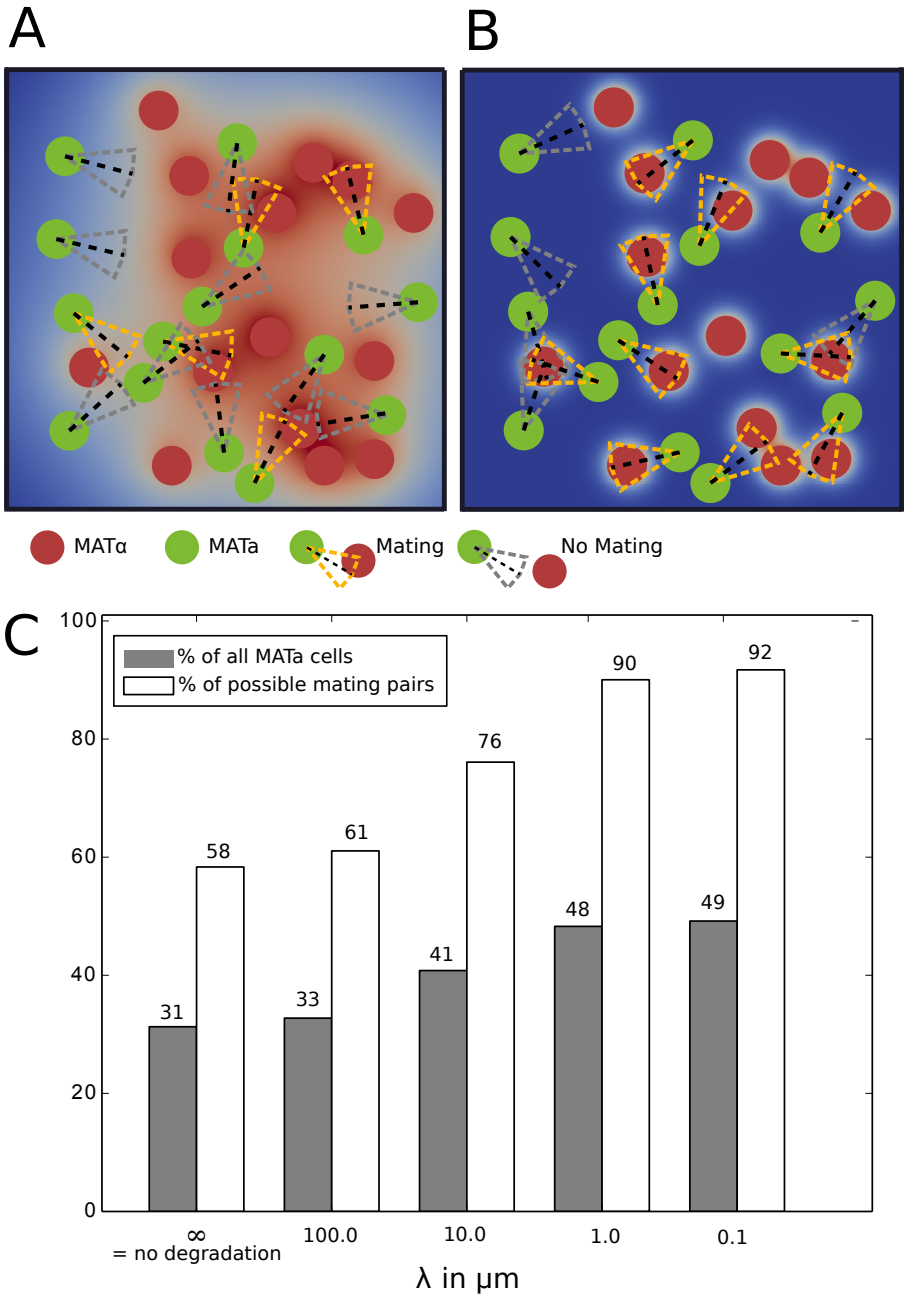

Figure 2.5: **Simulations of model 0 for different assumption on the Bar1 activity.** **A:** Example of a simulation of 15 *MAT***a** and 15 *MAT*$\boldsymbol{\alpha}$ cells with $\lambda = 100\ \mu m$. Dashed segments indicate orientation of the *MAT***a** cells on the basis of the local pheromone gradient as well as the potential reach of the mating projection. Orange segments indicate potential mating successes (segment is touching a *MAT*$\boldsymbol{\alpha}$ cell). Segments assumed to be two times the cell diameter of the corresponding *MAT***a** long and 45° (angle at the cell centre) wide. **B:** Same arrangement of cells as in (**A**), but simulated with $\lambda = 0.1\mu m$. Due to the Bar1 activity the number of potential mating successes rises from 5 (in **A**) to 10 (**B**). **C:** Simulation of 10000 cells (5000 *MAT*$\boldsymbol{\alpha}$, 5000 *MAT***a**) in random arrangements for different values of λ. Grey bars indicate the fraction of the total number *MAT***a** cells that were successfully oriented, while white bars indicate the percentage of successfully oriented cells corresponding to the number of the maximal possible mating pairs regarding the given cell arrangement.

five different values of λ. Each simulation was repeated 50 times. A successful match of cells of opposite mating type was calculated as follows: It was assumed that a cell manages to reach a mating partner if a prescribed triangular segment (compare Figure 2.5 **A,B**) of length 1.5× cell diameter and an angle of 45° reaches a potential mating partner. Cells were assumed to have a diameter of 5 μm for these simulations. Furthermore, an algorithm was used to calculate the maximal number of mating pairs depending on the cell distances, e.g. in case a $MAT\mathbf{a}$ cell is only surrounded by other $MAT\boldsymbol{\alpha}$ cells and no $MAT\boldsymbol{\alpha}$ cell is close enough, there was no successful orientation possible for this $MAT\mathbf{a}$ cell. This leads to two different statistical numbers, which are the total fraction of successful mating pairs compared to the number of $MAT\mathbf{a}$ cells and the number of mating pairs compared to the highest possible number of mating events. Both values were calculated for each simulation and the average over all simulations was plotted in Figure 2.5**C**.

The obtained results were comparable to the results from Barkai et al. (1998). High values of λ led to many falsely oriented cells, whereas low values of λ led to very accurately oriented cells. It should be noted that for high values of λ the improvement is only slight. From no Bar1($\lambda = \infty$) to a low Bar1 level ($\lambda = 100\ \mu m$) there was only an improvement from 58% to 61%. For one magnitude less $\lambda = 10\ \mu m$ the efficiency was much better, but still only at 76%. Note, that for λ to change by a factor of 10 the Bar1 actvity has to be increased by a factor of 100.

In a subsequent work (Rappaport and Barkai, 2012), the same author argued that using the estimated diffusion coefficient of $D_\alpha \approx 300\ \mu m^2/s$ and a degradation rate $K_B \approx 1/60\ s^{-1}$, the constant becomes $\lambda \approx 134\ \mu m$. Since yeast cells usually have a diameter of $4\ \mu m - 8\ \mu m$ and mating projections are rarely longer then the cell diameter, it was argued that the degradation term does not act in the effective distances relevant for mating. For higher Bar1 activity levels assumed in Jin et al. (2011) and Diener et al. (2014), we still have $\lambda > 20\ \mu m$, which is far from the value of λ that is needed for strong improvement of the alignment. In the next section I shall work out a second important role of Bar1 in regulating absolute pheromone concentrations and coordinating of mating and vegetative growth.

Model 1: A Trade-off Between Vegetative Growth and Mating

Since a high Bar1 activity also lowers the pheromone concentration dramatically, there is a trade-off between sharp unambiguous pheromone gradients and the necessity to secret large amounts of pheromone and Bar1. Here, this trade-off is investigated by parameterizing the system with values obtained from Diener et al. (2014). The communication motif is shown in Figure 2.6 **A,B**. $MAT\boldsymbol{\alpha}$ cells secrete $\boldsymbol{\alpha}$-factor which is sensed by the $MAT\mathbf{a}$ cells. The cell cycle is only arrested if the sensed concentration reaches a certain threshold. In this case cells polarize, orient along the pheromone gradient and initiate

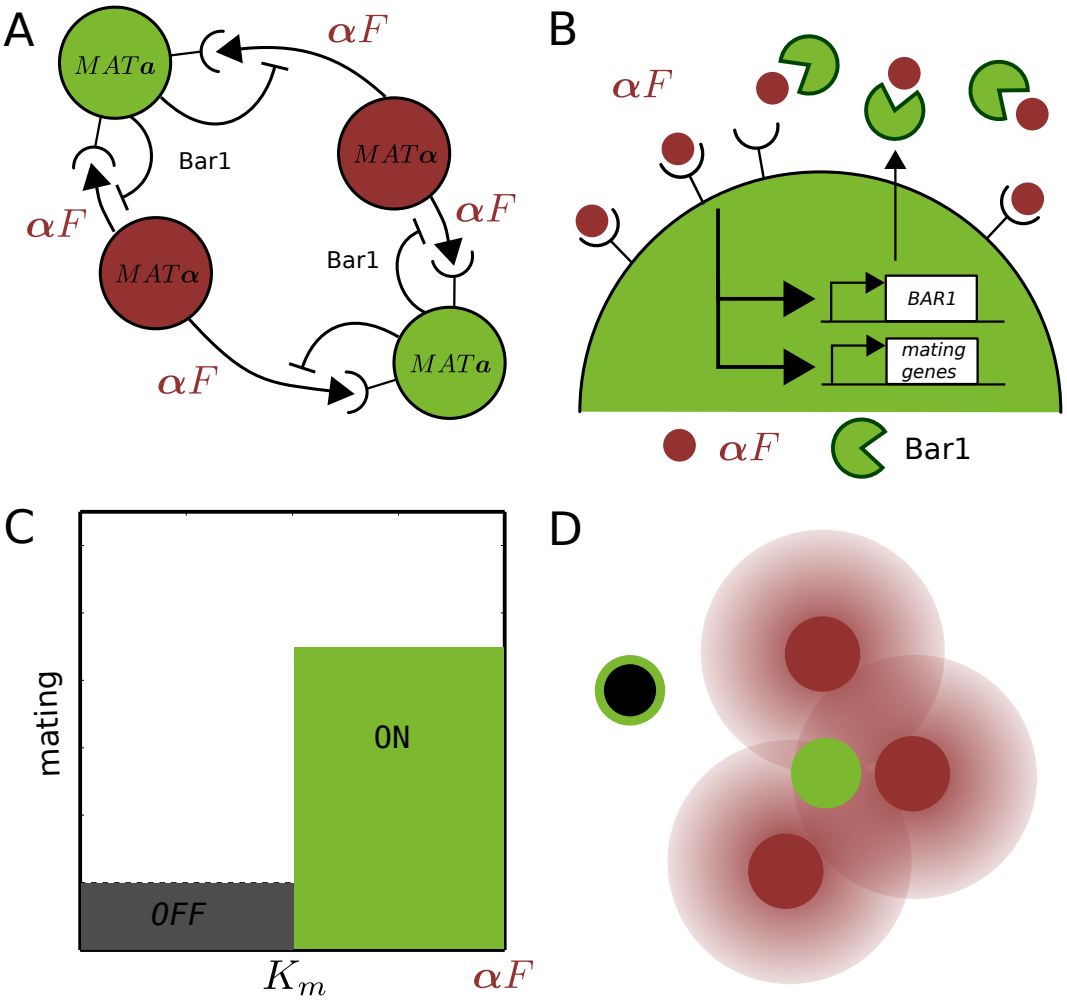

Figure 2.6: **Intercellular communication motif for model 1. A:** $MAT\boldsymbol{\alpha}$ cells secrete $\boldsymbol{\alpha}$-factor, which is sensed by $MAT\mathbf{a}$ cells. In turn $MAT\mathbf{a}$ cells degrade $\boldsymbol{\alpha}$-factor by secreting Bar1. **B:** Upon pheromone sensing the expression of Bar1 as well as mating relevant genes is increased. **C:** If the sensed $\boldsymbol{\alpha}$-factor concentration reaches the threshold value K_m the cell cycle is arrested and mating relevant genes are expressed. **D:** Illustration of an arrangement with three $MAT\boldsymbol{\alpha}$ cells (red) and two $MAT\mathbf{a}$ cells (green). $MAT\boldsymbol{\alpha}$ cells secrete $\boldsymbol{\alpha}$-factor (light red), which diffuses through the extracellular space. The $MAT\mathbf{a}$ cell that senses a high pheromone ($> K_m$) concentration arrests its cell cycle (green), the other $MAT\mathbf{a}$ cell (black, green ring) continues its cell cycle.

mating. Therefore, cells can be "on" (mating is initiated, cycle is arrested) or "off" (no mating, cell cycle is continued). A sketch of this process is shown in Figure 2.6 **C,D**. All parameters used are shown in Table 2.1. For the parameterization the cells are no longer assumed to be point sources, but spheres with radius R_i with $i \in \{1, \ldots, N_\alpha\}$. The pheromone secretion of the $MAT\boldsymbol{\alpha}$ cells was described as a Neumann boundary condition on the surface of each $MAT\boldsymbol{\alpha}$ cells:

$$-D\nabla\alpha(\mathbf{x}) \cdot \mathbf{n} = J_{\alpha,i}. \tag{2.13}$$

In this case the steady state solution reads

$$\begin{aligned} \alpha_i(\mathbf{x}) &= \alpha_i^S \frac{R_i}{\|\mathbf{x} - \mathbf{x}_i\|} \exp\left(-(\|\mathbf{x} - \mathbf{x}_i\| - R_i) \cdot \sqrt{\frac{K_B}{D_\alpha}}\right), \\ \alpha_i^S &= J_{\alpha,i} \frac{R_i}{R_i\sqrt{D_\alpha \cdot K_B} + D_\alpha}. \end{aligned} \tag{2.14}$$

Here, α_i^S is the concentration on the surface of the *i-th* cell. Let P_α be a production rate of pheromone molecules per time and volume (with units nM/s), which is assumed to be constant. The production rate of pheromone molecules per time for the *i-th* $MAT\boldsymbol{\alpha}$ cell is given by $p_i = V_i^{\text{cell}} \cdot P_\alpha$ and, hence, depends on the cell volume. The flux $J_{\alpha,i}$ is computed from $J_{\alpha,i} = P_\alpha \cdot V_i^{cell}/A^{cell} = P_\alpha \cdot R_i/3$. In equilibrium the total molecular mass of pheromone in the medium that is attributed to the *i-th* $MAT\mathbf{a}$ cell is given by

$$\int_{\mathbb{R}^3} \alpha_i(\mathbf{x}) dV = \begin{cases} 4\pi \frac{D_\alpha}{K_B} \alpha_i^S R_i & K_B \neq 0, \\ \infty & K_B = 0.. \end{cases} \tag{2.15}$$

(See Appendix A for derivation). These pheromone distributions are summed up for all $MAT\boldsymbol{\alpha}$ cells, which results in the total $\boldsymbol{\alpha}$-factor concentration:

$$\alpha(\mathbf{x}) = \sum_{i=1}^{N_\alpha} \alpha_i^S \frac{R_i}{\|\mathbf{x} - \mathbf{x}_i\|} \exp\left(-(\|\mathbf{x} - \mathbf{x}_i\| - R_i) \cdot \sqrt{\frac{K_B}{D_\alpha}}\right). \tag{2.16}$$

Note, that although we parameterized the system assuming a spherical cell, the system is still based on the assumption that in fact all cells are monitoring. In experiments carried out in Diener et al. (2014), the cells sedimented on the ground of glass bottom dishes. Therefore, I assumed a zero-flux boundary condition for the pheromones on this surface. To describe the influence of the surface on the cells, I used the method of imaginary charges which is described in Jackson (1983). I applied this method to the diffusion model (see Appendix A 7.1). I assumed a surface in the x-y-plane with cell positions $\mathbf{x}_i = (x_i, y_i, R_i)$, where R_i is the radius of cell i. The auxiliary cell positions are denoted with $\hat{\mathbf{x}}_i = (x_i, y_i, -R_i)$. The accumulated pheromone distribution was calculated

from

$$\alpha(\mathbf{x}) = \sum_{i=1}^{N_\alpha} \alpha_i^S R_i \left[\frac{1}{\|\mathbf{x} - \mathbf{x}_i\|} \exp\left(-(\|\mathbf{x} - \mathbf{x}_i\| - R_i) \cdot \sqrt{\frac{K_B}{D_\alpha}} \right) + \frac{1}{\|\mathbf{x} - \hat{\mathbf{x}}_i\|} \exp\left(-(\|\mathbf{x} - \hat{\mathbf{x}}_i\| - R_i) \cdot \sqrt{\frac{K_B}{D_\alpha}} \right) \right]. \tag{2.17}$$

In this case the pheromone distribution of each single cell is given by

$$\alpha_i(\mathbf{x}) = \alpha_i^S R_i \left[\frac{1}{\|\mathbf{x} - \mathbf{x}_i\|} \exp\left(-(\|\mathbf{x} - \mathbf{x}_i\| - R_i) \cdot \sqrt{\frac{K_B}{D_\alpha}} \right) + \frac{1}{\|\mathbf{x} - \hat{\mathbf{x}}_i\|} \exp\left(-(\|\mathbf{x} - \hat{\mathbf{x}}_i\| - R_i) \cdot \sqrt{\frac{K_B}{D_\alpha}} \right) \right]. \tag{2.18}$$

The total number of pheromone molecules attributed to this cell is given by integration of its pheromone contribution over the upper half space ($\mathbb{R} \times \mathbb{R} \times \mathbb{R}^+$), which represents the space above the glass bottom dish. Integration gives

$$\int\limits_{\mathbb{R}\times\mathbb{R}\times\mathbb{R}^+} \alpha_i(\mathbf{x}) dV = \begin{cases} 4\pi \frac{D_\alpha}{K_B} \alpha_i^S R_i & K_B \neq 0, \\ \infty & K_B = 0. \end{cases} \tag{2.19}$$

which is the same as in Equation (2.15). Simulations with a number of different values for K_B are shown in Figure 2.7, where the pheromone distribution along the x-y-plane was plotted. For low Bar1 activity a high fraction of $MAT\mathbf{a}$ cells arrested their cell cycle to initiate mating. This occurred even when there was no mating partner in their reach (Figure 2.7 **A**). For intermediate Bar1 activity levels, a lower fraction of cells arrested their cell cycle only if a mating partner was in reach, which led to a much higher mating efficiency (Figure 2.7 **B**). [2] However, if the Bar1 activity was too high $MAT\mathbf{a}$ cells only arrested their cell cycle if they were stimulated by more than one mating partner and if a mating partner was very close (Figure 2.7 **C**).

Simulations were performed for three different cell densities, six different levels of Bar1 activity as well as two different diffusion coefficients, 150 $\mu m^2/s$ (Youk and Lim, 2014) and 360 $\mu m^2/s$ (Diener et al., 2014).[3] The simulation outcome is shown in Figure 2.8. The fraction of arrested $MAT\mathbf{a}$ cells was plotted versus the fraction of $MAT\mathbf{a}$ cells that are "on" and are well enough oriented to reach a mating partner. While the fraction of "on" cells decreases with higher Bar1 activity, the number of mating events decreased much slower,

[2] For a yeast cell with arrested cell cylce, 'mating efficiency' refers to the probability to successfully orient and reach a close enough mating partner.

[3] Note that there are two different ranges of values for the diffusion coefficient of $\boldsymbol{\alpha}$-factor in the literature. The higher values are used as 330 μm^2 (Segall, 1993), 300 μm^2 (Rappaport and Barkai, 2012) and 360 $\mu m^2/s$ (Diener et al., 2014). The lower range of diffusion coefficients is given by 127 μm^2 (Andrews et al., 2010), 125 μm^2 (Jin et al., 2011) and 150 μm^2 (Youk and Lim, 2014).

leading to a higher mating efficiency. In conclusion, this means that unnecessary cell cycle arrest is avoided for higher Bar1 concentrations. However, for low cell densities concentration levels were low as well, which led to a lower fraction of cells that were "on". For these low cell densities, higher concentrations of Bar1 inhibit cell cycle arrest as well as mating events completely.

The viscostiy of the extracellular medium is another important aspect, which effects the diffusion of the pheromone molecules in the extracellular medium and has a severe impact on cellular communication. A medium with high viscosity results in a slow pheromone diffusion coefficient, while a medium like water with low viscosity results in a fast diffusion coefficient of pheromones. The overall accuracy is much lower for faster diffusion (Figure 2.8 **A**) than for slower diffusion (Figure 2.8 **B**), since signalling is more localized in this case.

The simulation outcome can be compared with experimental measurements (Figure 2.9). Here, the number of diploid formations was measured over time and for different cell densities. The results from the computations can only be compared with the numbers obtained after 1 h to 2 h (see Figure 2.9 **A**) before the next cell division cycle is finished. After that time the number of diploids is growing as well as the cell density increases. Also, a comparison has to be done with care, since not every cell that arrests and orients in the right direction initially, will take part in a successful zygote/diploid formation. Therefore, the computations performed are upper bounds for the experimentally observed numbers. In addition, the complementary pheromone **a**-factor has not been considered yet, which will be addressed in models 3a and 3b.

Aspects of Distances, Time Scales and Dimension

Here, an overview on spatial and temporal scales that are important for the extracellular communication process is given. First, the diffusion coefficient is discussed, which has a severe impact on the signalling behaviour. As in Andrews et al. (2010), Diener et al. (2014), and Youk and Lim (2014), the diffusion of the pheromone $\boldsymbol{\alpha}$-factor can be estimated using the Stokes-Einstein relation

$$D = \frac{k_B T}{6\pi\eta r_M}, \tag{2.20}$$

where k_B is the Boltzman constant, T is the temperature, η is the viscosity of the medium and r_M is the molecular radius of one pheromone molecule. Since it is generally assumed that r_M scales with the molecular weight M as $r_M \sim M^{1/3}$, a 1000-fold change in the molecular weight causes the diffusion coefficient to change by a factor of 10. Although I used a more elaborated formula for the molecular density and radius for peptides as well as proteins from Fischer et al. (2004) (see Appendix 7.1 for details), the scaling roughly holds. Therefore, the dominant term that governs the diffusion coefficient is the viscosity of the extracellular medium. Note that in Andrews et al. (2010), a viscosity of $\eta = 2.0 mPa \cdot s$ was assumed for the medium in an ascus, which can also be assumed for media like grape juice. This results in a slow

Variable	Value	Description	Model(s)
D_α	360 $\frac{\mu m^2}{s}$	diffusion rate of $\boldsymbol{\alpha}$-factor (estimated see Appendix A)	all
D_a	350 $\frac{\mu m^2}{s}$	diffusion rate of **a**-factor (estimated see Appendix A)	3
P_α	360.0 nM/s	production rate of $\boldsymbol{\alpha}$-factor by $MAT\boldsymbol{\alpha}$ cells	0,1,2
R	2.5 μm	cell radius	0
R_i	2 μm - 3.5 μm	radius of the *i-th* cell	1-3
$K_{M,a}$	5.5 nM	minimal **a**-factor concentration needed for cell cycle arrest	1-3
$K_{M,\alpha}$	5.5 nM	minimal $\boldsymbol{\alpha}$-factor concentration needed cell cycle arrest of $MAT\mathbf{a}$ cells	1-3
$k_{0,\text{bar1}}$	0.24 s^{-1}	basal Bar1 activity	2-3
$k_{1,\text{bar1}}$	0.6 s^{-1}	pheromone induced Bar1 activity	2-3
P_α^{base}	180.0 nM/s	basal production rate of $\boldsymbol{\alpha}$-factor by $MAT\boldsymbol{\alpha}$ cells	3
P_α^+	360.0 nM/s	induced production rate of $\boldsymbol{\alpha}$-factor by $MAT\boldsymbol{\alpha}$ cells	3
P_a^{base}	90.0 nM/s (3a), 180.0 nM/s (3b)	basal production rate of **a**-factor by $MAT\boldsymbol{\alpha}$ cells	3
P_a^+	180.0 nM/s (3a), 360.0 nM/s (3b)	induced production rate of **a**-factor by $MAT\boldsymbol{\alpha}$ cells	3
H_a	-	Hill coefficient for induction of $\boldsymbol{\alpha}$-factor secretion by $MAT\boldsymbol{\alpha}$ cells due to **a**-factor sensing	3
H_α	-	Hill coefficient for induction of **a**-factor secretion by $MAT\mathbf{a}$ cells due to $\boldsymbol{\alpha}$-factor sensing	3
$k_{0,\text{afb1}}$	0.24 s^{-1}	basal Afb1-activity	3b
$k_{1,\text{afb1}}$	0.6 s^{-1}	pheromone induced Afb1-activity	3b

Table 2.1: Overview of parameters and their values used in models 0-3. Note that if not otherwise states 'model 3' refers to models 3a and 3b.

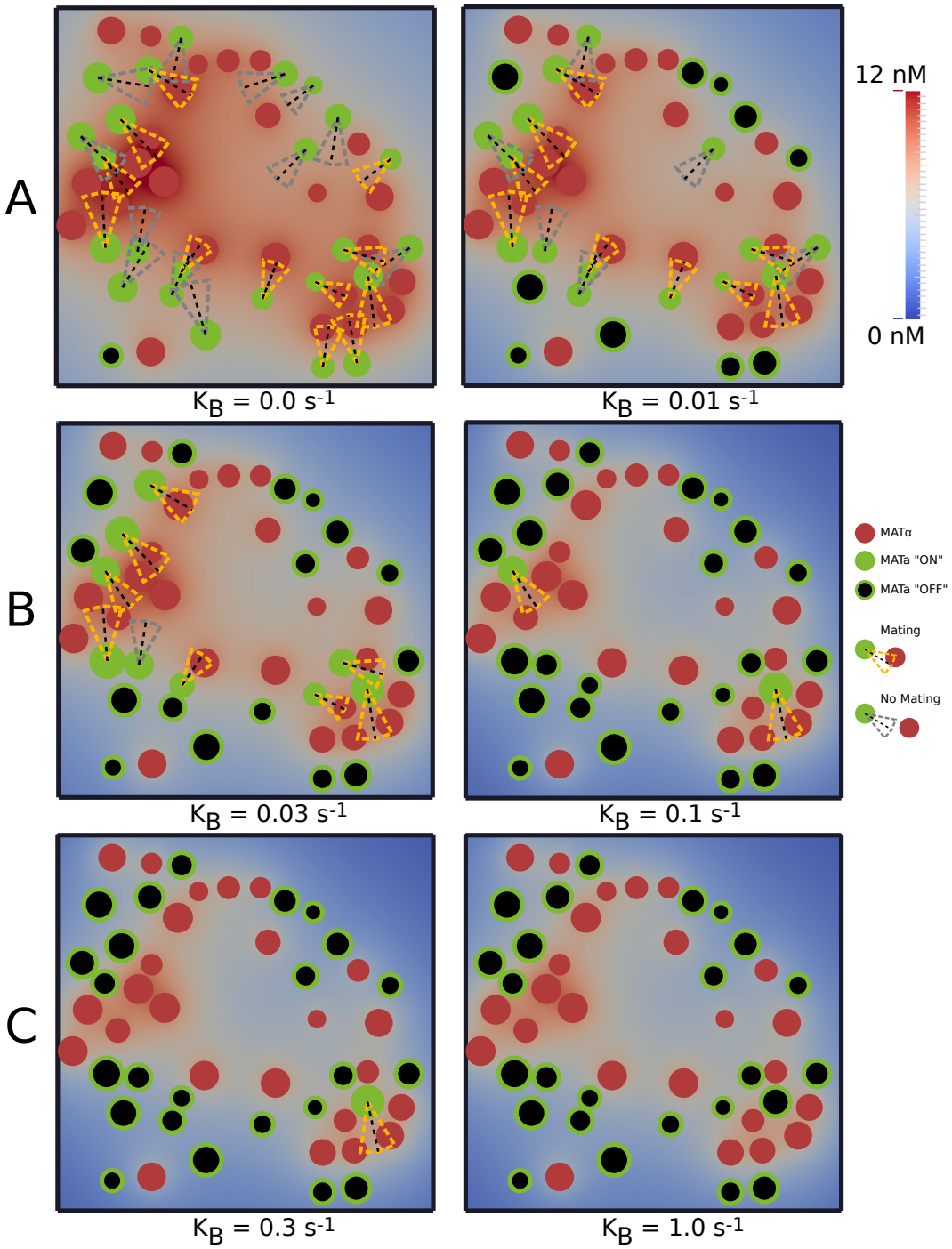

Figure 2.7: **Simulations of model 1 with varying Bar1 activity.** An arrangement with 25 *MAT*$\boldsymbol{\alpha}$ and 25 *MAT***a** cells was simulated for different levels of Bar1 activity (values are indicated below the images). Dashed segments indicate the range and orientation of arrested *MAT***a** cells (green), while non-arrested *MAT***a** cells are coloured in black. In case cells were able to reach a mating partner (which is not already occupied by a closer *MAT***a** cell), dashed segments are highlighted in red. **A:** For low Bar1 activity a high fraction of *MAT***a** cells arrest their cell cycle, independent of their actual proximity to a mating partner. **B:** For intermediate Bar1 activity levels, cells arrest their cell cycle only if a mating partner is close enough, which leads to higher mating efficiency. **C:** In case of high Bar1 activity mating is rare, since *MAT***a** cells do not arrest their cell cycle.

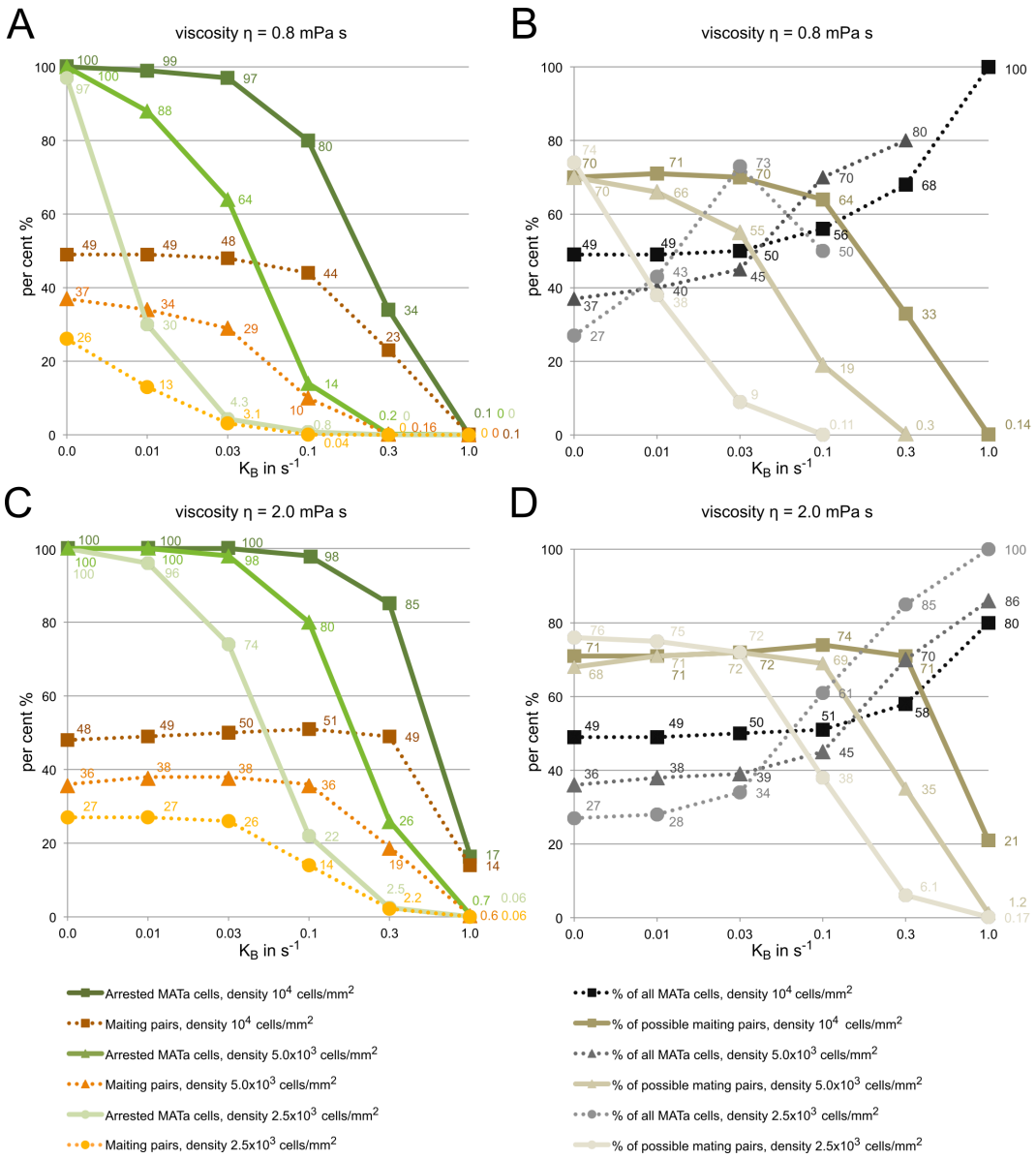

Figure 2.8: **Simulations of model 1 for different cell densities, viscosities and Bar1 activity levels.** Simulations were performed with randomized arrangements of 10,000 cells for each density, viscosity and level of Bar1 activity. **A:** Simulations with low viscosity and fast diffusion, $D_\alpha = 360\ \mu m^2/s$. Green coloured curves indicate the fraction of arrested $MAT\mathbf{a}$ cells for different densities, while orange coloured curves indicate the fraction of $MAT\mathbf{a}$ cells that successfully oriented towards a mating partner. **B:** Curves correspond to the simulations in **(A)**, in which squares, triangles, and circles belong to the same set of parameters and simulations. The dark grey and light grey curves indicate the fraction of mating successes corresponding to the number of arrested $MAT\mathbf{a}$ cells and the number of maximal possible mating events in the given cell arrangement. **C:** Simulation for high viscosity and slow diffusion coefficient, $D_\alpha = 150\ \mu m^2/s$. The same colour-coding as in **A** was used. **D:** Curves correspond to the simulations in **(C)**. The same colour-coding as in **(B)** was used.

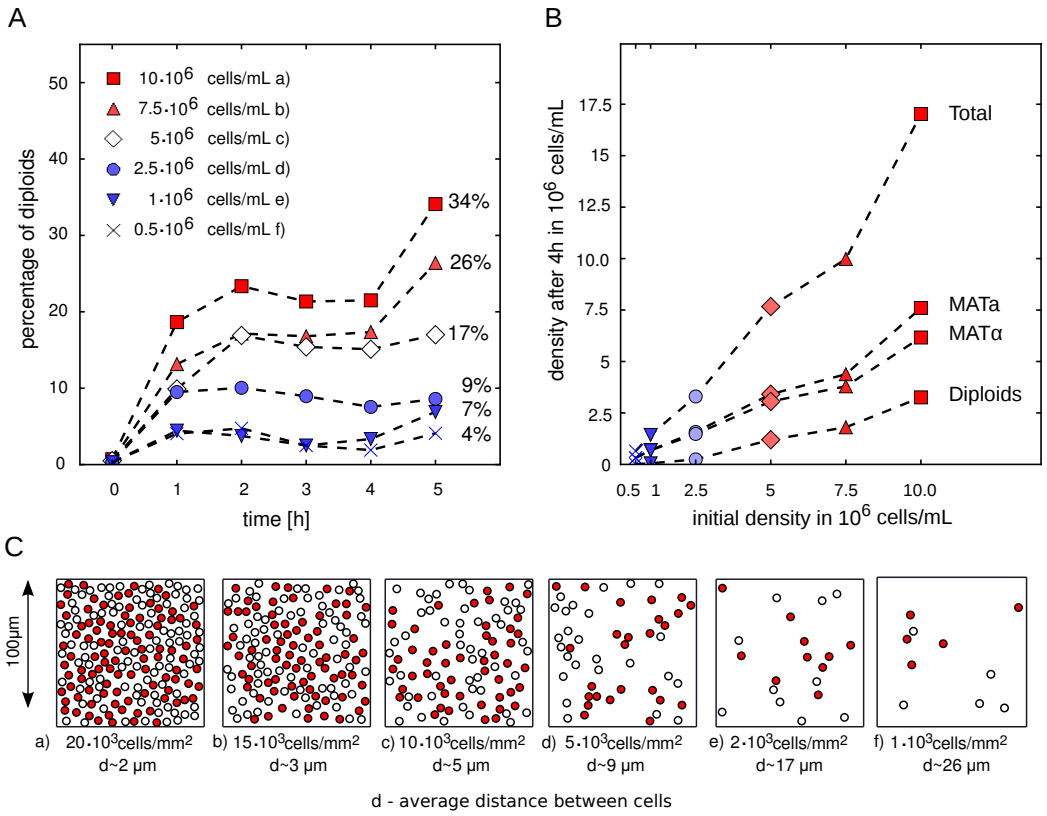

Figure 2.9: **Dependence of diploid formation rate on cell densities.** **A:** Fraction of diploids in mixed populations (50% *MAT***a** 50% *MAT*$\boldsymbol{\alpha}$) measured over time (each data point comprises 5.000 to 260.000 counted cells). The initial cell density at time 0 *h* is indicated in the legend. **B:** Absolute cell numbers of *MAT***a**, *MAT*$\boldsymbol{\alpha}$ and diploid cells after 4 *h*. Note that there is a slightly stronger increase in cell numbers of *MAT***a** cells compared to *MAT*$\boldsymbol{\alpha}$ cells. **C:** Illustration of intercellular distances for populations with various cell densities. These densities correspond to the densities used in the experiments. Figure from Diener et al. (2014).

diffusion coefficient of 127 $\mu m^2/s$. For usual SD or YPD medium a much lower water-like viscosity of $\eta = 0.8\ mPa \cdot s$ has to be assumed, which results in a fast diffusion coefficient of $D_\alpha \approx 360\ \mu m^2/s$. This is also in agreement with empirical estimates of the diffusion coefficient of 330 $\mu m^2/s$ from Segall (1993).

The influence of the diffusion coefficient and Bar1 activity on the pheromone distribution was plotted in Figure 2.10 **A, B**. Here, the steady state distribution was calculated for one secreting cell. Variation of the Bar1 activity changes the concentration profile only slightly in the physical range given in (Jin et al., 2011; Rappaport and Barkai, 2012; Diener et al., 2014) and deploys its impact only for longer distances in the order of $\approx \sqrt{D_\alpha/K_B}$ (compare Figure 2.10 **A**). The order of $\lambda = \sqrt{D_\alpha/K_B}$ varied from $\lambda \approx 19\ \mu m$ to $\lambda \approx 190\ \mu m$, for $K_B = 1.0\ s^{-1}$ to $K_B = 0.01\ s^{-1}$, respectively. However, the diffusion has a much more severe impact on the concentration level at the surface and in the vicinity of the cell. Recall, the pheromone concentration at the cell surface is given by $\alpha_i^S = J_{i,\alpha}\frac{R}{R\sqrt{D_\alpha \cdot K_B}+D_\alpha}$ (compare equation 2.14). Since $R\sqrt{D_\alpha \cdot K_B} << D_\alpha$ in the range of physiological Bar1 activity levels, we get $\alpha_i^S \approx J_{i,\alpha}R_i/D_\alpha$. Doubling the diffusion coefficient roughly halves the generated concentration at the cell surface. Therefore, a slower diffusion coefficient leads to a higher pheromone concentrations around the secreting cell (compare Figure 2.10 **B**).

The time scales at which the pheromone propagates and accumulates are investigated in the following. In the case of zero degradation $K_B = 0$, the time dependent RD equation (2.9) can be solved analytically and is given by (Francis and Palsson, 1997):

$$\begin{aligned}\alpha^{\text{nodeg}}(r,t) = \frac{J_{\alpha,i}R}{2Dr}\sqrt{\frac{4Dt}{\pi}}\Bigg[&\exp(-\frac{(r-R)^2}{4Dt}) - \exp(-\frac{(r+R)^2}{4Dt}) \\ &- |r-R|\sqrt{\frac{\pi}{4Dt}}erfc\left(\frac{|r-R|}{\sqrt{4Dt}}\right) \\ &+|r+R|\sqrt{\frac{\pi}{4Dt}}erfc\left(\frac{|r+R|}{\sqrt{4Dt}}\right)\Bigg]. \qquad (2.21)\end{aligned}$$

Here $r = \|\mathbf{x} - \mathbf{x}_i\|$ and without loss of generality the secreting cell is placed at the origin of co-ordinates meaning $\mathbf{x}_i = 0$. The solution of equation (2.9) with nonzero degradation is obtained from

$$\alpha(r,t) = K_B \int_0^t \alpha^{\text{nodeg}}(r,t')\exp(-K_B t')dt' + \alpha^{\text{nodeg}}(r,t)\exp(-K_B t). \quad (2.22)$$

Note that for time-dependent 3D diffusion with degradation no solution is known to the author and, therefore, the integral was solved numerically for the time dependent solution shown in Figure 2.10 **C**. For a closed form of the one-dimensional problem assuming a point source, I refer to (Bergmann et al., 2007). Here, a calculation of the explicit form was circumvented by using the notion of accumulation times as recently introduced in Berezhkovskii et al. (2011). The steady state solution of equation (2.9) is denoted by $\alpha^{SS}(r)$. The

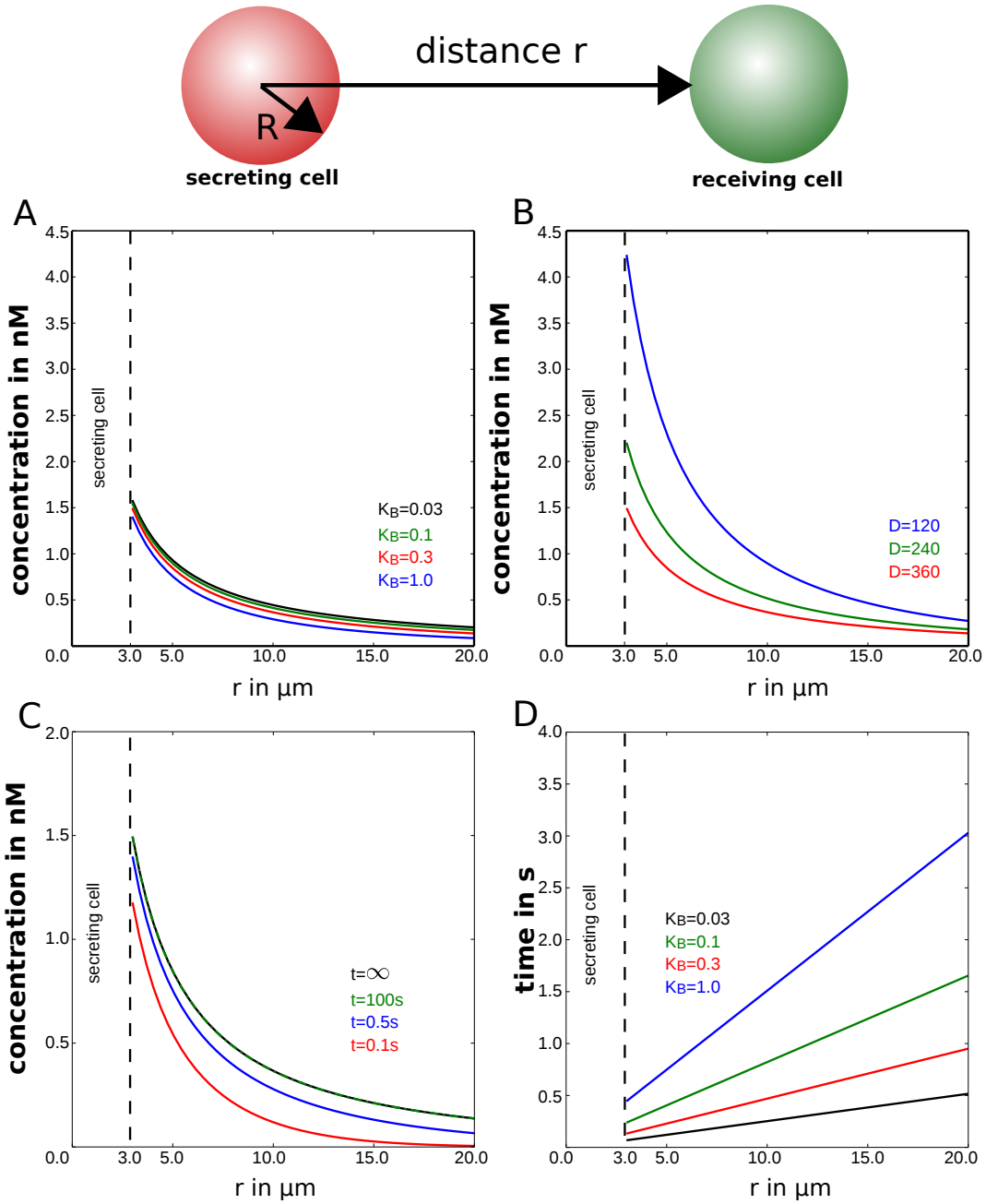

Figure 2.10: **Parameter dependencies on the pheromone distribution induced by a single cell.** Concentration profiles induced by a cell with radius $R = 3\ \mu m$ with midpoint at $\mathbf{x} = (0, 0, 0)$ were calculated. **A:** The Bar1 activity influences the pheromone concentration only in distant regions and thereby, prevents activation of distant cells. However, the impact of Bar1 activity on the pheromone concentration at the cell surface is only marginal. **B:** The impact of the diffusion coefficient on the pheromone concentration is more pronounced for short distances. Values given in the literature ranging from 125 $\mu m^2/s$ (Jin et al., 2011) to 330 $\mu m^2/s$ (Segall, 1993) or 360 $\mu m^2/s$ (Diener et al., 2014) are covered. **C:** The concentration profile was calculated for $D = 360\ \mu m^2/s$ and $K_B = 0.03 s^{-1}$ for different time points and compared to the steady state solution (at $t = \infty$). **D:** Calculation of local accumulation times (see main text for definition) for 360 $\mu m^2/s$ and different Bar1 activity levels. The pheromone concentration reaches steady state levels in the vicinity of the secreting cell in the order of seconds.

fraction of this steady state level that accumulated at distance r and time t is expressed as

$$\rho(r,t) = \frac{\alpha^{SS}(r) - \alpha(r,t)}{\alpha^{SS}(r)}. \tag{2.23}$$

The difference $\rho(r,t_1) - \rho(r,t_2)$ can be interpreted as the fraction of the steady state level $\alpha^{SS}(r)$ that accumulated in the time interval $[t_1, t_2]$. In an infinitesimal time interval $[t, t+dt]$ the fraction of pheromone accumulation at steady state is given by $-\frac{\partial\rho(r,t)}{\partial t}dt$. Note, that $\frac{\partial\rho(\mathbf{x},t)}{\partial t}$ satisfies

$$\int_0^\infty \frac{\partial\rho(r,t)}{\partial t}dt = 1, \tag{2.24}$$

since $\alpha(r,0) \equiv 0$. Based on this expression the local accumulation time is defined as (Berezhkovskii et al., 2011)

$$\tau(r) = -\int_0^\infty t\frac{\partial\rho(r,t)}{\partial t}dt.$$

Although a closed analytical form of the solution cannot be derived in most cases for source-diffusion-degradation (SDD) models, in some cases a closed form of the accumulation times can be derived. I used the result from Gordon et al. (2013) to obtain the accumulation time for equation (2.9), which is given by

$$\tau(r) = \frac{r-R}{2\sqrt{D_\alpha K_B}} + \frac{R}{2K_B(R+\sqrt{D_\alpha/K_B})}. \tag{2.25}$$

The accumulation times are plotted in Figure 2.10 **D** for different levels of Bar1 activity. Note, that the pheromone concentration profile is established within seconds in distances that are relevant for mating. Since mating and directed growth is a process that is occurring in time periods larger than 1 h, the steady state approximation for the diffusion equation is a reasonable assumption.

An important aspect that may lead to alterations or disturbances of the communication is the environment and confinements, which lead to a reduction of spatial dimensions. In Jin et al. (2011) $MAT\boldsymbol{\alpha}$ cells were positioned in a microfluidic chamber of height $h = 5\ \mu m$. This height is just about the average diameter of haploid cells. Therefore, diffusion is limited to two spatial dimensions, the steady state pheromone distribution caused by one cell is therefore given by

$$\alpha_i^{2\mathrm{D}}(\mathbf{x}) = \frac{J_{\alpha,i}}{\sqrt{D_\alpha K_B}}\frac{K_0(r\sqrt{K_B/D_\alpha})}{K_1(R\sqrt{K_B/D_\alpha})}. \tag{2.26}$$

If we consider a thin tube, where diffusion essentially takes place in 1D and the steady state pheromone distribution reads

$$\alpha_i^{1\mathrm{D}}(r) = \frac{J_{\alpha,i}}{\sqrt{D_\alpha K_B}}\exp\left(-(r+R)\sqrt{K_B/D_\alpha}\right). \tag{2.27}$$

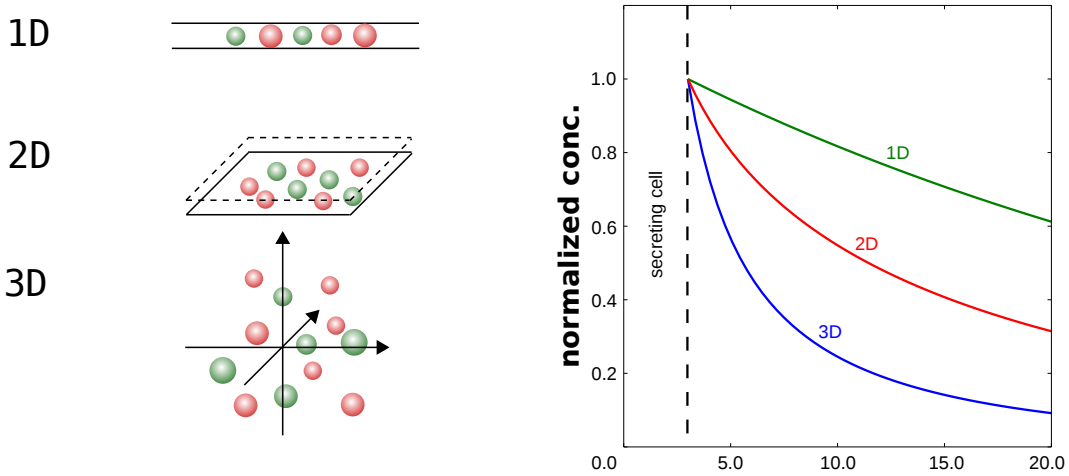

Figure 2.11: **Pheromone distribution in domains with different dimensionality.** The potential impact of system boundaries on the pheromone distribution. **1D:** A on-dimensional distribution might be assumed for cell trapped in a tube. **2D:** Cells in a very thin fluid layer as in a microfluidic device used in Jin et al. (2011) justifies the assumption of 2D diffusion. **3D:** In the case of 3D diffusion the pheromone levels drop faster. The distributions were normalized corresponding to the concentration at the cell surface.

Note, that further interactions with the system boundaries might be taken into consideration. Pheromones might be absorbed by some surfaces or its diffusion might be hindered. For instance, the pheromone **a**-factor has different molecular properties than $\boldsymbol{\alpha}$-factor. **a**-factor is hydrophobic and, therefore, it might stick to some surfaces, which would again lead to different pheromone profiles.

Model 2: Collective Secretion of Bar1 Improves Adaptation to Different Cell Densities

One of the central findings in Diener et al. (2014) was the quantification of the Bar1 activity levels, which are increased upon pheromone stimulation. The relation of $\boldsymbol{\alpha}$-factor stimulation and Bar1 response was described by a Hill-curve, which was fitted to the microscopy data (compare Figure 2.3). The constants $k_{0,bar1}$ and $k_{1,bar1}$, which describe the basal and increased Bar1 activity, were calibrated to a density of $\rho = 10^4\ cells/mm^2$. To perform simulations with different cell densities, the Bar1 activity has to be normalized to the actual density of the (sub)population as in Diener et al. (2014)

$$\tilde{k}_{0,bar1} = k_{0,bar1} \cdot \frac{N_a}{\mathcal{A}}, \tag{2.28}$$

$$\tilde{k}_{1,bar1} = k_{1,bar1} \cdot \frac{N_a}{\mathcal{A}}, \tag{2.29}$$

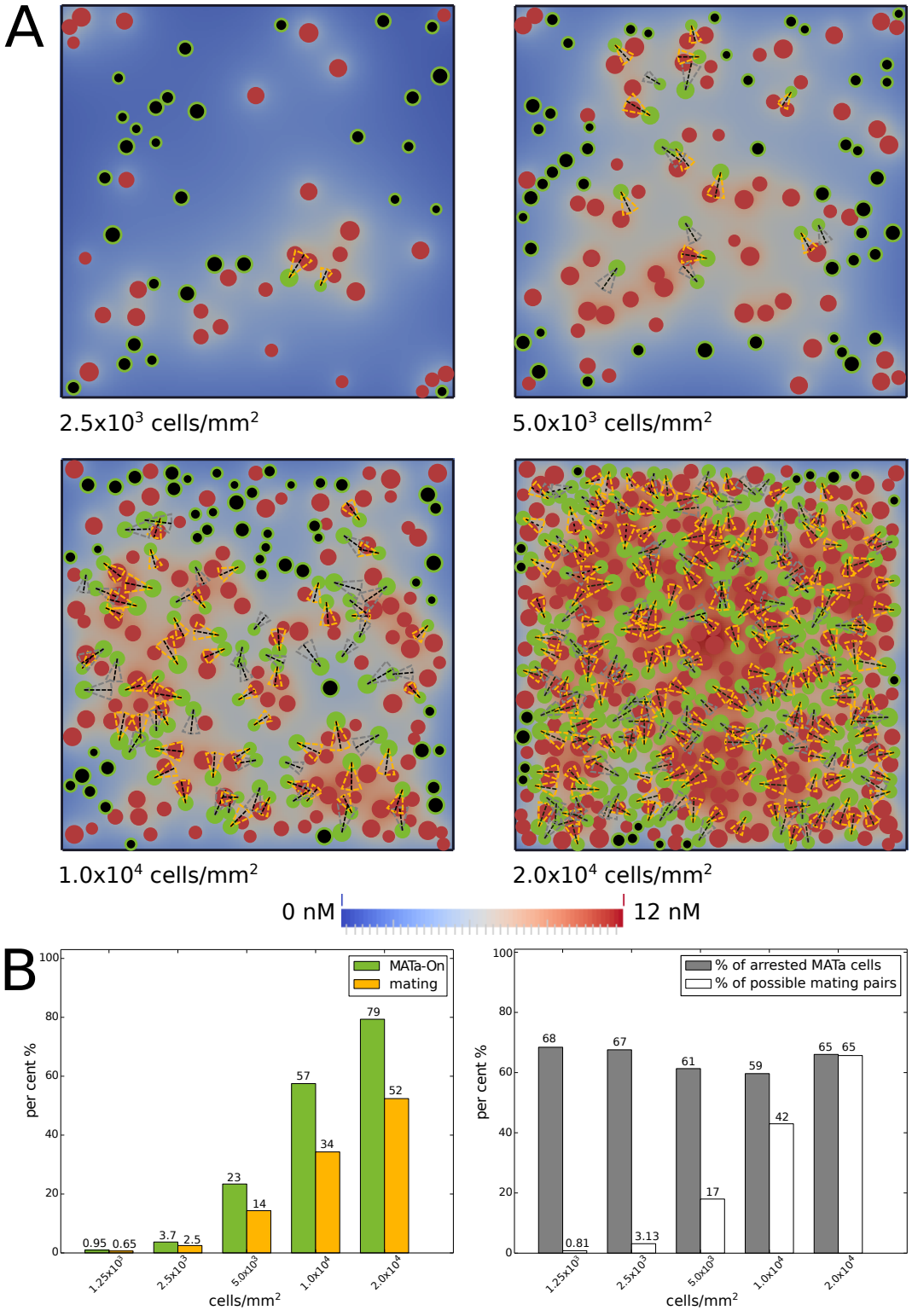

Figure 2.12: **Dynamic adaptation of Bar1 activity levels allows mating at different densities.** Simulations of model 2 for different cell densities. **A:** Examples of simulations for four different cell densities. The $\boldsymbol{\alpha}$-factor distribution is shown as well as the orientation of the cells as in Figures 2.5 and 2.7. **B:** The fraction of arrested cells is indicated by green bars, the fraction of successfull mating events as orange bars. Simulations with 10,000 cells were performed for each density. Grey and white bars indicate the fraction of mating successes corresponding to the number of arrested *MAT***a** cells and the number of maximal possible mating events in the given cell arrangement, respectively.

where $\mathcal{A}$ is the area occupied by the subpopulation. The Bar1 activity is then calculated from

$$K_B = \tilde{k}_{0,bar1} + \tilde{k}_{1,bar1} \frac{S_\alpha^h}{K_{m,\alpha} + S_\alpha^h}, \tag{2.30}$$

where S_α is the average concentration of $\boldsymbol{\alpha}$-factor, sensed by the $MAT\mathbf{a}$ cells. Therefore, simulations were performed for different cell densities of mating mixes with 100 $MAT\mathbf{a}$ and 100 $MAT\boldsymbol{\alpha}$ cells each (compare Figure 2.12). The cells were again randomly distributed on a rectangular area $\mathcal{A}$ with side length l. The length l was calculated for each cell density ρ from

$$l = \sqrt{\frac{N_a + N_\alpha}{\rho}}, \tag{2.31}$$

in order to perform the following simulations. Six different densities where assumed ranging from $\rho = 1.25 \cdot 10^3$ $cells/mm^2$ to $2.0 \cdot 10^4$ $cells/mm^2$. The simulations show that for small densities, $\boldsymbol{\alpha}$-factor concentration levels do not reach the levels to arrest more than a few cells and turn them "on" to initiate mating. However, despite the low densities, there were a few successful mating events. These mating events would not occur if Bar1 was higher than its basal level and not adapted by the cell population. For higher cell densities more cells arrested their cell cycle and performed mating, but still there are some cells with no cell cycle arrest and vegetative growth (compare Figure 2.12). The mating efficiency, which is the fraction of arrested cells that are successful in mating, is kept at a remarkable constant level around $60\% - 70\%$. Therefore, in comparison to model 1, where Bar1 levels are not regulated (see Figure 2.8) a modulated level of Bar1 keeps the mating efficiency high over a large range of cell densities. Furthermore, it allows the dual modes of "on" (mating) and "off" (vegetative growth) to occur over a large range of cell densities.

Model 3: The Complementary Pheromone: a-factor and Induced Pheromone Response

While there have been numerous experimental studies on the response of $MAT\mathbf{a}$ cells to $\boldsymbol{\alpha}$-factor (Segall, 1993; Jin et al., 2011; Ventura et al., 2014; Kelley et al., 2015) - to only name a few - there have been only very few studies that investigated the response to **a**-factor (Rogers et al., 2012; Jones and Bennett, 2011). One reason is the hydrophobic nature of **a**-factor that makes experiments with **a**-factor difficult. Also all recent computational models known to me, which describe spatial pheromone distributions of yeast cells, only consider the interplay of $\boldsymbol{\alpha}$-factor and Bar1 (Barkai et al., 1998; Andrews et al., 2010; Jin et al., 2011; Rappaport and Barkai, 2012; Diener et al., 2014). However, it was shown that **a**-factor leads to induction of $\boldsymbol{\alpha}$-factor secretion

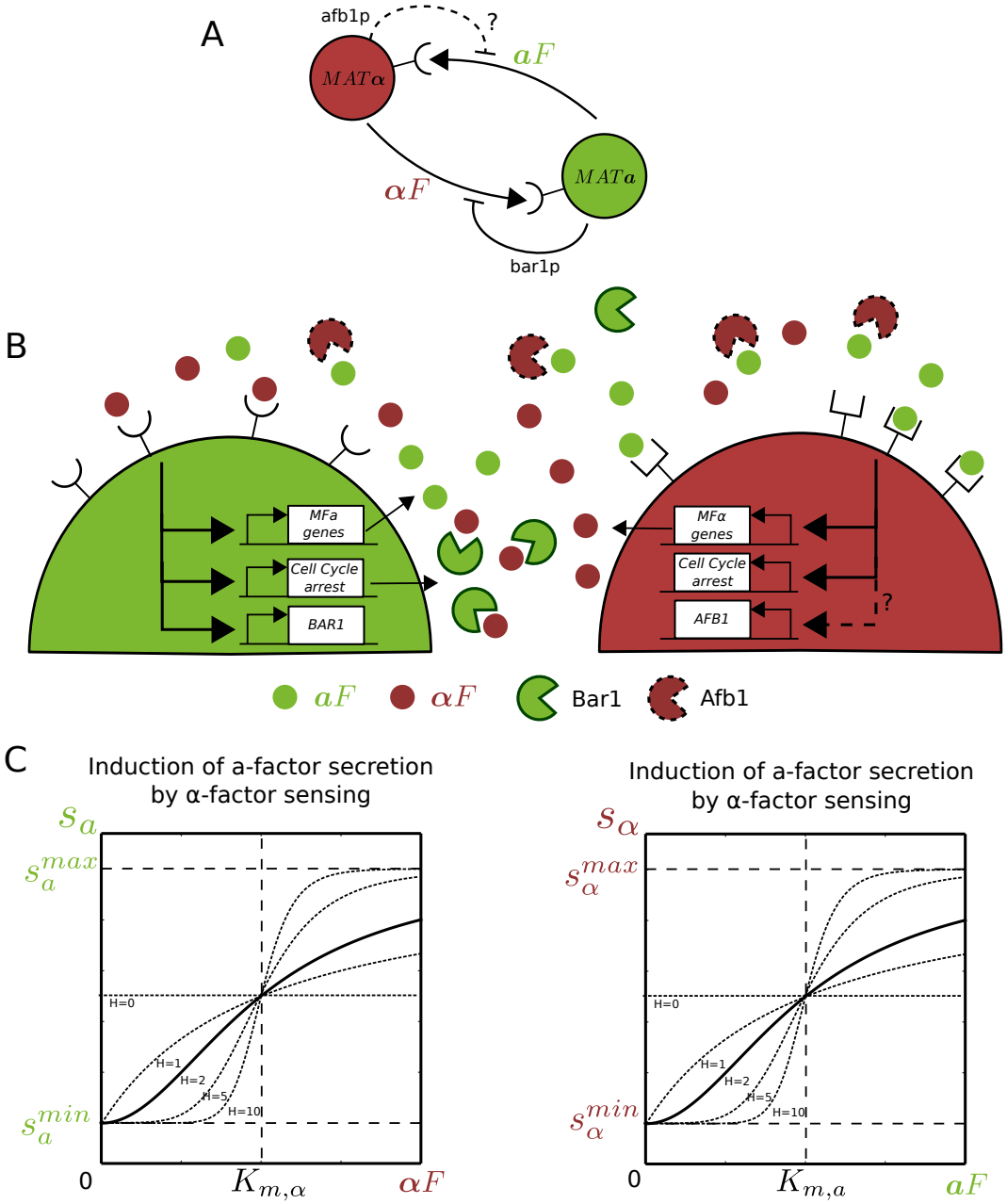

Figure 2.13: **Communication motif for Model 3. A:** *MAT*$\boldsymbol{\alpha}$ cells secrete $\boldsymbol{\alpha}$-factor and *MAT***a** cells secrete **a**-factor and Bar1. Furthermore, the possibility of an extracellular **a**-factor blocker called Afb1 (Huberman and Murray, 2013) is tested. **B:** *MAT***a** cells secrete **a**-factor as well as Bar1. Sensing of **a**-factor increases Bar1 and **a**-factor secretion. *MAT***a** cells secrete **a**-factor and Bar1. *MAT*$\boldsymbol{\alpha}$ cells secrete $\boldsymbol{\alpha}$-factor. Sensing of **a**-factor increases $\boldsymbol{\alpha}$-factor secretion. Furthermore, the possibility of an extracellular **a**-factor blocker called Afb1 (Huberman and Murray, 2013) is tested. **C:** The induction of *MAT***a** cells secreting **a**-factor by sensing of $\boldsymbol{\alpha}$-factor *vice versa* the induction of *MAT*$\boldsymbol{\alpha}$ cells secreting $\boldsymbol{\alpha}$-factor by sensing of **a**-factor is modelled *via* Hill functions. A higher Hill coefficient leads to higher levels of mutual induction for high local cell densities or close neighbours of opposite mating type.

(Rogers et al., 2012) and *vice versa* that $\boldsymbol{\alpha}$-factor stimulation leads to higher secretion levels of **a**-factor (Huberman and Murray, 2013). Furthermore, it was shown that both mating types show the mating probability towards the mating partner with the strongest pheromone signal (Jackson and Hartwell, 1990b). Therefore, the mutual pheromone induction might be essential for the mating process as well as choice of the fittest mating partner.

It is usually assumed that **a**-factor is as well diffusing through the extracellular space. Recently, it has also been reported in Huberman and Murray (2013) that there is an **a**-factor blocker, which is named Afb1[4]. However, whether a complementary protease is needed, has not been investigated so far. Therefore, two different models are tested in the following: In model 3a, it is assumed that there is no protein in the extracellular medium that degrades **a**-factor and takes the same role as Bar1, which leads to an essentially asymmetric communication. In model 3b, it is assumed that there is a complementary protein in the extracellular medium with the same role as Bar1. A sketch of both communication motifs is shown in Figure 2.13.

Model 3a: High Mutual Pheromone Induction Compensates for a Complementary Extracellular Protease for a-factor

The distributions of $\boldsymbol{\alpha}$-factor and **a**-factor are described by the following system of RD equations

$$\frac{\partial \alpha(\mathbf{x},t)}{\partial t} = D_\alpha \Delta\alpha(\mathbf{x},t) - K_B \cdot \alpha(\mathbf{x},t), \tag{2.32}$$

$$\frac{\partial a(\mathbf{x},t)}{\partial t} = D_a \Delta a(\mathbf{x},t), \tag{2.33}$$

which hold in the extracellular medium. The basal production rates for P_α^{base} and P_a^{base} denote the basal pheromone production rates of $\boldsymbol{\alpha}$-factor and **a**-factor, respectively. The increased production rates for $\boldsymbol{\alpha}$-factor and **a**-factor were denoted by P_α^+ and P_a^+, respectively. Similar to model 1 and model 2 the flux rates on the surface of the $MAT\mathbf{a}$ and $MAT\boldsymbol{\alpha}$ cells are calculated from

$$J_{i,\alpha}^{\text{base}} = P_\alpha^{\text{base}} \cdot R_{i,\alpha}/3, \qquad J_{i,\alpha}^{+} = P_\alpha^{+} \cdot R_{i,\alpha}/3, \tag{2.34}$$

$$J_{j,a}^{\text{base}} = P_a^{\text{base}} \cdot R_{j,a}/3, \qquad J_{j,a}^{+} = P_a^{+} \cdot R_{j,a}/3. \tag{2.35}$$

where $R_{i,\alpha}$ and $R_{j,a}$ are the radii of the *i-th* $MAT\boldsymbol{\alpha}$ and *j-th* $MAT\mathbf{a}$ cell, with $i \in \{1,\ldots,N_\alpha\}$ and $j \in \{1,\ldots,N_a\}$. The mutual excitation and induction of

[4] An overview of the finding can also be found in the following article on the *Saccharomyces* Genome Database, http://www.yeastgenome.org/gender-bending-in-yeast.

fluxes is described *via* Hill functions (compare Figure 2.13):

$$J_{i,\alpha} = J_{i,\alpha}^{\text{base}} + J_{\alpha,i}^{+} \frac{S_{a,i}^{H_a}}{K_a^{H_a} + S_{a,i}^{H_a}}, \tag{2.36}$$

$$J_{j,a} = J_{j,a}^{\text{base}} + J_{a,j}^{+} \frac{S_{\alpha,j}^{H_\alpha}}{K_\alpha^{H_\alpha} + S_{\alpha,j}^{H_\alpha}}. \tag{2.37}$$

Here, $S_{a,i}$ is the **a**-factor concentration sensed by the *i-th* $MAT\boldsymbol{\alpha}$ cell and $S_{\alpha,j}$ is the sensed $\boldsymbol{\alpha}$-factor concentration by the *j-th* $MAT\mathbf{a}$ cell. Furthermore, H_a and H_α are Hill coefficients that modulate the response by determining the steepness of the response curves. With these quantities, we can describe the secretion of the cell by flux boundary conditions

$$-D\nabla\alpha(\mathbf{x},t)\cdot\mathbf{n} = J_{i,\alpha} \qquad \text{on the boundary of the } MAT\boldsymbol{\alpha} \text{ cells,} \tag{2.38}$$

$$-D\nabla a(\mathbf{x},t)\cdot\mathbf{n} = J_{j,a} \qquad \text{on the boundary of the } MAT\mathbf{a} \text{ cells.} \tag{2.39}$$

As in models 0-2, it was assumed that the pheromone concentration is completely diluted far away from this cell, i.e.

$$\lim_{\|\mathbf{x}-\mathbf{x}_i\|\to\infty} \alpha_i(\mathbf{x},t) = 0, \tag{2.40}$$

$$\lim_{\|\mathbf{x}-\mathbf{x}_j\|\to\infty} a_j(\mathbf{x},t) = 0. \tag{2.41}$$

where α_i and a_j are the concentrations induced by the *i-th* $MAT\boldsymbol{\alpha}$ cell and *j-th* $MAT\mathbf{a}$ cell, respectively. Therefore, the analytical solution from Equation 2.6 can be employed for the pheromone distribution of **a**-factor. For $\boldsymbol{\alpha}$-factor the solution is similar as in the models 0 - 2.

A simulation outcome for a mating mix of 100 $MAT\mathbf{a}$ and 100 $MAT\boldsymbol{\alpha}$ cells is shown in Figure 2.14, where the Hill coefficients for **a**-factor and $\boldsymbol{\alpha}$-factor induction were set to $H_\alpha = H_a = 2$. A statistics for simulations for equal $MAT\mathbf{a}$ and $MAT\boldsymbol{\alpha}$ mixes are shown in Figure 2.15 for Hill coefficients $(H_\alpha, H_a) = (0,0), (1,1), (2,2), (10,10)$. In the simulations, it was observed that larger Hill coefficients resulted in a stronger segregation of low and high cell densities. For the highest Hill coefficients $(H_\alpha, H_a) = (10,10)$, there were almost no "on" cells in low cell densities. However, for higher densities almost all cells were "on". Notably, the mating efficiency increased for higher levels of mutual induction. Due to the lack of a protease that degrades **a**-factor, more $MAT\boldsymbol{\alpha}$ cells arrest their cell cycle. The effect of higher fractions of arrested $MAT\boldsymbol{\alpha}$ leads to the effect, that $MAT\boldsymbol{\alpha}$ cells divide and proliferate less. This was also observed in the experiments shown in Figure 2.9 and Figure 2.19, where populations with equal mating type ratios turn into populations with an unequal mating type ratio with more $MAT\mathbf{a}$ cells than $MAT\boldsymbol{\alpha}$ cells. However, the effect was more pronounced in the experiments carried out in Figure 2.19 than in Figure 2.9.

Motivated by this observation I also tested the model for unequal mating mix ratios with 50 $MAT\mathbf{a}$ cells and 150 $MAT\boldsymbol{\alpha}$ cells. A simulation outcome

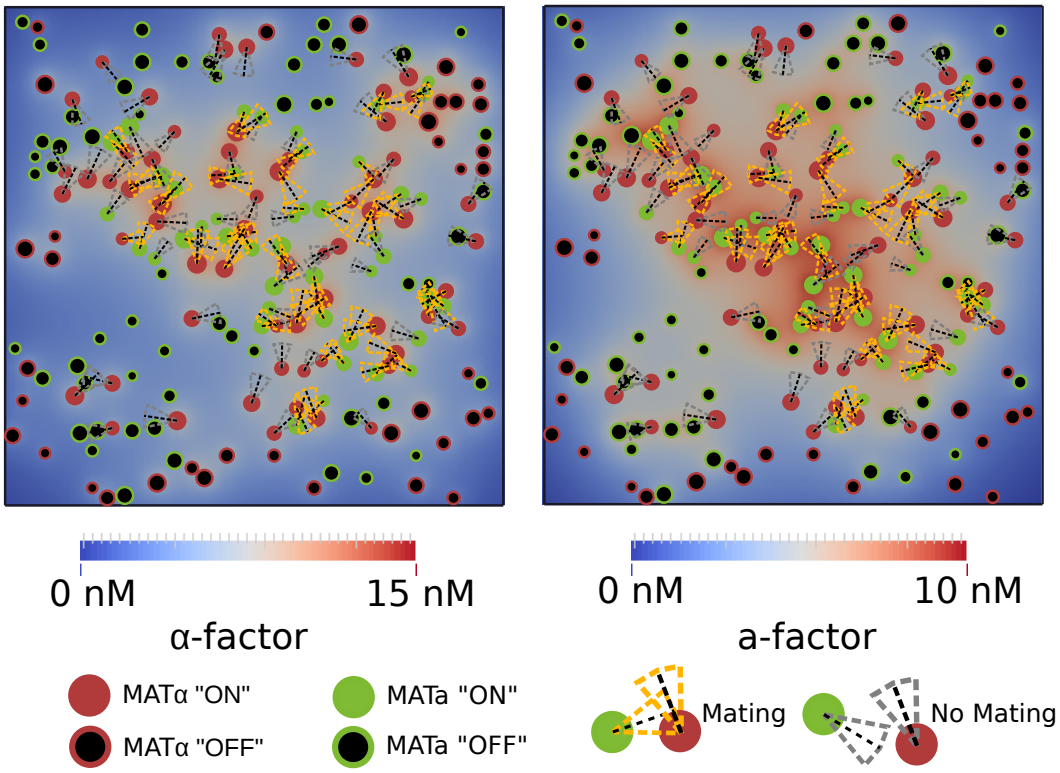

Figure 2.14: **Model3a: α-factor and a-factor distribution in a mixed cell population.** A mating mix of 100 *MAT***a** cells (green) and 100 *MAT*$\boldsymbol{\alpha}$ cells (red). Red cells are *MAT*$\boldsymbol{\alpha}$ cells, where red filled cells indicate *MAT***a** cells that are "on" and black filled cells indicate *MAT*$\boldsymbol{\alpha}$ cells that are "off". The orientation of all *MAT***a** as well as *MAT*$\boldsymbol{\alpha}$ cells that are "on" is indicated with a dashed segment as in models 0 - 2. A successful orientation is counted if these segments touch or overlap. Mating events are indicated by orange segments for *MAT***a** or *MAT*$\boldsymbol{\alpha}$ cells, respectively.

for $(H_a, H_\alpha) = (0, 0)$ and $(H_a, H_\alpha) = (10, 10)$ is shown in Figure 2.16. These simulations were repeated 50 times for each combination of $(H_a, H_\alpha) = (0, 0)$, $(1, 1)$, $(2, 2)$, $(10, 10)$ and six different densities. The outcome is shown in Figure 2.17. For small Hill coefficients almost all $MAT\boldsymbol{\alpha}$ cells were "on" while almost all $MAT\mathbf{a}$ cells were "off", which led to very low mating efficiency. For larger Hill coefficients the number of "on" $MAT\mathbf{a}$ cells and "on" $MAT\boldsymbol{\alpha}$ cells converged, which leads to a significantly higher level of coordination among neighbouring cells. Therefore, assuming asymmetric communication, larger Hill coefficients lead to an increased mating efficiency and robustness towards unequal mating mixes with more $MAT\mathbf{a}$ than $MAT\boldsymbol{\alpha}$ cells.

Model 3b: Testing for the Bar1 Complement Afb1 (a-factor Barrier)

Here, the assumption of extracellular Afb1 is tested. The same RD equations as in model 3a were used to model the pheromone distribution of $\boldsymbol{\alpha}$-factor and $\mathbf{a}$-factor, but the term $-K_A \cdot a(\mathbf{x}, t)$ is added, which yields the following equation system:

$$\frac{\partial \alpha(\mathbf{x}, t)}{\partial t} = D_\alpha \Delta \alpha(\mathbf{x}, t) - K_B \cdot \alpha(\mathbf{x}, t), \tag{2.42}$$

$$\frac{\partial a(\mathbf{x}, t)}{\partial t} = D_\alpha \Delta a(\mathbf{x}, t) - K_A \cdot a(\mathbf{x}, t). \tag{2.43}$$

Since there is no data available for the diffusion properties or enzyme kinetics of Afb1, I assumed a symmetric communication motif, in which Afb1 behaves similar to Bar1.

Simulations for mating mixes of 100 $MAT\mathbf{a}$ and 100 $MAT\boldsymbol{\alpha}$ cells were performed for Hill coefficients $(H_\alpha, H_a) = (0, 0), (1, 1), (2, 2), (10, 10)$ and six different densities as for model 3a. A statistics for simulations for equal $MAT\mathbf{a}$ and $MAT\boldsymbol{\alpha}$ mixes are shown in Figure 2.18 for Hill coefficients $(H_\alpha, H_a) = (0, 0), (1, 1), (2, 2), (10, 10)$. As in model 3a, larger Hill coefficients resulted in a stronger segregation of low and high cell densities. For the highest Hill coefficients $(H_\alpha, H_a) = (10, 10)$, there were almost no "on" cells in low cell densities. However, for higher densities almost all cells were "on". In contrast to model 3a, the mating efficiency stayed almost the same for the high-density cultures and did not improve with larger Hill coefficients. The overall number of mating events increased with larger Hill coefficients, but only an increase of about 10% was observed for the high cell densities of $10^4 cells/mm^2$ and $2.0 \cdot 10^4 cells/mm^2$. Notably, the mating efficiency as well as number of total mating events is almost the same for higher Hill coefficients for both models 3a and 3b. Therefore, mutual pheromone induction has the potential to overcome the need for a complementary extracellular protease Afb1.

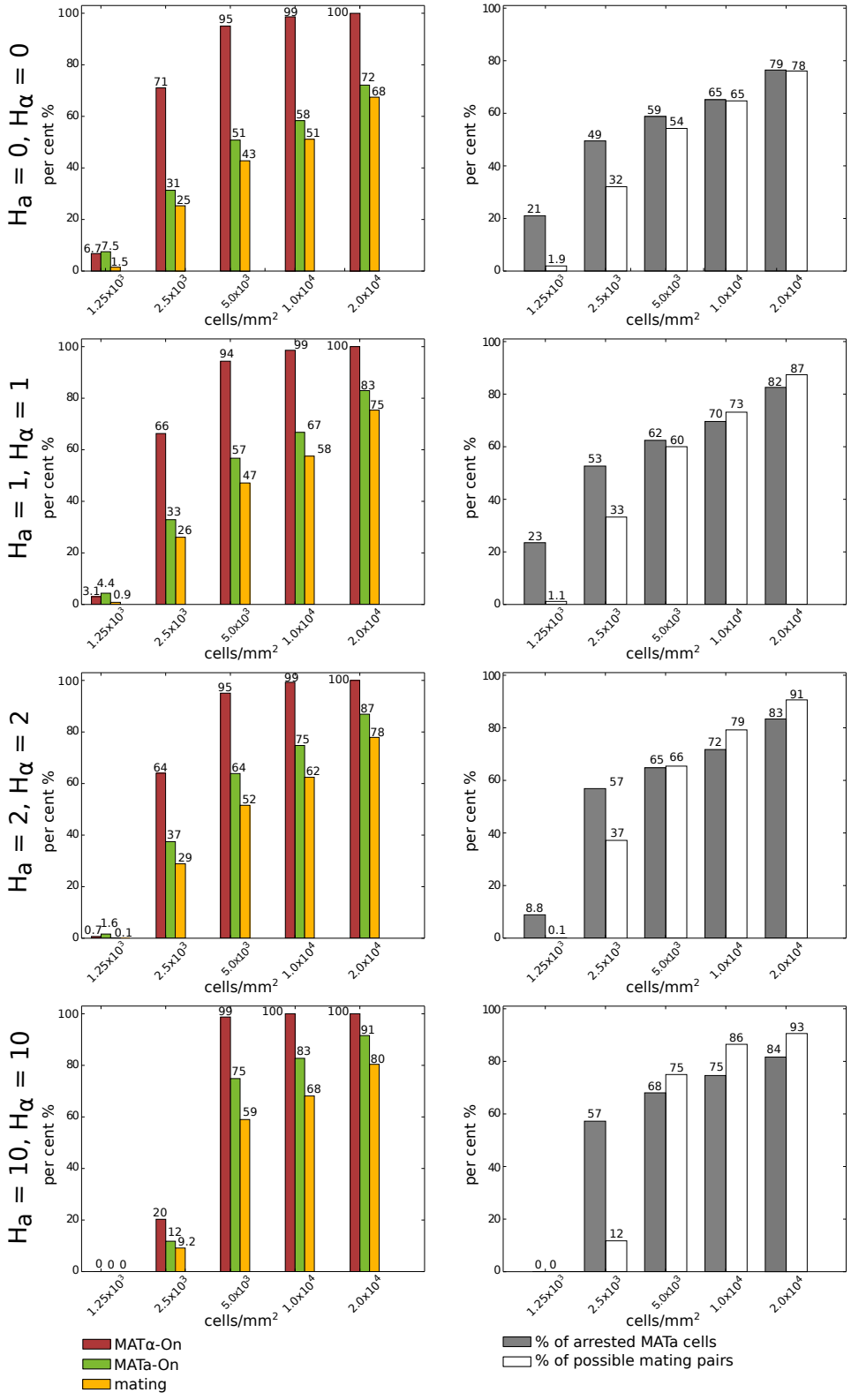

Figure 2.15: **Simulations of model 3a for different Hill coefficients for induction of the pheromone response.** In the case of high mutual induction - with Hill coefficents $(H_a, H_\alpha) = (10, 10)$ - the number of mating events for densities $> 5.0 \times 10^3$ $cells/mm^2$ increased significantly, while the number for lower cell densities was significantly reduced.

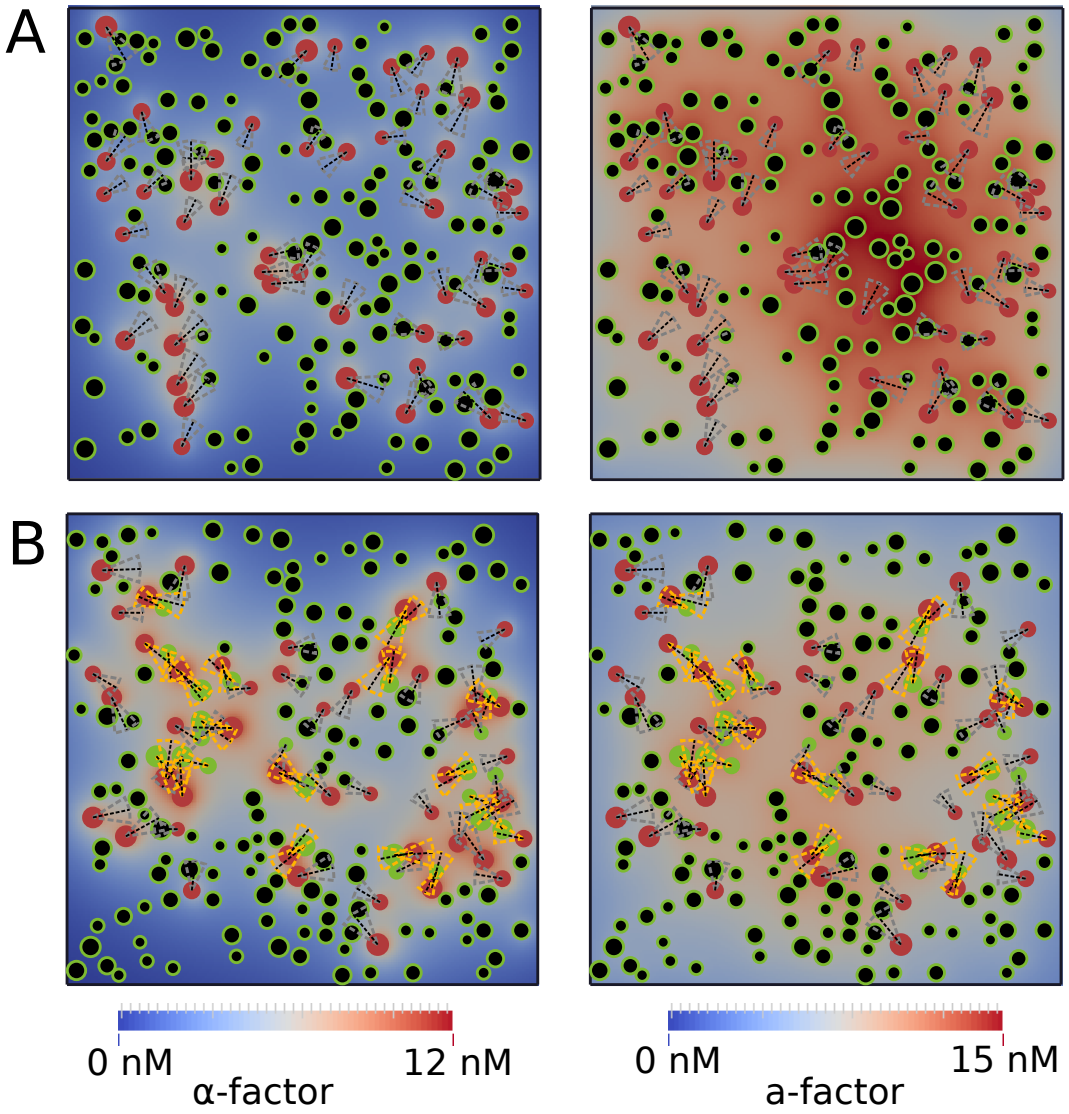

Figure 2.16: **Simulations of model 3a for a culture with an unequal mix of mating types.** Simulations with 50 $MAT\boldsymbol{\alpha}$ and 150 $MAT\mathbf{a}$ cells. The $\boldsymbol{\alpha}$-factor distribution is shown on the left, while the **a**-factor distribution is shown on the right. **A:** The Hill coefficents $(H_a, H_\alpha) = (0, 0)$ were used, meaning no mutual induction of pheromone secretion. The $\boldsymbol{\alpha}$-factor concentration levels [left] were too low to arrest any $MAT\mathbf{a}$ cells and no mating events were observed. On the contrary, **a**-factor levels are high [right] and all $MAT\boldsymbol{\alpha}$ cells were arrested. **B:** The Hill coefficents $(H_a, H_\alpha) = (10, 10)$ were used, meaning high mutual induction of pheromone secretion. 17 mating events were observed. The $\boldsymbol{\alpha}$-factor concentration levels [left] was higher than in **(A)**, while **a**-factor levels were lower than in **(A)**.

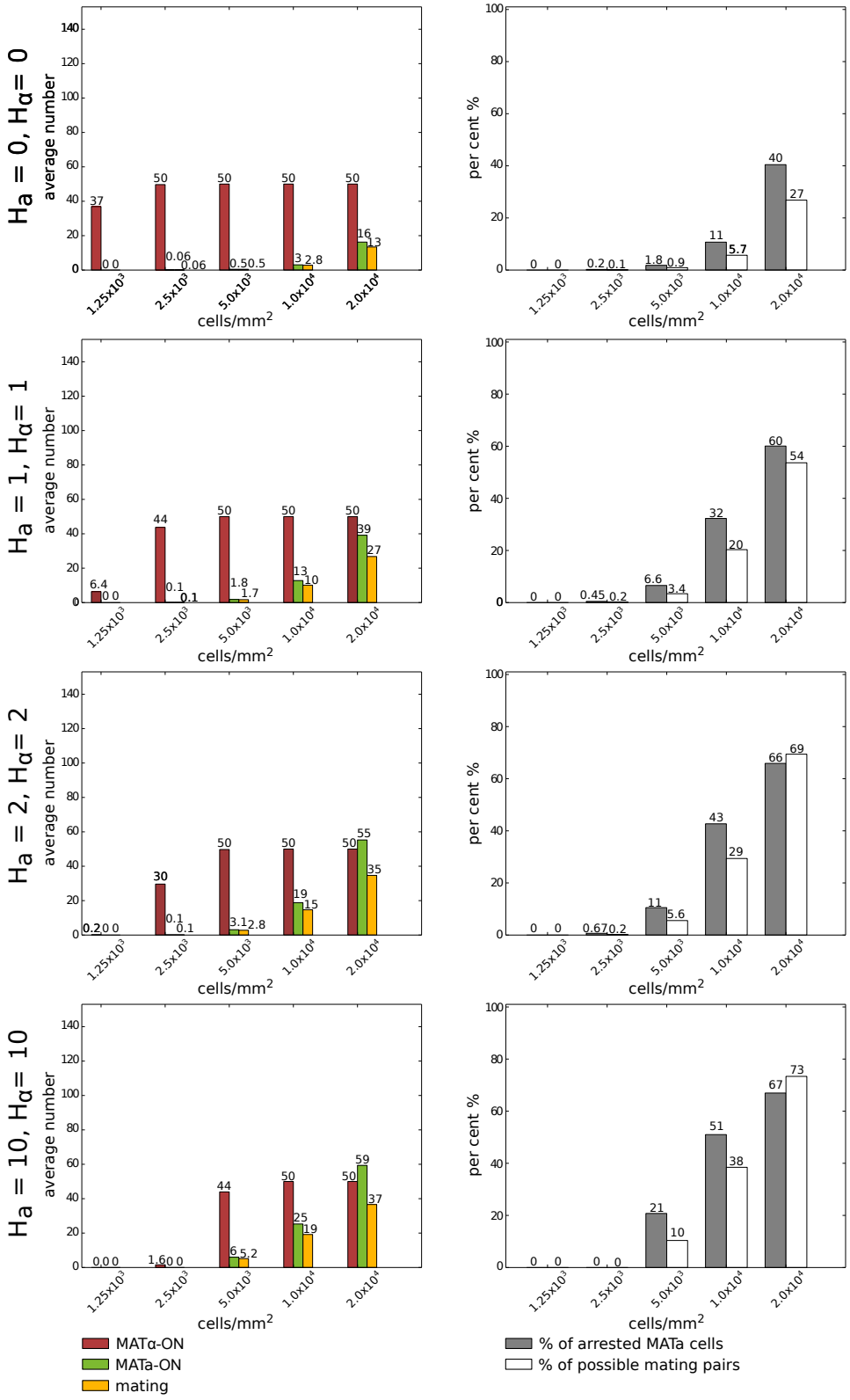

Figure 2.17: **Simulations of model 3a for a culture with an unequal mix of mating types for different Hill coefficients.** An unequal mating mix with 50 $MAT\boldsymbol{\alpha}$ and 150 $MAT\mathbf{a}$ cells was assumed for each simulation. Simulations were repeated 50 times for each density and set of Hill coefficients. As in the setup shown in Figure 2.15, high mutual induction with Hill coefficents $(H_a, H_\alpha) = (10, 10)$ increased the number of mating events for densities $> 5.0 \times 10^3$ $cells/mm^2$ significantly, while the number for lower cell densities was significantly reduced.

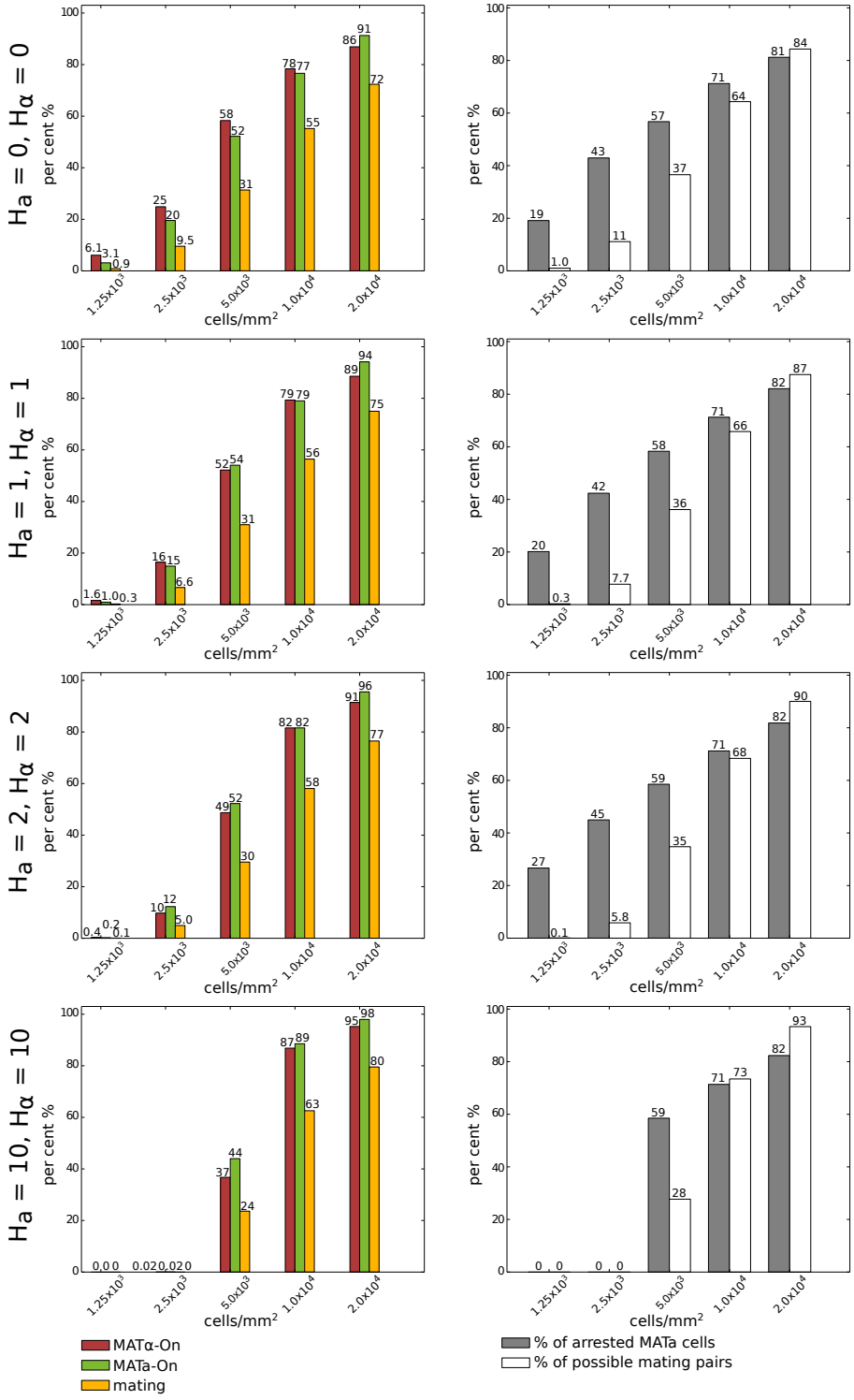

Figure 2.18: **Simulations of model 3b for a culture with an equal mix of mating types for different Hill coefficients.** The set of hill coefficents $(H_a, H_\alpha) = (10, 10)$ with high values, meaning high mutual induction of pheromone secretion levels, prevented mating in low densities, but improved mating significantly in higher cell densities $> 10.0 \times 10^3$ $cells/mm^2$.

Discussion and Outlook

The models tested in this chapter, were based on the null hypothesis (Barkai et al., 1998) and were step by step refined to capture new aspects of yeast communication during mating. Mutual induction of the pheromone response, as implemented in models 3a and 3b, showed significantly higher levels of mating efficiency, compared to models 1 and 2 without mutual induction. In Barkai et al. (1998), high pheromone gradients were only achieved with excessive Bar1 activity levels. Here, it was shown that mutual induction leads accurately oriented cells with Bar1 activity levels in the physiological regime suggested in Jin et al. (2011) and Diener et al. (2014). The work in Diener et al. (2014) provides a foundation for the study of collective behaviour that occurs in mixed cultures of haploid yeast cells of opposite mating type. However, this study focused on the induction of $MAT\mathbf{a}$ cells by $\boldsymbol{\alpha}$-factor and neglected the induction of $MAT\boldsymbol{\alpha}$ cells by **a**-factor. A systematic study of mating mixes in the same way as carried out in Diener et al. (2014) for the complementary pheromone would allow to fit the models 3a and 3b to real data.

The models tested in this chapter, may be refined in various directions. An interesting possibility goes back to the source-sink diffusion (SSD) model introduced by Francis Crick in Crick (1970) for the development during embryogenesis. Here, it was suggested that cells in tissues might act as monitors, as absorbers or reflectors with respect to extracellular signalling molecules. Also it was pointed out, that hydrophobic and non-hydrophobic molecules behave differently, e.g. they might adhere more or less strongly to the surface and thereby reduce the amount of freely diffusing entities. This makes the yeast system a most interesting test case, since we have $\boldsymbol{\alpha}$-factor a non-modified peptide, and **a**-factor a modified lipopeptide with hydrophobic molecular properties. As shown in Endres and Wingreen (2008), absorbing cells are better at measuring signalling gradients as well as concentrations than mere monitoring cells. This was also suggested for yeast cells, since periplasmic Bar1 is already active before reaching the extracellular destination (Ballensiefen and Schmitt, 1997).

To test for absorption mechanisms and a quantification of their impact in yeast communication should be tested with further modelling. Therefore, I would suggest partial absorption of molecules could be modelled as Robin boundary condition:

$$-D\nabla a(\mathbf{x},t)\cdot\mathbf{n} = -\eta a(\mathbf{x},t) \text{ on the cell surface.} \tag{2.44}$$

Here, $\eta > 0$ is a constant representing the strength of absorption. A high level of absorption corresponds to larger η values, whereas $\eta = 0$ corresponds to total reflection. In the automata model this could be implemented with the method of imaginary charges (Jackson, 1983), where absorbing cells are treated as "negative" charges. This mechanism was also suggested (Rappaport and Barkai, 2012). However, the modelling of absorbing or sticky boundary conditions is still a question of current research (Peskir, 2014).

Though this extension might be very interesting for certain cell types, the question remains if it is important for the yeast mating system. If yeast cells act as perfect absorbers as hypothesized in merely theoretical studies (Endres and Wingreen, 2008). First of all, yeast has a cell wall and though it is a porous medium there is still a debate about the pore size. For a recent review on ambiguous experimental studies on this topic I refer to (Casadevall et al., 2009). Here, a question which fraction of pheromone molecules passes through the wall and is captured by the receptors or degraded by periplasmic protease. In the case of Bar1 it has been shown that periplasmic Bar1 is active before reaching the extracellular destination (Ballensiefen and Schmitt, 1997), it is widely accepted that a reasonable fraction is found in the extracellular medium as well (Andrews et al., 2010; Jin et al., 2011; Diener et al., 2014). In case of the potential complementary protease Afb1 it was suggested that Afb1 has a Glycosylphosphatidylinositol (GPI) anchor, and might therefore be attached to outer plasma membrane and can only act there (Huberman and Murray, 2013). The localization of the protease might serve the function to desensitize cells and also to avoid accumulation of foreign pheromone in the periplasm of the opposing mating partner. Whether the absorption of pheromone is large enough to actually shape the extracellular gradients, depends on pore size and number as well as protease activity. More detailed experimental investigations are needed on the molecular properties and surface interactions of the **a**-factor and $\boldsymbol{\alpha}$-factor to go further and refine the models.

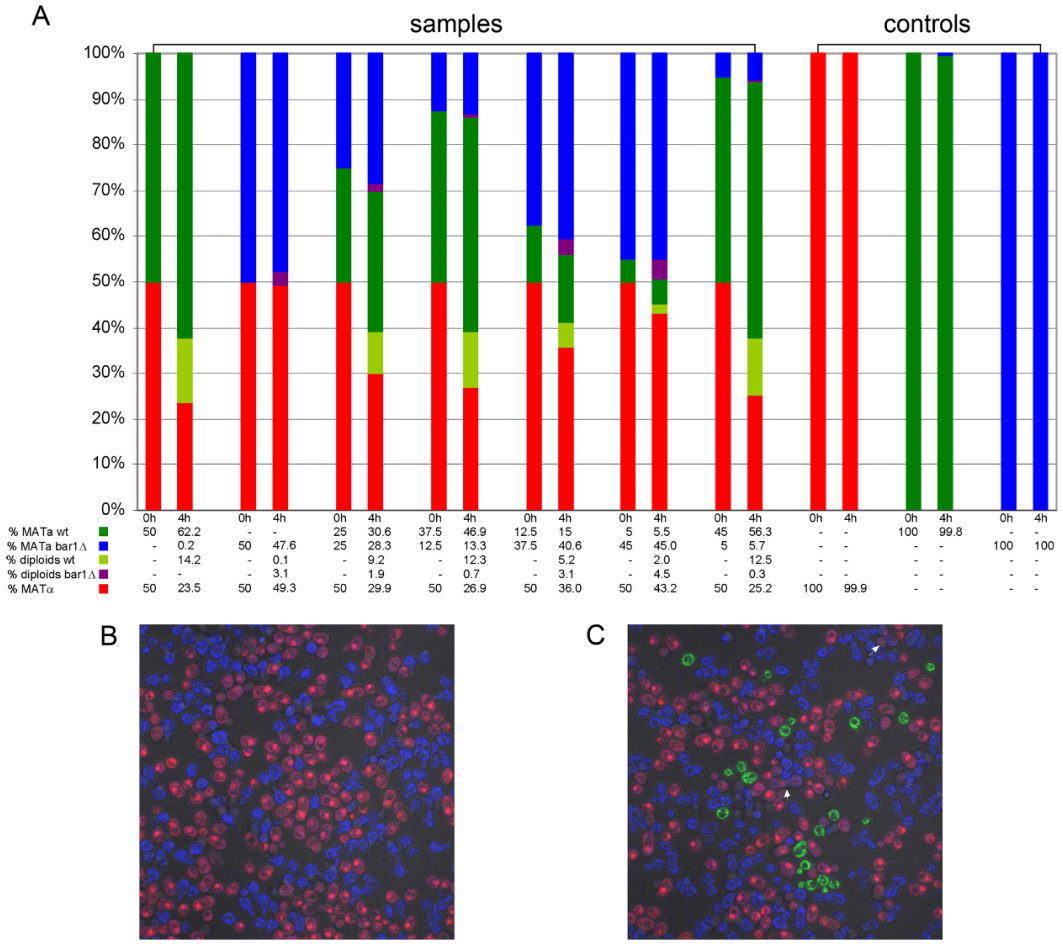

Figure 2.19: **The influence of *MAT*a *bar*1Δ cells on the mating of wild type mixes A:** Different mixes of cultures initially containing *MAT*$\boldsymbol{\alpha}$ cells (marked with mCherry) and varying fractions of wild type *MAT***a** cells (marked with Rpl9A-GFP) and *MAT***a** *bar*1Δ cells (marked with RPl9a-TagBFP2). The fraction of haploid *MAT*$\boldsymbol{\alpha}$ (red), *MAT***a** (green), *MAT***a** *bar*1Δ (blue) cells as well as diploid *MAT*$\boldsymbol{\alpha}$-*MAT***a** (light green) and *MAT*$\boldsymbol{\alpha}$-*MAT***a** *bar*1Δ (purple) cells after 4h is shown. **B:** Confocal merged image of a mixed culture initially containing 50% *MAT*$\boldsymbol{\alpha}$ and 50% *MAT***a** *bar*1Δ cells. **C:** Confocal merged image of a mixed culture containing 50% *MAT*$\boldsymbol{\alpha}$ cells, 45% *MAT***a** *bar*1Δ cells and 5% wild type *MAT***a** cells. Some mating events are marked with white arrows. The colours in the microscopic images and in the table **A** are concurrent. Figure was taken from Diener et al. (2014).

3

Modelling Eukaryotic Cell Polarization Exemplified for Mating Decisions of *S. cerevisiae*

Cell polarity is an overarching aspect of eukaryotic cell biology. A family of small GTPases controls the process of cell polarization in most eukaryotic cells. Small GTPases include molecules such as Cdc42 and Rac in animal and fungal cells (Etienne-Manneville, 2004; Wu et al., 2013) as well as Rop in plant cells (Yang and Lavagi, 2012). These small GTPases usually occur in an active GTP-bound and an inactive GDP-bound form. In the GTP-bound form they are anchored into the membrane and can diffuse slowly. Local accumulation of the activated GTP-bound form defines the site of polarity and determines the site of subsequent morphological changes. The activation of small GTPases are triggered by external or internal cues and even if these cues are ambiguous, the healthy system guarantees a distinct site of polarity with a controlled extent. Cell polarization carried out by small GTPases is a functional module and, therefore, an understanding of the polarization process is important for many organisms in health and disease. This chapter is focused on the small GTPase Cdc42 and its role in yeast budding and shmooing.

Cell Polarity & small GTPases

In the previous chapter, we investigated how haploid yeast cells communicate *via* pheromones. If the pheromone concentration is high enough yeast cells arrest their cell cycle and initiate the shmooing process towards a potential mating partner. In contrast, if the pheromone concentration is low, the cells continue their cell cycle, initiate budding and give rise to a new daughter cell. This chapter addresses the following question: How do yeast cells orient and respond to often conflicting pheromone signals sent by their potential mating partners, and how can mating as well as budding patterns be explained? Yeast cells employ an elaborated polarization mechanism that is at play during budding and shmooing with slight modifications (compare Figure 3.1). In previous chapter was built on a simplified version of the polarization module assuming that all cells polarize exactly along the pheromone gradient. However, the situation becomes more complex when pheromone gradients change during shmooing or if the signal is so ambiguous that cells shmoo along a default direction, which is determined by some internal state. In this chapter, I shall address various situations and environmental cues that yeast cells respond to.

Yeast Mating

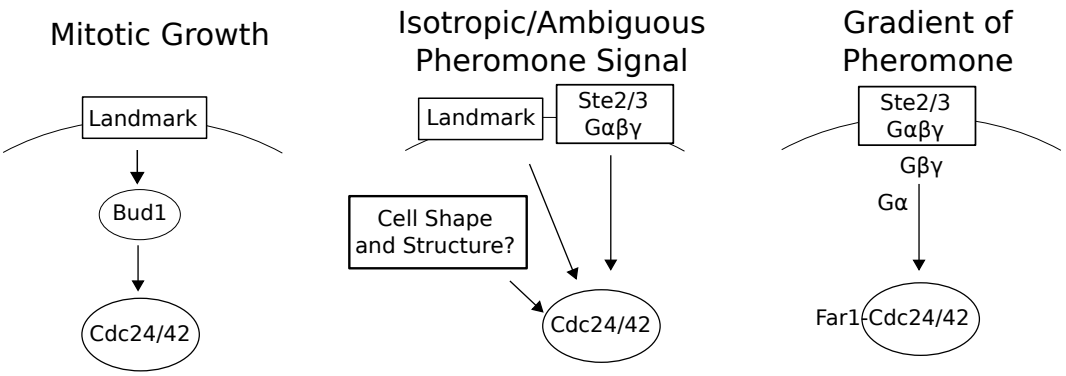

Figure 3.1: **Different growth modes occuring in yeast mating mixes.**

Yeast Budding

The central molecule that controls cell polarity in yeast is the small Rho GTPase Cdc42. Experiments have shown that yeast cells lacking Cdc42 are unable do bud and remain round (Adams et al., 1990). In the absence of external cues the emergence of the bud site is specified by the Ras-family GTPase Rsr1/Bud1, an immobile cortical landmark protein, which is inherited from the previous cell division. This inheritance of bud markers leads to an axial budding pattern in the case of haploid yeast cells. Cdc42 cycles between and active GTP-bound and an inactive GDP-bound state. Cdc42 can be prenylated and subsequently anchored into the membrane. *Vice versa* membrane-bound Cdc42 can be removed from the membrane by Rdi1, its guanosine nucleotide dissociation inhibitor (GDI). Active membrane-bound Cdc42-GTP levels can be increased by guanine nucleotide exchange factors (GEFs) or reduced by GTPase-activating proteins (GAPs). Here, the major GEF controlling the Cdc42p activity and cell polarization is Cdc24. Since total molecule numbers of Cdc42 are relatively constant during the polarization process, the interplay of positive feedbacks and deactivation leads to a competition of potential polarization sites for cytoplasmic Cdc42, which results in a distinct site of polarity. A sketch of this process is shown in Figure 3.3.

The budding pattern, in which landmark proteins and bud scars inherited from the previous cell divisions determine the site of bud emergence could be perturbed systematically in a number of experiments. For instance, Cdc42 overexpression led to cells that formed multiple buds (Caviston et al., 2002), which were randomly distributed. Furthermore, Cdc42 overexpression also decreases the requirements for GEF activity that is necessary for polarization. A spontaneously forming polarization cap, which randomly explores the cell periphery, was observed for $rsr1\Delta$ mutants. The ability to polarize was further tested for the dependence on actin. Treatment of $rsr1\Delta$ mutants with the actin-depolymerizing drug latranculin A caused cells to spontaneously polarize and establish a random but stable axis of polarity (Ozbudak et al., 2005). These experiments demonstrated that Cdc42p activation is necessary and sufficient to cause spontaneous cell polarization. For a review on budding patterns in diploids and zygotes I refer to (Chang and Peter, 2003; Wu et al., 2013; Tartakoff, 2015).

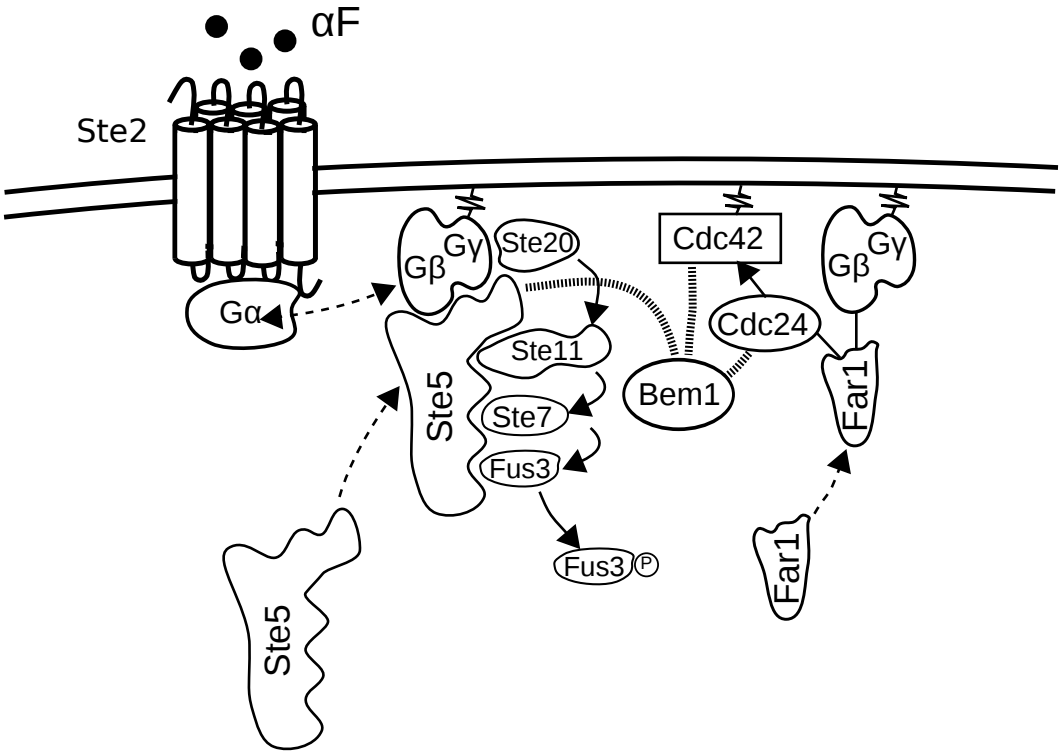

Figure 3.2: **Pheromone induced activation of Cdc42 and subsequent polarization.** Pheromones are captured and recognized by G-protein-coupled receptors (GPCRs), which cause activation and dissociation of heterotrimeric G-proteins $G\alpha\beta\gamma$. $G\beta\gamma$ recruits the MAPK scaffold (Ste5) to the membrane, leading to the activation of the MAPK cascade, which processes the signal to the nucleus. In the centre of this chapter is the polarization process which occurs on the membrane. $G\beta\gamma$ recruits Far1p to the site of activation, which causes the accumulation of the GEF Cdc24p. This process leads further to the activation and accumulation of active membrane-bound Cdc42, which determines the site of polarity.

Yeast Pheromone Response

During mating Cdc42 activation is induced by the G-protein-coupled receptors (GPCRs) Ste2 or Ste3 for $MAT\mathbf{a}$ or $MAT\boldsymbol{\alpha}$ cells, respectively. Upon pheromone stimulation heterotrimeric G-proteins $G\alpha\beta\gamma$ are activated and dissociate into a $G\alpha$ and a $G\beta\gamma$ sub-unit (compare Figure 3.2). $G\beta\gamma$ recruits Far1p, which causes the accumulation of the GEF Cdc24p at the site of receptor stimulation (Bardwell, 2004). Subsequently, Cdc42 accumulates at the site of highest activation, e.g the cell polarizes along the pheromone gradient. Even if the gradient is very shallow or ambiguous a unique site of polarity is formed. In the case of isotropic pheromone stimulation, cells have found to be influenced by former bud scars, but can also shmoo in a random direction. If cells are shaken or stimulated for a long time with pheromone, cells are able to form multiple shmoos in different directions (Bidlingmaier and Snyder, 2004; Diener et al., 2014).

Various theoretical models have been developed to describe different as-

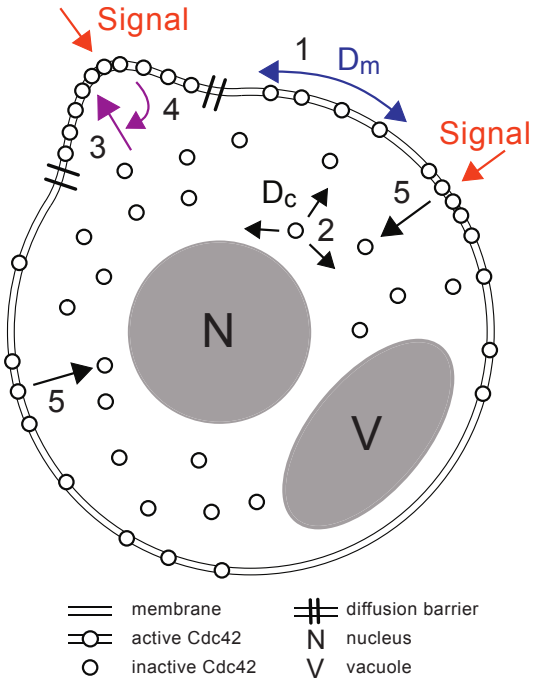

Figure 3.3: A sketch of the cycling process of signalling molecules between cytosol and membrane: (1) lateral diffusion with coefficient D m of active signalling molecules along the membrane; (2) free cytosolic diffusion with coefficient D c of inactive signalling molecules; (3) association of cytoplasmic molecules to the membrane; (4) positive feedback, i.e. enhanced recruitment of cytoplasmic molecules to the location of active signalling molecules; (5) dissociation of signalling molecules from the membrane. Figure from Giese et al. (2015)

pects of the polarization for organisms such as fish keratocytes, *Dictyostelium discoideum*, neutrophils or yeast. Many of these models are based on reaction-diffusion (RD) models, which are formulated in partial differential equations (PDEs) in time and space. In case of the yeast system, these models described the shuttling of Cdc42 on different levels of details such as in (Ozbudak et al., 2005; Otsuji et al., 2007; Altschuler et al., 2008; Mori et al., 2008; Goryachev and Pokhilko, 2008; Chou et al., 2008; Okada et al., 2013; Klünder et al., 2013). Note that for other model organisms, in particular for motile cells such as fish karatocytes, F-actin plays an important role (Falcke, 2015). In this case, the distribution of actin binding molecules has to be described *via* reaction-diffusion-advection equations and the Rho-GTPase cycling has to be connected to the F-actin dynamics (Holmes et al., 2012; Edelstein-Keshet et al., 2013). Here, I shall concentrate merely on the small GTPase dynamics, which is the driving force for polarity in yeast and works also independent of active transport (Ozbudak et al., 2005; Jilkine and Edelstein-Keshet, 2011).

Reaction-Diffusion Models

The leading questions of this chapter are: How do yeast cells sense their own shape? How is a stable growth and unique axis of Polarity maintained during shmoo formation? What determines preferred sites of polarity in case of ambiguous signals? Which factors introduce a bias on the polarization axis? A Turing-type mechanism as well as a phase separation mechanism was tested to provide answers to these questions. These mechanisms were investigated using a 1D model formulation in order to understand basic properties of the non-linear kinetics. The equations were extended into 2D, which allows investigations with respect to (i) potential geometry sensing in case of the shmoo shape, (ii) the dependencies on cell size and robustness to other model parameters, (iii) the influence of diffusion inhomogeneities on the membrane and (iv) the potential impact of organelles on the polarization behaviour. Finally, the system is extended to more complex geometries in 3D that reflect the case of multiple shmoo formation under isotropic pheromone or ambiguous pheromone stimulation.

Chapter Outline

Comparison of a Turing-type and a Phase Separation Mechanism

Patterns arising in cell polarization have been described by various RD models for different model organisms. In some cases, different polarization mechanisms result in superficially similar patterns and, therefore, a distinction of these mechanisms is only possible by testing a large set of different perturbations and external cues. In Giese et al. (2014, 2015), colleagues and I investigated two different models that were proposed for yeast polarization. The first mechanism is of Turing-type (Goryachev and Pokhilko, 2008), the other is a phase separation mechanism (Mori et al., 2008). Here, I aim to summarize the results from Giese et al. (2014, 2015) and put them into a wider context.

Classically, the basic mechanisms of pattern formation are formulated in a one-dimensional representation of the cell (Jilkine and Edelstein-Keshet, 2011).

This allows for disentangling cell geometry and spatial inhomogeneities from the underlying interactions of diffusion and reaction kinetics. An interval $[0, L]$ is assumed as computational domain, which allows two interpretations: (i) the interval represents the circumference of the cell with both ends of the interval glued together; (ii) the interval represents a cell diameter transect and the interval ends represent front and back of the cell. A two component RD systems was employed, where the concentration of active Rho GTPase (membrane-bound) is represented as a function $u(\mathbf{x}, t)$, and the concentration of inactive Rho GTPase (cytosolic) is represented as a function $v(\mathbf{x}, t)$. Both functions, $u(\mathbf{x}, t)$ and $v(\mathbf{x}, t)$, depend on space, $\mathbf{x}$, and time, t. The set of RD equations that describe the dynamics reads

$$\frac{\partial u}{\partial t} = D_m \frac{\partial^2 u}{\partial x^2} + f(u, v), \qquad x \in [0, L],\ t \in [0, T], \tag{3.1}$$

$$\frac{\partial v}{\partial t} = D_c \frac{\partial^2 v}{\partial x^2} - f(u, v), \tag{3.2}$$

with some initial concentrations $u(\cdot, 0)$ and $v(\cdot, 0)$ in $[0, L]$ and zero-flux boundary conditions

$$\frac{\partial u}{\partial x}(0, t) = \frac{\partial u}{\partial x}(L, t) = \frac{\partial v}{\partial x}(0, t) = \frac{\partial v}{\partial x}(L, t) = 0. \tag{3.3}$$

This RD system covers three different processes: (i) diffusion of active Rho GTPases on the membrane where D_m is the diffusion coefficient; (ii) diffusion of inactive Rho GTPases in the cytosol where D_c is the cytosolic diffusion coefficient; (iii) reaction processes are described by a function $f(u, v)$, which is given by

$$f(u, v) := f^{\text{cyc}}(u, v) + k_S v, . \tag{3.4}$$

Here, $f^{\text{cyc}}(u, v)$ denotes the reaction kinetics of the employed model. The function k_S represents signals that influence or trigger the polarization process. A sketch of the shuttling process of the small Rho GTPase Cdc42 is shown in Figure 3.3. Note, that this RD system is mass conservative, meaning

$$\underbrace{\int_0^L u \, \mathrm{d}x}_{\text{mass of active Rho GTPase}} + \underbrace{\int_0^L v \, \mathrm{d}x}_{\text{mass of inactive Rho GTPase}} = M \tag{3.5}$$

where M is the total mass the total mass of signalling molecules in the system.

The reaction kinetics $f(u, v)$ can obtain different forms. Here, the reaction kinetics from Goryachev and Pokhilko (2008) and Mori et al. (2008) were chosen as representatives of the Turing-type mechanism and phase separation mechanism, respectively. The Turing-type model from Goryachev and Pokhilko is referred to as GOR model in the remainder. In the original work the model exists in two different versions. The first is an eight component system that describes the actin-independent signalling pathway involved in the

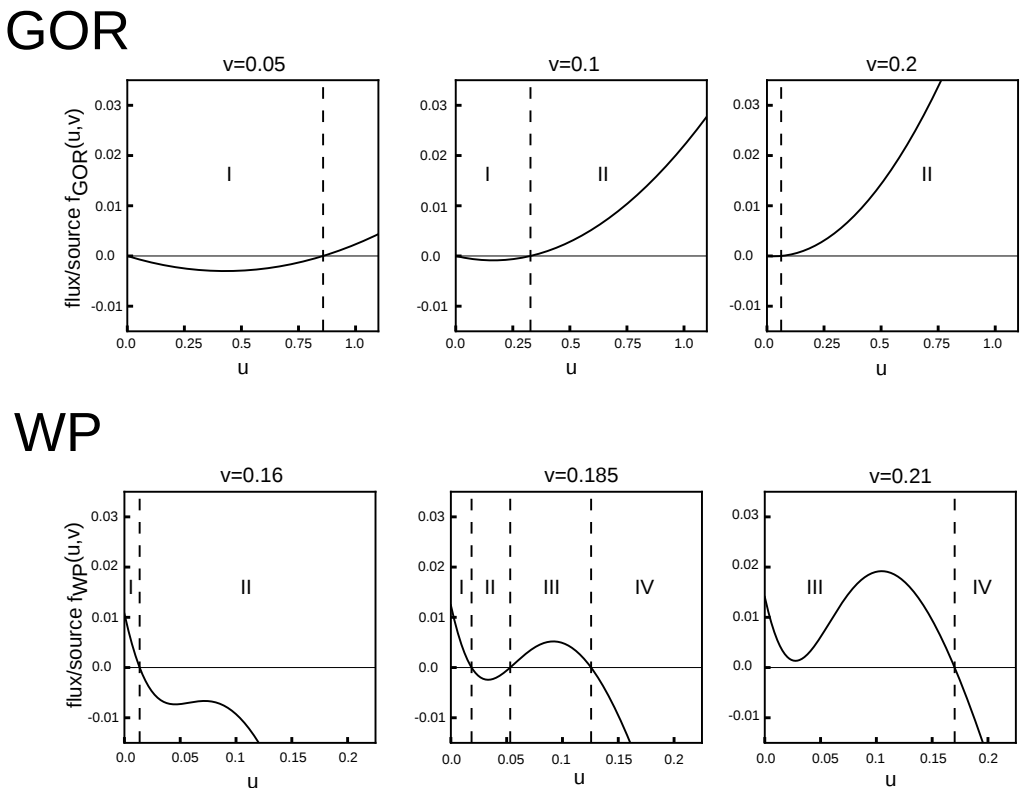

Figure 3.4: **Kinetics of the GOR and WP model.** The right hand side of both models, plotted for a fixed volume concentration v. In case of the GOR model, we obtain two homogeneous steady states. The first steady state at $u_1 = 0$ is stable while the second at $u_2 > 0$ is unstable and transient, since we have a membrane/cytosolic flux onto the membrane for $u > u_2$ (region II in the plots) and a flux to the cytosol for $u < u_2$ (region I in the plots). In case of the WP model, we observe a bimodal behaviour. For the shown range of values for v, we can either have one, two or three steady states. If there are three steady states, say u_1 , u_2 and u_3 with $u_1 < u_2 < u_3$, the steady states u_1 and u_3 are stable while u_2 is transient. If the membrane concentration u is in the regions I or III of the plots, there is a flux from the cytosol to the membrane. If the membrane concentration u is in the regions II or IV, there is a flux from the membrane to the cytosol. The figure was taken from Giese et al. (2015).

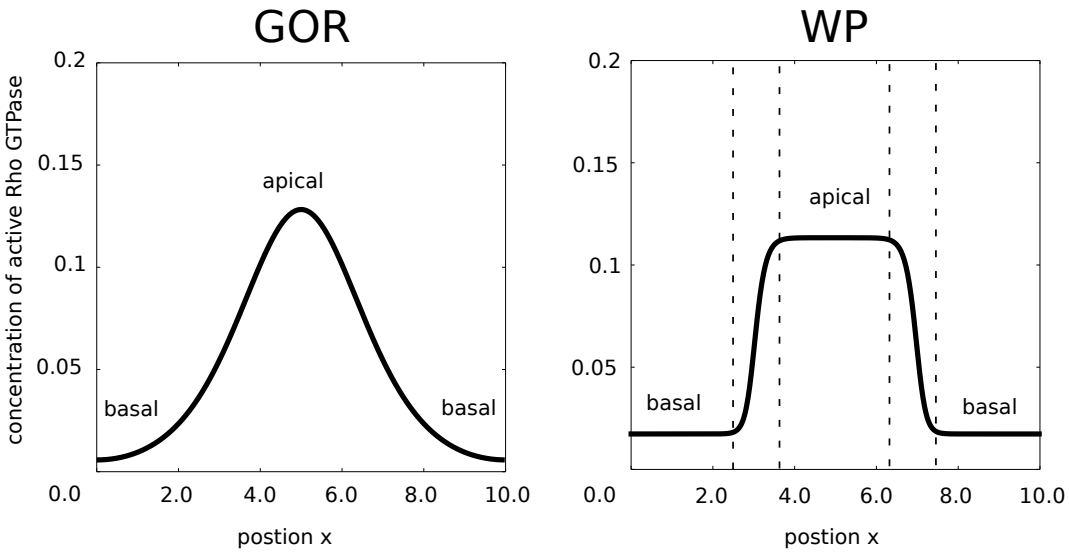

Figure 3.5: **Distribution of active Rho GTPase for the GOR and WP model.**

yeast budding process. The second is a condensed version with two components that captures the main dynamics and revealed the Turing-type mechanism by in-depth analysis. The latter was used in this work, and its reaction kinetics is given by

$$f^{\mathrm{cyc}}(u,v) = f^{\mathrm{GOR}}(u,v) := \alpha E_c u^2 v + \beta E_c u v - \gamma u. \tag{3.6}$$

Here, the term $\alpha E_c u^2 v + \beta E_c u v$ describes the positive feedback on the Cdc42 activation mediated by its GEFs. In the original model E_c accounts for the Bem1-Cdc42 complex and is assumed to be constant for simplicity. Note, that the term $\alpha E_c u^2 v$, which is quadratic in u, accounts for the positive feedback of Cdc42 on its on activation. The dissociation of active GTP-bound Cdc42 carried out by its GAPs and GDIs is described by the degradation term γu. The reaction kinetics $f^{\mathrm{GOR}}(u,v)$ was plotted as a function of u for different cytosolic concentrations v, see Figure 3.4. In the parameter range of interest, the function $f^{\mathrm{GOR}}(\cdot, v)$ has two roots $u^- = 0$ and $u^+ > 0$. The root u^- corresponds to a stable homogeneous steady state of the system, while the root u^+ corresponds to an unstable steady state. If the system is in the homogeneous steady state u^+ a small spatial perturbation of causes the system to break symmetry and run into a polarized steady state. To obtain conditions on the parameter that are necessary for this symmetry break, a classical linear stability analysis can be performed as in (Turing, 1952). Note, here that the GOR system is not exactly a Turing system as proposed in (Turing, 1952), since no mass is generated in the system. The conditions that are needed for the emergence of a symmetry break are therefore different. Results for an analysis of this system can be found in Otsuji et al. (2007) and Giese et al. (2014).

As representative of the phase separation mechanism, I employed the wave-pinning (WP) model. This model was investigated in a number of studies such as in Jilkine and Edelstein-Keshet (2011), Mori et al. (2008, 2011), and Walther

model	parameter/entity	value	unit	description
GOR & WP	u	-	$\mu m\ \mu M$	concentration of the membrane-bound species
	v	-	μM	concentration of the cytosolic species
	$f(u,v)$	-	$\mu m\ \mu M/s$	density of flux at the membrane-cytosolic interface
	D_m	-	$\mu m^2/s$	diffusion coefficient for the membrane-bound species
	D_c	-	$\mu m^2/s$	diffusion coefficient for the cytosolic species
GOR	α	3.3	$\mu m^{-1}\ \mu M^{-2}\ s^{-1}$	cooperative positive feedback
	β	0.67	$\mu M^{-1}\ s^{-1}$	noncooperative binding to membrane
	γ	0.017	$1/s$	rate of basal dissociation from membrane
	E_c	0.1	-	membrane-bound Cdc24-Bem1 complex
WP	k_0	0.067	$\mu m/s$	rate of basal activation
	δ	1.0	$1/s$	rate of basal dissociation
	γ	1.0	$\mu m/s$	maximal rate of autoactivation of u
	K	0.1	$\mu m\ \mu M$	concentration of u resulting in half-maximal rate of autoactivation

Table 3.1: Overview of variables and constants. Note that $1\,\mu M$ = 1.0E-21 $mol/\mu m^3$. From Giese et al. (2015).

model	parameter	value		description
GOR	D_m^{GOR}	0.0025	$\mu m^2/s$	diffusion coefficients used in Goryachev and Pokhilko (2008)
	D_c^{GOR}	$1.0 - 10.0$	$\mu m^2/s$	
WP	D_m^{WP}	0.1	$\mu m^2/s$	diffusion coefficients used in Mori et al. (2008)
	D_c^{WP}	10.0	$\mu m^2/s$	
GOR & WP	D_m^{cons}	0.015	$\mu m^2/s$	consensus diffusion coefficients used in this work
	D_c^{cons}	3.0	$\mu m^2/s$	(geometric mean of extreme values found in the references)

Table 3.2: Sets of diffusion coefficients. From Giese et al. (2015).

et al. (2012). Its reaction kinetics reads

$$f^{\mathrm{cyc}}(u,v) = f^{\mathrm{WP}}(u,v) := v\left(k_0 + \frac{\gamma u^n}{K^n + u^n}\right) - \delta u. \tag{3.7}$$

This kinetics assumes a basal activation rate k_0 and an inactivation rate δ. A Hill function describes a positive feedback from the active form u on its own activation. Here, γ is the maximal activation rate and K represents a saturation constant. In the remainder, I assume a Hill coefficient of $n = 2$. The reaction kinetics $f^{\mathrm{WP}}(u,v)$ was plotted as a function of u for different cytosolic concentrations v, see Figure 3.4. In the parameter range, which is relevant for polarization, the function $f^{\mathrm{WP}}(\cdot,v)$ has three roots $0 < u^- < u^T < u^+$. The roots u^- and u^+ correspond to the stable homogeneous steady state of the system. Here, u^- is referred to as the unexcited state and u^+ as the excited state. The third root u^T corresponds to a transient unstable steady state. In all simulations shown in this chapter, the WP system was started in the unexcited homogeneous steady state, where $v_0 \equiv 0.2\ \mu M$ and $u_0 \equiv 0.026\ \mu m\ \mu M$ were used as initial conditions. A spatially heterogeneous signal on the membrane caused the system to split into three phases, an excited phase, an unexcited phase and a transition phase. Local excitation by a signal causes the emergence of a traveling wave which is pinned due to global mass conservation and leads to a stable polarized state. An example of the distribution of the active GTP-bound form of signalling molecules for the Turing-type and the phase separation mechanism is shown in Figure 3.5.

A Bulk-Surface Reaction-Diffusion Model for Mass Conservative Systems

To account for the influence of cell geometry on cell polarisation, the 1D models from the previous section were extended into 2D and 3D. Note, that additionally to the investigations of 2D cell shapes in Giese et al. (2014, 2015), also 3D shapes were investigated in this thesis. The computational representation of the cell comprises the cell membrane, the cytosol as well as inner membranes that enclose organelles like the vacuole or the nucleus. The cytosolic volume is denoted by V^{cyt} and is limited by its boundary surface $\partial V^{\mathrm{cyt}} = M^{\mathrm{cell}} \cup M^{\mathrm{org}}$. Here, M^{cell} and M^{org} represent the cell membrane and the inner membranes, respectively. The boundary of some domain D is denoted by ∂D. A sketch of the boundaries is shown in Figure 3.6.

In contrast to the one-dimensional models in the previous section, the RD equations in 2D and 3D describe reaction and diffusion processes on different computational domains. The active membrane-bound form of signalling molecules, represented by the function $u(\mathbf{x},t)$, is a function defined on the outer membrane M^{cell} with units molecules per area. The inactive cytosolic form, represented by the function $v(\mathbf{x},t)$, is a function in the volume V^{cyt} with units molecules per volume. Note, in the 2D case, M^{cell} is a one-dimensional

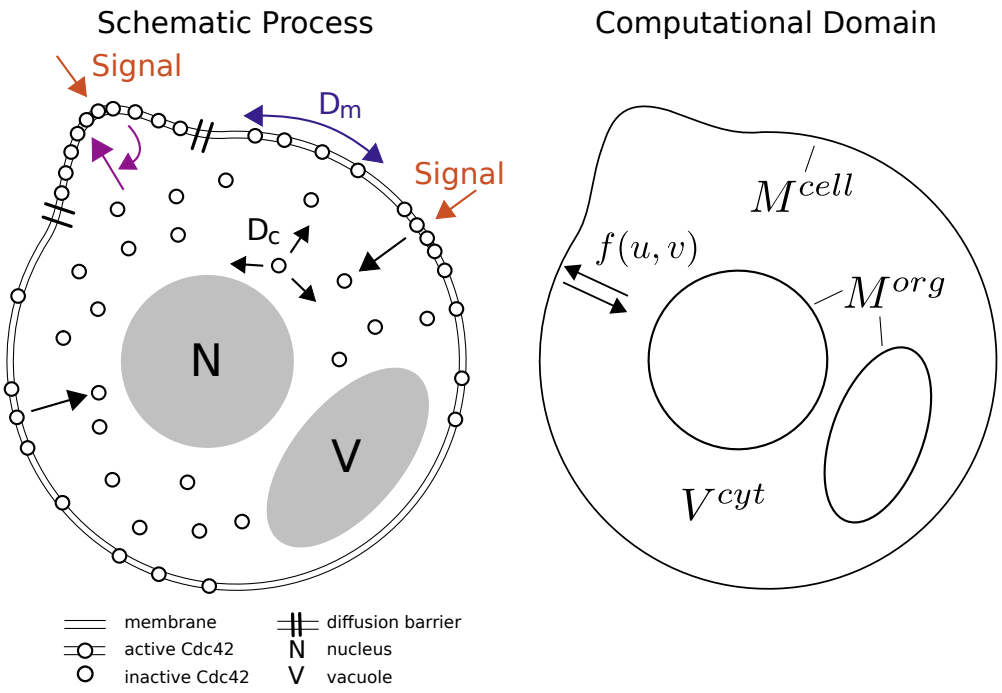

Figure 3.6: **Boundaries of the computational domain.** The schematic cell polarization process is shown next to the computational domain. The cytosolic volume is represented as a two-dimensional bulk domain V^{cyt} . Its boundary ∂V^{cyt} consists of closed hyper surfaces M^{cell} and M^{org}, which describe the outer cell membrane and the organelles membranes. This figure was taken from Giese et al. (2015).

curve enveloping the 2D cytosolic domain V^{cyt}. In the 3D case, M^{cell} is a 2D manifold enclosing 3D volume V^{cyt}.

The reaction shuttling between membrane-bound and cytosolic signalling molecules is naturally given by a flux at the membrane-cytosolic interface. This flux is described by the reaction kinetics $f(u, v)$ as given in the previous section. The RD model equations read

$$\frac{\partial u}{\partial t} = \nabla_\Gamma \cdot (D_m \nabla_\Gamma u) + f(u, v) \qquad \text{on } M^{\text{cell}} \times [0, T], \tag{3.8}$$

$$\frac{\partial v}{\partial t} = \nabla \cdot (D_c \nabla v) \qquad \text{in } V^{\text{cyt}} \times [0, T]. \tag{3.9}$$

Note, that the cytosolic species v only interacts with the membrane-bound species u on the cell membrane M^{cell} and, hence, there is no extra reaction term in the volume equation (3.9). The boundary conditions for the cytosolic equation (3.9) are given by

$$-D_c \nabla v \cdot \mathbf{n} = f(u, v) \qquad \text{on } M^{\text{cell}} \times [0, T], \tag{3.10}$$

$$-D_c \nabla v \cdot \mathbf{n} = 0 \qquad \text{on } M^{\text{org}} \times [0, T]. \tag{3.11}$$

Here, $\mathbf{n}$ denotes the vector field of outer unit normals on M^{cell} and M^{org}, respectively. The initial concentrations at time $t = 0$ are given by

$$u(\mathbf{x}, 0) = u_0(\mathbf{x}) \quad \text{and} \quad v(\mathbf{x}, 0) = v_0(\mathbf{x}). \tag{3.12}$$

In summary, these equations comprise three types of processes which occur simultaneously: **(a)** Diffusion of $u(\mathbf{x}, t)$ on the curved membrane where the diffusion coefficient $D_m(\mathbf{x})$ is a function in space in order to allow for spatial diffusion inhomogeneities and ∇_Γ denotes the surface gradient operator in $\mathbf{x}$ which accounts for curvature of Γ, see (Elliott and Ranner, 2012). **(b)** Diffusion of $v(\mathbf{x}, t)$ in the cytosol with diffusion coefficient $D_c(\mathbf{x})$ where ∇ denotes the usual gradient operator in $\mathbf{x}$ with respect to standard Cartesian coordinates in Euclidean space. **(c)** The reaction processes on the membrane described by a flux at the membrane-cytosolic interface with $J = f(u, v)$ are modelled as a source term for the membrane-bound complex in equation (3.8) and as a Robin-like boundary condition for the cytosolic concentration $v(\mathbf{x}, t)$ in equation (3.10). Note, that the flux $f(u, v)$ naturally obtains the unit molecules per area and time. For $f(u, v) > 0$ a flux from the cytosol onto the membrane is obtained whereas for $f(u, v) < 0$ the active form u dissociates into the cytosol.

This system of equations is mass conservative, since the source term in equation (3.8) and boundary condition (3.10) balance each other. Thus, the total mass of active and inactive signalling molecules is constant in time, meaning

$$\underbrace{\int_{M^{\text{cell}}} u(\mathbf{x}, t) \, \mathrm{d}A}_{\text{mass on the cell membrane}} + \underbrace{\int_{V^{\text{cyt}}} v(\mathbf{x}, t) \, \mathrm{d}V}_{\text{mass in the cytosol}} = M \tag{3.13}$$

for all $t \in [0, T]$, where $M \in \mathbb{R}$ is a constant. A derivation can be found in Giese et al. (2015). Note, that in the 2D case, the surface integral is an integral along the one-dimensional curve enveloping the cell and the volume integral is an integral over a two-dimensional domain, which represents a slice of the cell. Therefore, the unit for M becomes molecules per height. To obtain actual molecule numbers in the cell slice, M needs to be integrated along the height of the cell slice.

Geometry Sensing Properties of Cell Polarization Mechanisms

Intracellular gradients of signalling molecules have the potential to regulate cellular growth or chemotactic movement (Brown and Kholodenko, 1999; Nalbant et al., 2004). Since Meyers et al. (2006) it is widely accepted, that intracellular signalling can be influenced by cell size and shape. The notion of "geometry sensing" has been termed in recent studies as the ability of signalling systems to react and adapt to certain cell shapes (Thalmeier et al., 2016). While some mechanisms for cell shape regulation are based on mechano-sensing (Vogel and Sheetz, 2006) others are based on non-linear reaction-diffusion systems (Halatek and Frey, 2012). The latter kind of mechanicms are in the focus of the remainder. Here, I want to test the Turing-type and the phase separation mechanism for their ability to adapt and react to shapes that typically occur during the mating process of yeast.

In a first setup, a cell with a characteristic shmoo shape and a circular cell were excited with a homogeneous signal (compare Figure 3.7 **A**). The unexcited homogeneous steady state was assumed as initial condition for both cell shapes and both models, the WP and GOR model. The signal, as defined in equation 3.4, was applied for a time period of $\Delta t = 100s$ with an amplitude of $k_S \equiv 0.03 \mu m/s$. There were no spatial heterogeneities in the case of the circular cell and, therefore, the circular cell does not polarize. After the stimulus was removed the system returned to its original homogeneous steady state for both polarization mechanisms. Interestingly, for the non-circular cell a different effect was observed. The surface to volume ratio differs in the apical part and basal part of the cell and, therefore, the homogeneous stimulation causes a greater take up of the cytoplasmic pool of signalling molecules in the apical part than in the basal part. This effect creates a cytosolic gradient with lower concentration on the apical side than on the basal side. Since the flux of molecules onto the membrane depends on the local cytosolic concentration, the concentration of membrane-bound molecules grows faster in the basal region of the membrane than in the apical region of the membrane. This effect caused an initial symmetry break, which resulted in polarization on the basal side, for both systems. In case of the WP model, polarization was established faster (less than $100s$) than for the GOR model ($\sim 1000s$).

In a second setup, two conflicting stimuli were applied on the cell surface.

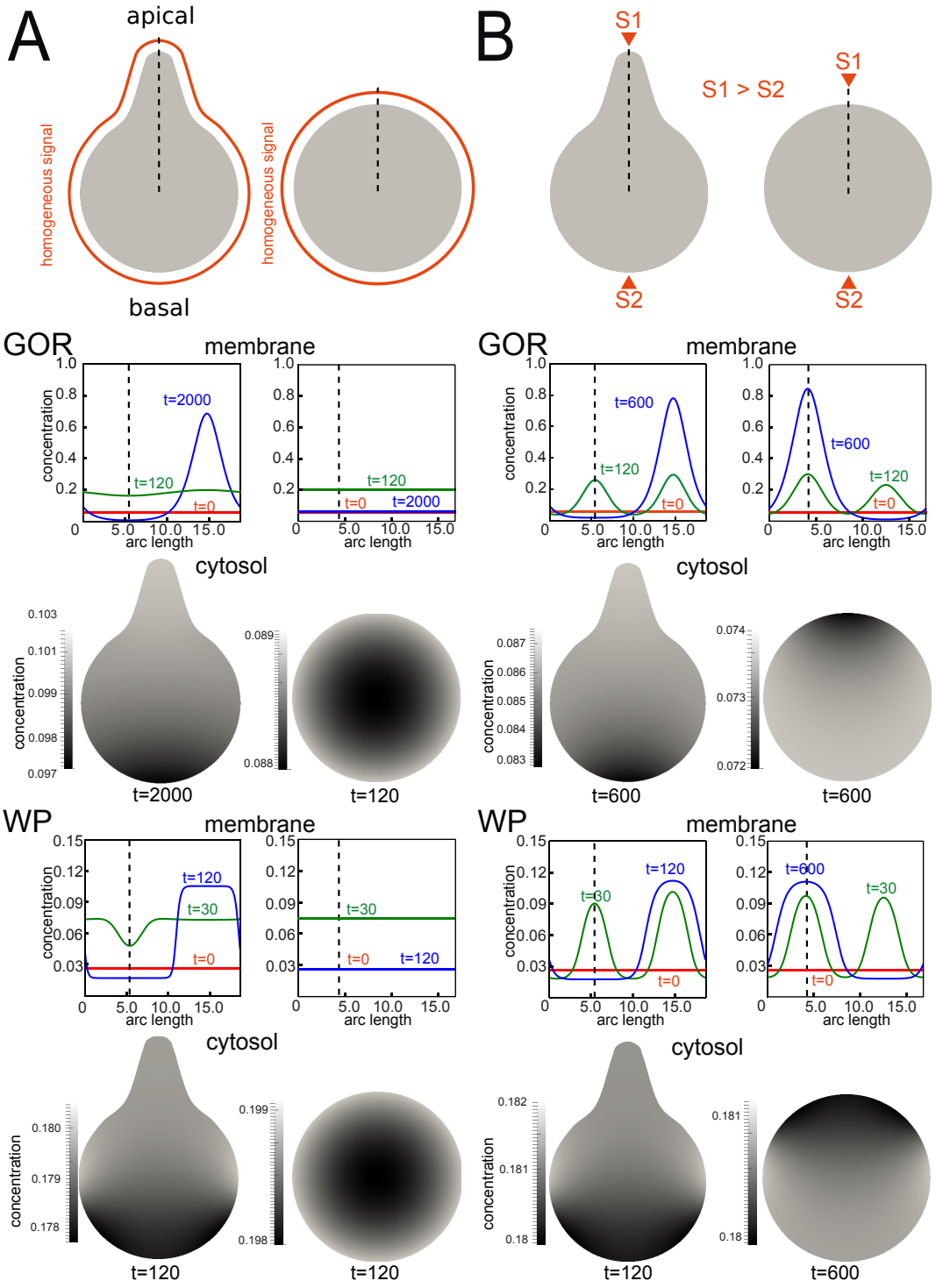

Figure 3.7: **Simulations of the GOR and the WP model for different signals and cell shapes.** (A) The GOR and the WP model were excited with a spatially homogeneous signal for $\Delta t = 100s$, $k_S \equiv 0.03\mu m/s$. Since no spatial perturbations were present in the circular cel, no polarization occurred. However, homogeneous excitation of the non-circular cell led to cluster formation opposite to the protrusion. (B) The GOR and the WP model were simulated for a cell with a protrusion and a circular cell. The signal comprised two competing stimuli S1 and S2. The amplitude of S1 was chosen 10% larger than the amplitude of S2. This figure was taken from Giese et al. (2015).

These two localized stimuli are given by

$$k_S(\mathbf{x},t) = \begin{cases} S_1, & \text{if } t < t_1 \text{ and } \|\mathbf{x}_{S_1} - \mathbf{x}\| < w, \\ S_2, & \text{if } t < t_2 \text{ and } \|\mathbf{x}_{S_2} - \mathbf{x}\| < w, \\ 0, & \text{otherwise.} \end{cases} \tag{3.14}$$

Here, w specified the width of the excited surface area. The system was excited with two competing stimuli at positions $\mathbf{x}_{S_1}$ and $\mathbf{x}_{S_2}$ on the cell membrane, where each stimulus covered 5% of the cell surface. Both stimuli were applied with different amplitudes, $S_1 = 0.44\,\mu m/s$ and $S_2 = 0.4\,\mu m/s$, for a short period of time $\Delta t = 10\,s$, i.e. $t_1 = t_2 = 10\,s$. For the circular cell, the stimuli $S1$ and $S2$, were applied at opposite ends of the cell surface. For the non-circular cell, the stronger stimulus $S1$ was applied in the apical part at the end of the protrusion, while the weaker stimulus was applied $S2$ in the basal part (compare Figure 3.7 **B**). In case of the circular cell, a symmetry break with two membrane-bound clusters emerged. The stronger stimulus $S1$ induced a faster growing cluster that dominated the smaller cluster at the site of $S2$. Eventually, the cell polarized at the site of the stronger stimulus while the smaller cluster vanished. This outcome was observed for both models. For the non-circular cell a reversed outcome was observed. The mating projection acted as a kind of 'bottle neck' for the cluster that was induced in the apical part at the site of $S1$. Eventually, the cluster at $S1$ grew slower than at the site of $S2$, which resulted in a polarized state in the basal part of the cell.

An interpretation of this effect is given by the narrow escape problem (Schuss et al., 2007). The emerging clusters at the site of $S1$ and $S2$ acts as an absorber of cytosolic molecules. For an arbitrary molecule in the cytosol the mean time to get absorbed by the emerging cluster , is longer in the apical part than in the basal part. A related problem has been investigated for dendritic spines, where the time was calculated for a molecule to reach and get absorbed in the narrow end of the spine. For a review of the narrow escape problem, I refer to (Schuss, 2012).

In a previous study (Diener et al., 2014), colleagues and I observed yeast cells that formed multiple shmoos. When yeast cells where simulated with uniformly distributed pheromone, cells formed consecutive mating projections in distinct directions. This effect was also observed when cells where shaken and constantly disturbed. In both setups, cells usually formed shmoos at another site of the first mating projection. In Bidlingmaier and Snyder (2004) and Moore et al. (2008), it was shown that polarization of consecutive shmoos formed in an oscillatory manner over time periods of several hours. Note that the initial polarization takes place on a time scale of minutes.

These observations motivated a third setup with computational domains that represent different shmoo shapes in 3D as shown in Figure 3.8. Here, I investigated the impact on the geometry for the WP model. A noisy signal was used to stimulate the cell surface. The noise was assumed to be spatially uncorrelated. It was generated by selecting independent and identically distributed stationary random variables over a given time period $[t_1, t_2]$ for each node on the surface of the computational mesh. These values were assigned to

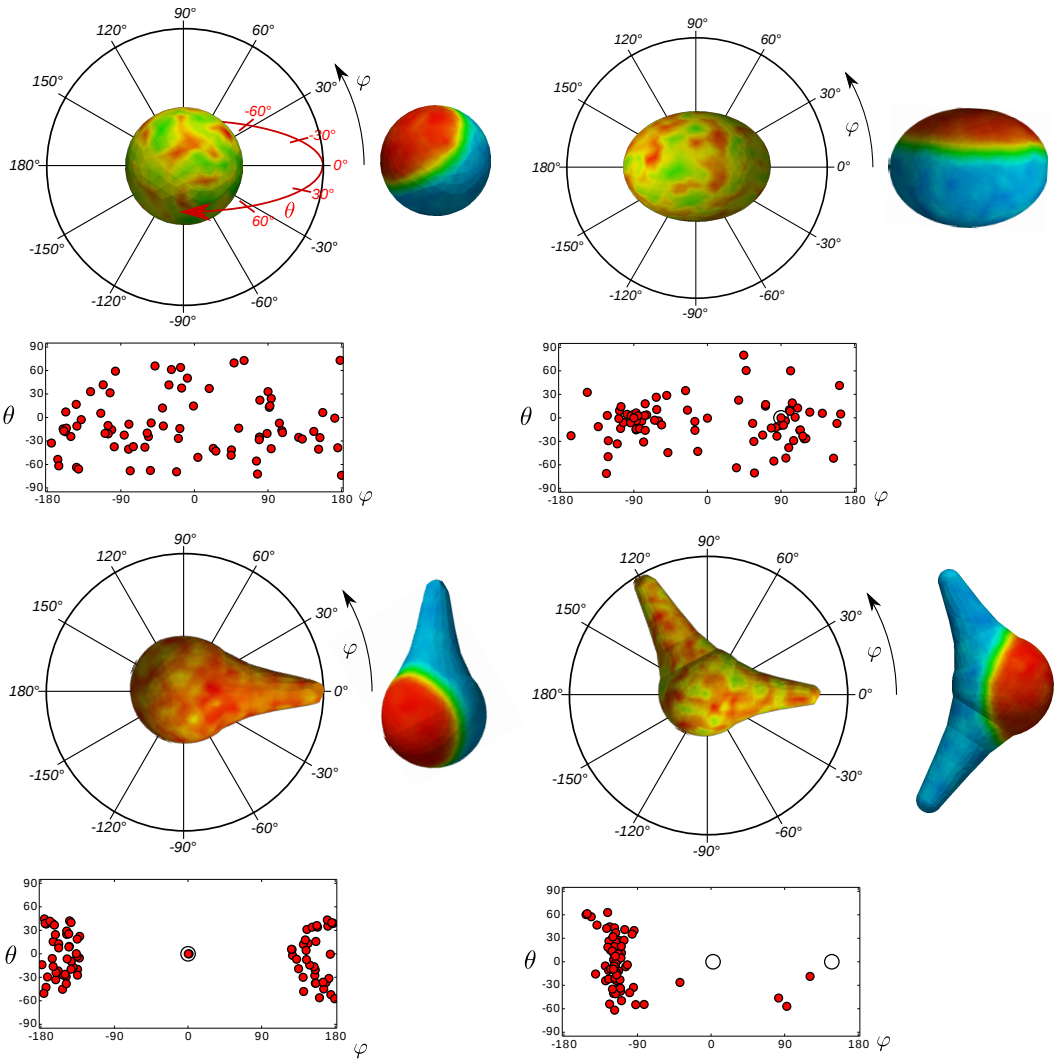

Figure 3.8: **Polarization Behaviour for Shapes with Multiple Shmoos.** 80 Simulations were performed for each cell shape and the coordinates of the centre of the polarization sites were visualized in a scatterplot. In the scatter plot, the polar and azimuthal angle are shown, where the centre of the spherical coordinates was set to the centre of mass of each cell shape. Larger blank circle indicate the locations of the shmoo tip(s) in the spherical coordinate system.

the function $k_S(\mathbf{x}, t)|_{t\in[t_1,t_2]}$. I used a log-normal distribution with mean $\mu = 0$ and standard deviation $\sigma = 0.1$. The noisy signal was changed over time by regenerating $k_S(\mathbf{x}, t)$ in time intervals of length $\Delta t = t_1 - t_2 = 5\,s$.

The four different cell shapes were a spherical cell, an ellipsoid, a cell with one mating projection and a cell with two mating projections. Simulations were repeated 80 times for each of these four cell shapes. For each simulation, the polarization site was plotted in a spherical coordinate system as shown in Figure 3.8. Simulations of a spherical cell resulted - as expected - in randomly distributed polarization sites. The ellipsoidal shape resulted in a slightly biased distribution of polarization sites at the long edges and less polarization events at the ends of the ellipsoid. The result for the shapes with one or two mating projections were distinct. Simulations of a cell with one mating projection led to an accumulation of polarization sites in the basal part. Interestingly, the polarization sites were distributed in a circular region around the opposite end of the mating projection. To reflect this distribution the second mating projection was assumed to be located in a 120° angle. Here, simulations resulted in a distribution of polarization sites in a much more confined region than for the other tested shapes. Polarization sites occurred most frequently on the site between the two mating projections.

For the WP model it was hypothesized, that polarization for cell shapes in 3D might most likely occur where mean curvature is minimal (Mori et al., 2008). For the non-spherical shapes used in this work mean curvature is minimal at the ends of the ellipsoid and in the transition regions from mating projection to the basal part. This effect seems also to play an important role here. There are, however, several competing effects. First of all, taking a finite cytosolic diffusion into account, the narrow escape problem plays a role and distances of the emerging cluster to the pool of cytosolic molecules. Second, the local surface to volume ratio, which can be related to the local mean curvature, influences the growth of the cluster on the membrane. Third, the interface of the cluster on a 2D surface is a thin stripe, which separates the phase of active membrane-bound molecules from the phase of inactive molecules on the membrane. This interface is naturally minimized during cluster formation. This effect, for example, can also explain stable clusters with centre at the tip of the mating projection. In conclusion, shapes in 3D are more complex and more studies have to be performed to explain the interplay of the mentioned spatial effects.

There are already analytical investigations of the shape dependence (Halatek and Frey, 2012; Thalmeier et al., 2016) of a bulk-surface reaction-diffusion system for elliptic shapes in 2D. Here, using a linear stability analysis it was shown that due to a geometry dependence of the reaction-diffusion patterns, oscillations are more likely to occur along the long axis of an elliptic cell shape. It would be interesting to develop a linear stability analysis for special cases of more complex 3D shapes.

Linear Stability Analysis of the Bulk-Surface Reaction-Diffusion System

The ability of non-linear reaction-diffusion systems to break symmetry, such as presented in Sections 3.1 and 3.2, depends on its parameters. There are different possibilities for the analysis of such systems. A classical method is the linear stability analysis as performed by Turing (1952) for 1D system. This analysis can be extended to bulk-surface reaction-diffusion systems as in Levine and Rappel (2005), Klünder et al. (2013) and Giese et al. (2015). This approach is based on a linearization around the homogeneous steady state, and the model behaviour is analysed in the linear regime. Recent approaches have also focused on the non-linear dynamics. One of them is the local perturbation analysis introduced in Edelstein-Keshet et al. (2013) and Holmes et al. (2015). The local perturbation analysis is based on the simplification $D_c \to \infty$ and $D_m = 0$, which results in a system of ODEs. Complex reaction-diffusion systems can be investigated with this analysis method, however, the interplay of fast and slow diffusion is neglected. Another method for investigation of the non-linear regime is the weakly non-linear stability analysis, which was applied for a class of 1D reaction-diffusion models in Rubinstein et al. (2012). This analysis, however, goes beyond the scope of this study and, therefore, the linear stability analysis was performed for the WP and GOR model in this study.

In (Giese et al., 2015), a linear stability for the 2D bulk-surface reaction-diffusion system was performed. Here, this analysis is extended to the 3D system. For this analysis the following simplifications were assumed. First, the computational domain was considered to be a sphere of radius R. Second, it was assumed that there is no spatial inhomogeneity on the membrane and in the cytosol. For the subsequent analysis, the equations from Section 3.2 were transformed into spherical coordinates (r, ϕ, θ). The Laplace-Beltrami operator on the boundary can then be expressed as

$$\Delta_{\theta,\phi} = \frac{1}{R^2}\frac{1}{\sin\theta}\frac{\partial}{\partial\theta}\left(\sin\theta\frac{\partial}{\partial\theta}\right) + \frac{1}{R^2}\frac{1}{\sin^2\theta}\frac{\partial^2}{\partial^2\phi}.$$

Note that the Laplace operator becomes $\Delta = \Delta_r + \Delta_{\theta,\phi}$, where $\Delta_r := \frac{\partial^2}{\partial r^2} + \frac{1}{r}\frac{\partial}{\partial r}$. Expressed in spherical coordinates, the equations from Section 3.2 then read

$$\frac{\partial u(\theta,\phi,t)}{\partial t} = D_m\Delta_{\phi,\theta}u(\theta,\phi,t) + f(u(\theta,\phi,t), v(R,\theta,\phi,t)), \tag{3.15}$$

$$\frac{\partial v(r,\theta,\phi,t)}{\partial t} = D_c\big[\Delta_r + \Delta_{\theta,\phi}\big]v(r,\theta,\phi,t), \tag{3.16}$$

for $r \in [0, R)$, $\theta \in [0, \pi)$ and $\phi \in [0, 2\pi)$. The boundary condition for the cytosolic equation (3.16) reads

$$-D_c\frac{\partial}{\partial r}v(r,\theta,\phi,t)\Big|_{r=R} = f(u(\theta,\phi,t), v(R,\theta,\phi,t)), \tag{3.17}$$

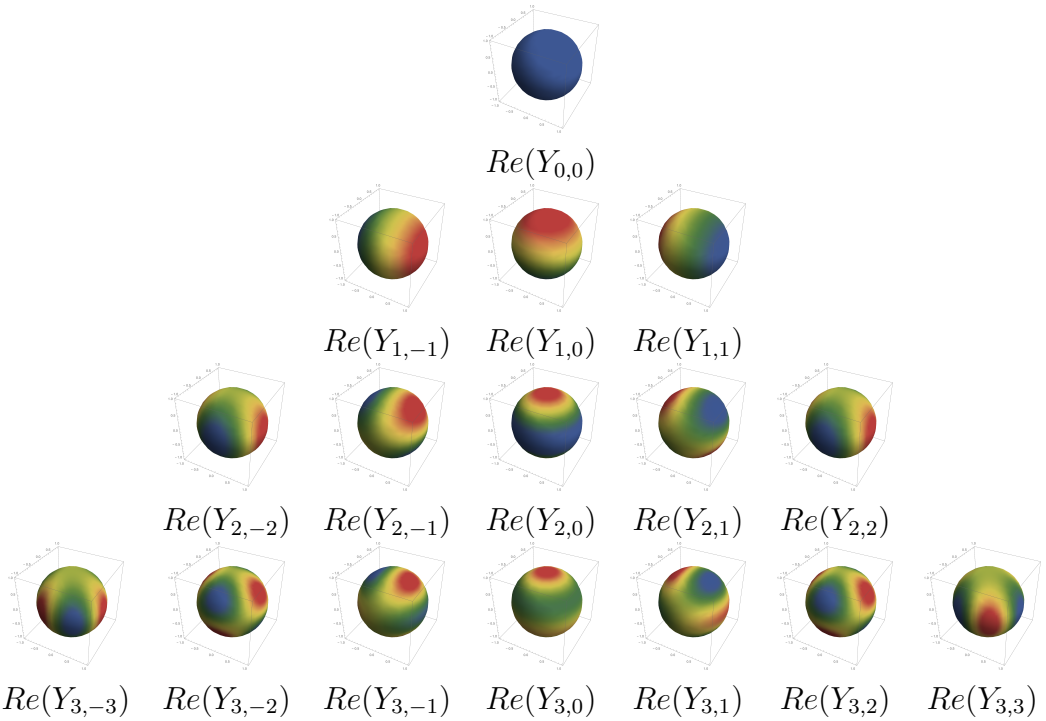

Table 3.3: **Illustration of spherical harmonics.** The real part $Re(Y_{k,l})$ of the spherical harmonics was plotted up to order $k = 3$ as used for the analysis of the bulk-surface reaction-diffusion system.

for $\theta \in [0, \pi)$ and $\phi \in [0, 2\pi)$. Let $(\bar{u}_0, \bar{v}_0)$ be a steady state of our system such that $f(\bar{u}_0, \bar{v}_0) = 0$. Small perturbations from this steady state were described by functions $\xi_m = u - \bar{u}_0$ and $\xi_c = v - \bar{v}_0$. For these perturbations, we have

$$\begin{aligned}\frac{\partial \xi_m}{\partial t}(\theta, \phi, t) &= D_m \Delta_{\theta,\phi} \xi_m(\theta, \phi, t) \\ &\quad + f_u(\bar{u}_0, \bar{v}_0|_{r=R}) \xi_m(\theta, \phi, t) + f_v(\bar{u}_0, \bar{v}_0|_{r=R}) \xi_c(r, \theta, \phi, t), \qquad (3.18)\\ \frac{\partial \xi_c}{\partial t}(r, \theta, \phi, t) &= D_c \big[\Delta_r + \Delta_{\theta,\phi}\big] \xi_c(r, \theta, \phi, t) \qquad (3.19)\end{aligned}$$

in the linear regime, and the linearized boundary condition becomes

$$-D_c \frac{\partial}{\partial r} \xi_c(r, \theta, \phi, t)\Big|_{r=R} = f_u(\bar{u}_0, \bar{v}_0|_{r=R}) \xi_m(\theta, \phi, t) + f_v(\bar{u}_0, \bar{v}_0|_{r=R}) \xi_c(R, \theta, \phi, t). \qquad (3.20)$$

The eigenfunctions of the Laplace-Beltrami operator are given by spherical harmonics $Y_{k,l}$ (compare Table 3.3), since $r^2 \Delta_{\theta,\phi} Y_{k,l}(\theta, \phi) = -k(k+1) Y_{k,l}(\theta, \phi)$. The functions ξ_c and ξ_m were expanded as

$$\begin{aligned}\xi_m(\theta, \phi, t) &= \sum_{k=0}^{\infty} \sum_{l=-k}^{k} \xi_m^{k,l} Y_{k,l}(\theta, \phi) \exp(\lambda_{k,l} t),\\ \xi_c(r, \theta, \phi, t) &= \sum_{k=0}^{\infty} \sum_{l=-k}^{k} \xi_c^{k,l} i_k(r\sqrt{\lambda_k / D_c}) Y_{k,l}(\theta, \phi) \exp(\lambda_{k,l} t),\end{aligned}$$

where the functions i_k are modified spherical Bessel functions of the first kind. For the analysis, the growth modes λ_k were calculated to characterize systems behaviour. Note that λ_k does not depend on l (see Appendix 7.2 for details). For $\lambda_k > 0$ the corresponding term in the expansion is growing with time, while for $\lambda_k < 0$ the corresponding term is negligible. The following estimate for λ_k was derived

$$f_u(\bar{u}_0, \bar{v}_0|_{r=R}) - \frac{D_m k(k+1)}{R^2} - \underbrace{\frac{f_u(\bar{u}_0, \bar{v}_0|_{r=R}) f_v(\bar{u}_0, \bar{v}_0|_{r=R})}{\frac{D_c k}{R} + f_v(\bar{u}_0, \bar{v}_0|_{r=R})}}_{*}$$
$$\leq \lambda_k \leq f_u(\bar{u}_0, \bar{v}_0|_{r=R}) - \frac{D_m k(k+1)}{R^2}, \tag{3.21}$$

where $(\bar{u}_0, \bar{v}_0)$ denotes a steady state of the system (see Appendix 7.2 for derivation). The term (*) becomes small for large cytosolic diffusion coefficients D_c and the approximation $\lambda_k \approx f_u(\bar{u}_0, \bar{v}_0|_{r=R}) - \frac{D_m k(k+1)}{R^2}$ can be used. This approximation shows how the diffusion coefficient D_m for the active membrane-bound molecules counteracts the positive feedback $f_u(\bar{u}_0, \bar{v}_0|_{r=R})$. Furthermore, it can be observed that for larger cell sizes the term $\frac{D_m k(k+1)}{R^2}$ gets smaller and allows for multiple polarization sites to emerge. From the approximation (3.21) it follows that for $R_- < \sqrt{\frac{2D_m}{f_u(\bar{u}_0, \bar{v}_0|_{r=R})}}$, there are no growing eigenmodes and, therefore, no spontaneous polarization is possible. In the case of larger cells with $R_+ > \sqrt{\frac{6D_m}{f_u(\bar{u}_0, \bar{v}_0|_{r=R})}}$, there is more than one growing eigenmode, and multiple polarization sites can emerge.

The eigenmodes were calculated numerically and their dependence on crucial model parameters was investigated. For the GOR model, the analysis was performed in the non-zero homogeneous steady state $(\bar{u}_0, \bar{v}_0)$ as given in Section 3.1. The WP model was linearized around the transient steady state $(\bar{u}_0^T, \bar{v}_0)$. A plot of the growth modes λ_k for $k = 1, 2, 3$ is shown in Figure 3.9 **A,B**. In laboratory experiments, it was shown that overexpression of Cdc42 resulted in multiple polarization sites and the dependency on the GEF was reduced (Caviston et al., 2002). Corresponding to this observation the total number of signalling molecules was plotted against the model parameter expressing the positive feedback. In case of the GOR model, the parameter E_c was varied and in case of the WP model the dependence on γ was investigated (see Figure 3.9 **D**). The GOR modelled showed a larger regime of possible molecule numbers that lead to the emergence of a single polarization site upon perturbation. Furthermore, a large molecule number can compensate for a slow positive feedback. In contrast, the range of possible molecule numbers that allowed polarization was much more confined for the WP model. There is an upper and lower bound for the molecule number that led to polarization. A stronger positive feedback, however, led to a wider range of molecule numbers. The general interplay of the cytosolic diffusion coefficient D_c and D_m is shown in Figure 3.9 **C**. While for the WP model multiple polarisation sites emerge for a wide range of diffusion coefficients, the GOR model did not polarize for fast diffusion on the membrane.

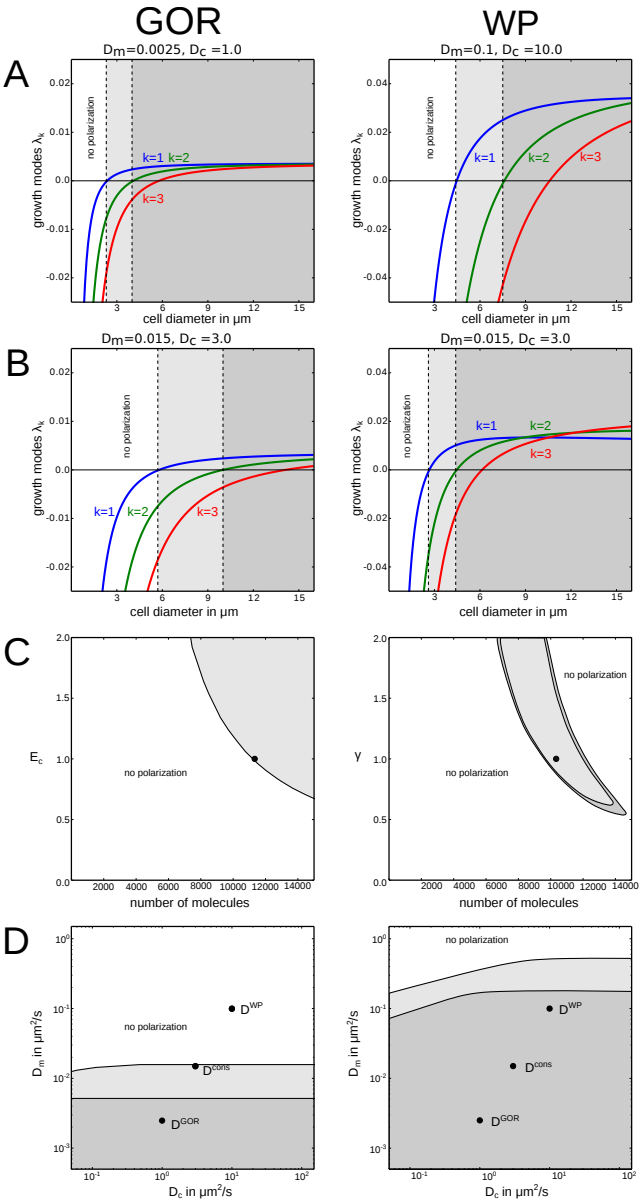

Figure 3.9: **Parameter study based on linear stability analysis for the 3D system. A:** Dependence of growth modes on the cell size. If all growth modes are negative (white region), the homogeneous steady state is stable. In case $\lambda_1 > 0$ and $\lambda_2, \lambda_3 < 0$ (light grey region), exactly one cluster emerges. If also $\lambda_2 > 0$ or $\lambda_3 > 0$ (dark grey region), multiple transient polarization sites can occur in the linear regime. **B:** Same setup as in **(A)**, but with different diffusion coefficients (the diffusion coefficients used are specified above the plots). **C:** Phase portrait of positive feedback and total molecule number variation in a slice through the cell of height $1\mu m$. (white: no polarization; light grey: exactly one cluster; dark grey: multiple transient clusters possible). **D:** Interdependence of polarization behaviour and diffusion coefficients (same colour coding as in (B) and (C)). Black dots show the extreme values used in the literature (Goryachev and Pokhilko, 2008; Mori et al., 2008).

Note that there are some significant changes in the results for the 2D and 3D bulk-surface reaction-diffusion system. In Giese et al. (2015), a linear stability analysis for the 2D system has been performed (compare Figure 3.10). The surface was carried out by using a Fourier series with summands $\exp(\lambda_k)\cos(k\phi)$ and $\exp(\lambda_k)\sin(k\phi)$. Here, $\cos(k\phi)$ and $\sin(k\phi)$ corresponded to the polar harmonics (compare Figure 3.10 **A**). An approximation for the Eigenmodes was given by $\lambda_k^{2D} \approx f_u(\bar{u}_0, \bar{v}_0|_{r=R}) - \frac{D_m k^2}{R^2}$ for fast cytosolic diffusion. From this approximation it follows, that in general $\lambda_k^{3D} < \lambda_k^{2D}$ is expected (compare equation 3.21). In 3D, the lower R^- and upper bounds R^+ for cell sizes, where only a unique polarization site emerges is shifted to larger cell sizes. This difference can also be observed in the plots, where the growth modes were computed numerically. The GOR system polarizes only for cells with a diameter $> 5\mu m$ in the case the consensus diffusion coefficients, D_m^{cons} and D_c^{cons}, were used. However, the regime for a unique polarisation site was very narrow for the original diffusion coefficients, D_m^{GOR} and D_c^{GOR}. For the WP model the dependence on the diffusion coefficients was less pronounced.

Diffusion Barriers on the Membrane

Heterogeneities on the membrane that influence diffusion play an important role in signalling. Diffusion barriers on the membrane in yeast are mediated for instance by cytoskeletal scaffolding proteins known as septins. In a recent experimental study it was shown that the polarization cap is controlled and confined by septins in the region of the mating projection (Kelley et al., 2015). In a combined approach of modelling and experiments, it was also shown that septin structures form a ring in the early phase of bud formation and confine the distribution of membrane-bound Cdc42 (Okada et al., 2013). It was also reported that structures like bud scars influence cell polarization during budding as well as mating (Tartakoff, 2015).

As in the setup in Section 3.3, simulations were performed with a shmoo-shaped cell as shown in Figure 3.11. In a first setup, a signal with two point stimuli (compare equation 3.14) were applied on the cell surface, but this time with equal strength $S_1 = S_2$ to compare the effect of cell shape, and diffusion barriers on the membrane. Two different kinds of barriers were tested, a one-sided and a two-sided barrier (compare Figure 3.11 **A**). For the two-sided barrier, both models polarized at the apical side. The diffusion barrier counteracts the diffusive transport away from stimulus S1 and, therefore, acts as a positive feedback on cluster formation. For the one-sided barrier both models behaved differently. While the GOR model polarized on the apical side, the WP model was not able to resolve the conflict in the given time frame ($t < 2000s$), and polarized on the basal and apical end. The outcome for the same setup without diffusion barrier is shown in Figure 3.11, which resulted in polarization on the basal site.

The same setup was repeated, but with a graded stimulus, which was given

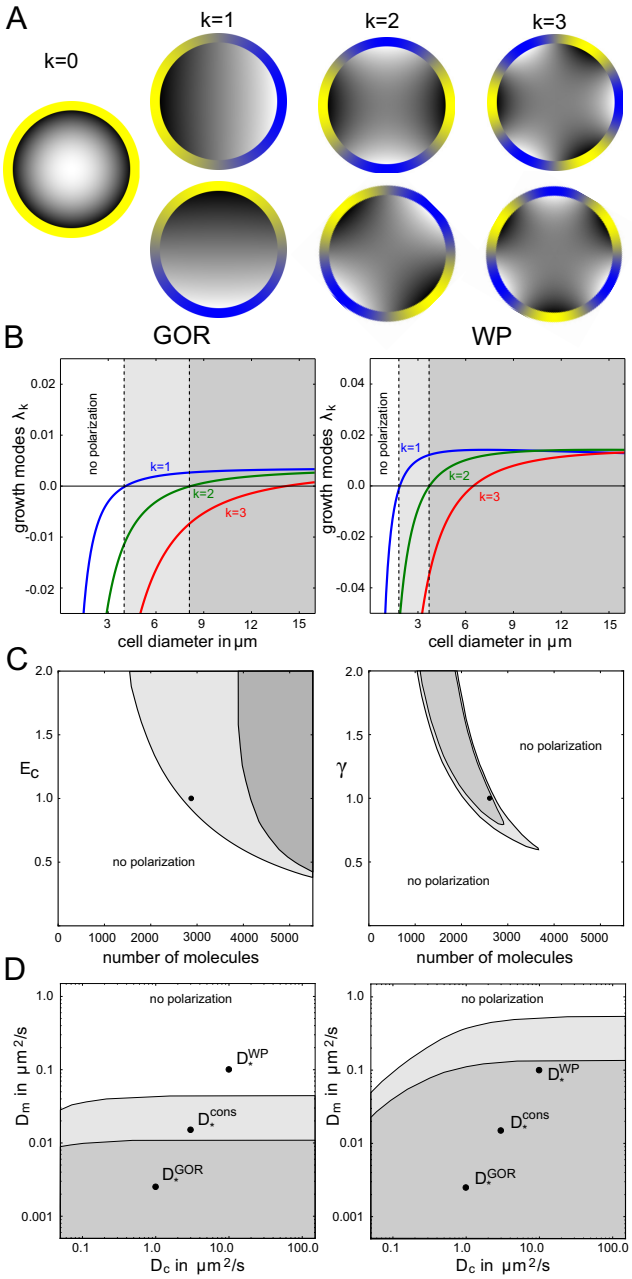

Figure 3.10: **Parameter study based on linear stability analysis.** (A) Schematic illustration of the fundamental solutions for different wave numbers k. Here, high and low concentration on the membrane is indicated by yellow and blue, respectively. High and low concentration in the cytosol is indicated by light grey and dark grey, respectively. (B) Dependence of growth modes on the cell size. If all growth modes are negative (white region), the homogeneous steady state is stable. In case $\lambda_1 > 0$ and $\lambda_2, \lambda_3 < 0$ (light grey region), exactly one cluster emerges. If also $\lambda_2 > 0$ or $\lambda_3 > 0$ (dark grey region), multiple transient polarization sites can occur in the linear regime. (C) Phase portrait of positive feedback and total molecule number variation. (white: no polarization; light grey: exactly one cluster; dark grey: multiple transient clusters possible). (D) Interdependence of polarization behaviour and diffusion coefficients (same colour coding as in (B) and (C)). Black dots show the extreme values used in the literature Mori et al. (2008); Goryachev and Pokhilko (2008). Figure from Giese et al. (2015).

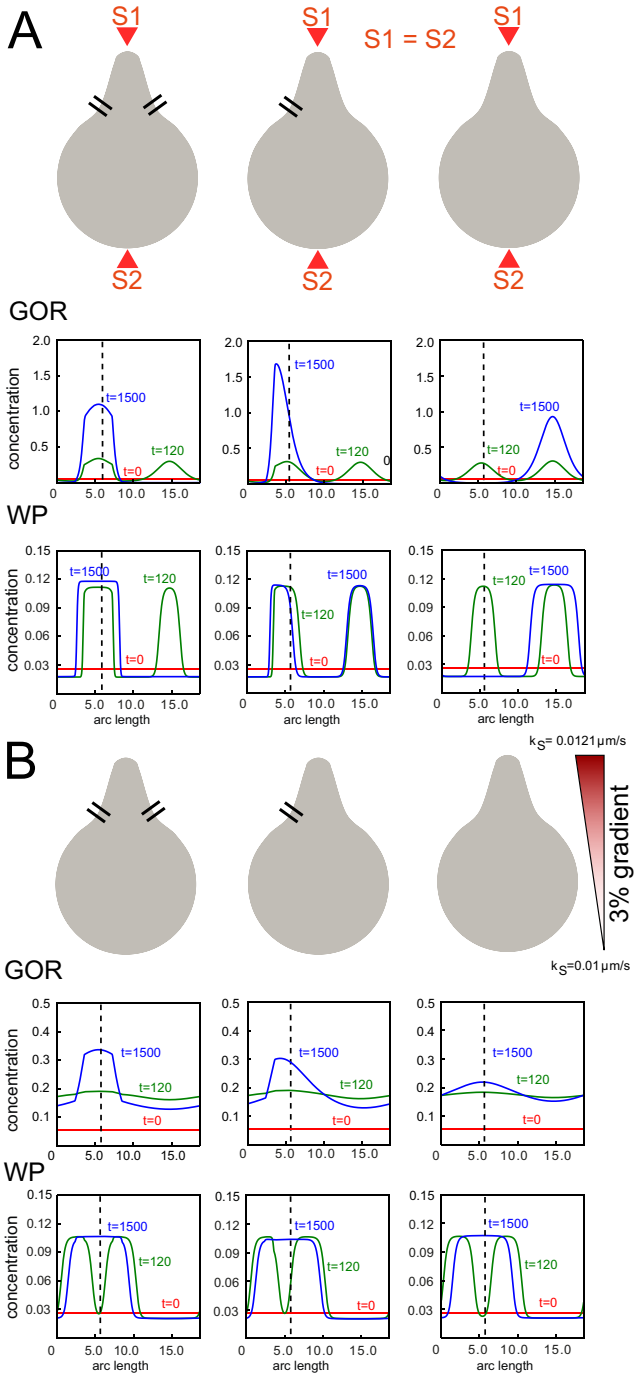

Figure 3.11: **The influence of diffusion barriers on the membrane was investigated for the GOR and the WP model.** (A) In contrast to section (A), the stimuli S1 and S2 were chosen equally strong in order to compare the influence of the shape with the effect of the barriers. Two diffusion barriers with 10- fold slower membrane diffusion were placed around the location of stimulus S1 [left column]. A single barrier with 10-fold slower diffusion was placed at the left-hand side next to the location of stimulus S1 [centre column]. (B) A graded signal was used to trigger cell polarization. Again we examined two diffusion barriers [left column], one diffusion barrier [centre column] and no barrier for comparison [right column]. Figure from Giese et al. (2015).

by

$$k_S(\mathbf{x}, t) = c_0 + c_1 \cdot \big(x_2 - (\mathbf{x}_{min})_2\big). \tag{3.22}$$

Here, $\mathbf{x}_{min}$ denotes the lowest point along the x_2-direction of the two dimensional cell at the basal site of the cell. The parameters $c_0 = 0.01\,\mu m/s$ and $c_1 = 3.0 \cdot 10^{-5}\,\mu m/s$ were used in this setup. Here, both models exhibited a different behaviour. The GOR model polarized at the apical site for the one- and two-sided barrier. In the case of no barrier, however, the system was not able to break symmetry, even after a long time ($t < 2000s$). The WP model was much more sensitive to the stimulation and polarized in all cases at the apical site.

In summary, for both cases the two-sided diffusion barriers enhanced cluster formation. For the GOR model the one-sided barrier also steered the centre of the cluster towards the diffusion barrier. This was not observed for the WP model, where we only have a low and a high concentration level except of a small transition layer.

Potential Influence of Organelles in the Cytosol

Eukaryotic cells comprise numerous structures and organelles such as the Golgi apparatus, the endoplasmic reticulum, the cytoskeleton or the nucleus, to name only a few. Advances in imaging techniques allow the tracking of molecules *in vivo* and infer transport properties that are influenced by internal structures of the cell (Barkai et al., 2012; Spokoini et al., 2012; Smith et al., 2015). This raises the question how organelles and internal structures in the cytosol bias cell polarization.

In this setup, organelles of different size and shape were placed into the cytosol. They mimic large cytosolic diffusion barriers such as the vacuole or the nucleus. A zero flux condition was assumed on the surface of these organelles (compare equation 3.11). First, a large elliptic organelle was placed into the cytosol as shown in Figure 3.12. The same noise stimulus as in Section 3.3 was applied on the surface of the cell. The simulations were repeated 100 times for the GOR and WP model. For both models gradually different outcomes were observed. While for the WP model a strong influence was observed, only a small bias was observed for the GOR model. Both models polarized less frequently behind the large organelle. Interestingly, simulations of the WP model resulted in an accumulation of polarization events in the neighbourhood (but not behind) the large organelle. This effect was much less pronounced for the GOR model.

The same setup was repeated, but with an additional small round organelle that was placed at the opposite to the large organelle. For the WP model this resulted in a large change of the distribution of polarization sites. The polarization sites accumulated in the neighbourhood of both organelles but less confined than in the case of only one organelle. For the GOR model the same effect was observed, but less pronounced.

The effect can again be explained by the narrow escape problem. A growing cluster of active membrane-bound molecules behind a large organelle acts like a sink shielded by an obstacle. Therefore this cluster absorbs a smaller fraction of cytosolic molecules than a cluster that is located at a site without limited diffusion. Apart from this major effect it is noteworthy that a complex pattern of gradients is formed due to the introduction of organelles. If a polarization cluster forms further away from the organelle, diffusive transport is limited by the organelle and a cytosolic gradient is formed with higher cytosolic concentration behind the organelle.

Discussion and Outlook

Cell polarization is a prerequisite for living cells during fundamental processes such as cell division, chemotaxis and morphogenesis. The ability of polarization mechanisms to adapt to cell shape and spatial structures in the cytosol or on the membrane is a crucial aspect which needs to be addressed by computational models and laboratory experiments. In this chapter, a Turing-type and a phase separation mechanism were tested *in silico* in situations typical for the mating yeast. Here, the GOR model and the WP model were chosen as representatives for the Turing-type and phase separation mechanism, respectively. Four different aspects of polarization behaviour were investigated: (i) the adaptation of cell polarization to cell shape; (ii) the dependence of spontaneous symmetry breaking on crucial parameters and cell size and shape; (iii) the effect of diffusion barriers on the membrane; (iv) the effect of diffusion barriers in the cytosol induced by large organelles.

A comparison of Turing-type and phase separation mechanisms with respect their sensitivity to cell geometry has been already carried out in an abstracted setting with moving geometries (Orlandini et al., 2013), however, with some important differences. In accordance with the results shown in this thesis, the authors found the Turing-type mechanism to be less influenced by shape than the phase separation mechanism. Orlandini et al. (2013) concluded that it might be beneficial for cells to disentangle their polarization behaviour from their cell shape. On the contrary, from the results shown in this thesis, it can be inferred that it might be beneficial for yeast cells to employ a mechanism that is shape dependent. In case of ambiguous pheromone signals, it is was reported that the shmoo forms at the site of the last cell division. However, if mating was not successful cells formed mating projections in distinct directions similar to the pattern observed in Figure 3.8. This has been reported in several experimental studies (Bidlingmaier and Snyder, 2004; Moore et al., 2008; Diener et al., 2014). Furthermore, stability analysis has shown that the GOR model is very sensitive to changes in diffusion on the membrane. This was also observed in the setup for the diffusion barriers in Section 3.5. For the GOR model concentration levels of the polarized state change with the type of barrier two-sided or one-sided. For the WP model the concentration of the excited phase at the polarization site is precisely con-

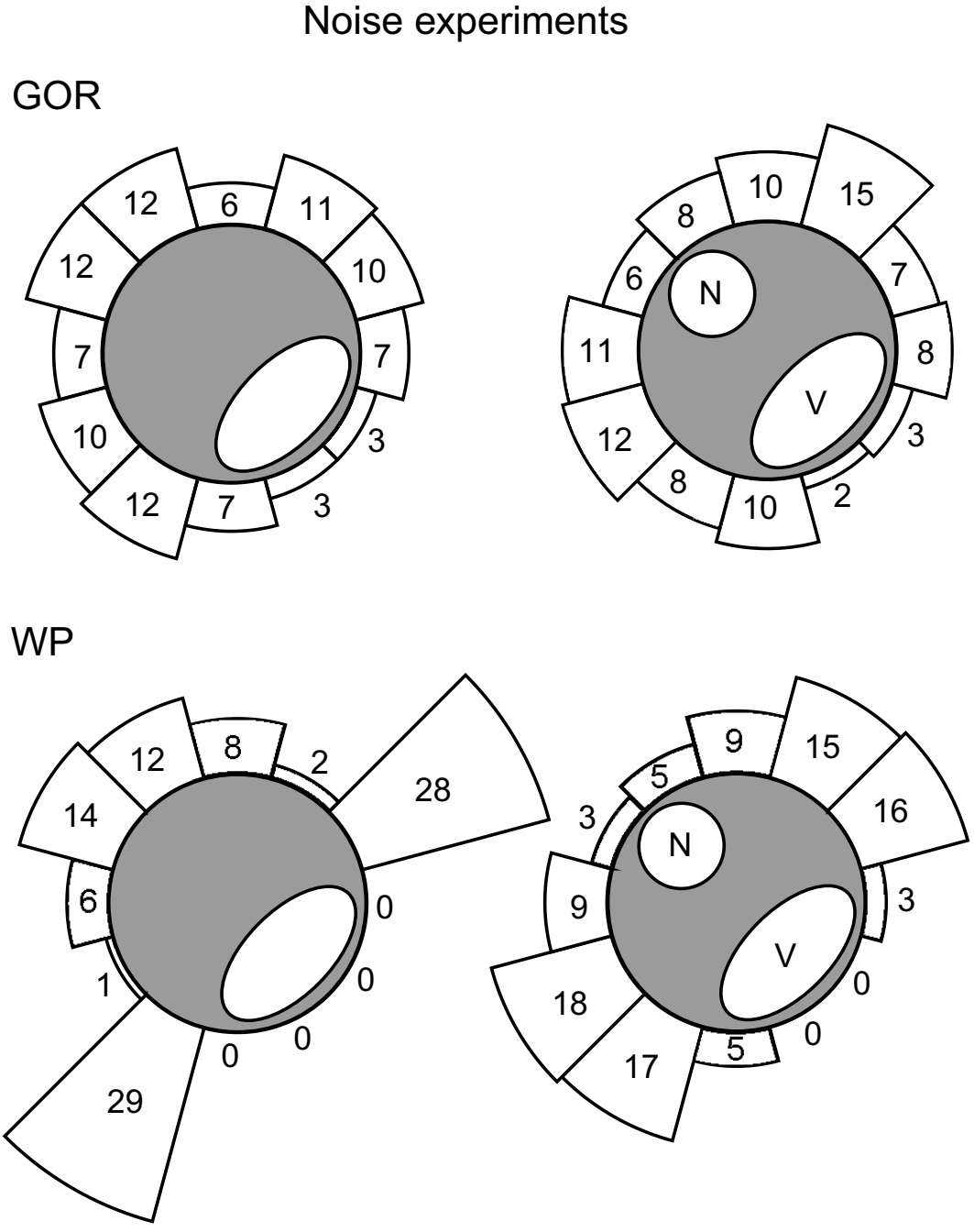

Figure 3.12: **The influence of cytosolic diffusion barriers was investigated for the GOR and the WP model, see results section (D).** Organelles (represented by circles or ellipses) which serve as diffusion barriers are placed at different positions. Simulations with different noisy signals were performed for each geometry and model. The number of polarization events is plotted on the cell surface. Figure from Giese et al. (2015).

trolled by the saturation constant K. The WP model is more likely than the GOR model to form multiple polarization sites upon perturbations of an initially homogeneous state. The emergence of multiple polarization sites in the initial phase, however, has been recently reported in Wu et al. (2016). The diffusion coefficient for membrane-bound Cdc42 in yeast of $D_m = 0.037\mu m^2/s$ for in Freisinger et al. (2013) is different from the value $D_m = 0.0025\mu m^2/s$ in Goryachev and Pokhilko (2008) and Okada et al. (2013), which was used in the original work for the GOR model. The GOR model was explicitly derived for cell polarization in yeast and it was hypothesized that a Turing-type mechanism explains the yeast polarization. However, the results shown here indicate that the kinetics of a phase separation mechanism describe the polarization during yeast mating better than the Turing-type mechanism.

The model extension into 2D or 3D can reveal important aspects of model behaviour. While the classical 1D framework allows for an understanding of the reaction kinetics and general dynamics, effects of cell shape and size can only be reliable investigated in higher dimensions. In 1D, the spatial domains representing the membrane and the cytosol are the same, while they differ in 2D and 3D. This also implies a different surface to volume ratio, which is $2/R$ for a circular cell in 2D and $3/R$ for a spherical cell in 3D. Therefore, the surface to volume scaling is essentially different than in 1D, where the ratio is 1. The behaviour already changed from a 1D extension to a 2D extension as was investigated in (Giese et al., 2014). The differences of the stability analysis in 2D and 3D were shown in this chapter. Recent studies on the analysis of shape dependence in bulk-surface reaction-diffusion systems were carried out in 2D and not in 3D (Halatek and Frey, 2012; Thalmeier et al., 2016). This owes the fact that setups of 3D simulations as well as analytical investigations are challenging. Here, 2D simulations provide a good trade-off between computational feasibility and the level of geometrical detail that can be represented. Many aspects of the system behaviour in 2D and 3D are essentially the same. However, conclusions on physiological parameters such as the measured diffusion coefficients, molecule numbers or feedback strength have to be done with care in reduced models with a 1D or 2D computational domain. Therefore, a 3D stability analysis and simulations of 3D cell geometries were performed in this thesis.

The GOR and WP models provide general insights into properties of the GTPase cycling. However, in future studies the interplay of these models with other processes has to be taken into account. For instance in yeast, the interplay of these models and the polarized cytoskeleton, which comprises septins, actin and microtubules would be interesting (Bi and Park, 2012). A promising conception for modeling the polarization of the cytoskeleton in yeast was described in Hawkins et al. (2009). Also the details of vesicle trafficking and endo- and exocytosis (Chou et al., 2012) need to be addressed. In Okada et al. (2013), the GOR model was coupled with a model for septin formation as well as endo- and exocytosis. However, important aspects of cell wall mechanics have not been addressed and also the process of endo- and exocytosis remains very elusive.

In other motile cell types as fish keratocytes, fibroblasts or *Dictyostelium discoideum* the effect of cell movement as well as the role of F-actin plays a key role (Falcke, 2015; Razbin et al., 2015). In a computational study from Holmes et al. (2012), the minimal WP model was coupled to the F-actin dynamics and the occurrance of actin-waves. In contrast, the results shown in this chapter were based on static geometries. This assumption can be justified for yeast, where the growth of the mating projection takes more than $1h$, while the polarization process takes place in the time scale of minutes. For motile cells the influences of cell shape that were presented here, might be even more pronounced. In Neilson et al. (2011), it has been shown for the slime mould *Dictyostelium discoideum* that the leading edge of pseudopods split into two distinct pseudopods. These two pseudopods merge again and the process is continued. This pattern was explained mechanistically with the dilution of signalling molecules on the membrane at the leading edge that occurs when a pseudopod is extended. The results shown in this chapter give two additional explanations. First, an extending pseudopod causes a narrowing of the enclosed volume, which locally limits the recruitment of molecules onto the cell surface. Second, the extension of a pseudopod also causes a dilution of signalling molecules in the cytosol. This gives an explanation on the level of reaction-diffusion mechanisms, where shape changes are based on a simplified driving force. In a full model for growing or motile cells, the interplay of cell polarization, changing cell shapes and cell mechanics needs to be addressed. The latter is investigated and discussed in the next chapter.

4

Mechanical Modelling of the Yeast Mating Morphogenesis

In the previous Chapter 3, the polarization behaviour of yeast, which initiates morphology changes, was investigated. Subsequent morphological changes that are induced by mechanical forces are focus of this chapter. Bacteria, fungal cells and plant cells are enclosed by a wall that provides protection and defines their cellular shape. In *S. cerevisiae*, the cell wall is the main structure that maintains cellular shape and integrity. The cell wall is a strong and elastic structure, which comprises 10% - 25% of the total cell mass and protects the yeast cell from harsh and abrupt environmental influences. For instance, yeast living in a sugar rich environment of a grape can experience an osmotic shock caused by rainfall (Levin, 2011). The cell wall is constantly remodelled and altered with changing environmental conditions. Moreover, the yeast cell wall has to be remodelled at various stages of the cell's life cycle including cell division, shmoo and zygote formation. This chapter is focused on the remodelling of the yeast cell wall during mating.

The Yeast Cell Wall Determines the Cell Shape

The yeast cell wall comprises an inner and an outer cell wall layer. The inner layer is mainly composed of the polysacharides β-1,3-glucan, β-1,6-glucan and β-1,4-linked N-acetylglucosamine also referred to as chitin. The outer layer is mainly composed of mannoproteins (Cabib and Arroyo, 2013). The cell wall is $80nm$ to $120nm$ thick and, therefore, the ratio of cell wall thickness to cell radius commonly varies around 1/30 to 1/25 (Smith et al., 2000). The cell wall integrity pathway regulates cell wall composition and thickness. As explained in the previous chapter the polarization during mating is initiated by signalling. The polarization and direction of growth is determined by the pheromone signalling pathway and its interaction with the small GTPases Cdc42 and Rho1. The small GTPase Rho1 is recruited by the $G\beta\gamma$-complex upon pheromone stimulation to the site of polarized growth (Bar et al., 2003). The local growth and cell wall strengthening is mainly controlled by the transmembrane receptors Mid2 and Mtl1, which activate the cell wall integrity pathway upon cell wall stress.

Not much is known about the chemical basis of cell wall alterations (De Nobel and Barnett, 1991; Cabib and Arroyo, 2013). Evidence for chitin enrichment during the formation of a mating projection of the shmoo has been found in (Schekman and Brawley, 1979) and it was suggested that chitin enrichment

is regulated by Rho1 and Pkc1 (Valdivia and Schekman, 2003a). The cell wall growth is mediated by exocytosis and it is noteworthy to mention that the cell wall is a structure that is outside the plasma membrane. Many steps of the cell wall synthesis are, therefore, prepared inside the cell or plasma membrane, while the cell wall is outside of the cell. The break up of crosslinks, the insertion of wall material and the formation of new crosslinks has to be organized in the periplasm, where common energy sources such as ATP are not present.

The cell wall properties have been measured and tested with a number of different methods. One method is to perform compression experiments as in (Smith et al., 2000). Properties such as the surface modulus, Young's modulus and the average breaking strain of *S. crevisiae* were determined. Other methods rely on atomic force microscopy experiments (AFM), which are capable of revealing spatial resolution of mechanical cell wall properties. Further advances have been made with AFM techniques that provide high spatial as well as temporal resolution (Dufrêne et al., 2013). The experimental AFM data that build the basis of the subsequent theoretical investigations are given in Goldenbogen et al. (2016). The AFM measurements provide insight into turgor pressure, local elasticity and cell wall thickness. For indentation experiments the classical models of Sneddon (Sneddon, 1965) and Hertz (Johnson et al., 1971) are most commonly used. However, the analysis and interpretation of AFM data is not trivial and there have been a number of recent theoretical investigations to obtain parameters such as turgor pressure and the local Young's Modulus from AFM force-indentation curves (Vella et al., 2012b,a; Digiuni et al., 2015).

Quantitative modelling is needed to provide deeper mechanistic insights in processes that can now be observed in great detail experimentally. The data obtained with advanced force spectroscopy and imaging techniques needs to be integrated and connected with modelling approaches that can represent cellular shape and structures. Many models based on continuum mechanics for thin shells have been employed to describe shape changing processes of walled cells such as bacteria (Chang and Huang, 2014), fungi (Drake and Vavylonis, 2013) and plants (Hamant et al., 2008).

However, the shape changes for *S. cerevisiae* has been mostly explained only by signalling (Slaughter et al., 2009; Chou et al., 2012; Angermann et al., 2012), while mechanical properties of the cell wall were neglected. There are a number of models describing the cell wall of plant cells (Boudaoud, 2003; Campàs and Mahadevan, 2009; Dumais et al., 2006; Hamant et al., 2008; Fayant et al., 2010) or the remodelling of the cell wall of the yeast *S. pombe* during elongation and cell division (Minc et al., 2009; Chang and Huang, 2014; Drake and Vavylonis, 2013; Abenza et al., 2015). However, a detailed spatio-temporal mechanical model for the cell wall of *S. cerevisiae* is not known to me. Although there are some similarities between *S. pombe* and *S. cerevisiae* both cells have different shapes and the underlying mechanisms are different in various aspects. This gap needs to be filled by modelling the mechanical properties of the cell wall during mating of the *S. cerevisiae*.

In this chapter, a mechanical model of the cell wall of the yeast *S. cerevisiae*

is explained and constructed. This model has also been used in a combined approach of modelling and experimental AFM data in Goldenbogen et al. (2016). However, here I want to present certain details and aspects that have not been discussed in Goldenbogen et al. (2016). First, a model for pressurized cells is used to capture general relations between turgor pressure, cell wall thickness and in-plane stresses that occur in steady state. A linear constitutive relationship for elastic materials with inhomogeneous material properties was assumed. Second, this model is extended to a dynamic cell wall model with plastic growth. A Lockhart-like model for stress dependent growth is assumed and tested for different elasticity patterns, as obtained from atomic force microscopy (AFM) data.

Modelling Cell Wall Mechanics and Growth

The Cell as a Pressure Vessel

The yeast morphogenesis during mating is shaped by an interplay of turgor pressure, cell wall stresses, varying material properties of the cell wall as well as cell wall synthesis (compare Figure 4.1). Walled cells are commonly modelled as pressure vessels, where the turgor pressure is assumed to play a driving force in morphogenesis. The turgor pressure generates forces that act on the cell wall and causes cell wall stresses. These stresses cause plastic growth, i.e. an irreversible cell wall expansion.

Helfrich Potential

Almost one hundred years ago the mathematician and biologist D'Arcy Wentworth Thompson was among the first to explain the growth and form of organism as well as single cells using physical principles (Thompson, 1942). In the case of cells he proposed that mainly turgor pressure and surface tension govern the cell shape, which is also included in the later developed Helfrich potential (Helfrich, 1973) for biological membranes. Additionally to the surface tension, also other energy contributions as the bending energy are included in the Helfrich potential. The Helfrich Potential has been used to explain the formation and shape of vesicles (Seifert, 1997) as well as the shape of motile cells such as fish keratocytes (Elliott et al., 2012). However, many cells from bacteria and fungal cells to plant cells are bounded by a cell wall that surrounds the plasma membrane. Since cell walls are usually much thicker and stiffer than membranes, it is assumed that the cell wall determines the cell shape. For modelling the cell wall of plant cells or fungi it is commonly assumed that the cell wall behaves as an elastic material in a certain regime and deforms in a plastic manner as soon as a certain threshold of strain or stress is reached (Lockhart, 1965; Boudaoud, 2003).

The mechanical energy is composed of the stretching, bending and pressure energies (Boudaoud, 2003):

$$W = \underbrace{\frac{1}{2}\int_A \left(\lambda \operatorname{tr}(\mathcal{E})^2 + \mu \operatorname{tr}(\mathcal{E}^2)\right)\, \mathrm{d}A}_{\text{Stretching Energy}} + \underbrace{\frac{1}{2}\kappa \int_A (H - c_0)^2 \, \mathrm{d}A}_{\text{Bending energy}} - \underbrace{PV}_{\text{Pressure Energy}} .$$

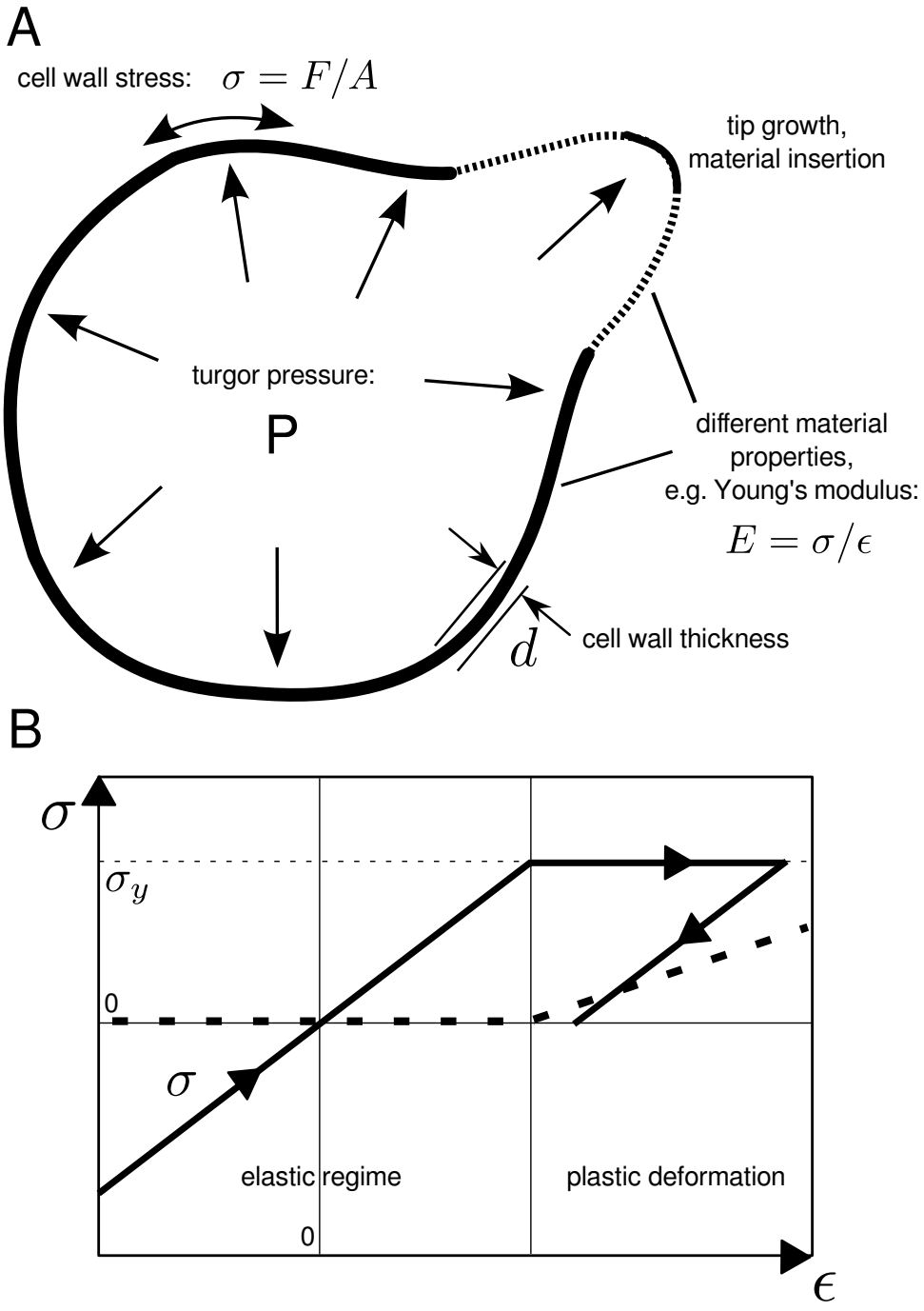

Figure 4.1: **Conceptual figure describing the cell wall mechanics. A:** The cell wall as a pressurized elastic shell. The formation of the shmoo shape is an interplay of turgor pressure, heterogeneous distribution of the Young's modulus, cell wall thickness and plastic growth. **B:** Strain-stress profile (strain: ϵ, stress: σ).The cell wall is assumed to deform elastically as long as the cell wall stress σ is below a yield threshold σ_y. Above this yield threshold the cell wall deforms irreversibly. The growth rate is indicated by a dashed line. Part **B** of the figure was adapted and modified from Boudaoud (2003).

This energy accounts for three different aspects: **(i)** $\mathcal{E}$ is the strain tensor and λ and μ are the Lamé coefficients. The relative change in area is accounted for in the term $tr(\mathcal{E}) = \frac{\Delta a}{a}$ which is part of the elastic stretching energy of the Helfrich Potential. This term is often also referred as surface tension (Elliott et al., 2012). However, the classical Helfrich Potential does not account for shear forces, since the ideal membrane behaves like a fluid, where molecules can rearrange. In a rigid cell wall the shear forces, which are given by $\mathrm{tr}(\mathcal{E}^2)$, are important and cannot be neglected. **(ii)** In the term for the bending energy, H denotes the mean curvature of the cell wall and c_0 its spontaneous curvature. The coefficient κ is the bending modulus. **(iii)** P is the turgor pressure and V the cell volume. The pressure energy is given by the product of pressure and volume.

Depending on the cell type and assumed conditions either the stretching energy or bending energy govern the cell shape (Boudaoud, 2003). In a computational study with *S. pombe* the influence of these energy terms were investigated in depth (Atilgan et al., 2015), but the stretching energy has been found to be the governing energy term. This assumption was also made in a number of other cell wall models (Hamant et al., 2008; Fayant et al., 2010; Dumais et al., 2006; Bernal et al., 2007; Drake and Vavylonis, 2013; Campàs and Mahadevan, 2009). In yeast, the ratio $h/R < 0.04$ is small compared to the occurring strains $\epsilon > 0.2$ in the basal part of the cell and the strains in the mating projection are even higher due to the reduced Young's modulus, as will be discussed later in this chapter. In the remainder, the elastic stretching energy of the cell wall is assumed to govern the shape evolution while the contribution of the bending energy is assumed to be negligible.

Cell Wall Stresses

The turgor pressure is constantly acting on the inner surface of the cell wall and balances with the cell wall stresses in equilibrium. Since the thickness of the wall is small compared to the cell diameter, the yeast cell wall can be considered as a thin pressurized shell. Stresses are defined as forces per area, where in the case of the cell wall the areas are cross sections through the cell wall. Commonly it is assumed that the cell wall deforms only slightly in normal direction, which means that the wall thickness remains constant upon loading. Therefore, only in-plane stresses are considered to be important in the remainder of this chapter. The in-plane stresses act tangential to the cell wall as shown in Figure 4.2. They can be expressed in terms of the principal stresses. In case of an axisymmetric geometry, these principal stresses are given by the circumferential stress σ_θ and meridional stress σ_s. For a spherical or cylindrical geometry, the stresses and strains can be computed by explicit analytical expressions depending on the radius r of the sphere or cylinder. For a sphere both principal stresses are equal and are computed from (Chang and

Huang, 2014):

$$\sigma_s = \sigma_\theta = \frac{Pr}{2d}, \tag{4.1}$$

where r is the radius of the sphere. The circumferential and meridional stress for a cylinder are different and given by

$$\sigma_s = \frac{Pr}{2d}, \tag{4.2}$$

$$\sigma_\theta = \frac{Pr}{d}. \tag{4.3}$$

For general axisymmetric cell shapes, the principal stresses can be expressed depending on the local curvature. The standard parameterization of a surface of revolution is given by

$$\begin{aligned} x &= \phi(u)\cos\theta, \\ y &= \phi(u)\sin\theta, \\ z &= \psi(u), \end{aligned} \tag{4.4}$$

where r and ψ are functions describing the distance from the z-axis and the z-coordinate, respectively. The principal curvatures are given by

$$\begin{aligned} \kappa_s &= \frac{sgn(\phi)(\phi''\psi' - \phi'\psi'')}{(\phi^2 + \psi^2)^{3/2}}, \\ \kappa_\theta &= \frac{\psi'}{|\phi|\sqrt{\phi^2 + \psi^2}}. \end{aligned} \tag{4.5}$$

The corresponding stresses can be expressed in terms of curvatures (Fluegge, 1973):

$$\sigma_s = \frac{P}{2d\kappa_\theta}, \tag{4.6}$$

$$\sigma_\theta = \frac{P}{2d\kappa_\theta}\left(2 - \frac{\kappa_s}{\kappa_\theta}\right). \tag{4.7}$$

In summary, the stresses in equilibrium depend only on the geometry at steady state. For a shmoo shape as shown in (Figure 4.3), the stresses in the base part take the highest values, while the stresses in the shaft are comparably low. The stress at the tip is very sensitive towards small geometrical variations (Dumais et al., 2006). A flat tip with low curvature results in high stresses, while a sharp or pointed tip with high local curvature results in low stresses.

A commonly used stress criterion for plastic growth is the von Mises criterion. For principal plane stress the von Mises stress is given by Yu (2006):

$$\sigma^{\mathrm{VM}} = \sqrt{\sigma_s^2 + \sigma_\theta^2 - \sigma_s\sigma_\theta}. \tag{4.8}$$

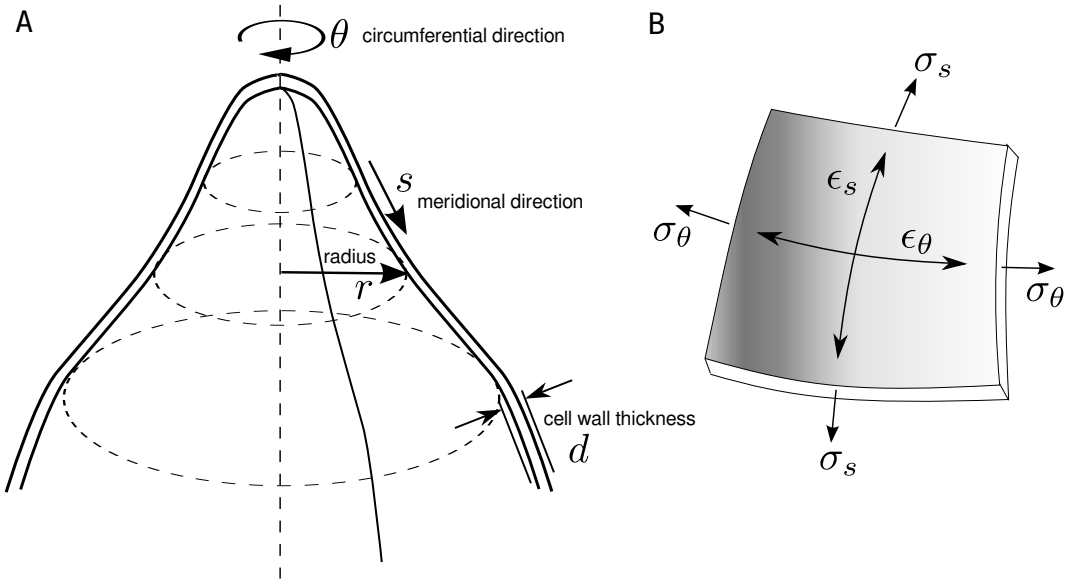

Figure 4.2: **Principal stresses and curvatures A:** Geometrical variables that describe the axisymmetric cell shape. The meridional direction is denoted by s and the circumferential direction by θ. The radius r describes the distance to the z-axis. **B:** Principal stresses and strains for one surface patch. Here, ϵ_s and σ_s denote the meridional strain and stress, respectively. ϵ_θ and σ_θ denote the circumferential strain and stress, respectively.

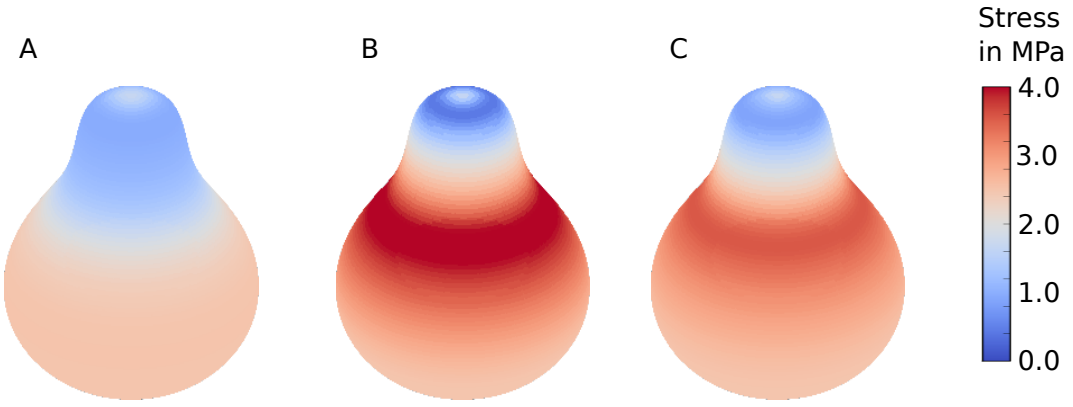

Figure 4.3: **Distribution of meridional (A), circumferential (B) and von Mises stress (C).** The stresses were calculated exemplified for a typical shmoo shape.

A plot of the von Mises stress for a typical shmoo shape is shown in Figure 4.3. Note that for a sphere of radius the von Mises stress is given by

$$\sigma^{\mathrm{VM}} = \sigma_s = \sigma_\theta = \frac{Pr}{d}, \tag{4.9}$$

while for a cylinder

$$\sigma^{\mathrm{VM}} = \sqrt{\left(\frac{Pr}{2d}\right)^2 + \left(\frac{Pr}{d}\right)^2 - 2\left(\frac{Pr}{2d}\right)^2} = \frac{3Pr}{4d}. \tag{4.10}$$

In general it holds $\min\{\sigma_s, \sigma_\theta\} < \sigma^{\mathrm{VM}} < \max\{\sigma_s, \sigma_\theta\}$.

A Linear Elastic Constitutive Relationship

The cell wall is assumed to be an elastic material. To obtain an analytical description between turgor pressure, Young's modulus and cell shape, a simple linear constitutive relationship is assumed. This linear relationship is determined by the Young's modulus and the Poisson ratio (Fluegge, 1973):

$$\begin{pmatrix}\epsilon_s(s)\\ \epsilon_\theta(s)\end{pmatrix} = \frac{1}{E(s)}\begin{pmatrix}1 & -\nu\\ -\nu & 1\end{pmatrix}\begin{pmatrix}\sigma_s(s)\\ \sigma_\theta(s)\end{pmatrix}. \tag{4.11}$$

Here, $\epsilon_s(s)$ and $\epsilon_\theta(s)$ are the meridional and circumferential stresses. In this description, the Young's modulus $E(s)$, the principal stresses $\sigma_s(s)$ and $\sigma_\theta(s)$ as well as the principal strains $\epsilon_s(s)$ and $\epsilon_\theta(s)$, are functions of the arc length s (see Figure 4.2). The arc length is measured starting from the base point of the shmoo shape, opposite of the tip. In Bernal et al. (2007), a model for a lily pollen tube was developed, where an elastic cell wall deforms and growth only at the tip. The model serves as basis for the following derivations, but was slightly adapted to the setup of a shmooing yeast cell. For simplification it is assumed that there are two distinct regions: (i) an elastic region and (ii) a region of growth which is described by a small circular region with radius r_{tip} at the shmoo tip. Intracellular vesicles were found to be directed to the tip during the shmooing process (Baba et al., 1989) and, hence, we considered material insertion and cell wall synthesis to occur only at the tip of the mating projection. Therefore, the assumption of pure elastic material at the tip must fail and the tip was consequently excluded from strain and elasticity calculations.

Inserting the expression for the meridional and circumferential stress (see equation 4.7) in the constitutive relationship (equation 4.11) results in:

$$\epsilon_s = \frac{1}{E(s)}(\sigma_s(s) - \nu\sigma_\theta(s)) = \frac{1}{E(s)}\left(\frac{P}{2h\kappa_\theta} - \nu\frac{P}{2h\kappa_\theta}\left(2 - \frac{\kappa_s}{\kappa_\theta}\right)\right), \tag{4.12}$$

$$\epsilon_\theta = \frac{1}{E(s)}(\sigma_\theta(s) - \nu\sigma_s(s)) = \frac{1}{E(s)}\left(\frac{P}{2h\kappa_\theta}\left(2 - \frac{\kappa_s}{\kappa_\theta}\right) - \nu\frac{P}{2h\kappa_\theta}\right). \tag{4.13}$$

The principal strains can be calculated from

$$\epsilon_s = \frac{ds(s) - dS(s)}{dS(s)}, \tag{4.14}$$

$$\epsilon_\theta = \frac{r(s) - R(s)}{R(s)}. \tag{4.15}$$

S is the meridional arc length of the relaxed shape measured from the base end and, accordingly, dS denotes a small relaxed and ds the actual extend of a small surface patch of the cell wall in meridional direction. Similarly, $R(s)$ denotes the relaxed radius and $r(s)$ the actual extended radius. With these notations we get:

$$\begin{aligned}\epsilon_\theta = \frac{r(s) - R(s)}{R(s)} &= \frac{1}{E(s)}(\sigma_\theta(s) - \nu\sigma_s(s)) \\ &= \frac{1}{E(s)}\left(\frac{P}{2h\kappa_\theta}\left(2 - \frac{\kappa_s}{\kappa_\theta}\right) - \nu\frac{P}{2h\kappa_\theta}\right).\end{aligned} \tag{4.16}$$

Furthermore, we assumed, that the velocity at the front for the material insertion is fixed in space. To determine the positions of inserted material, the following equation has to be solved (Bernal et al., 2007):

$$ds(s) = \left(\left(\frac{r(s)}{R(s)} - 1\right)\frac{(1-2\nu)\kappa_\theta(s) + \kappa_s(s)}{(2-\nu)\kappa_\theta(s) - \kappa_s(s)} + 1\right) dS(s). \tag{4.17}$$

With this relationship the points of the relaxed shape and the extended natural shape of the cell under pressure can be identified (see Figure 4.4 **C**). According to equation (4.16), the Young's modulus can be calculated from

$$E(s) = \frac{R(s)}{r(s) - R(s)}\left(\frac{P}{2h\kappa_\theta}\left(2 - \frac{\kappa_s}{\kappa_\theta}\right) - \nu\frac{P}{2h\kappa_\theta}\right). \tag{4.18}$$

From the known deformation status of the relaxed and extended cell shape, the spatial distribution of the Young's modulus was derived, which is required for maintaining the shmoo shape at steady state (see Figure 4.4). The characteristic of the spatial distribution of E is determined by the interplay of stresses and strains. As expected, the Young's modulus is uniformly distributed in the base part, but despite lower stresses in the protrusion region, the Young's modulus is reduced at the shaft. However, the Young's modulus is slightly larger at the neck. As stated above, the model does not allow for the calculation of the Young's modulus at the tip, where material is inserted. The assumption of elastic deformation, constant turgor pressure, a confined region of growth at the tip and the given shmoo-like shape, the Young's modulus has to be heterogeneous, with lower values in the mating projection.

In Goldenbogen et al. (2016), the general elasticity pattern predicted by the steady state elasticity model was confirmed. A lower cell wall elasticity in the region of the mating projection was found for pheromone stimulated yeast cells. Moreover, a region of stiffer material was found at the tip in

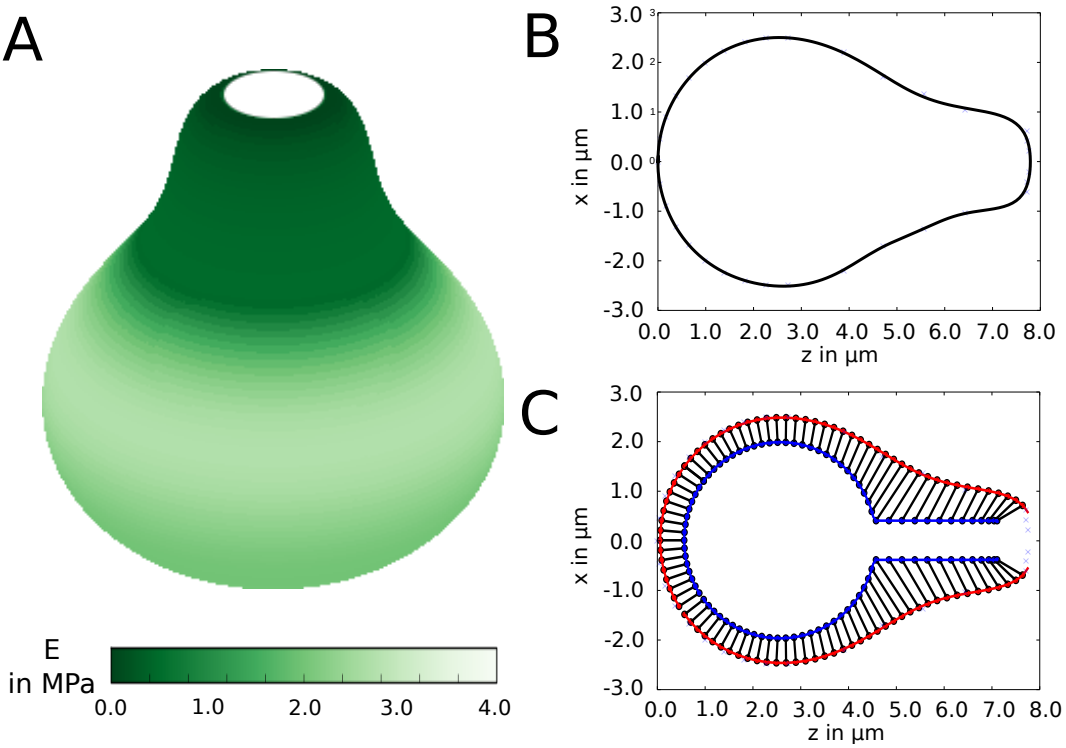

Figure 4.4: **Distribution of the Young's modulus A:** Distribution of the Young's Modulus for the given cell shape, dark green shows low values & white high values **B:** The outline of the cell shape, which was also used in Figure 4.3 for the calculation of cell wall stresses. The extended radius at the base was assumed to be $r_{\text{base}} = 2.5\ \mu m$, while the radius at the shaft of the mating projection was assumed to be $r_{\text{shaft}} = 1.0\ \mu m$. **C:** Blue and red dots describe the shape of the relaxed shape and actual shape, respectively. The relaxed shape is assumed to contain a spherical part with radius $R_{\text{base}} = 2.0\ \mu m$ and a growth zone of radius $R_{\text{tip}} = 0.5\ \mu m$.

Variable	Value	Description	Model(s)
P	0.2 MPa	turgor pressure	dynamic model & steady state model
ν	0.5	Poisson ratio	dynamic model & steady state model
d	100 nm	cell wall thickness	dynamic model & steady state model
E_{base}	2.6 MPa	Young's modulus in the base region	dynamic model
E_{shaft}	0.47 MPa	Young's modulus at the shaft of the mating pojection	dynamic model
E_{tip}	2.6 MPa	Young's modulus at the tip	dynamic model
R_{base}	2.0 μm	relaxed radius for the base	dynamic model & steady state model
r_{base}	2.5 μm	initial expanded radius	dynamic model & steady state model
R_{tip}	2.0 μm	radius of increased Young's modulus at the tip	dynamic model
R_{shaft}	1.0 μm	radius of reduced Young's modulus at the shaft	dynamic model
R_{growth}	1.0 μm	radius of growth at the tip	dynamic model & steady state model
σ_Y	0.4	yield stress	dynamic model
γ	0.004 $MPa^{-1}s^{-1}$	growth rate	dynamic model

Table 4.1: **Overview of parameters used for the steady state and dynamic cell wall model.**

the presumed growth zone. While the steady state model provided insights on general relationships of important quantities in walled cells, it does not account for plastic growth. Also the relaxed as well as extended cell shape are an input of the model while the elasticity, stress and strain distribution are an output. In the following, a dynamic cell wall model is constructed, where *vice versa* the elasticity distribution obtained from the AFM measurements is an input and the shape is the output.

Dynamic Cell Wall Model

In this section, a dynamic cell wall model is constructed as in Goldenbogen et al. (2016). In addition, a general elasticity framework on the basis of a continuous formulation of the elasticity equations is introduced.

Continuous Elasticity

We assume that the cell wall can be represented as a shell with thickness d. This shell is described as an evolving surface $\Gamma(t) \subset \mathbb{R}^3$. The evolution of the cell wall shall be described by a deformation function $\Phi(t, \mathbf{x}) : \mathbb{R}^3 \to \mathbb{R}^3$. In the classical elasticity the displacement $u(t, \mathbf{x}) := \Phi(t, \mathbf{x}) - \mathbf{x}$ is used to describe deformational changes. The *right Cauchy-Green deformation tensor* $\mathcal{C}$ is defined as:

$$\mathcal{C} = \nabla\Phi^T \nabla\Phi. \tag{4.19}$$

This leads to the *Green-Lagrange strain tensor*, which depends on $\mathcal{C}$ and is defined as:

$$\mathcal{E} = \frac{1}{2}(C - I) = \frac{1}{2}\{(\nabla u + I)^T(\nabla u + I) - I\} = \frac{1}{2}(\nabla u^T + \nabla u + \nabla u^T \nabla u). \tag{4.20}$$

The elastic cell wall energy as in equation (4.1) comprises the dilatation or surface energy and shear energy:

$$W = \underbrace{\int_M \lambda \cdot \mathrm{tr}(\mathcal{E})^2 dA}_{\text{dilatation/surface energy}} + \underbrace{\int_M \mu \cdot \mathrm{tr}(\mathcal{E}^2) dA}_{\text{shear energy}} \tag{4.21}$$

The *second Piola-Kirchhoff* stress tensor $\mathcal{S}$ is calculated from:

$$\mathcal{S} := \lambda \cdot \mathrm{tr}(\mathcal{E}) I + \mu \cdot \mathcal{E}, \tag{4.22}$$

where λ and μ are the Lamé coefficients. The *first Piola-Kirchhoff* stress tensor T can be deduced from the *second Piola-Kirchhoff* stress tensor by:

$$\mathcal{T} := \nabla\Phi \cdot \mathcal{S}. \tag{4.23}$$

This leads to the law of motion that was used to describe dynamic cell shape changes:

$$div(\mathcal{T}) + \rho\mathcal{R} = \rho\frac{d^2\Phi}{dt^2}, \tag{4.24}$$

where ρ is the mass density and $\mathcal{R}$ describes forces on the body, such as gravity. Here, $\mathcal{R} \equiv 0$ is assumed.

Discrete Elasticity

There are different ways to solve the equation of motion in order to obtain the cell shape evolution. A finite element method has been used in (Fayant et al., 2010). The growth was modelled in iterative loading cycles and the computational domain was remeshed after each cycle. There are also a number of heuristic methods with spring networks, which allow for comparably easy

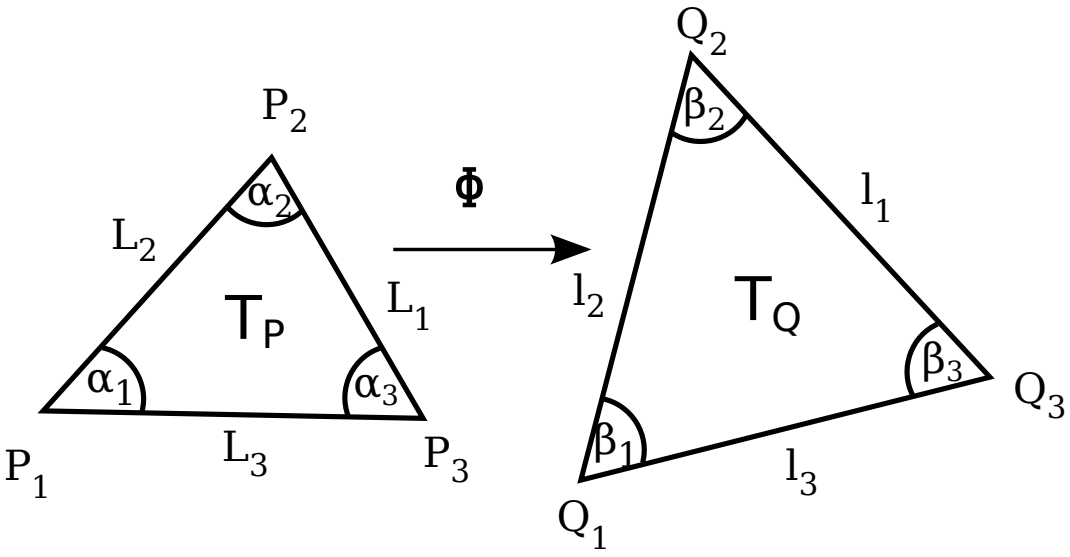

Figure 4.5: **Deformation of a single triangle.** The vertices of the relaxed triangle T_P are denoted by P_1,P_2 and P_3, while the vertices of deformed triangle T_Q are denoted by Q_1,Q_2 and Q_3. L_1, L_2 and L_3 describe the relaxed lengths of edges of T_P and, correspondingly, l_1, l_2 and l_3 the extended lengths of T_Q.

implementation and refinement (Chen and Boyle, 2014), but are numerically unstable. The method from Delingette (2008), which is based on a biquadratic spring model for triangular elements, was used in this thesis. This method employs a triangular surface mesh as basis. The Green-Lagrange strain tensor was solved exactly for each triangle in the mesh and used to calculate the contribution of each triangle to the elastic cell wall energy. The elastic forces, which result from changes of elastic cell wall energy, were used to formulate the equation of motion. I extended the framework for plastic growth by deforming the reference triangle appropriately, if a given yield criterion was reached. Here, the von Mises stress was calculated from the linear stress tensor for each triangle. Furthermore, the framework (Delingette, 2008) was extended for mesh refinement. If the area of a triangle exceeded a given threshold, the triangle was refined and split into for similar triangles. Therefore, continuous growth was implemented without remeshing of the computational domain.

A Single Triangle

First, we start to calculate the *Green-Lagrange strain tensor* and the deformation energy for a single triangle as in Delingette (2008). Let us assume a triangle T in the two dimensional space $\mathbb{R}^2$, where the points of the original triangle are denoted by P_1, P_2, P_3 and the points of the transformed triangle are denoted by Q_1, Q_2, Q_3 (compare Figure 4.5). T_P the rest triangle, and the deformed triangle $\Phi(T_P)$ is denoted by T_Q and their areas with A_P and A_Q, respectively. The density of the membrane energy for a single triangle is given

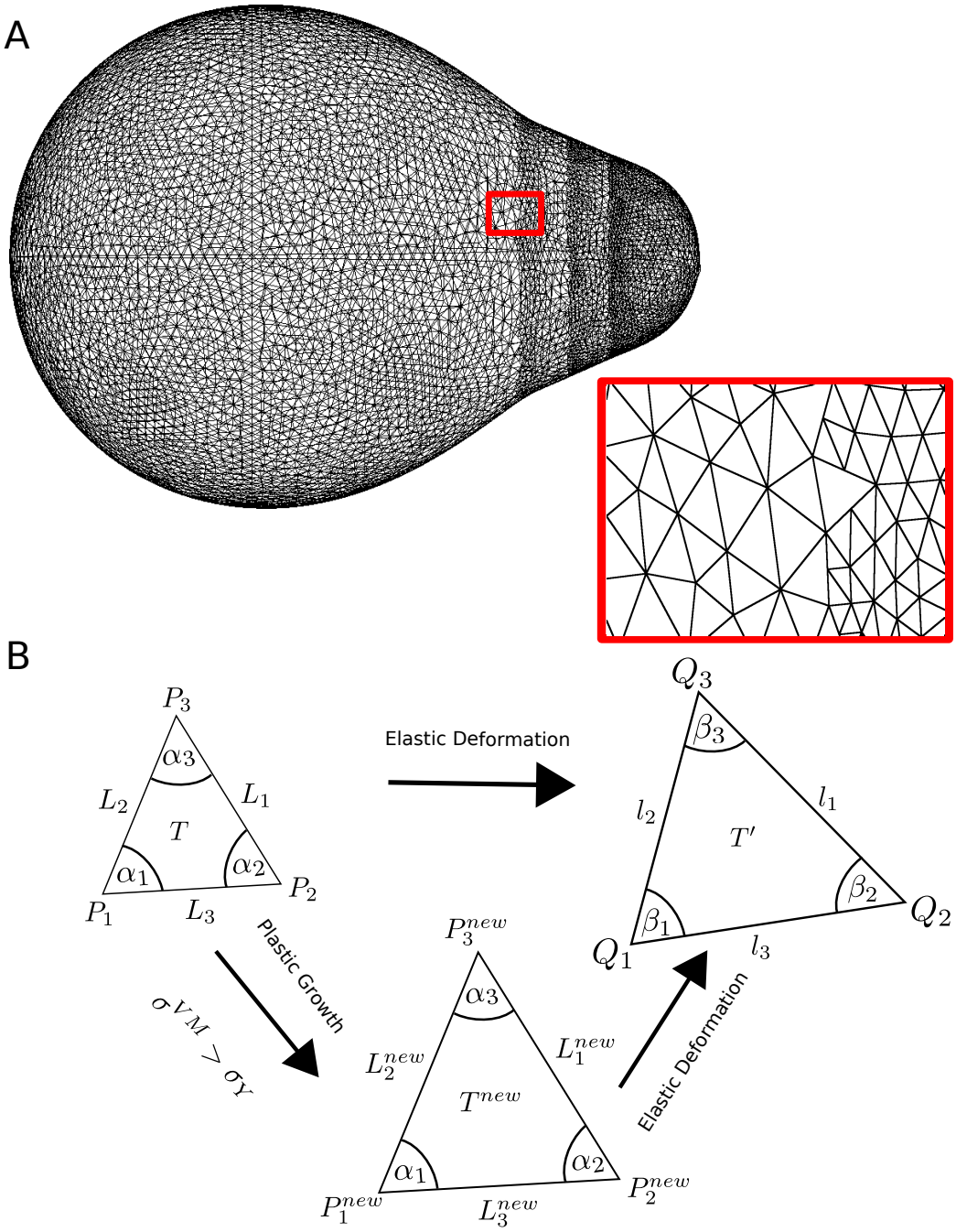

Figure 4.6: **The cell wall is represented by a triangular surface mesh. A:** A triangular surface mesh representing a growing cell. Triangular elements are refined if this element reaches a given size limit. The red box shows a section of the mesh with hanging nodes. **B:** Each triangular element T can deform elastically, which results in an apparent state T'. In case the von Mises stress σ^{VM} of a given triangle reaches the yield stress σ_Y, the relaxed state of the triangle deforms irreversibly.

by

$$W(T_P) = \frac{\lambda}{2}\mathrm{tr}(\mathcal{E})^2 + \frac{\mu}{2}\mathrm{tr}(\mathcal{E}^2). \tag{4.25}$$

From Delingette (2008), we get the following relations [1]:

$$\mathrm{tr}(\mathcal{C}) = \frac{1}{2A_P}(l_1^2 \cot\alpha_1 + l_2^2 \cot\alpha_2 + l_3^2 \cot\alpha_3), \tag{4.26}$$

$$\mathrm{tr}(\mathcal{E}) = \frac{1}{4A_P}((l_1^2 - L_1^2)\cot\alpha_1 + (l_2^2 - L_2^2)\cot\alpha_2 + (l_3^2 - L_3^2)\cot\alpha_3), \tag{4.27}$$

$$\det(\mathcal{C}) = \frac{A_Q^2}{A_P^2}. \tag{4.28}$$

Using these relations, the term $\mathrm{tr}(\mathcal{E}^2)$, which accounts for the shear forces (see equation 4.21), can be calculated from

$$\mathrm{tr}(\mathcal{E}^2) = \mathrm{tr}(\mathcal{E})^2 - 2\det(\mathcal{E}) = \frac{1 + \mathrm{tr}(\mathcal{E}) + \mathrm{tr}(\mathcal{E})^2 - \det\mathcal{C}}{2}. \tag{4.29}$$

Furthermore, note that for in-plane elasticity the Lamé coefficients are given by

$$\lambda = \frac{E\nu}{1-\nu^2}, \qquad \mu = \frac{E(1-\nu)}{1-\nu^2}, \tag{4.30}$$

where E is the Young's modulus and ν the Poisson ratio. With these relationships we can compute the density of the deformation energy for a single triangle:

$$\begin{aligned} W(T_P) &= \frac{\lambda}{2}\mathrm{tr}(\mathcal{E})^2 + \frac{\mu}{2}\mathrm{tr}(\mathcal{E}^2) \\ &= \sum_{i=1}^{3} \frac{k_i^T}{4}(l_i^2 - L_i^2)^2 + \sum_{i\neq j}^{3} \frac{c_k^T}{2}(l_i^2 - L_i^2)(l_j^2 - L_j^2), \end{aligned} \tag{4.31}$$

where

$$k_i^T = E \cdot d \cdot \frac{2\cot^2\alpha_i + 1 - \nu}{16(1-\nu^2)A_P}, \tag{4.32}$$

$$c_k^T = E \cdot d \cdot \frac{2\cot\alpha_i \cot\alpha_j - 1 + \nu}{16(1-\nu^2)A_P}. \tag{4.33}$$

The forces at each node of the triangle can then be computed from

$$\begin{aligned} \mathbf{F}_i^{\text{elastic}}(T_P) &= -\left(\frac{\partial W(T_P)}{\partial Q_i}\right)^T \\ &= \sum_{j\neq i} k_k^T (l_k^2 - L_k^2)^2 (\mathbf{Q}_j - \mathbf{Q}_i) \end{aligned} \tag{4.34}$$

$$+ \sum_{i\neq j} (c_j^T (l_i^2 - L_i^2)^2 + c_i^T (l_j^2 - L_j^2)^2)(\mathbf{Q}_j - \mathbf{Q}_i), \tag{4.35}$$

[1] Note that this a correction of the fromula presented in the original work from Delingette (2008) (see Appendix C).

where $\mathbf{Q}_i$ with $i = 1, 2, 3$, are the coordinates of the corners of the deformed triangle. The first sum corresponds to the tensile stiffness, the second sum to the angular stiffness. The total force at each node of the triangular mesh is computed from the sum of the forces that result from the turgor pressure and the counteracting elastic forces:

$$\mathbf{F}_{T_P,i} = \mathbf{F}^{\text{turgor}}_{T_P,i} + \mathbf{F}^{\text{elastic}}_{T_P,i}. \tag{4.36}$$

The forces that result from the turgor pressure P are given by:

$$\mathbf{F}^{\text{turgor}}_{T_P,i} = \frac{1}{3} A_Q P \mathbf{n}_T, \tag{4.37}$$

where $\mathbf{n}_T$ is the outward pointing unit normal with regard to the extended triangle T_Q. Therefore, the total force $A_Q P \mathbf{n}_T$ is equally distributed among each of the three corners. The equation of motion was computed for each vertex of the triangular surface mesh as follows. Let $\mathbf{x}_n$ be a vertex of this triangular surface mesh. With m_n we denote the number of triangles that share this vertex. These triangles are numbered as T_Q^1, T_Q^2, ... $T_Q^{m_n}$ and the forces that act on this vertex as $\mathbf{F}^1$, $\mathbf{F}^2$, ... $\mathbf{F}^{m_n}$, which are computed as stated in equation (4.36). Then the law of motion is given by

$$\frac{d^2}{dt^2}\mathbf{x}_n = \sum_{i=1}^{m_n} \frac{1}{M_n} \mathbf{F}^i. \tag{4.38}$$

The mass M_n is computed from the area of the relaxed triangles A_P^1, A_P^2, ... $A_P^{m_n}$ which share the vertex $\mathbf{x}_n$:

$$M_n = \frac{1}{3} \sum_{i=1}^{m_n} \rho A_P^i d, \tag{4.39}$$

where ρ is the cell wall density and $\rho A^i d$ the mass of the triangular cell wall patch A_P^i. The resulting ODE equation system was integrated numerically using an explicit solver.

Computation of the Yield Stress

The von Mises yield criterion was computed for each triangle by:

$$\sigma_{VM} = \sqrt{\sigma_1^2 + \sigma_2^2 - \sigma_1 \sigma_2}, \tag{4.40}$$

where σ_1 and σ_2 are the principal stresses. They were computed from the linear stress tensor, which is given by:

$$\mathcal{S} = \lambda \cdot \text{tr}(\mathcal{E}) I + \mu \cdot \mathcal{E}. \tag{4.41}$$

The trace of $\mathcal{S}$ and the determinant of $\mathcal{S}$ are given by

$$\text{tr}(\mathcal{S}) = 2\lambda \text{tr}(\mathcal{E}) I + \mu \text{tr}(\mathcal{E}), \tag{4.42}$$

$$\det(\mathcal{S}) = (\lambda^2 + \lambda\mu)\text{tr}(\mathcal{E})^2 + \frac{\mu^2}{4}(\det(\mathcal{C}) - \text{tr}(\mathcal{C}) + 1). \tag{4.43}$$

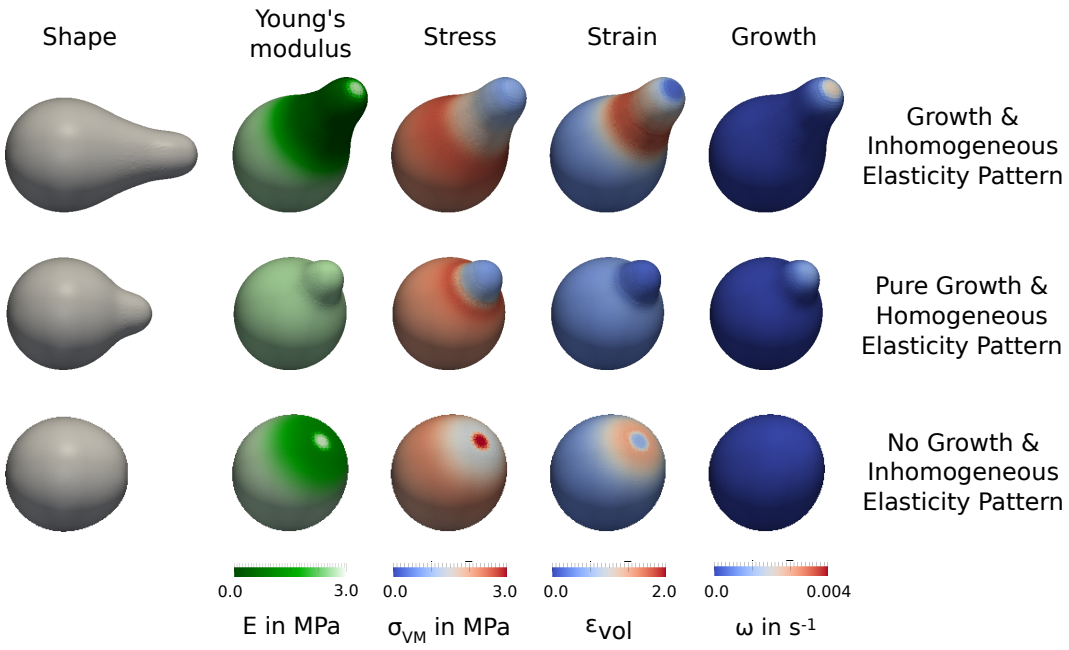

Figure 4.7: **Simulations of the dynamic model cell wall model with different elasticity patterns.**

Using these relations, the von Mises stress criterion can be computed from

$$\sigma_{VM} = \sqrt{\mathrm{tr}(\mathcal{S})^2 - 3\det(\mathcal{S})}. \tag{4.44}$$

See Appendix C for derivation of these relationships.

Plastic Deformations

The plastic deformations were implemented by remodelling the relaxed states of the triangular mesh as shown in Figure 4.6. A Lockhart-like stress-dependent growth was assumed (Lockhart, 1965). If a given yield threshold is reached, the irreversible wall expansion is a linear function of the stress. Therefore, the rate of expansion was calculated for every triangle T_P from

$$\omega(T_P) = \begin{cases} \Phi(\mathbf{x})\left(\sigma_{VM}(T_P) - \sigma_Y\right), & \text{if } \sigma_{VM}(T_P) > \sigma_Y, \\ 0, & \text{else,} \end{cases} \tag{4.45}$$

where σ_{VM} is the von Mises stress for the triangle T_P, σ_Y the yield limit and $\Phi(\mathbf{x})$ a given extensibility. The extensibility describes the distribution of growth factors, which are distributed around the tip. For the extensibility a generalized normal distribution is assumed as in (Drake and Vavylonis, 2013):

$$\Phi(\mathbf{x}) = \gamma \exp\left(-\frac{\|\mathbf{x} - \mathbf{x}_{\mathrm{tip}}\|^q}{qR^q_{\mathrm{Growth}}}\right). \tag{4.46}$$

In the remainder $q = 2$ was assumed. Let L_i be the resting length at the intersection of the two triangles T_P and T'_P. The expansion rate of the resting

length L_i is then given by

$$\frac{1}{L_i}\frac{dL_i}{dt} = \frac{1}{2}(\omega(T_P) + \omega(T_P')). \tag{4.47}$$

A simulation with the parameters given in Table 4.1 is shown in Figure 4.7. In this setup the influence of the elasticity pattern on the cell growth was illustrated, which is shown in Figure 4.7. In this Figure, the shape, the von Mises stress, the volumetric strain and the expansion rate were plotted. Note that the volumetric strain was computed from

$$\varepsilon_{\text{vol}} = \text{tr}(\mathcal{E}). \tag{4.48}$$

In Figure 4.7 **A**, the elasticity distribution was assumed to be E_{base} in the base region, E_{shaft} in the region of the mating projection and E_{tip} at the tip. The simulation result showed the typical shmoo shape with a soft transition from the base part to the shmoo tip. In contrast, for homogeneous elasticity the shmoo was much smaller (Figure 4.7 **B**). Furthermore, the stress at the neck of the growing cell was higher than for the scenario with cell wall softening. A simulation with heterogeneous elasticity but without growth resulted in an egg-like shape but did not yield the classical shmoo shape (Figure 4.7 **C**). Note that the von Mises stress distribution of σ^{VM} in Figure 4.7 **A** resembles the stress pattern derived analytically in Figure 4.3. The time course of cell growth with elasticity pattern and plastic growth is shown in Figure 4.8.

Discussion and Outlook

A description of cell wall mechanics is essential to understand processes as yeast mating, budding and zygote formation. In this chapter, the morphogenesis during the yeast mating process was modelled using an approach based on continuum mechanics. First, a model for pressurized cells was used to capture general relations between turgor pressure, cell wall thickness and in-plane stresses that occur under the steady state assumption. A linear constitutive relationship for elastic materials with inhomogeneous material properties was assumed. Solving this equation for the classical shmoo shape yielded an inhomogeneous distribution of the Young's modulus with lower values in the region of the shaft. Second, this model was extended to a dynamic cell wall model with plastic growth. Here, stress dependent growth as suggested by Lockhart was assumed. It could be shown that a distinct elasticity pattern is able to control cell shape and growth patterns.

This study was based on an elastic cell wall with heterogeneous elasticity and plastic cell wall growth. Note that this is a minimal model provided the given data, but there are a number of other aspects that might be addressed in future research and are discussed in the remainder. In the model equations the quotient of Young's modulus and cell wall thickness is an invariant E/d. Therefore, a change in the Young's modulus can be compensated by a thicker cell wall. However, the cell wall thickness was reported to be in the regime of

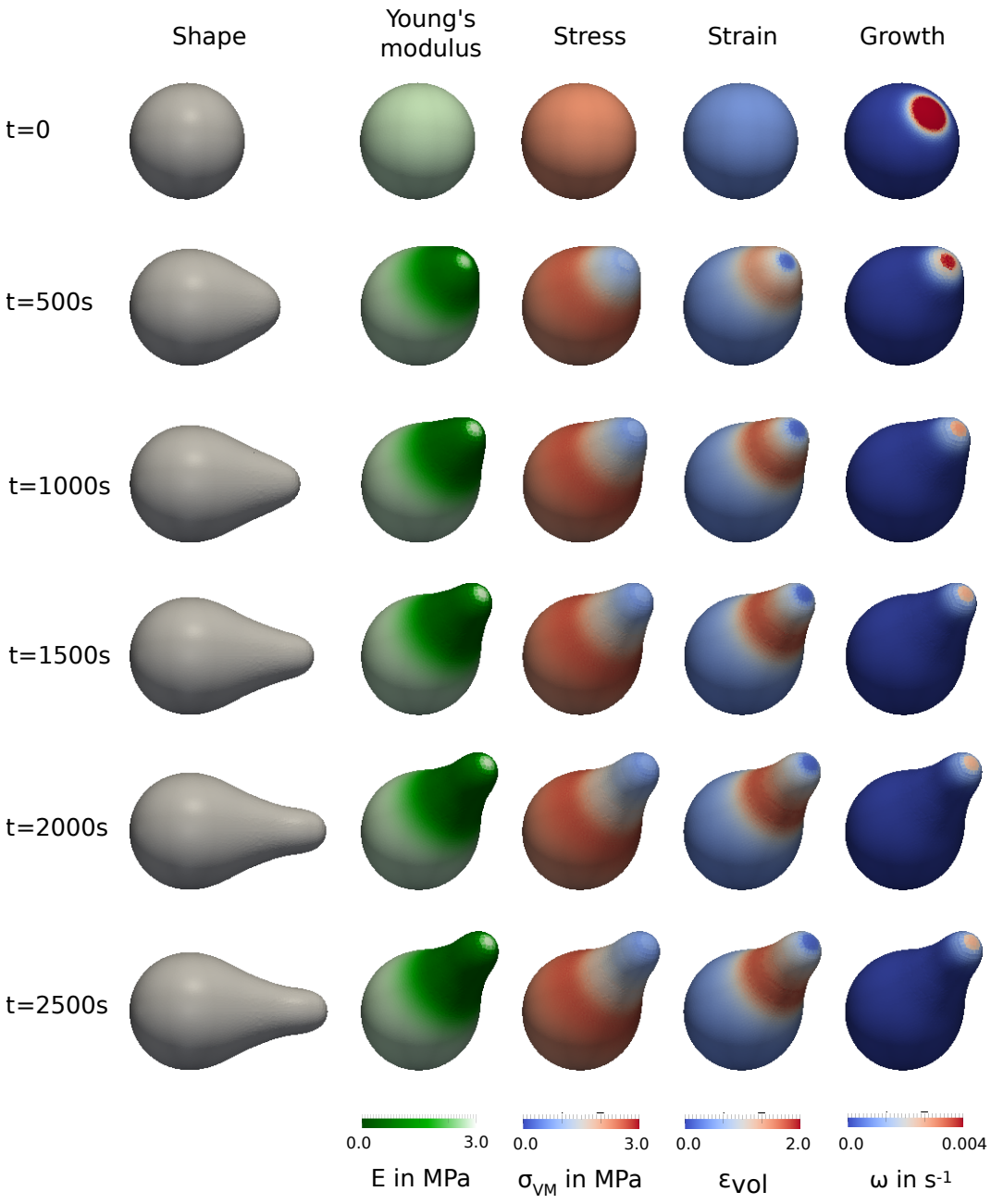

Figure 4.8: **Time course for a simulation of the dynamic cell wall model with plastic growth and inhomogeneous elasticity distribution.** Parameter values were obtained from Goldenbogen et al. (2016).

$80 - 120\ nm$, and therefore the cell wall thickness, which was assumed 100 nm here, can only compensate 20% change in E/d. Furthermore, studies using electron microscopy, such as in Baba et al. (1989), did not report significant reductions of cell wall thickness during the mating process. Therefore, the cell wall was assumed to be of constant thickness.

Anisotropy could as well explain different cell shapes (Geitmann and Ortega, 2009), but I am not aware of finding for material anisotropy in yeast. However, the elasticity pattern with measured values for the Young's modulus and the classical growth model are sufficient to explain the occurring cell shapes. Findings of an anisotropic cell wall have not been reported yet and therefore, the cell wall model provides a minimal model given the measured values and the growth assumption. Also studies for other yeasts as *S. pombe* have reported not anisotropy (Atilgan et al., 2015; Drake and Vavylonis, 2013). The bending has been neglected as for other studies of walled cells (Dumais et al., 2006; Drake and Vavylonis, 2013; Hamant et al., 2008). Some studies have taken bending into account and found in a computational study that bending energy is negligible for large deformations, where the stretching energy is dominant (Atilgan et al., 2015). It might be interesting to investigate the effect of bending at the tip, where the elasticity and curvature are high. This will be addressed in future studies and can be included in the framework shown here as in Atilgan and Sun (2007) andAtilgan et al. (2015).

For the yeast mating morphogenesis there are no models based on cell wall mechanics to the best of my knowledge. However, there have been a number of models based on signalling. For example in Slaughter et al. (2009) and Chou et al. (2012), the yeast morphology during budding and mating was solely explained by the distribution of signalling molecules such as Cdc42. In Angermann et al. (2012), the process of mating morphogenesis and fusion of cells modelled by a detailed model of the pheromone MAPK cascade. However, the shape has been approximated with rectangular voxels and the curved cell surface as well as cell wall mechanics have been neglected. In Okada et al. (2013), the interactions of septins and endo- and exocytoses was modelled to explain the emergence of a bud in combination with the GOR model, but still the cell wall mechanics was neglected. All these processes interlock with each other and each process alone can explain parts of the process. The simulations in this chapter were based on a simple normal distribution of signalling molecules as the most natural assumption on the distribution of Cdc42 and material insertion.

A computational method for the combination of mechanics and signalling based on a surface finite element method (SFEM) was, for instance, developed in (Elliott et al., 2012) and applied to motile non-walled cells. This computational approach could in principle also be used here in order to combine cell wall mechanics and signalling. However, in motile cells such as fish keratocytes the surface area remains nearly constant and shape changes occur due to forces acting on the cell surface. These forces actually arise from the F-actin network that drives the leading edge (Falcke and Zimmermann, 2014). In yeast, the shape changes occur on a much longer time scale and the surface of yeast cells

actually grows in total during mating. The driving forces of morphogenesis in yeast are cell wall elasticity changes, local material insertion and plastic growth. In future approaches, signalling, the cytoskeleton and cell wall mechanics have to be combined to model the yeast morphogenesis in different situations.

5

Summary & Outlook

In this thesis, I have investigated general biological phenomena occurring in eukaryotic cells, exemplified by the mating process of yeast. The key aspects of this process that I examined were (i) intercellular communication of cells *via* pheromones, (ii) the initial symmetry break and implementation of cell polarity, and (iii) subsequent morphogenetic changes which lead to shmoo formation. Taking an interdisciplinary approach, concepts from physics and mathematics were used to develop quantitative models and frameworks on the basis of fluorescence and atomic force microscopy (AFM) data.

In Chapter 2, the communication motifs of mating yeast cells, which communicate *via* pheromones $\boldsymbol{\alpha}$-factor and **a**-factor, were investigated in mixed populations of $MAT\mathbf{a}$ and $MAT\boldsymbol{\alpha}$ cells. I constructed cellular automata models on the basis of reaction-diffusion (RD) equations. These models have shown that there is a trade-off between vegetative growth and mating, which is regulated by the protease Bar1, which sharpens pheromone gradients making them less ambiguous, but at the same time also decreases pheromone concentration levels. Since the capability of yeast cells to produce high pheromone concentrations is limited, the Bar1 response has to be balanced adequately for successful mating. Furthermore, I have shown that an induced Bar1 response is necessary to balance pheromone concentrations over a wide range of cell densities. This model was extended to cover the secretion of **a**-factor and the response to the complementary pheromone by increased pheromone production. Different levels of mutual pheromone induction resulted in a switch-like behaviour of cells, dependent on the local cell density of their subpopulation, as well as higher mating rates.

In Chapter 3, different patterns of polarization behaviour of mating yeast were investigated. The functional polarization module describing the shuttling of the small Rho GTPase Cdc42 regulates cell polarity during the mating as well as the budding process. Polarization patterns were investigated upon changes of cell geometry and diffusion barriers on the membrane and in the cytosol, by testing two different polarization mechanisms: 1) a Turing-type mechanism proposed in Goryachev and Pokhilko (2008), and 2) a phase-separation mechanism proposed in Mori et al. (2008). The model representative of mechanism 1) was referred to as GOR model, while the model representative of mechanism 2) was referred to as wave-pinning (WP) model. A simple one-dimensional implementation was employed to show general differences in con-

centration profiles and polarization behaviour. This implementation was then extended into higher dimensions to investigate the influence of cell shape and spatial diffusion inhomogeneities. The WP model was found to be more influenced by cell shape than the GOR model. The same was found for the introduction of barriers in the cytosol. The influence of cell geometry was compensated for diffusion barriers on the membrane for both models. These diffusion barriers are implemented by cytoskeletal structures such as septins. Simulations using a random stimulus showed that the full three-dimensional model was able to explain the occurrence of distinct shmoos, which were observed for cells exposed to ambiguous pheromone gradients.

In Chapter 4, the cell wall morphogenesis of yeast during shmooing was investigated using a model based on continuum mechanics. A steady state model for pressurized shells was used to describe the relations between Young's modulus, cell shape, cell wall thickness and turgor pressure. Given elastic deformation of isotropic cell wall material, constant turgor pressure and a confined growth zone at the tip, the model suggests a softening of the cell wall in the apical region. This is supported by atomic force microscopy (AFM) data that suggests inhomogeneous cell wall elasticity with a a softening in the apical region, except for a spot of higher elasticity at the shmoo tip. To model growth at the tip, a dynamic cell wall model was employed to simulate reversible elastic and irreversible plastic cell wall deformation. A Lockhart-like model for stress-dependent growth was assumed for cell wall growth and tested for different elasticity patterns, as obtained from atomic force microscopy (AFM) data.

Communication Principles of Fungi and Beyond

Complex communication motifs emerge during the mating of *S. cerevisiae*. Research on this issue has mainly focused on the pheromone response of *MAT***a** cells to the unmodified peptide $\boldsymbol{\alpha}$-factor (Barkai et al., 1998; Andrews et al., 2010; Rappaport and Barkai, 2012; Jin et al., 2011; Youk and Lim, 2014), whereas the gradient formation of **a**-factor and the influence of mutual pheromone induction on mating has not yet been investigated. One reason for this gap in the research lies in difficulties of performing experiments with **a**-factor, which is a modified peptide with hydrophobic properties. However, modification of proteins and peptides, such as through the attachment of farnesyl groups, can turn out to be of great relevance in many eukaryotic cells (Gelb et al., 2006). Here, the **a**-factor is a prime example of such modified signalling molecules (Anderegg et al., 1988; Gelb et al., 2006). Therefore, it is important to go further and investigate its role in intercellular communication in yeast, with a focus on its diffusion properties in different media and interactions with various surfaces. As shown in Chapter 2, pheromone gradients in cultures of haploid yeast cells can be reconstructed using computational methods.

Modified Peptides

Another important aspect of pheromone signalling is temporal control of communication. For instance, *MAT***a** cells arrest for several hours when treated

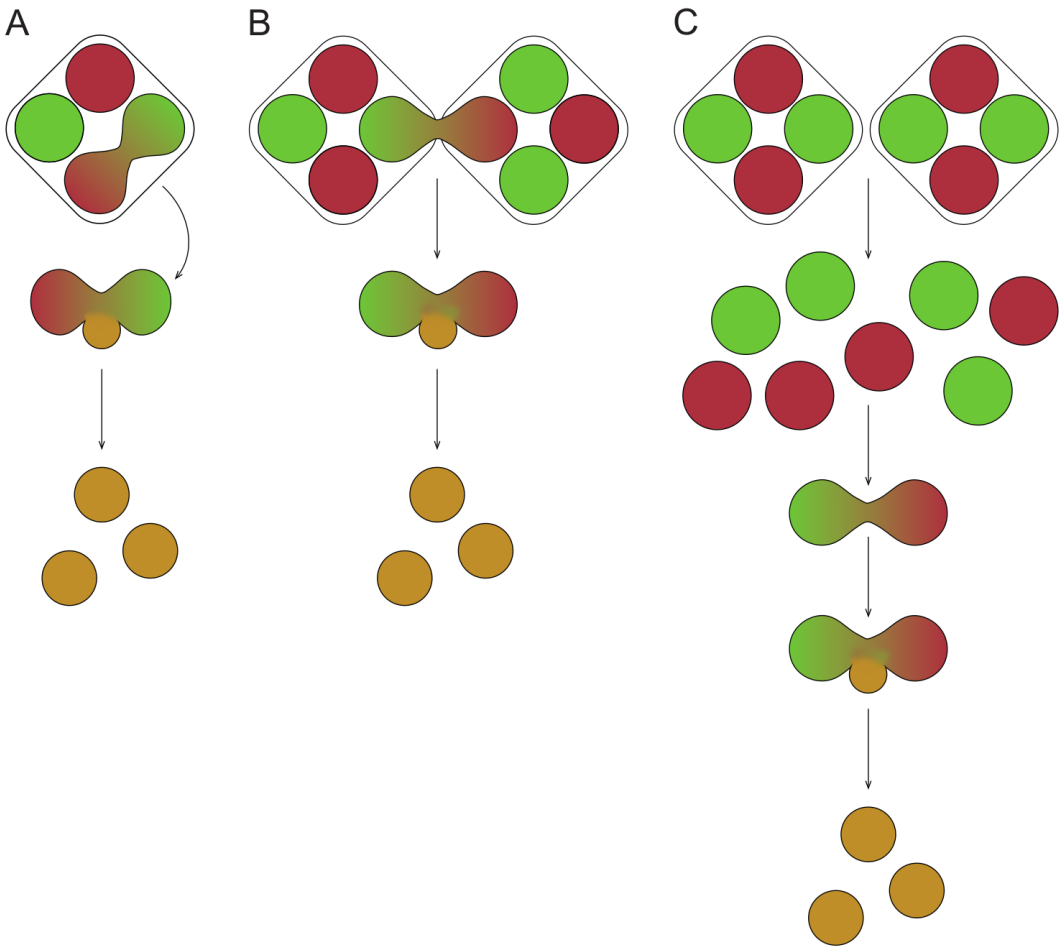

Figure 5.1: **Different possibilities of the sexual life cycle of yeast. A:** Mating of spores occurs in the ascus. **B:** Spores from two different asci mate. **C:** Spores cross out by mitosis or the ascus wall is dissolved. Free haploid cells mate with one another. Partially adopted from Murphy and Zeyl (2010).

with pheromone, while $MAT\boldsymbol{\alpha}$ cells arrest more transiently (Huberman and Murray, 2013). This might be a further mechanism to compensate against asymmetric communication. Here, a question also arises regarding how pheromone secretion is coordinated temporally. Estimates in the literature concerning the number of secreted $\boldsymbol{\alpha}$-factor molecules vary by about more than one order of magnitude, from 550 molecules/s basal secretion (Rogers et al., 2012) to 6,000 molecules/s (Youk and Lim, 2014; Huberman and Murray, 2013). Even with 6,000 molecules/s, for a cell having a diameter of $d = 5\ \mu m$, this results in $\approx 1\ nM - 4\ nM$ concentration at the surface of a $MAT\boldsymbol{\alpha}$ cell, depending on the diffusion coefficient and media. The concentration needed for cell cycle arrest is larger than 5 nM and, therefore, must rely on a collective mechanism. (Murphy and Zeyl, 2010; Billiard et al., 2012) have shown that, for wild yeast, there is a surprisingly high outcrossing rate from ascii. This might be explained by the fact that two single $MAT\boldsymbol{\alpha}$ spores are not able to activate two other $MAT\mathbf{a}$ in an ascus, if the wall is already partially digested or very porous. This would cause the spores to first divide and spread and, then, only mate when cell density becomes high enough. It might also be possible that two of the four spores mate, while the other slower ones have first to divide and grow in order to mate. Different alternatives for the life cycle are shown in Figure 5.1. Also, because of mutual induction and the fact that cells orient towards the partner with highest pheromone production (Jackson and Hartwell, 1990b), this causes selection of cells appearing to have the best metabolism and that can optimally cope with the new environment. Pheromone secretion rates are, therefore, likely to be dependent on media. My computational model suggests that mutual induction leads to selection with respect to a metabolism that enables high pheromone production rates. Ways to optimize the temporal control of secretion are interesting extensions of the model. For instance, it might be tested whether a wave-like mutual increase of pheromone secretion improves mating coordination in the culture.

Temporal Control

Comparison with other yeast species might also be useful, since *Candida* species have been reported to secrete Bar1 protease as well. Moreover, it has been shown that inter-species interactions mediated by Bar1 are possible (Jones et al., 2015), since Bar1 it is also able to degrade pheromones in other *Candida* species as well as *S. cerevisiae*. This is a surprising finding, since *Candida* species and *S. cerevisiae* are only very remotely related. Other studies of *Candida albicans* have led to the hypothesis that asymmetric communication is needed to communicate across different distances, where an insoluble lipopeptide might be employed for short-range signalling and an unmodified peptide for long-range communication (Whiteway, 2011). Comparing the similarities in the communication principles of different yeasts might be a fruitful path for future research. The approach laid out in Chapter 2 might equally as well be employed for other communication systems, not only in fungi but also in bacteria.

Others Yeast Species and Bar1

Experiments with mixed populations of mating yeast and consequent computational analysis has the potential to reveal further insight into cell communication principles. In Youk and Lim (2014), $MAT\mathbf{a}$ cells were modified

to be able to secrete and sense $\boldsymbol{\alpha}$-factor, thus allowing communication to be investigated in populations with only one cell type. It was found that different motifs of mutual interaction exhibited interesting communication patterns that adapt to different cell densities and promote a switch-like behaviour of mutual activation. In Gonçalves-Sá and Murray (2011), the communication of haploid *S. cerevisiae* has been modified such that mating yeast was able to communicate with two lipopeptides as well as two peptides. The receptors and peptides were introduced from other yeasts, such as *Schizophyllum commune*, *Schizosaccharomyces pombe* and *Sordaria macrospora*. Therefore, it seems that yeast mating mixes might be used to experimentally explore systems with more than two different cell types. Since these processes are very complex and non-intuitive, they need to be accompanied by computational modelling such as that presented in Chapter 2.

Cellular organisation is important for many organisms, and communication *via* pheromones is used widespread across the spectrum of living beings, from fungi to mammalian cells. As has been pointed out in Gelb et al. (2006), protein prenylation and associated modifications of peptides and protein bear great potential for incorporation into therapeutic interventions. The **a**-factor is a prominent example of a modified peptide that is employed for cellular communication in the yeast *S. cerevisiae*. So it would seem that organisation in tissues and also developmental processes could be studied in more detail if molecular communication motifs were to be translated into higher scales. The signalling of morphogens, which are transported by diffusion, is usually assumed to act on length scales of less than 100 cells (Crick, 1970; Wartlick et al., 2009). The model approach used in Chapter 2 might, therefore, be used to bridge the cap from single cells to gradient formation in tissues, which are usually modelled with a continuum reaction-diffusion model, where the entity of a single cell is neglected.

Control of Growth and Shape

The interplay between cell wall growth and signalling is essential and needs to be precisely controlled. In Chapter 3, I have demonstrated how two common non-linear reaction-diffusion systems adapt their behaviour to a cell's shape, even if the binding of signalling to the membrane is assumed to be not directly curvature-dependent and transport processes depend only on diffusion, This insight has also been found in a number of recent studies other model organisms (Halatek and Frey, 2012; Orlandini et al., 2013; Thalmeier et al., 2016). The results in Chapter 3 indicate that the GOR and the WP mechanisms are less likely to initially polarize in cell protrusions than in the basal part of the cell. This can be interpreted as a generic feature of the cell polarization mechanisms that counteracts spurious deformations and prevents uncontrolled growth. However, my analysis was only performed for the initial phase of polarization. Once a polarization site is established, however, the polarization cap is stabilized by the cytoskeleton (Kelley et al., 2015). Here, then, the

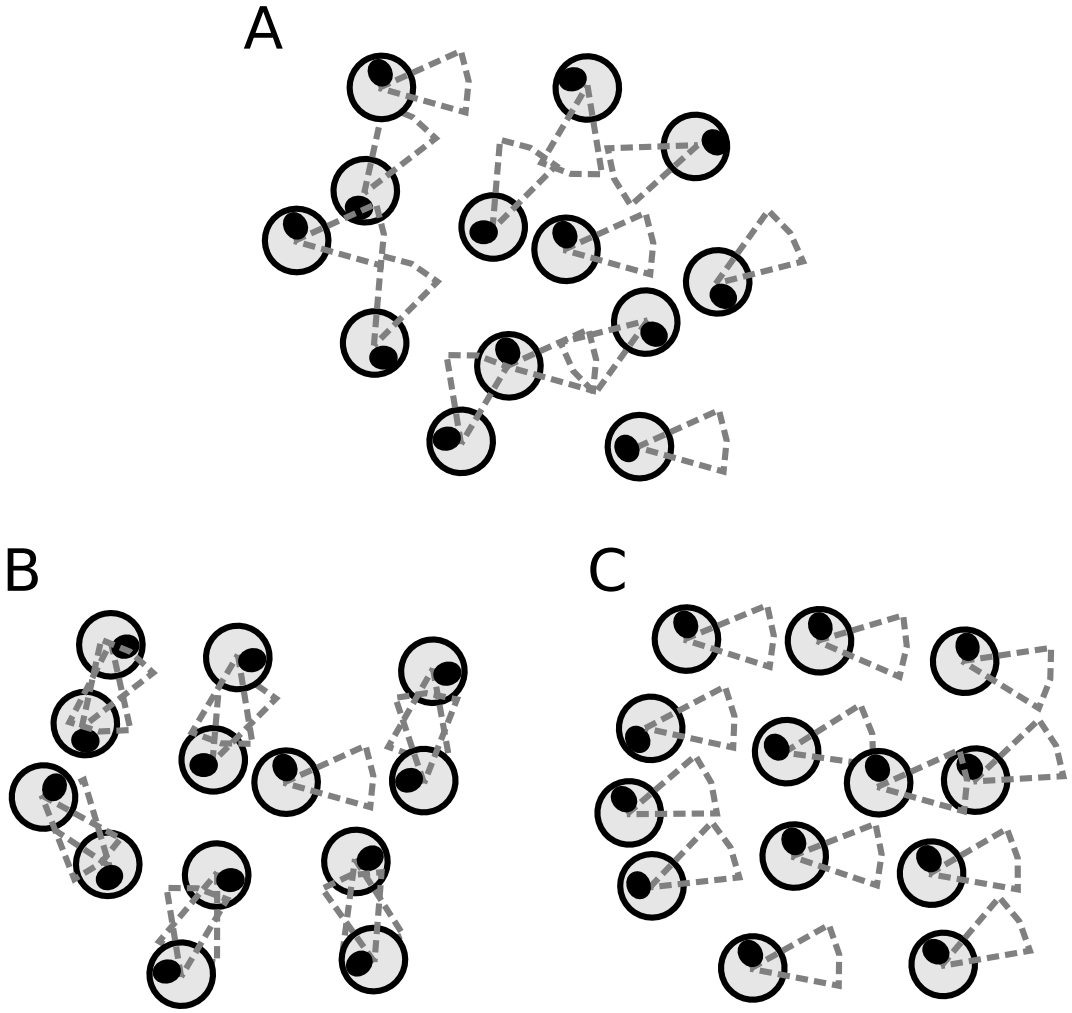

Figure 5.2: **Different levels of order in a multicellular organisms. A:** Cells are randomly oriented. Dashed segments indicate the current state of polarity. The organelle (black oval) indicates some intracellular orientation or default orientation. **B:** Cells are oriented towards cells of opposite mating type, as occurs during the mating of yeast. **C:** An extracellular gradient aligns cells towards a source.

question is how is growth stopped?

In setups, where pheromone stimulated cells formed multiple shmoos or grow chemotropically, growth has to be controlled. In Hilioti et al. (2008), oscillatory shmoo formation was explained *via* oscillation of phosphorylated Fus3, which is regulated by Sst2 and Msg5. It was also found that phosphorylated Fus3 forms gradients (Maeder et al., 2007) and that the formation of gradients in the MAPK cascades has the potential to regulate cell size (Muñoz-García et al., 2009). Here, MAPK cascades cause intracellular gradients with precisely defined concentration plateaus that abruptly decay. Therefore, spatial MAPK cascading has the potential to transmit information about cell size relative to the nucleus. Milicic (2014) has investigated the influence of shmoo morphologies on MAPK signalling as well as the positioning of organelles.

Shape Control by MAPK Signalling

The organisation of organelles might also be studied in this context. In the Chapter 3, I have indicated that the positioning of organelles has the potential to change intracellular gradients and bias polarization decisions. In processes such as cell fusion, including zygote formation in yeast, the position of the nuclei has to be coordinated. The same holds for cell division, where organelles and protein aggregates have to be distributed and guided by signalling (Spokoini et al., 2012). Meanwhile, the interaction of MAPK signalling gradients with the Golgi has been found to be important (Hwang et al., 2014). Therefore, the spatial organization of compartments by reaction-diffusion patterns needs further investigation. Here, modelling approaches such as that presented in Chapter 3 might be extended and used for further studies.

Cell Wall Mechanics and Tissues

The relationship between signalling and cell wall mechanics is still not well understood. Polarization mechanisms, as discussed in Chapter 3, break symmetry after pheromone stimulation and initiate cell shape changes. According to Goldenbogen et al. (2016), measurements of cell wall elasticity indicate that material properties change at a very early stage, before directed growth is initiated. The question is, how does signalling control these changes on a chemical basis? Furthermore, subsequent exo- and endocytosis has to be coordinated, which is assumed to be mediated by the cell wall integrity pathway, where the transmembrane receptors Mid2 and Mtl1 play a key role. It has been assumed that cell wall growth is stress-dependent for plant cells. However, how do receptors measure cell wall stresses and how vesicles are directed to the appropriate place is not yet understood during yeast mating.

Moreover, there are a number of additional and related questions regarding the yeast life cycle that remain unanswered (Tartakoff, 2015). For instance, it still remains an open question how fusion and cell wall dissolution are orchestrated (Huberman and Murray, 2014). The cell wall is built of two layers having different chemical structures. When the outer wall is dissolved, a prezygote is formed. Then the outer wall is re-inforced and the plasma membrane dissolved. These events require a precise chemical regulation, as does turgor

pressure as well. Insertion of a new cell wall is also precisely controlled by the cell wall integrity pathway. There are a number of further riddles regarding ascospores and how the outbreak from the ascus happens on a mechanical level (compare Figure 5.1). An interesting study has addressed the regulation of spore walls and their mechanics for *S. pombe* (Bonazzi et al., 2014). To my knowledge, such a model does not yet exist for *S. cerevisiae*.

The methods presented in this thesis, can be extended to plant cells and mechanical interactions in multicellular systems, as plant cells also have walls and their study relies on very similar computational methods, even though the chemical details will be quite different (Geitmann and Ortega, 2009). The interaction of walled cells in plant tissues also needs to be precisely coordinated. The question here is how multicellular organisms organize themselves. One proposed explanation is that orientations are specified through stresses in the tissue and mechanical cues, as in plant morphogenesis during development of flowers (Boudon et al., 2015) or the shoot apex in *Arabidopsis* (Hamant et al., 2008). Another possibility is the transmission of chemical cues and the establishment of polarity (Kennaway et al., 2011; Maire and Youk, 2015). In Hamant et al. (2008), a few cells in the shoot apex have been modelled. However, for large tissues a transition from single cell mechanics, where each cell is modelled as an identity needs to be complemented by large-scale models, where the tissue is assumed to be a continuum, such as in Weichert et al. (2010).

There is a demand for modelling strategies from engineering that can complement existing experimental observations. Here, I have examined several aspects of yeast mating behaviour using methods form engineering, physics and mathematics, which has enabled description of crucial biological processes that appear to go beyond those that formulated solely in verbal language. FEM frameworks, such as FEniCs and DUNE, employed here have not had widespread application in the life sciences but, as my results seem to indicate, can provide many necessary tools for addressing important questions. But further interdisciplinary interactions are required to take these advances forward.

In summary, the approaches adopted in this study to investigate the choreography of yeast mating might be extended in various ways. Many cellular systems communicate *via* diffusible molecules, and the modelling of communication between multiple and different cell types and molecules is a promising avenue towards understanding organization in tissues. In Chapter 2, I investigated the behaviour of two cell types and their regulation. Not only absolute concentration levels of signalling molecules are important but also the formation of gradients and the orientation of cells. As for yeast during mating, there might be some preferred directions of cellular orientation, depending on some internal state. As shown in Chapter 3, organelles in the cytosol have the potential to bias the direction of cellular orientation. Therefore, tissues might be considered in an analogous manner to the Ising model in physics (see Figure 5.2). This could also play a role for the invasion of surfaces or biofilm formation, and the internal orientation of cells might be also be important. The mechanics of a single cell was investigated in Chapter 4, and an extension

along similar lines to cells in contact, as during cell fusion, among yeast spores in an ascus or in dense subpopulation could be pursued. The process of cell communication, cell polarity and morphogenesis interlock with each other and can be linked to important processes that occur, in many different variations, in other eukaryotic organisms.

The (Un)Reasonable (In)Effectiveness of Mathematics in Biology: An Interdisciplinary Approach

In bringing this thesis to a close, let us re-examine the opening quotation from Heisenberg's *Physik und Philosophie* (Heisenberg, 1990): "If we consider living organisms to be physical or chemical systems, they will behave as such". In light of these words, the following question arises: How should we describe biological phenomena? Should we use verbal language, the language of physics, chemistry, a programming language or mathematics? The systems biology approach is a highly interdisciplinary domain, where researchers from the life sciences work together with researchers from the classical quantitative sciences, such as engineering, physics and mathematics. Consequently, the language of systems biology can be considered to be a fusion of all of these different modes of expression and, thus, no clear answer can be given to this question. However, there are a number of concepts that can unify and standardize quantitative approaches, such as the systems biology markup language (SBML). Models for signalling, metabolism and other biological processes are unified and can be translated *via* the computer into various languages, such as mathematical equations or transformed into the visual representation of, for example, reaction networks. But especially for computer simulations and quantitative tests of models and concepts, physical laws described in mathematical language are key.

The question is: How useful are such attempts to foster research in the life sciences, and can they lead to the kind of unifying quantitative concepts that are common in physics? Interestingly, there are basically two different answers to this question. There have been theoretical concepts and models, such as Michaelis-Menten kinetics, Turing patterns or the mathematical description of biochemical oscillations that have become very useful and standard methods in quantitative biology. This success makes theoreticians likely to take a Platonist point of view and believe in overarching theoretical relationships and physical laws being a product of thought (Wigner, 1960). However, empirically minded scientists are likely to share the opposite view (Abbott, 2013). [1] Despite the success of physical concepts and mathematics, there are ambiguous views on the effectiveness of physical laws and elegant mathematical formulations to

[1] The two articles "The Unreasonable Effectiveness of Mathematics in the Natural Sciences" (Wigner, 1960) and "The Reasonable Ineffectiveness of Mathematics"(Abbott, 2013) have motivated this last section.

describe the multifarious aspects of life.

These differences underline the importance of communication within interdisciplinary fields such as systems biology. Fawcett and Higginson (2012) have argued that the heavy reliance on equations impedes knowledge transfer, and a carefully worked out theory based on physical laws, which could convey important ideas to researchers, might just be ignored because of its level of detail and presentation in mathematical formulas. Therefore, it seems important to stress that communication with researchers from other fields as well as a constant iteration between theoretical and empirical methods is a key. Theoretical approaches in the life sciences will only be judged by their effectiveness in making predictions and their accessibility to fellow scientists in a wide variety of fields. This task is challenging for a theoretician such as myself, but it also makes the pursuit of science more rewarding and enjoyable.

List of Figures

List of Tables

6

Bibliography

Derek Abbott. The Reasonable Ineffectiveness of Mathematics. *Proceedings of the IEEE*, 101(10), 2013.

Juan F Abenza, Etienne Couturier, James Dodgson, Johanna Dickmann, Anatole Chessel, Jacques Dumais, and Rafael E Carazo Salas. Wall mechanics and exocytosis define the shape of growth domains in fission yeast. *Nature communications*, 6, 2015.

Milton Abramowitz and Irene A Stegun. *Handbook of mathematical functions: with formulas, graphs, and mathematical tables*, volume 55. Courier Corporation, 1964.

AE Adams, Douglas I Johnson, Richard M Longnecker, Barbara F Sloat, and John R Pringle. CDC42 and CDC43, two additional genes involved in budding and the establishment of cell polarity in the yeast Saccharomyces cerevisiae. *The Journal of cell biology*, 111(1):131–142, 1990.

Miquel Angel Adrover, Zhike Zi, Alba Duch, Jörg Schaber, Alberto Gonzalez-Novo, Javier Jimenez, Mariona Nadal-Ribelles, Josep Clotet, Edda Klipp, and Francesc Posas. Time-dependent quantitative multicomponent control of the G1-S network by the stress-activated protein kinase Hog1 upon osmostress. *Science Signaling*, 4(192):ra63–ra63, 2011.

Steven J Altschuler, Sigurd B Angenent, Yanqin Wang, and Lani F Wu. On the spontaneous emergence of cell polarity. *Nature*, 454(7206):886–889, 2008.

RJ Anderegg, R Betz, Steven A Carr, John W Crabb, and W Duntze. Structure of Saccharomyces cerevisiae mating hormone a-factor. Identification of S-farnesyl cysteine as a structural component. *Journal of Biological Chemistry*, 263(34):18236–18240, 1988.

Steven S. Andrews, Nathan J. Addy, Roger Brent, and Adam P. Arkin. Detailed Simulations of Cell Biology with Smoldyn 2.1. *PLoS Computational Biology*, 6(3), 2010. doi: 10.1371/journal.pcbi.1000705.

Bastian R Angermann, Frederick Klauschen, Alex D Garcia, Thorsten Prustel, Fengkai Zhang, Ronald N Germain, and Martin Meier-Schellersheim.

Computational modeling of cellular signaling processes embedded into dynamic spatial contexts. *Nat. Methods*, 9(3):283–9, March 2012. doi: 10.1038/nmeth.1861.

Erdinc Atilgan, Valentin Magidson, Alexey Khodjakov, and Fred Chang. Morphogenesis of the fission yeast cell through cell wall expansion. *Current Biology*, 25(16):2150–2157, 2015.

Erdinç Atilgan and Sean X Sun. Shape transitions in lipid membranes and protein mediated vesicle fusion and fission. *The Journal of chemical physics*, 126(9):095102, 2007.

M Baba, N Baba, Y Ohsumi, K Kanaya, and M Osumi. Three-dimensional analysis of morphogenesis induced by mating pheromone alpha factor in Saccharomyces cerevisiae. *Journal of cell science*, 94(2):207–216, 1989.

Kirsten Bacia, Sally A Kim, and Petra Schwille. Fluorescence cross-correlation spectroscopy in living cells. *Nature methods*, 3(2):83–89, 2006.

Wolfgang Ballensiefen and Hans Dieter Schmitt. Periplasmic Barl Protease of Saccharomyces Cerevisiae is Active Before Reaching its Extracellular Destination. *European journal of biochemistry*, 247(1):142–147, 1997.

Eli E Bar, Alexis T Ellicott, and David E Stone. Gbetagamma recruits Rho1 to the site of polarized growth during mating in budding yeast. *J. Biol. Chem.*, 278(24):21798–804, June 2003. doi: 10.1074/jbc.M212636200.

Lee Bardwell. A walk-through of the yeast mating pheromone response pathway. *Peptides*, 25(9):1465–1476, 2004.

Eli Barkai, Yuval Garini, and Ralf Metzler. Strange kinetics of single molecules in living cells. *Phys. Today*, 65(8):29, 2012.

Naama Barkai, Mark D Rose, and Ned S Wingreen. Protease helps yeast find mating partners. *Nature*, 396(6710):422–423, 1998.

Peter Bastian, Markus Blatt, Andreas Dedner, Christian Engwer, Robert Klöfkorn, Ralf Kornhuber, Markus Ohlberger, and Oliver Sander. A generic grid interface for parallel and adaptive scientific computing. Part II: Implementation and tests in DUNE. *Computing*, 82(2-3):121–138, 2008a.

Peter Bastian, Markus Blatt, Andreas Dedner, Christian Engwer, Robert Klöfkorn, Markus Ohlberger, and Oliver Sander. A generic grid interface for parallel and adaptive scientific computing. Part I: abstract framework. *Computing*, 82(2-3):103–119, 2008b.

Alexander M Berezhkovskii, Christine Sample, and Stanislav Y Shvartsman. Formation of morphogen gradients: local accumulation time. *Physical Review E*, 83(5):051906, 2011.

Sven Bergmann, Oded Sandler, Hila Sberro, Sara Shnider, Eyal Schejter, Ben-Zion Shilo, and Naama Barkai. Pre-steady-state decoding of the Bicoid morphogen gradient. *PLoS Biol*, 5(2):e46, 2007.

Roberto Bernal, Enrique Rojas, and Jacques Dumais. The mechanics of tip growth morphogenesis: what we have learned from rubber balloons. *Journal of Mechanics of Materials and Structures*, 2(6):1157–1168, 2007.

Erfei Bi and Hay-Oak Park. Cell polarization and cytokinesis in budding yeast. *Genetics*, 191(2):347–387, 2012.

Scott Bidlingmaier and Michael Snyder. Regulation of polarized growth initiation and termination cycles by the polarisome and Cdc42 regulators. *The Journal of cell biology*, 164(2):207–218, 2004.

S Billiard, M Lopez-Villavicencio, ME Hood, and T Giraud. Sex, outcrossing and mating types: unsolved questions in fungi and beyond. *Journal of evolutionary biology*, 25(6):1020–1038, 2012.

Daria Bonazzi, Jean-Daniel Julien, Maryse Romao, Rima Seddiki, Matthieu Piel, Arezki Boudaoud, and Nicolas Minc. Symmetry breaking in spore germination relies on an interplay between polar cap stability and spore wall mechanics. *Dev. Cell*, 28(5):534–46, March 2014. doi: 10.1016/j.devcel.2014.01.023.

David Botstein. It's the Data! *Molecular Biology of the Cell*, 21(1):4, 2010.

David Botstein and Gerald R Fink. Yeast: an experimental organism for 21st Century biology. *Genetics*, 189(3):695–704, November 2011. doi: 10.1534/genetics.111.130765.

Arezki Boudaoud. Growth of walled cells: from shells to vesicles. *Phys. Rev. Lett.*, 91(1):018104, July 2003.

Frédéric Boudon, Jérôme Chopard, Olivier Ali, Benjamin Gilles, Olivier Hamant, Arezki Boudaoud, Jan Traas, and Christophe Godin. A computational framework for 3D mechanical modeling of plant morphogenesis with cellular resolution. *PLOS Comput Biol*, 11(1):e1003950, 2015.

Dietrich. Braess. *Finite Elements: Theory, Fast Solvers, and Applications in Solid Mechanics, Third edition*. Cambridge University Press, 2007.

Guy C Brown and Boris N Kholodenko. Spatial gradients of cellular phosphoproteins. *FEBS letters*, 457(3):452–454, 1999.

Anne-Christine Butty, Peter M Pryciak, Linda S Huang, Ira Herskowitz, and Matthias Peter. The role of Far1p in linking the heterotrimeric G protein to polarity establishment proteins during yeast mating. *Science*, 282(5393):1511–1516, 1998.

Enrico Cabib and Javier Arroyo. How carbohydrates sculpt cells: chemical control of morphogenesis in the yeast cell wall. *Nat. Rev. Microbiol.*, 11(9): 648–55, September 2013. doi: 10.1038/nrmicro3090.

Scott Camazine, Jean-Louis Deneubourg, Nigel R Franks, James Sneyd, Guy Theraulaz, and Eric Bonabeau. Self-organizing biological systems, 2001.

Otger Campàs and L Mahadevan. Shape and dynamics of tip-growing cells. *Curr. Biol.*, 19(24):2102–7, December 2009. doi: 10.1016/j.cub.2009.10.075.

Arturo Casadevall, Joshua D Nosanchuk, Peter Williamson, and Marcio L Rodrigues. Vesicular transport across the fungal cell wall. *Trends in microbiology*, 17(4):158–162, 2009.

Juliane P Caviston, Serguei E Tcheperegine, and Erfei Bi. Singularity in budding: a role for the evolutionarily conserved small GTPase Cdc42p. *Proceedings of the National Academy of Sciences*, 99(19):12185–12190, 2002.

Yee-Hung Mark Chan and Wallace F Marshall. Organelle size scaling of the budding yeast vacuole is tuned by membrane trafficking rates. *Biophys. J.*, 106(9):1986–96, May 2014. doi: 10.1016/j.bpj.2014.03.014.

Fred Chang and Kerwyn C Huang. How and why cells grow as rods. *BMC biology*, 12(1):54, 2014.

Fred Chang and Matthias Peter. Yeasts make their mark. *Nature cell biology*, 5(4):294–299, 2003.

Mingzhu Chen and Fergal J Boyle. Investigation of membrane mechanics using spring networks: application to red-blood-cell modelling. *Mater Sci Eng C Mater Biol Appl*, 43:506–16, October 2014. doi: 10.1016/j.msec.2014.07.043.

Raymond E Chen and Jeremy Thorner. Function and regulation in MAPK signaling pathways: lessons learned from the yeast Saccharomyces cerevisiae. *Biochimica et Biophysica Acta (BBA)-Molecular Cell Research*, 1773 (8):1311–1340, 2007.

Ching-Shan Chou, Nie Qing, and Yi Tau-Mu. Modeling Robustness Tradeoffs in Yeast Cell Polarization Induced by Spatial Gradients. *PLoS ONE*, 3(9): e3103, 09 2008. doi: 10.1371/journal.pone.0003103.

Ching-Shan Chou, Travis I Moore, Steven D Chang, Qing Nie, and Tau-Mu Yi. Signaling regulated endocytosis and exocytosis lead to mating pheromone concentration dependent morphologies in yeast. *FEBS letters*, 586(23):4208–4214, 2012.

Philippe G. Ciarlet. *Finite Element Method for Elliptic Problems*. Society for Industrial and Applied Mathematics, Philadelphia, PA, USA, 2002. ISBN 0898715148.

David C. Clary. Quantum dynamics in the smallest water droplet. *Science*, 351(6279):1267–1268, March 2016.

Iain D Couzin, Jens Krause, Richard James, Graeme D Ruxton, and Nigel R Franks. Collective memory and spatial sorting in animal groups. *Journal of theoretical biology*, 218(1):1–11, 2002.

Francis Crick. Diffusion in embryogenesis. *Nature*, 225(5231):420–422, 1970. doi: 10.1038/225420a0.

Fred Cross, Leland H Hartwell, Catherine Jackson, and James B Konopka. Conjugation in Saccharomyces cerevisiae. *Annual review of cell biology*, 4 (1):429–455, 1988.

JG De Nobel and JA Barnett. Passage of molecules through yeast cell walls: A brief essay-review. *Yeast*, 7(4):313–323, 1991.

Thomas S Deisboeck and Iain D Couzin. Collective behavior in cancer cell populations. *Bioessays*, 31(2):190–197, 2009.

Erez Dekel and Uri Alon. Optimality and evolutionary tuning of the expression level of a protein. *Nature*, 436(7050):588–592, 2005.

Herve Delingette. Triangular springs for modeling nonlinear membranes. *Visualization and Computer Graphics, IEEE Transactions on*, 14(2):329–341, 2008.

Christian Diener. *Localized signaling and communication during yeast mating*. PhD thesis, Freie Universität Berlin, Germany, 2012.

Christian Diener, Gabriele Schreiber, Wolfgang Giese, Gabriel del Rio, Andreas Schröder, and Edda Klipp. Yeast mating and image-based quantification of spatial pattern formation. *PLoS Comput. Biol.*, 10(6):e1003690, June 2014. doi: 10.1371/journal.pcbi.1003690.

Simona Digiuni, Annik Berne-Dedieu, Cristina Martinez-Torres, Judit Szecsi, Mohammed Bendahmane, Alain Arneodo, and Françoise Argoul. Single Cell Wall Nonlinear Mechanics Revealed by a Multiscale Analysis of AFM Force-Indentation Curves. *Biophys. J.*, 108(9):2235–48, May 2015. doi: 10.1016/j.bpj.2015.02.024.

Henrik G Dohlman and Jeremy Thorner. Regulation of G protein-initiated signal transduction in yeast: paradigms and principles. *Annual review of biochemistry*, 70(1):703–754, 2001.

Tyler Drake and Dimitrios Vavylonis. Model of fission yeast cell shape driven by membrane-bound growth factors and the cytoskeleton. *PLoS Comput Biol*, 9(10):e1003, 2013.

Yves F Dufrêne, David Martínez-Martín, Izhar Medalsy, David Alsteens, and Daniel J Müller. Multiparametric imaging of biological systems by force-distance curve-based AFM. *Nature methods*, 10(9):847–854, 2013.

Jacques Dumais, Sidney L Shaw, Charles R Steele, Sharon R Long, and Peter M Ray. An anisotropic-viscoplastic model of plant cell morphogenesis by tip growth. *International Journal of Developmental Biology*, 50(2/3):209, 2006.

W Duntze, V MacKay, and T R Manney. Saccharomyces cerevisiae: a diffusible sex factor. *Science*, 168(3938):1472–3, June 1970.

G. Dziuk. Finite Elements for the Beltrami operator on arbitrary surfaces. In *Partial Differential Equations and Calculus of Variations*, volume 1357 of *Lecture Notes in Mathematics*, pages 142–155. Springer, 1988. ISBN 978-3-540-50508-2.

G. Dziuk and C.M. Elliott. Surface Finite Elements for Parabolic Equations. *Journal of Computational Mathematics*, 25(4):385–407, 2007.

Gerhard Dziuk. An algorithm for evolutionary surfaces. *Numerische Mathematik*, 58(1):603–611, 1990.

Leah Edelstein-Keshet, William R Holmes, Mark Zajac, and Meghan Dutot. From simple to detailed models for cell polarization. *Philosophical Transactions of the Royal Society of London B: Biological Sciences*, 368(1629): 20130003, 2013.

Jens Elgeti, Roland G Winkler, and Gerhard Gompper. Physics of microswimmers—single particle motion and collective behavior: a review. *Reports on progress in physics*, 78(5):056601, 2015.

Charles M. Elliott and Thomas Ranner. Finite element analysis for a coupled bulk–surface partial differential equation. *IMA Journal of Numerical Analysis*, 2012. doi: 10.1093/imanum.

Charles M Elliott, Björn Stinner, and Chandrasekhar Venkataraman. Modelling cell motility and chemotaxis with evolving surface finite elements. *Journal of The Royal Society Interface*, 2012. doi: 10.1098/rsif.2012.0276.

Robert G Endres and Ned S Wingreen. Accuracy of direct gradient sensing by single cells. *Proceedings of the National Academy of Sciences*, 105(41): 15749–15754, 2008.

Scott Erdman and Michael Snyder. A filamentous growth response mediated by the yeast mating pathway. *Genetics*, 159(3):919–928, 2001.

Sandrine Etienne-Manneville. Cdc42-the centre of polarity. *Journal of cell science*, 117(8):1291–1300, 2004.

M Falcke and J Zimmermann. Polymerization, bending, tension: What happens at the leading edge of motile cells? *The European Physical Journal Special Topics*, 223(7):1353–1372, 2014.

Martin Falcke. Concentration profiles of actin-binding molecules in lamellipodia. *Physica D: Nonlinear Phenomena*, 2015.

Tim W Fawcett and Andrew D Higginson. Heavy use of equations impedes communication among biologists. *Proceedings of the National Academy of Sciences*, 109(29):11735–11739, 2012.

Pierre Fayant, Orlando Girlanda, Youssef Chebli, Carl-Eric Aubin, Isabelle Villemure, and Anja Geitmann. Finite element model of polar growth in pollen tubes. *Plant Cell*, 22(8):2579–93, August 2010. doi: 10.1105/tpc.110.075754.

Frederic Festy, Simon M Ameer-Beg, Tony Ng, and Klaus Suhling. Imaging proteins in vivo using fluorescence lifetime microscopy. *Molecular bioSystems*, 3(6):381–391, 2007.

Hannes Fischer, Igor Polikarpov, and Aldo F Craievich. Average protein density is a molecular-weight-dependent function. *Protein Science*, 13(10):2825–2828, 2004.

Siegfried Fluegge. Stresses in shells. *Berlin: Springer, 1973, 2nd ed.*, 1, 1973.

Karl Francis and Bernhard O Palsson. Effective intercellular communication distances are determined by the relative time constants for cyto/chemokine secretion and diffusion. *Proceedings of the National Academy of Sciences*, 94(23):12258–12262, 1997.

Tina Freisinger, Ben Klünder, Jared Johnson, Nikola Müller, Garwin Pichler, Gisela Beck, Michael Costanzo, Charles Boone, Richard A Cerione, Erwin Frey, et al. Establishment of a robust single axis of cell polarity by coupling multiple positive feedback loops. *Nature communications*, 4:1807, 2013.

Peter Friedl, Joseph Locker, Erik Sahai, and Jeffrey E Segall. Classifying collective cancer cell invasion. *Nature Cell Biology*, 14(8):777–783, 2012.

Harald Garcke. Kepler, Kristalle und Computer. *Mathematik und numerische Simulationen helfen Kristallwachstum zu verstehen*, 2505(20):219–228, 2012.

Anja Geitmann and Joseph KE Ortega. Mechanics and modeling of plant cell growth. *Trends in plant science*, 14(9):467–478, 2009.

Michael H Gelb, Lucas Brunsveld, Christine A Hrycyna, Susan Michaelis, Fuyuhiko Tamanoi, Wesley C Van Voorhis, and Herbert Waldmann. Therapeutic intervention based on protein prenylation and associated modifications. *Nature chemical biology*, 2(10):518–528, 2006.

AV Getling and O Brausch. Cellular flow patterns and their evolutionary scenarios in three-dimensional Rayleigh-Bénard convection. *Physical Review E*, 67(4):046313, 2003.

Christophe Geuzaine and Jean-François Remacle. Gmsh: A 3-D finite element mesh generator with built-in pre-and post-processing facilities. *International Journal for Numerical Methods in Engineering*, 79(11):1309–1331, 2009.

Wolfgang Giese. Numerische Behandlung einer linearen Reaktions-Diffusions-Gleichung mit einer Anwendung in der interzellulaeren Kommunikation bei Hefezellen, 2010.

Wolfgang Giese, Martin Eigel, Sebastian Westerheide, Christian Engwer, and Edda Klipp. Influence of cell shape, inhomogeneities and diffusion barriers in cell polarization models. *WIAS Preprint*, 1(1959), 2014.

Wolfgang Giese, Martin Eigel, Sebastian Westerheide, Christian Engwer, and Edda Klipp. Influence of cell shape, inhomogeneities and diffusion barriers in cell polarization models. *Physical biology*, 12(6):066014, 2015.

André Goffeau, BG Barrell, Howard Bussey, RW Davis, Bernard Dujon, Heinz Feldmann, Francis Galibert, JD Hoheisel, Cr Jacq, Michael Johnston, et al. Life with 6000 genes. *Science*, 274(5287):546–567, 1996.

Albert Goldbeter. Computational approaches to cellular rhythms. *Nature*, 420 (6912):238–245, 2002.

Björn Goldenbogen, Wolfgang Giese, Marie Hemmen, Jannis Uhlendorf, Andreas Herrmann, and Edda Klipp. Dynamics of cell wall elasticity pattern shapes the cell during yeast mating morphogenesis. *Open Biology*, 6(9): 160136, 2016.

Joana Gonçalves-Sá and Andrew Murray. Asymmetry in sexual pheromones is not required for ascomycete mating. *Current Biology*, 21(16):1337–1346, 2011.

Andrew Gordon, Alejandro Colman-Lerner, Tina E Chin, Kirsten R Benjamin, C Yu Richard, and Roger Brent. Single-cell quantification of molecules and rates using open-source microscope-based cytometry. *Nature methods*, 4(2): 175–181, 2007.

Peter V Gordon, Cyrill B Muratov, and Stanislav Y Shvartsman. Local accumulation times for source, diffusion, and degradation models in two and three dimensions. *The Journal of chemical physics*, 138(10):104121, 2013.

Jeff Gore, Hyun Youk, and Alexander Van Oudenaarden. Snowdrift game dynamics and facultative cheating in yeast. *Nature*, 459(7244):253–256, 2009.

Andrew B Goryachev and Alexandra V Pokhilko. Dynamics of Cdc42 network embodies a Turing-type mechanism of yeast cell polarity. *FEBS letters*, 582 (10):1437–1443, 2008.

Gert-Martin Greuel. Kristalle und Mathematik. *Mitteilungen der Deutschen Mathematiker-Vereinigung*, 22(4):212–217, 2014.

Jacob Halatek and Erwin Frey. Highly canalized MinD transfer and MinE sequestration explain the origin of robust MinCDE-protein dynamics. *Cell Reports*, 1(6):741–752, 2012.

Olivier Hamant, Marcus G Heisler, Henrik Jönsson, Pawel Krupinski, Magalie Uyttewaal, Plamen Bokov, Francis Corson, Patrik Sahlin, Arezki Boudaoud, Elliot M Meyerowitz, et al. Developmental patterning by mechanical signals in Arabidopsis. *science*, 322(5908):1650–1655, 2008.

Leland H Hartwell. Nobel lecture: Yeast and cancer. *Bioscience reports*, 22 (3):373–394, 2002.

Leland H Hartwell, John J Hopfield, Stanislas Leibler, and Andrew W Murray. From molecular to modular cell biology. *Nature*, 402:C47–C52, 1999.

Rhoda J Hawkins, Olivier Benichou, Matthieu Piel, and Raphael Voituriez. Rebuilding cytoskeleton roads: Active-transport-induced polarization of cells. *Physical Review E*, 80(4):040903, 2009.

Werner Heisenberg. *Physik und Philosophie*. S. Hirzel, 5. edition, 1990.

W Helfrich. Elastic properties of lipid bilayers: theory and possible experiments. *Z. Naturforsch*, 28(11):693–703, 1973.

I Herskowitz. Life cycle of the budding yeast Saccharomyces cerevisiae. *Microbiol. Rev.*, 52(4):536–53, December 1988.

James B Hicks and Ira Herskowitz. Evidence for a new diffusible element of mating pheromones in yeast. *Nature*, 260:246–248, 1976.

Zoe Hilioti, Walid Sabbagh, Saurabh Paliwal, Adriel Bergmann, Marcus D Goncalves, Lee Bardwell, and Andre Levchenko. Oscillatory phosphorylation of yeast Fus3 MAP kinase controls periodic gene expression and morphogenesis. *Current biology*, 18(21):1700–1706, 2008.

Klaus Peter Hofmann, Christian MT Spahn, Reinhart Heinrich, and Udo Heinemann. Building functional modules from molecular interactions. *Trends in biochemical sciences*, 31(9):497–508, 2006.

William R Holmes and Leah Edelstein-Keshet. A comparison of computational models for eukaryotic cell shape and motility. *PLoS Comput Biol*, 8(12): e1002793, 2012.

William R Holmes, Anders E Carlsson, and Leah Edelstein-Keshet. Regimes of wave type patterning driven by refractory actin feedback: transition from static polarization to dynamic wave behaviour. *Physical biology*, 9(4):046005, 2012.

William R Holmes, May Anne Mata, and Leah Edelstein-Keshet. Local perturbation analysis: a computational tool for biophysical reaction-diffusion models. *Biophysical journal*, 108(2):230–236, 2015.

JJ Hopfield. Physics, computation, and why biology looks so different. *Journal of Theoretical Biology*, 171(1):53–60, 1994.

Lori B Huberman and Andrew W Murray. Genetically engineered transvestites reveal novel mating genes in budding yeast. *Genetics*, 195(4):1277–1290, 2013.

Lori B Huberman and Andrew W Murray. A model for cell wall dissolution in mating yeast cells: polarized secretion and restricted diffusion of cell wall remodeling enzymes induces local dissolution. *PLoS ONE*, 9(10):e109780, 2014. doi: 10.1371/journal.pone.0109780.

John D Hunter et al. Matplotlib: A 2D graphics environment. *Computing in science and engineering*, 9(3):90–95, 2007.

Yongyun Hwang, Praveen Kumar, and Abdul I Barakat. Intracellular regulation of cell signaling cascades: how location makes a difference. *Journal of mathematical biology*, 69(1):213–242, 2014.

Catherine L Jackson and Leland H Hartwell. Courtship in Saccharomyces cerevisiae: an early cell-cell interaction during mating. *Molecular and cellular biology*, 10(5):2202–2213, 1990a.

Catherine L Jackson and Leland H Hartwell. Courtship in S. cerevisiae: both cell types choose mating partners by responding to the strongest pheromone signal. *Cell*, 63(5):1039–1051, 1990b.

John David Jackson. *Klassische Elektrodynamik*. Walter de Gruyter, 2. auflage edition, 1983.

Alexandra Jilkine and Leah Edelstein-Keshet. A comparison of mathematical models for polarization of single eukaryotic cells in response to guided cues. *PLoS computational biology*, 7(4):e1001121, April 2011. ISSN 1553-7358. doi: 10.1371/journal.pcbi.1001121.

Meng Jin, Beverly Errede, Marcelo Behar, Will Mather, Sujata Nayak, Jeff Hasty, Henrik G Dohlman, and Timothy C Elston. Yeast dynamically modify their environment to achieve better mating efficiency. *Sci Signal*, 4(186): ra54, August 2011. doi: 10.1126/scisignal.2001763.

KL Johnson, K Kendall, and AD Roberts. Surface energy and the contact of elastic solids. In *Proceedings of the Royal Society of London A: Mathematical, Physical and Engineering Sciences*, volume 324, pages 301–313. The Royal Society, 1971.

Eric Jones, Travis Oliphant, P Peterson, et al. Open source scientific tools for Python, 2001.

Stephen K Jones and Richard J Bennett. Fungal mating pheromones: choreographing the dating game. *Fungal Genet. Biol.*, 48(7):668–76, July 2011. doi: 10.1016/j.fgb.2011.04.001.

Stephen K Jones, Starlynn C Clarke, Charles S Craik, and Richard J Bennett. Evolutionary Selection on Barrier Activity: Bar1 Is an Aspartyl Protease with Novel Substrate Specificity. *mBio*, 6(6):e01604–15, 2015.

Eric Karsenti. Self-organization in cell biology: a brief history. *Nature Reviews Molecular Cell Biology*, 9(3):255–262, 2008.

Joshua B Kelley, Gauri Dixit, Joshua B Sheetz, Sai Phanindra Venkatapurapu, Timothy C Elston, and Henrik G Dohlman. RGS proteins and septins cooperate to promote chemotropism by regulating polar cap mobility. *Curr. Biol.*, 25(3):275–85, February 2015. doi: 10.1016/j.cub.2014.11.047.

Richard Kennaway, Enrico Coen, Amelia Green, and Andrew Bangham. Generation of diverse biological forms through combinatorial interactions between tissue polarity and growth. *PLoS Comput Biol*, 7(6):e1002071, 2011.

Hiroaki Kitano. Computational systems biology. *Nature*, 420(6912):206–10, November 2002. doi: 10.1038/nature01254.

Edda Klipp. Modelling dynamic processes in yeast. *Yeast*, 24(11):943–959, 2007.

Edda Klipp. Computational yeast systems biology: a case study for the MAP kinase cascade. *Methods Mol. Biol.*, 759:323–43, 2011. doi: 10.1007/978-1-61779-173-4_19.

Edda Klipp, Bodil Nordlander, Roland Krüger, Peter Gennemark, and Stefan Hohmann. Integrative model of the response of yeast to osmotic shock. *Nature biotechnology*, 23(8):975–982, 2005.

Edda Klipp, Wolfram Liebermeister, Anselm Helbig, Axel Kowald, and Jörg Schaber. Systems biology standards—the community speaks. *Nature biotechnology*, 25(4):390–391, 2007.

Edda Klipp, Wolfram Liebermeister, Christoph Wierling, Axel Kowald, Hans Lehrach, and Ralf Herwig. *Systems biology*. John Wiley & Sons, 2013.

Frans M Klis, Pieternella Mol, Klaas Hellingwerf, and Stanley Brul. Dynamics of cell wall structure in Saccharomyces cerevisiae. *FEMS microbiology reviews*, 26(3):239–256, 2002.

Ben Klünder, Tina Freisinger, Roland Wedlich-Söldner, and Erwin Frey. GDI-mediated cell polarization in yeast provides precise spatial and temporal control of Cdc42 signaling. *PLoS Comput Biol*, 9(12):e1003396, 2013.

Bente Kofahl and Edda Klipp. Modelling the dynamics of the yeast pheromone pathway. *Yeast*, 21(10):831–850, 2004.

Matthias König, Hermann-Georg Holzhütter, and Nikolaus Berndt. Metabolic gradients as key regulators in zonation of tumor energy metabolism: A tissue-scale model-based study. *Biotechnology journal*, 8(9):1058–1069, 2013.

Toshiyuki Koto. IMEX Runge-Kutta schemes for reaction-diffusion equations. *Journal of Computational and Applied Mathematics*, 215(1):182–195, 2008. ISSN 0377-0427. doi: 10.1016/j.cam.2007.04.003.

Arthur D Lander. Pattern, growth, and control. *Cell*, 144(6):955–969, 2011.

Eric S Lander, Lauren M Linton, Bruce Birren, Chad Nusbaum, Michael C Zody, Jennifer Baldwin, Keri Devon, Ken Dewar, Michael Doyle, William FitzHugh, et al. Initial sequencing and analysis of the human genome. *Nature*, 409(6822):860–921, 2001.

Carolyn A Larabell and Keith A Nugent. Imaging cellular architecture with X-rays. *Curr. Opin. Struct. Biol.*, 20(5):623–31, October 2010. doi: 10.1016/j.sbi.2010.08.008.

David E Levin. Regulation of cell wall biogenesis in Saccharomyces cerevisiae: the cell wall integrity signaling pathway. *Genetics*, 189(4):1145–75, December 2011. doi: 10.1534/genetics.111.128264.

H Levine and WJ Rappel. Membrane-bound Turing patterns. *Physical review. E, Statistical, nonlinear, and soft matter physics*, 72(6 Pt 1):061912, December 2005. ISSN 1539-3755. doi: 10.1103/physreve.72.061912.

MA Lewis and JD Murray. Modelling territoriality and wolf-deer interactions. *Nature*, 366(6457):738–740, 1993.

Kenneth G Libbrecht. The physics of snow crystals. *Reports on progress in physics*, 68(4):855, 2005.

James A Lockhart. An analysis of irreversible plant cell elongation. *Journal of theoretical biology*, 8(2):264–275, 1965.

Alfred J Lotka. Contribution to the theory of periodic reactions. *The Journal of Physical Chemistry*, 14(3):271–274, 1910.

Celine I Maeder, Mark A Hink, Ali Kinkhabwala, Reinhard Mayr, Philippe IH Bastiaens, and Michael Knop. Spatial regulation of Fus3 MAP kinase activity through a reaction-diffusion mechanism in yeast pheromone signalling. *Nature Cell Biology*, 9(11):1319–1326, 2007.

Théo Maire and Hyun Youk. Molecular-Level Tuning of Cellular Autonomy Controls the Collective Behaviors of Cell Populations. *Cell Systems*, 1(5):349–360, 2015.

CR McCudden, MD Hains, RJ Kimple, DP Siderovski, and FS Willard. G-protein signaling: back to the future. *Cellular and Molecular Life Sciences*, 62(5):551–577, 2005.

Jason Meyers, Jennifer Craig, and David J Odde. Potential for control of signaling pathways via cell size and shape. *Current biology*, 16(17):1685–1693, 2006.

Leonor Michaelis and Maud L Menten. Die kinetik der invertinwirkung. *Biochem. z*, 49(333-369):352, 1913.

Susan Michaelis and Jemima Barrowman. Biogenesis of the Saccharomyces cerevisiae pheromone a-factor, from yeast mating to human disease. *Microbiology and Molecular Biology Reviews*, 76(3):626–651, 2012.

Gregor Milicic. Zeitschrittverfahren für gekoppelte Reaktions-Diffusionsgleichungen mit Anwendungen in der Biophysik, 2014.

Nicolas Minc, Arezki Boudaoud, and Fred Chang. Mechanical forces of fission yeast growth. *Curr. Biol.*, 19(13):1096–101, July 2009. doi: 10.1016/j.cub.2009.05.031.

Alex Mogilner, Jun Allard, and Roy Wollman. Cell polarity: quantitative modeling as a tool in cell biology. *Science*, 336(6078):175–9, April 2012. doi: 10.1126/science.1216380.

T.I. Moore, C.S. Chou, Q. Nie, N.L. Jeon, and T.M. Yi. Robust spatial sensing of mating pheromone gradients by yeast cells. *PLoS One*, 3(12):e3865, 2008.

Yoichiro Mori, Alexandra Jilkine, and Leah Edelstein-Keshet. Wave-Pinning and Cell Polarity from a Bistable Reaction-Diffusion System. *Biophysical Journal*, 94(9):3684–3697, May 2008. ISSN 00063495. doi: 10.1529/biophysj.107.120824.

Yoichiro Mori, Alexandra Jilkine, and Leah Edelstein-Keshet. Asymptotic and bifurcation analysis of wave-pinning in a reaction-diffusion model for cell polarization. *SIAM journal on applied mathematics*, 71(4):1401–1427, 2011.

Javier Muñoz-García, Zoltan Neufeld, and Boris N. Kholodenko. Positional Information Generated by Spatially Distributed Signaling Cascades. *PLoS Computational Biology*, 5(3), 2009. doi: 10.1371/journal.pcbi.1000330.

Helen A Murphy and Clifford W Zeyl. Yeast sex: surprisingly high rates of outcrossing between asci. *PLoS One*, 5(5):e10461, 2010.

Ukichirō Nakaya. *Snow crystals: natural and artificial*. Harvard University Press, xii edition, 1954.

Singo Nakazawa. Cell polarity as the" logos" of morphogenesis. *Cytologia*, 54 (2):293–298, 1989.

Perihan Nalbant, Louis Hodgson, Vadim Kraynov, Alexei Toutchkine, and Klaus M Hahn. Activation of endogenous Cdc42 visualized in living cells. *Science*, 305(5690):1615–1619, 2004.

K Nasmyth. A prize for proliferation. *Cell*, 107(6):689–701, December 2001.

Matthew P Neilson, Douwe M Veltman, Peter J M van Haastert, Steven D Webb, John A Mackenzie, and Robert H Insall. Chemotaxis: a feedback-based computational model robustly predicts multiple aspects of real cell behaviour. *PLoS Biol.*, 9(5):e1000618, May 2011. doi: 10.1371/journal.pbio.1000618.

Timothy Newman. Water is a molecular liquid. *Physical biology*, 11(3):033001, 2014.

Frank Noé. Beating the Millisecond Barrier in Molecular Dynamics Simulations. *Biophysical journal*, 108(2):228–229, 2015.

Satoshi Okada, Marcin Leda, Julia Hanna, Natasha S Savage, Erfei Bi, and Andrew B Goryachev. Daughter cell identity emerges from the interplay of Cdc42, septins, and exocytosis. *Developmental cell*, 26(2):148–161, 2013.

E Orlandini, D Marenduzzo, and AB Goryachev. Domain formation on curved membranes: phase separation or Turing patterns? *Soft Matter*, 9(39):9311–9318, 2013.

Mikiya Otsuji, Shuji Ishihara, Carl Co, Kozo Kaibuchi, Atsushi Mochizuki, and Shinya Kuroda. A mass conserved reaction-diffusion system captures properties of cell polarity. *PLoS computational biology*, 3(6):e108, June 2007. ISSN 1553-7358. doi: 10.1371/journal.pcbi.0030108.

Ertugrul M Ozbudak, Attila Becskei, and Alexander van Oudenaarden. A system of counteracting feedback loops regulates Cdc42p activity during spontaneous cell polarization. *Developmental cell*, 9(4):565–571, 2005.

Goran Peskir. On Boundary Behaviour of One-Dimensional Diffusions: From Brown to Feller and Beyond, 2014.

Paola Picotti, Mathieu Clément-Ziza, Henry Lam, David S Campbell, Alexander Schmidt, Eric W Deutsch, Hannes Röst, Zhi Sun, Oliver Rinner, Lukas Reiter, et al. A complete mass-spectrometric map of the yeast proteome applied to quantitative trait analysis. *Nature*, 494(7436):266–270, 2013.

Ilya Prigogine and René Lefever. Symmetry breaking instabilities in dissipative systems. II. *The Journal of Chemical Physics*, 48(4):1695–1700, 1968.

Noa Rappaport and Naama Barkai. Disentangling signaling gradients generated by equivalent sources. *J Biol Phys*, 38(2):267–78, March 2012. doi: 10.1007/s10867-011-9240-x.

Lord Rayleigh. LIX. On convection currents in a horizontal layer of fluid, when the higher temperature is on the under side. *The London, Edinburgh, and Dublin Philosophical Magazine and Journal of Science*, 32(192):529–546, 1916.

Mohammadhosein Razbin, Martin Falcke, Panayotis Benetatos, and Annette Zippelius. Mechanical properties of branched actin filaments. *Physical biology*, 12(4):046007, 2015.

Simone Reber and Anthony A Hyman. Emergent properties of the metaphase spindle. *Cold Spring Harbor perspectives in biology*, 7(7):a015784, 2015.

Radclyffe L Roberts and Gerald R Fink. Elements of a single MAP kinase cascade in Saccharomyces cerevisiae mediate two developmental programs in the same cell type: mating and invasive growth. *Genes & development*, 8 (24):2974–2985, 1994.

David W Rogers, Ellen McConnell, and Duncan Greig. Molecular quantification of Saccharomyces cerevisiae -pheromone secretion. *FEMS Yeast Res.*, 12(6):668–74, September 2012. doi: 10.1111/j.1567-1364.2012.00817.x.

Siegfried Roth. Mathematics and biology: a Kantian view on the history of pattern formation theory. *Development genes and evolution*, 221(5-6):255–279, 2011.

Boris Rubinstein, Brian D Slaughter, and Rong Li. Weakly nonlinear analysis of symmetry breaking in cell polarity models. *Physical biology*, 9(4):045006, 2012.

Jörg Schaber, Bente Kofahl, Axel Kowald, and Edda Klipp. A modelling approach to quantify dynamic crosstalk between the pheromone and the starvation pathway in baker's yeast. *FEBS Journal*, 273(15):3520–3533, 2006.

Kimberly A Schandel and Duane D Jenness. Direct evidence for ligand-induced internalization of the yeast alpha-factor pheromone receptor. *Molecular and Cellular Biology*, 14(11):7245–7255, 1994.

R Schekman and V Brawley. Localized deposition of chitin on the yeast cell surface in response to mating pheromone. *Proc. Natl. Acad. Sci. U.S.A.*, 76 (2):645–9, February 1979.

W.E. Schiesser. *The numerical method of lines*. Academic Press Inc., 1991. ISBN 0-12-624130-9. Integration of partial differential equations.

Johannes Schindelin, Ignacio Arganda-Carreras, Erwin Frise, Verena Kaynig, Mark Longair, Tobias Pietzsch, Stephan Preibisch, Curtis Rueden, Stephan Saalfeld, Benjamin Schmid, Jean-Yves Tinevez, Daniel James White, Volker Hartenstein, Kevin Eliceiri, Pavel Tomancak, and Albert Cardona. Fiji: an

open-source platform for biological-image analysis. *Nat. Methods*, 9(7):676–82, July 2012. doi: 10.1038/nmeth.2019.

Caroline A Schneider, Wayne S Rasband, Kevin W Eliceiri, et al. NIH Image to ImageJ: 25 years of image analysis. *Nat methods*, 9(7):671–675, 2012.

Z Schuss, A Singer, and David Holcman. The narrow escape problem for diffusion in cellular microdomains. *Proceedings of the National Academy of Sciences*, 104(41):16098–16103, 2007.

Zeev Schuss. The narrow escape problem—a short review of recent results. *Journal of Scientific Computing*, 53(1):194–210, 2012.

Jeffrey E Segall. Polarization of yeast cells in spatial gradients of alpha mating factor. *Proceedings of the National Academy of Sciences*, 90(18):8332–8336, 1993.

Udo Seifert. Configurations of fluid membranes and vesicles. *Advances in physics*, 46(1):13–137, 1997.

Brian D Slaughter, Arupratan Das, Joel W Schwartz, Boris Rubinstein, and Rong Li. Dual modes of cdc42 recycling fine-tune polarized morphogenesis. *Developmental cell*, 17(6):823–835, 2009.

A E Smith, Z Zhang, C R Thomas, K E Moxham, and A P Middelberg. The mechanical properties of Saccharomyces cerevisiae. *Proc. Natl. Acad. Sci. U.S.A.*, 97(18):9871–4, August 2000.

Carlas S Smith, Stephan Preibisch, Aviva Joseph, Sara Abrahamsson, Bernd Rieger, Eugene Myers, Robert H Singer, and David Grunwald. Nuclear accessibility of -actin mRNA is measured by 3D single-molecule real-time tracking. *J. Cell Biol.*, 209(4):609–19, May 2015. doi: 10.1083/jcb.201411032.

Sarah E Smith, Brian D Slaughter, and Jay R Unruh. Imaging methodologies for systems biology: Investigations of cell polarity. *Cell adhesion & migration*, 8(5):468–477, 2014.

Ian N. Sneddon. The relation between load and penetration in the axisymmetric boussinesq problem for a punch of arbitrary profile. *Int. J. Engng. Sci.*, 3:47–57, 1965.

Thomas W Spiesser, Clemens Kühn, Marcus Krantz, and Edda Klipp. Bud-Localization of CLB2 mRNA Can Constitute a Growth Rate Dependent Daughter Sizer. *PLoS Comput Biol*, 11(4):e1004223, 2015.

Rachel Spokoini, Ofer Moldavski, Yaakov Nahmias, Jeremy L England, Maya Schuldiner, and Daniel Kaganovich. Confinement to organelle-associated inclusion structures mediates asymmetric inheritance of aggregated protein in budding yeast. *Cell Rep*, 2(4):738–47, October 2012. doi: 10.1016/j.celrep.2012.08.024.

Alan M Tartakoff. Cell biology of yeast zygotes, from genesis to budding. *Biochimica et Biophysica Acta (BBA)-Molecular Cell Research*, 1853(7): 1702–1714, 2015.

Dominik Thalmeier, Jacob Halatek, and Erwin Frey. Geometry-induced protein pattern formation. *Proceedings of the National Academy of Sciences*, 113(3):548–553, 2016.

D'Arcy Wentworth Thompson. *On growth and form*. Cambridge University Press, 2nd edition, 1942.

Ty M Thomson, Kirsten R Benjamin, Alan Bush, Tonya Love, David Pincus, Orna Resnekov, C Yu Richard, Andrew Gordon, Alejandro Colman-Lerner, Drew Endy, et al. Scaffold number in yeast signaling system sets tradeoff between system output and dynamic range. *Proceedings of the National Academy of Sciences*, 108(50):20265–20270, 2011.

Derek Toomre and Dietmar J Manstein. Lighting up the cell surface with evanescent wave microscopy. *Trends in cell biology*, 11(7):298–303, 2001.

Katja Tummler, Clemens Kühn, and Edda Klipp. Dynamic metabolic models in context: biomass backtracking. *Integrative Biology*, 7(8):940–951, 2015.

Alan Mathison Turing. The chemical basis of morphogenesis. *Philosophical Transactions of the Royal Society of London B: Biological Sciences*, 237 (641):37–72, 1952.

Ralph H Turner and Lewis M Killian. *Collective behavior*. Prentice-Hall, 1957.

Friedemann Uschner and Edda Klipp. Information processing in the adaptation of Saccharomyces cerevisiae to osmotic stress: an analysis of the phosphorelay system. *Systems and synthetic biology*, 8(4):297–306, 2014.

Raphael H Valdivia and Randy Schekman. The yeasts Rho1p and Pkc1p regulate the transport of chitin synthase III (Chs3p) from internal stores to the plasma membrane. *Proceedings of the National Academy of Sciences*, 100(18):10287–10292, 2003a.

Raphael H Valdivia and Randy Schekman. The yeasts Rho1p and Pkc1p regulate the transport of chitin synthase III (Chs3p) from internal stores to the plasma membrane. *Proceedings of the National Academy of Sciences*, 100(18):10287–10292, 2003b.

Stefan Van Der Walt, S Chris Colbert, and Gael Varoquaux. The NumPy array: a structure for efficient numerical computation. *Computing in Science & Engineering*, 13(2):22–30, 2011.

Dominic Vella, Amin Ajdari, Ashkan Vaziri, and Arezki Boudaoud. Indentation of ellipsoidal and cylindrical elastic shells. *Phys. Rev. Lett.*, 109(14): 144302, October 2012a.

Dominic Vella, Amin Ajdari, Ashkan Vaziri, and Arezki Boudaoud. The indentation of pressurized elastic shells: from polymeric capsules to yeast cells. *J R Soc Interface*, 9(68):448–55, March 2012b. doi: 10.1098/rsif.2011.0352.

Alejandra C Ventura, Alan Bush, Gustavo Vasen, Matías A Goldín, Brianne Burkinshaw, Nirveek Bhattacharjee, Albert Folch, Roger Brent, Ariel Chernomoretz, and Alejandro Colman-Lerner. Utilization of extracellular information before ligand-receptor binding reaches equilibrium expands and shifts the input dynamic range. *Proceedings of the National Academy of Sciences*, 111(37):E3860–E3869, 2014.

Peter J Verveer and Philippe IH Bastiaens. Quantitative microscopy and systems biology: seeing the whole picture. *Histochemistry and cell biology*, 130 (5):833–843, 2008.

Viola Vogel and Michael Sheetz. Local force and geometry sensing regulate cell functions. *Nature reviews molecular cell biology*, 7(4):265–275, 2006.

Georg R Walther, Athanasius FM Marée, Leah Edelstein-Keshet, and Verônica A Grieneisen. Deterministic versus stochastic cell polarisation through wave-pinning. *Bulletin of mathematical biology*, 74(11):2570–2599, 2012.

Ortrud Wartlick, Anna Kicheva, and Marcos González-Gaitán. Morphogen gradient formation. *Cold Spring Harbor perspectives in biology*, 1(3): a001255, 2009.

Dongguang Wei, Scott Jacobs, Shannon Modla, Shuang Zhang, Carissa L Young, Robert Cirino, Jeffrey Caplan, and Kirk Czymmek. High-resolution three-dimensional reconstruction of a whole yeast cell using focused-ion beam scanning electron microscopy. *BioTechniques*, 53(1):41–8, July 2012. doi: 10.2144/000113850.

Frank Weichert, Andreas Schröder, Constantin Landes, Ali Shamaa, Said Kamel Awad, Lars Walczak, Heinrich Müller, and Mathias Wagner. Computation of a finite element-conformal tetrahedral mesh approximation for simulated soft tissue deformation using a deformable surface model. *Medical & biological engineering & computing*, 48(6):597–610, 2010.

Daniel K Wells, Yishan Chuang, Louis M Knapp, Dirk Brockmann, William L Kath, and Joshua N Leonard. Spatial and Functional Heterogeneities Shape Collective Behavior of Tumor-Immune Networks. *PLoS Computational Biology*, 11(4), 2015.

Hans V Westerhoff, Alexey Kolodkin, Riaan Conradie, Stephen J Wilkinson, Frank J Bruggeman, Klaas Krab, Jan H van Schuppen, Hanna Hardin, Barbara M Bakker, Martijn J Moné, et al. Systems biology towards life in silico: mathematics of the control of living cells. *Journal of mathematical biology*, 58(1-2):7–34, 2009.

Malcolm Whiteway. Yeast mating: trying out new pickup lines. *Current Biology*, 21(16):R626–R628, 2011.

Christian Widmann, Spencer Gibson, Matthew B Jarpe, and Gary L Johnson. Mitogen-activated protein kinase: conservation of a three-kinase module from yeast to human. *Physiological reviews*, 79(1):143–180, 1999.

Eugene P Wigner. The unreasonable effectiveness of mathematics in the natural sciences. Richard courant lecture in mathematical sciences delivered at New York University, May 11, 1959. *Communications on pure and applied mathematics*, 13(1):1–14, 1960.

J. Wloka. *Partial Differential Equations*. Cambridge University Press, 1987. ISBN 9780521277594.

Judith AH Wodke, Jacek Puchałka, Maria Lluch-Senar, Josep Marcos, Eva Yus, Miguel Godinho, Ricardo Gutiérrez-Gallego, Vitor AP Martins dos Santos, Luis Serrano, Edda Klipp, et al. Dissecting the energy metabolism in Mycoplasma pneumoniae through genome-scale metabolic modeling. *Molecular systems biology*, 9(1):653, 2013.

Lewis Wolpert. Cell polarity. *Philosophical Transactions of the Royal Society B: Biological Sciences*, 368(1629):20130419, 2013.

Fred S Wouters, Peter J Verveer, and Philippe IH Bastiaens. Imaging biochemistry inside cells. *Trends in cell biology*, 11(5):203–211, 2001.

Chi-Fang Wu, Natasha S Savage, and Daniel J Lew. Interaction between bud-site selection and polarity-establishment machineries in budding yeast. *Philosophical Transactions of the Royal Society of London B: Biological Sciences*, 368(1629):20130006, 2013.

Chi-Fang Wu, Jian-Geng Chiou, Maria Minakova, Benjamin Woods, Denis Tsygankov, Trevin R Zyla, Natasha S Savage, Timothy C Elston, and Daniel J Lew. Role of competition between polarity sites in establishing a unique front. *eLife*, 4:e11611, 2016.

Zhenbiao Yang and Irene Lavagi. Spatial control of plasma membrane domains: ROP GTPase-based symmetry breaking. *Current opinion in plant biology*, 15(6):601–607, 2012.

Tau-Mu Yi, Hiroaki Kitano, and Melvin I Simon. A quantitative characterization of the yeast heterotrimeric G protein cycle. *Proceedings of the National Academy of Sciences*, 100(19):10764–10769, 2003.

Hyun Youk and Wendell A Lim. Secreting and sensing the same molecule allows cells to achieve versatile social behaviors. *Science*, 343(6171):1242782, 2014.

Mao-Hong Yu. *Generalized plasticity*. Springer Science & Business Media, 2006.

7

Appendix

Appendix A

Estimation of the Diffusion Coefficients

The diffusion of $\boldsymbol{\alpha}$-factor was estimated using the Stokes-Einstein relation, which is given by

$$D = \frac{k_B T}{6\pi\eta r_M}. \tag{7.1}$$

Here, k_B is the Boltzmann's constant, T is the temperature, η is the solution viscosity and r_M is the particle radius. The values shown in Table 7.1 were used for the estimation of the diffusion coeffients of $\boldsymbol{\alpha}$-factor and **a**-factor. The molecular radius was calculated from Fischer et al. (2004):

$$\rho(M) = \rho_\infty + \Delta\rho_0 \exp(-M/K) = [1.410 + 0.145 \cdot \exp(-m/13))]\, g/cm^3. \tag{7.2}$$

This resulted in an estimate of the diffusion coefficents of

$$D_\alpha \approx 359\ \mu m^2/s, \tag{7.3}$$
$$D_a \approx 351\ \mu m^2/s. \tag{7.4}$$

Alternatively, the diffusion coefficient in water at $T = 30°C$ can also be caclulated as in Segall (1993) :

$$D = \frac{D_0}{M^{\frac{1}{3}}}. \tag{7.5}$$

Here, M is the molecular weight in Dalton and D_0 is an experimantally determined constant with the value 3800 $\mu m^2/s$. This calculation results in slightly lower values:

$$D_\alpha \approx 319\ \mu m^2/s, \tag{7.6}$$
$$D_a \approx 311\ \mu m^2/s. \tag{7.7}$$

Variable	Value	Description
	YIIKGVFWDPA[S-farnesyl]-$COOCH_3$	Structure of **a**-factor
	WHWLGLKPGQPMY	Structure of $\boldsymbol{\alpha}$-factor
M_α	1.684 kDa	molecular weight of one molecule $\boldsymbol{\alpha}$-factor
M_a	1.808 kDa	molecular weight of one molecule **a**-factor
ρ_α	1.537 g/cm^3 ($\approx 9.26 \cdot 10^8 kDa/\mu m^3$))	density of one molecule $\boldsymbol{\alpha}$-factor
ρ_a	1.536 g/cm^3 ($\approx 9.25 \cdot 10^8 kDa/\mu m^3$))	density of one molecule **a**-factor
r_α	$7.58 \cdot 10^{-4} \mu m$	
r_a	$7.76 \cdot 10^{-4} \mu m$	
T	$= 30°C$ ($= 303.15K$)	
η	$= 0.815\ mPa \cdot s$	viscosity for water at $T = 30°C$

Table 7.1: Parameters characterizing the pheromone $\boldsymbol{\alpha}$-factor and **a**-factor. Calculated with GenScript peptide calculator `https://www.genscript.com/ssl-bin/peptide_mw`.

Small Auto Degradation Ensures Physical Solution

The steady state solution to the diffusion equation with degradation for one secreting cell reads (compare equation (2.14))

$$\alpha(r) = \alpha^S \frac{R}{r} \exp(-\sqrt{\frac{K_B}{D}} r), \tag{7.8}$$

where $r = \|\mathbf{x} - \mathbf{x}_i\|$. Integration over the whole domain gives:

$$\begin{aligned}
&\int_\Omega \alpha(r) dV = \int_0^{2\pi} \int_0^{\pi} \int_0^{\infty} \alpha(r) r^2 \sin(\theta) dr d\theta d\phi \\
&= 4\pi\alpha^S R \int_0^{\infty} r \exp(-\sqrt{\frac{K_B}{D}} r) dr \\
&= \begin{cases} 4\pi\alpha^S R \left[-r\sqrt{\frac{D}{K_B}} \exp(-\sqrt{\frac{K_B}{D}} r) \Big|_0^{\infty} + \sqrt{\frac{D}{K_B}} \int_0^{\infty} \exp(-\sqrt{\frac{K_B}{D}} r) dr \right] & K_B \neq 0, \\ \infty & K_B = 0 \end{cases} \\
&= \begin{cases} 4\pi\alpha^S R \frac{D}{k} & K_B \neq 0, \\ \infty & K_B = 0. \end{cases}
\end{aligned}$$

Note that a physical solution is only obtained for $K_B \neq 0$.

Method of Imaginary Charges

In Barkai et al. (1998), point charges were distributed in space. However, in the lab experiments the cells sedimented on the ground of a surface. Therefore, I assumed a zero-flux boundary condition on the surface, i.e. no molecules are absorpted or secreted by the surface. To describe the influence of the cells on the surface I used the method of imaginary charges, which is described in Jackson (1983), and extended this method to the diffusion model. Suppose we have a point charge Q at position $\mathbf{x}_Q = (0, 0, d)$ above a reflective surface which is in the x_1-x_2 plane. In this case the solution with zero-flux boundary condition reads as

$$\Phi(\mathbf{x}, t) = \frac{Q}{\|\mathbf{x} - \mathbf{x}_Q\|} + \frac{Q}{\|\mathbf{x} + \mathbf{x}_Q\|}. \tag{7.9}$$

For the pheromone distribution I used the function

$$\alpha(\mathbf{x}, t) = \alpha^S \frac{R}{\|\mathbf{x} - \mathbf{x}_C\|} \exp(-\|\mathbf{x} - \mathbf{x}_C\|/\lambda) + \alpha^S \frac{R}{\|\mathbf{x} + \mathbf{x}_C\|} \exp(-\|\mathbf{x} + \mathbf{x}_C\|/\lambda), \tag{7.10}$$

where $\mathbf{x}_C = (0, 0, R)$, where R is the cell radius, and $\lambda = \sqrt{D/K_B}$. The gradient of $\alpha(\mathbf{x}, t)$ is given by

$$\begin{aligned}\nabla\alpha(\mathbf{x},t) = &-\alpha^S R\left(\frac{1}{\|\mathbf{x}-\mathbf{x}_C\|^2}+\frac{1}{\lambda\|\mathbf{x}-\mathbf{x}_C\|}\right)\exp(-\|\mathbf{x}-\mathbf{x}_C\|/\lambda)\frac{\mathbf{x}-\mathbf{x}_C}{\|\mathbf{x}-\mathbf{x}_C\|}\\ &-\alpha^S R\left(\frac{1}{\|\mathbf{x}+\mathbf{x}_C\|^2}+\frac{1}{\lambda\|\mathbf{x}+\mathbf{x}_C\|}\right)\exp(-\|\mathbf{x}+\mathbf{x}_C\|/\lambda)\frac{\mathbf{x}+\mathbf{x}_C}{\|\mathbf{x}+\mathbf{x}_C\|}.\end{aligned} \tag{7.11}$$

On the surface, which is the x_1-x_2 plane, we have $(\mathbf{x} \pm \mathbf{x}_C) \cdot \mathbf{n}_z = \pm R$ and $\|\mathbf{x} \pm \mathbf{x}_C\| = \sqrt{x_1^2 + x_2^2 + R^2}$. Therefore, the boundary condition on the reflective surface in the x_1-x_2 plane becomes

$$\begin{aligned}&J_{\text{flux}} = D\nabla\alpha(\mathbf{x},t)\cdot\mathbf{n}_z|_{x_3=0}\\ =&-D\alpha^S R\left(\frac{1}{x_1^2+x_2^2+R^2}+\frac{1}{\lambda\sqrt{x_1^2+x_2^2+R^2}}\right)\\ &\qquad\cdot\exp(-\sqrt{x_1^2+x_2^2+R^2}/\lambda)\frac{(-R)}{\sqrt{x_1^2+x_2^2+R^2}}\\ &-D\alpha^S R\left(\frac{1}{x_1^2+x_2^2+R^2}+\frac{1}{\lambda\sqrt{x_1^2+x_2^2+R^2}}\right)\\ &\qquad\cdot\exp(-\sqrt{x_1^2+x_2^2+R^2}/\lambda)\frac{R}{\sqrt{x_1^2+x_2^2+R^2}}\\ =&\quad 0.\end{aligned}$$

Furthermore, the steady state of the stationary reaction-diffusion equation $0 = D\Delta\alpha(\mathbf{x}, t) - K_B\alpha(\mathbf{x}, t)$ is still fulfilled by $\alpha(\mathbf{x}, t)$. Note, that the solution is excact, if the secreting cell is approximated by a point source. While the fact that the cell itself displaces its volume in the surrounding is not taken into account in this calculation.

Methods

The models 0 - 3 were implemented in python using the *NumPy* und *SciPy* packages. The export package PyEVTK was used to generate vtk data-files, which were visualized using ParaView. The microscopic images were analyzed using CellID (Gordon et al., 2007) and ImageJ (Schneider et al., 2012). Triangular meshes representing the computational domain were generated using Gmsh (Geuzaine and Remacle, 2009). To solve the RD equations numerically the open source framework DUNE (Bastian et al., 2008a) was used.

Appendix B

Stability Analysis for the Bulk Surface Equations in 3D

We start with the linearized form of the bulk-surface equations as in Chapter 3, Section 3.4. The linearized equations (3.18) and (3.19) in spherical coordinates are given by

$$\begin{aligned}\frac{\partial \xi_m}{\partial t}(\phi,\theta,t) &= D_m \Delta_{\phi,\theta}\xi_m(\phi,\theta,t) + f_u(\bar{u}_0,\bar{v}_0|_{r=R})\xi_m(\phi,\theta,t) \\ &\quad + f_v(\bar{u}_0,\bar{v}_0|_{r=R})\xi_c(r,\phi,\theta,t), \qquad (7.12)\\ \frac{\partial \xi_c}{\partial t}(r,\phi,\theta,t) &= D_c \Delta \xi_c(r,\phi,\theta,t) \qquad (7.13)\end{aligned}$$

with boundary condition (compare (3.20))

$$-D_m \nabla_r \xi_c(r,\phi,\theta,t)|_{r=R} = f_u(\bar{u}_0,\bar{v}_0)\xi_m(\phi,\theta,t) + f_v(\bar{u}_0,\bar{v}_0)\xi_c(r,\phi,\theta,t) \quad (7.14)$$

on the cell membrane. Here, $(\bar{u}_0,\bar{v}_0)$ is a given steady state, while $\xi_m = u - \bar{u}_0$, $\xi_c = v - \bar{v}_0$ describe small spatial disturbances from this steady state.

Linearized Equations in Spherical Coordinates

We expand the functions ξ_m and ξ_c using real spherical harmonics as follows:

$$\xi_m(\theta,\phi,t) = \sum_{k=0}^{\infty}\sum_{l=-k}^{k} \xi_m^{k,l} Y_{k,l}(\theta,\phi)\exp(\lambda_{k,l}t), \qquad (7.15)$$

$$\xi_c(r,\theta,\phi,t) = \sum_{k=0}^{\infty}\sum_{l=-k}^{k} \xi_c^{k,l} A^{k,l}(r) Y_{k,l}(\theta,\phi)\exp(\lambda_{k,l}t). \qquad (7.16)$$

Inserting this ansatz for the cytosolic species into the (7.13) yields for all integers $k > 0$ and l with $-k \le l \le k$:

$$\lambda_{k,l}\xi_c^{k,l} A^{k,l}(r) Y_{k,l}(\theta,\phi)\exp(\lambda_{k,l}t) = D_c \Delta\left[\xi_c^{k,l} A^{k,l}(r) Y_{k,l}(\theta,\phi)\exp(\lambda_{k,l}t)\right]. \qquad (7.17)$$

The real spherical harmonics are the eigenfunction of the spherical laplacian and we have the relationship

$$r^2 \Delta_{\theta,\phi} Y_{k,l}(\theta,\phi) = -k(k+1) Y_{k,l}(\theta,\phi). \qquad (7.18)$$

This yields

$$\begin{aligned}&r^2\lambda_{k,l}\xi_c^{k,l} A^{k,l}(r) Y_{k,l}(\theta,\phi)\exp(\lambda_{k,l}t) \qquad (7.19)\\ &= -k(k+1) D_c \xi_c^{k,l} A^{k,l}(r) Y_{k,l}(\theta,\phi)\exp(\lambda_{k,l}t) \\ &+ D_c r^2 \xi_c^{k,l} \Delta(A^{k,l}(r)) Y_{k,l}(\theta,\phi)\exp(\lambda_{k,l}t). \qquad (7.20)\end{aligned}$$

After cancelling, we get

$$r^2 A^{k,l}(r) = -k(k+1)D_c A^{k,l}(r) + D_c r^2 \Delta(A^{k,l}(r)). \tag{7.21}$$

The Laplace operator has the form $\Delta = \frac{\partial^2}{\partial^2 r} + \frac{2}{r}\frac{\partial}{\partial r}$, which leads to

$$0 = \left[r^2\partial_r^2 + 2r\partial_r - k(k+1) - \lambda_{k,l}r^2/D_c\right] A^{k,l}(r). \tag{7.22}$$

for all k, l. Mathematical solutions of this equation are modified spherical Bessel functions of the first kind $i_k(r\sqrt{\lambda_{k,l}/D_c})$. The i_k is related to the spherical Bessel of the first kind i_k by

$$i_k(x) = i^{-k} j_k(r\sqrt{ix}) \tag{7.23}$$

and the derivative by

$$\frac{\partial}{\partial r}[i_k\left(r\sqrt{\lambda_{k,l}/D_c}\right)] = \frac{\partial}{\partial r}[i^{-k} j_k\left(ir\sqrt{\lambda_{k,l}/D_c}\right)] \tag{7.24}$$

$$= i^{-k+1}\sqrt{\lambda_{k,l}/D_c}\frac{\partial j_k}{\partial r}\left(ir\sqrt{\lambda_{k,l}/D_c}\right). \tag{7.25}$$

For the representaion of the cytosolic perturbations we therefore get:

$$\xi_c(r,\theta,\phi,t) = \sum_{k=0}^{\infty}\sum_{l=-k}^{k} \xi_c^{k,l} i_k(r\sqrt{\lambda_{k,l}/D_v}) Y_{k,l}(\theta,\phi)\exp(\lambda_{k,l}t). \tag{7.26}$$

We insert this relationship for ξ_c into the boundary conditions (7.14)

$$-D_c\xi_c^{k,l}\partial_r i_k(r\sqrt{\lambda_{k,l}/D_c})|_{r=R} = f_u(\bar{u}_0,\bar{v}_0)\xi_m^{k,l} + f_v(\bar{u}_0,\bar{v}_0)\xi_c^{k,l} i_k(R\sqrt{(\lambda_{k,l}/D_c)}). \tag{7.27}$$

This equation can be solved for $\xi_c^{k,l}$, which gives

$$\xi_c^{k,l} = -\frac{f_u(\bar{u}_0,\bar{v}_0)\xi_m^{k,l}}{D_c\partial_r i_k(r\sqrt{\lambda_{k,l}/D_c})|_{r=R} + f_v(\bar{u}_0,\bar{v}_0) i_k(R\sqrt{\lambda_{k,l}/D_v})}. \tag{7.28}$$

Therefore, ξ_c can be expressed in terms of the coefficients for ξ_m:

$$\xi_c(r,\theta,\phi,t) = -\sum_{k=0}^{\infty}\sum_{l=-k}^{k} \frac{f_u(\bar{u}_0,\bar{v}_0)\xi_m^{k,l} i_k(r\sqrt{(}\lambda_{k,l}/D_c))Y_{k,l}(\theta,\phi)\exp(\lambda_{k,l}t)}{D_c\partial_r i_k(r\sqrt{\lambda_{k,l}/D_c})|_{r=R} + f_v(\bar{u}_0,\bar{v}_0) i_k(R\sqrt{(\lambda_{l,m}/D_v)})}. \tag{7.29}$$

Inserting this relationship into equation (7.12) gives for all k, l yields

$$\begin{aligned}
&\lambda_{k,l}\xi_m^{k,l} Y_{k,l}(\theta,\phi)\exp(\lambda_{k,l}t) \\
&= -\frac{D_m k(k+1)}{R^2}\xi_m^{k,l} Y_{k,l}(\theta,\phi)\exp(\lambda_{k,l}t) \\
&\quad + f_u(\bar{u}_0,\bar{v}_0)\xi_m^{k,l} Y_{k,l}(\theta,\phi)\exp(\lambda_{k,l}t) \\
&\quad + \frac{f_v(\bar{u}_0,\bar{v}_0) f_u(\bar{u}_0,\bar{v}_0)\xi_m^{k,l} i_k(R\sqrt{\lambda_{l,m}/D_v}) Y_{l,m}(\theta,\phi)\exp(\lambda_{k,l}t)}{D_c\partial_r i_k(r\sqrt{(}\lambda_{k,l}/D_c))|_{r=R} + f_v(\bar{u}_0,\bar{v}_0) i_l(R\sqrt{(\lambda_{k,l}/D_c)})}.
\end{aligned} \tag{7.30}$$

Cancellation of the nonzero terms results in an equation for $\lambda_{k,l}$

$$\begin{aligned}\lambda_{k,l} =& f_u(\bar{u}_0, \bar{v}_0) - \frac{D_m k(k+1)}{R^2} \\ & - \frac{f_u(\bar{u}_0, \bar{v}_0) f_v(\bar{u}_0, \bar{v}_0) i_k(R\sqrt{\lambda_{k,l}/D_c})}{D_c \partial_r i_k(r\sqrt{\lambda_{k,l}/D_c})|_{r=R} + f_v(\bar{u}_0, \bar{v}_0) i_k(R\sqrt{\lambda_{k,l}/D_c})}.\end{aligned} \tag{7.31}$$

Therefore, $\lambda_{k,l}$ only depends on k and, therefore, we set $\lambda_k = \lambda_{k,l}$ in the remainder:

$$\begin{aligned}\lambda_k =& f_u(\bar{u}_0, \bar{v}_0|_{r=R}) - \frac{D_m k(k+1)}{R^2} \\ & - f_u(\bar{u}_0, \bar{v}_0|_{r=R}) f_v(\bar{u}_0, \bar{v}_0|_{r=R}) \frac{i_k(R\sqrt{\lambda_k/D_c})}{D_c \frac{\partial}{\partial r} i_k(r\sqrt{\lambda_k/D_c})\big|_{r=R} + f_v(\bar{u}_0, \bar{v}_0|_{r=R}) i_k(R\sqrt{\lambda_k/D_c})}.\end{aligned} \tag{7.32}$$

Note that initial conditions for system (3.18) – (3.20) would be required in order to determine the free parameters $\xi_m^{k,l}$.

Having an equation for the parameters λ_k, we now want to identify conditions which lead to growing eigenmodes. Following (Abramowitz and Stegun, 1964), the derivative of i_k can be expressed as

$$\frac{\partial}{\partial r} i_k(r\sqrt{\lambda_k/D_c})\Big|_{r=R} = i_{k+1}(R\sqrt{\lambda_k/D_c})\sqrt{\lambda_k/D_c} + \frac{k}{R} i_k(R\sqrt{\lambda_k/D_c}). \tag{7.33}$$

Since $i_k(x) > 0$ for $x > 0$ and for all $k = 0, 1, 2, \ldots$, we have the inequality

$$\frac{\partial}{\partial r} i_k(r\sqrt{\lambda_k/D_c})\Big|_{r=R} \geq \frac{k}{R} i_k(R\sqrt{\lambda_k/D_c}). \tag{7.34}$$

We use this inequality for the derivative $\frac{\partial}{\partial r} I_k$ and furthermore assume $f_u(\bar{u}_0, \bar{v}_0|_{r=R}) > 0$ and $f_v(\bar{u}_0, \bar{v}_0|_{r=R}) > 0$. This holds true for the GOR model in the stable steady state and for the WP model in the transient steady state $(\bar{v}_0, \bar{u}_0^T)$, where phase separation occurs. Therfore, we obtain:

$$\lambda_k = f_u(\bar{u}_0, \bar{v}_0|_{r=R}) - \frac{D_m k(k+1)}{R^2} \tag{7.35}$$

$$- \frac{f_u(\bar{u}_0, \bar{v}_0|_{r=R}) f_v(\bar{u}_0, \bar{v}_0|_{r=R}) i_k(R\sqrt{\lambda_k/D_c})}{D_c \frac{\partial}{\partial r} i_k(r\sqrt{\lambda_k/D_c})\Big|_{r=R} + f_v(\bar{u}_0, \bar{v}_0|_{r=R}) i_k(R\sqrt{\lambda_k/D_c})} \tag{7.36}$$

$$\geq f_u(\bar{u}_0, \bar{v}_0|_{r=R}) - \frac{D_m k(k+1)}{R^2} - \frac{f_u(\bar{u}_0, \bar{v}_0|_{r=R}) f_v(\bar{u}_0, \bar{v}_0|_{r=R})}{\frac{D_c k}{R} + f_v(\bar{u}_0, \bar{v}_0|_{r=R})}. \tag{7.37}$$

This finally yields the following inequality for λ_k:

$$f_u(\bar{u}_0, \bar{v}_0|_{r=R}) - \frac{D_m k(k+1)}{R^2} - \frac{f_u(\bar{u}_0, \bar{v}_0|_{r=R}) f_v(\bar{u}_0, \bar{v}_0|_{r=R})}{\frac{D_c k}{R} + f_v(\bar{u}_0, \bar{v}_0|_{r=R})} \leq \lambda_k \tag{7.38}$$

and

$$\lambda_k \leq f_u(\bar{u}_0, \bar{v}_0|_{r=R}) - \frac{D_m k(k+1)}{R^2}. \tag{7.39}$$

In a physiological range, the term $\frac{f_u(\bar{u}_0,\bar{v}_0|_{r=R}) f_v(\bar{u}_0,\bar{v}_0|_{r=R})}{\frac{D_c k}{R} + f_v(\bar{u}_0,\bar{v}_0|_{r=R})}$ is very small and we get

$$\lambda_k \approx f_u(\bar{u}_0, \bar{v}_0|_{r=R}) - \frac{D_m k(k+1)}{R^2}. \tag{7.40}$$

Since $Y_{0,0} = \frac{1}{2}\sqrt{\frac{1}{\pi}}$, the fundamental solution $\xi_m^{0,0} Y_{0,0}(\theta, \phi) \exp(\lambda_{0,0} t)$ does not depend on the polar angle θ and azimuthal angle ϕ and, therefore, does not contribute to cellular asymmetry. Hence, we only consider wave numbers $k = 1, 2, 3, \ldots$ in the following. For cell sizes R_{small} with

$$\lambda_1 \approx f_u(\bar{u}_0, \bar{v}_0|_{r=R}) - \frac{2D_m}{R_{\text{small}}^2} < 0 \qquad \Leftrightarrow \qquad R_{\text{small}} < \sqrt{\frac{2D_m}{f_u(\bar{u}_0, \bar{v}_0|_{r=R})}}, \tag{7.41}$$

we have no growing eigenmodes since $\lambda_1 \gtrsim \lambda_2 \gtrsim \ldots$. For cell sizes R_{large} with

$$\lambda_2 \approx f_u(\bar{u}_0, \bar{v}_0|_{r=R}) - \frac{6D_m}{R_{\text{large}}^2} > 0 \qquad \Leftrightarrow \qquad R_{\text{large}} > \sqrt{\frac{6D_m}{f_u(\bar{u}_0, \bar{v}_0|_{r=R})}}, \tag{7.42}$$

we have more than one growing eigenmode and therefore several clusters.

Numerical methods used for simulations of the Bulk-Surface RD System

The bulk-surface RD system from Chapter 3, Section 3.2 were numerically solved with a FEM method. The following description of the method is a slightly adapted and modified excerpt of the numerical approach described in Giese et al. (2015).

To separate discretization in space and time, we use the well-known method of lines, see e.g. (Schiesser, 1991), and start with a semidiscretization in space using conforming first-order finite element methods based on triangular meshes. Given a triangular mesh which describes the geometrical setup introduced in Section 3.2, the equation for the volume species is treated by the standard conforming finite element approach, employing Lagrange basis functions of polynomial degree one. To treat the equation describing the membrane-bound species, we apply a surface finite element method on the boundary of the mesh using a restriction of the same volumetric basis functions. This enables implementing the numerical approach with tools provided by standard software frameworks for scientific computing. The idea of performing spatial discretization by combining the conforming finite element method and surface

finite elements on the same mesh is related to the procedure presented in Elliott and Ranner (2012), where a similar approach is used for the discretization of a coupled elliptic model problem.

With the method of lines, different schemes can be employed for the discretization in time. In accordance with our spatial discretization, we restrict ourselves to first-order schemes. We use both a fully implicit scheme and a semi-implicit scheme inspired by the implicit-explicit (IMEX) Euler method presented e.g. in (Koto, 2008). The idea of the IMEX method is to treat the spatially discretized reaction part of the system explicitly. Therefore, on the one hand the membrane equation and the cytosolic equation are decoupled and thus can be treated separately, and on the other hand the non-linearities are treated explicitly which enables using a linear solver. On the downside, an explicit treatment of the reaction part can affect the stability of the scheme in the reaction-dominated case and for a stiff reaction part in gereral (Koto, 2008). Our semi-implicit scheme decouples membrane and cytosolic equations while still treating the reaction part of each separate equation and its non-linearities implicitly. For each equation, this is done by treating only the unknowns of the other equation explicitly.

Weak formulation

First, we derive a weak formulation of model equations (3.8) – (3.11) in order to apply finite element methods for semidiscretization in space. Let $\mathcal{V}^{\text{bulk}} := H^1(V^{\text{cyt}})$ denote the usual Sobolev space containing weak solutions of elliptic equations in the bulk domain V^{cyt}. A natural counterpart containing weak solutions of elliptic equations on hypersurfaces are surface Sobolev spaces (Wloka, 1987; Dziuk, 1988; Dziuk and Elliott, 2007). To treat equation (3.8) on the closed hypersurface M^{cell}, we therefore define the surface Sobolev space $\mathcal{V}^{\text{sur}} := H^1(M^{\text{cell}})$.

Multiplication of model equations (3.8) and (3.9) with some test functions $\varphi_m \in H^1(M^{\text{cell}})$ respectively $\varphi_c \in H^1(V^{\text{cyt}})$ results in

$$\frac{d}{dt} \int\limits_{M^{\text{cell}}} u\, \varphi_m \,\mathrm{d}A = \int\limits_{M^{\text{cell}}} \nabla_\Gamma \cdot (D_m(x) \nabla_\Gamma u)\, \varphi_m \,\mathrm{d}A + \int\limits_{M^{\text{cell}}} f(u, v|_{M^{\text{cell}}})\, \varphi_m \,\mathrm{d}A, \tag{7.43}$$

$$\frac{d}{dt} \int\limits_{V^{\text{cyt}}} v\, \varphi_c \,\mathrm{d}V = \int\limits_{V^{\text{cyt}}} \nabla \cdot (D_c(x) \nabla v)\, \varphi_c \,\mathrm{d}V. \tag{7.44}$$

Application of the integration by parts formula for Sobolev spaces in (7.44), and its analog derivable from the surface divergence theorem (see (Dziuk and

Elliott, 2007) and references therein) in (7.43), yields

$$\frac{d}{dt}\int\limits_{M^{\mathrm{cell}}} u\,\varphi_m \,\mathrm{d}A = -\int\limits_{M^{\mathrm{cell}}} D_m(x)\nabla_\Gamma u\cdot\nabla_\Gamma\varphi_m \,\mathrm{d}A + \int\limits_{M^{\mathrm{cell}}} f(u,v|_{M^{\mathrm{cell}}})\,\varphi_m \,\mathrm{d}A, \tag{7.45}$$

$$\frac{d}{dt}\int\limits_{V^{\mathrm{cyt}}} v\,\varphi_c \,\mathrm{d}V = -\int\limits_{V^{\mathrm{cyt}}} D_c(x)\nabla v\cdot\nabla\varphi_c \,\mathrm{d}V + \int\limits_{\partial V^{\mathrm{cyt}}} \big(D_c(x)\nabla v\cdot\mathbf{n}\big)\,\varphi_c|_{\partial V^{\mathrm{cyt}}} \,\mathrm{d}A. \tag{7.46}$$

Due to the boundary conditions (3.10) and (3.11), together with $\partial V^{\mathrm{cyt}}$ being the disjoint union $M^{\mathrm{cell}} \cup M^{\mathrm{org}}$, this is equivalent to

$$\frac{d}{dt}\int\limits_{M^{\mathrm{cell}}} u\,\varphi_m \,\mathrm{d}A = -\int\limits_{M^{\mathrm{cell}}} D_m(x)\nabla_\Gamma u\cdot\nabla_\Gamma\varphi_m \,\mathrm{d}A + \int\limits_{M^{\mathrm{cell}}} f(u,v|_{M^{\mathrm{cell}}})\,\varphi_m \,\mathrm{d}A, \tag{7.47}$$

$$\frac{d}{dt}\int\limits_{V^{\mathrm{cyt}}} v\,\varphi_c \,\mathrm{d}V = -\int\limits_{V^{\mathrm{cyt}}} D_c(x)\nabla v\cdot\nabla\varphi_c \,\mathrm{d}V - \int\limits_{M^{\mathrm{cell}}} f(u,v|_{M^{\mathrm{cell}}})\,\varphi_c|_{M^{\mathrm{cell}}} \,\mathrm{d}A. \tag{7.48}$$

The weak formulation of model equations (3.8) – (3.11) now is to look for a solution $(u,v) \in L^2([0,T],\mathcal{V}^{\mathrm{sur}}) \times L^2([0,T],\mathcal{V}^{\mathrm{bulk}})$, such that for each $t \in [0,T]$

$$\frac{d}{dt}\int\limits_{M^{\mathrm{cell}}} u\,\varphi_m \,\mathrm{d}A = -\int\limits_{M^{\mathrm{cell}}} D_m(x)\nabla_\Gamma u\cdot\nabla_\Gamma\varphi_m \,\mathrm{d}A + \int\limits_{M^{\mathrm{cell}}} f(u,v|_{M^{\mathrm{cell}}})\,\varphi_m \,\mathrm{d}A$$
$$\text{for all } \varphi_m \in \mathcal{V}^{\mathrm{sur}}, \tag{7.49}$$

$$\frac{d}{dt}\int\limits_{V^{\mathrm{cyt}}} v\,\varphi_c \,\mathrm{d}V = -\int\limits_{V^{\mathrm{cyt}}} D_c(x)\nabla v\cdot\nabla\varphi_c \,\mathrm{d}V - \int\limits_{M^{\mathrm{cell}}} f(u,v|_{M^{\mathrm{cell}}})\,\varphi_c \,\mathrm{d}A$$
$$\text{for all } \varphi_c \in \mathcal{V}^{\mathrm{bulk}}. \tag{7.50}$$

Note that also the constant test functions $\varphi_m \equiv 1$ respectively $\varphi_c \equiv 1$ are permitted which yields mass conservation (3.13).

Semidiscretization in space

To obtain a semidiscretized system, we combine the conforming finite element approach (FEM) and a surface finite element method (SFEM). The FEM is a standard approach which is well-known to literature. See e.g. (Ciarlet, 2002; Braess, 2007) to gain an insight into the methodology. An SFEM developed in Dziuk (1988) can be seen as a natural generalization, as the idea of FEM is transfered to elliptic equations on hypersurfaces. Its extension (Dziuk and Elliott, 2007) to treating parabolic equations, like membrane equation (3.8), provides the basis for the SFEM that we use.

Both approaches are based on an approximation of the bulk domain V^{cyt} and the hypersurface M^{cell}, each by a triangulable geometrical object, and

corresponding meshes. For simplicity, we assume V^{cyt} to be a polyhedral domain that can be exactly represented by a triangular mesh $\mathcal{T}_h^{\mathrm{bulk}}$. With M^{cell} being part of the boundary of V^{cyt}, it corresponds to a set of boundary entities of $\mathcal{T}_h^{\mathrm{bulk}}$ which make up a surface mesh $\mathcal{T}_h^{\mathrm{sur}} \subset \mathcal{T}_h^{\mathrm{bulk}}$. Each method uses its corresponding mesh to set up a finite-dimensional function space usable for spatial discretization of the model equations. In particular, we replace the function spaces $\mathcal{V}^{\mathrm{sur}}$ and $\mathcal{V}^{\mathrm{bulk}}$ by finite-dimensional conforming function spaces $\mathcal{V}_h^{\mathrm{sur}} \subset \mathcal{V}^{\mathrm{sur}}$ respectively $\mathcal{V}_h^{\mathrm{bulk}} \subset \mathcal{V}^{\mathrm{bulk}}$ and seek a semidiscrete solution $(u_h, v_h) \in L^2([0,T], \mathcal{V}_h^{\mathrm{sur}}) \times L^2([0,T], \mathcal{V}_h^{\mathrm{bulk}})$, such that for each $t \in [0,T]$

$$\frac{d}{dt} \int\limits_{M^{\mathrm{cell}}} u_h \, \varphi_{m,h} \, \mathrm{d}A = - \int\limits_{M^{\mathrm{cell}}} D_m(x) \nabla_\Gamma u_h \cdot \nabla_\Gamma \varphi_{m,h} \, \mathrm{d}A + \int\limits_{M^{\mathrm{cell}}} f(u_h, v_h|_{M^{\mathrm{cell}}}) \, \varphi_{m,h} \, \mathrm{d}A$$
$$\text{for all } \varphi_{m,h} \in \mathcal{V}_h^{\mathrm{sur}}, \tag{7.51}$$

$$\frac{d}{dt} \int\limits_{V^{\mathrm{cyt}}} v_h \, \varphi_{c,h} \, \mathrm{d}V = - \int\limits_{V^{\mathrm{cyt}}} D_c(x) \nabla v_h \cdot \nabla \varphi_{c,h} \, \mathrm{d}V - \int\limits_{M^{\mathrm{cell}}} f(u_h, v_h|_{M^{\mathrm{cell}}}) \, \varphi_{c,h} \, \mathrm{d}A$$
$$\text{for all } \varphi_{c,h} \in \mathcal{V}_h^{\mathrm{bulk}}. \tag{7.52}$$

As discrete function spaces, we employ the node-based Lagrange spaces of polynomial degree one on $\mathcal{T}_h^{\mathrm{sur}}$ and $\mathcal{T}_h^{\mathrm{bulk}}$. With the basis functions $\left\{\varphi_{m,h}^{x_h}\right\}_{x_h \in \mathcal{X}_h^{\mathrm{sur}}}$ of $\mathcal{V}_h^{\mathrm{sur}}$ and the basis functions $\left\{\varphi_{c,h}^{x_h}\right\}_{x_h \in \mathcal{X}_h^{\mathrm{bulk}}}$ of $\mathcal{V}_h^{\mathrm{bulk}}$, where $\mathcal{X}_h^{\mathrm{sur}}$ and $\mathcal{X}_h^{\mathrm{bulk}}$ are the sets of nodes associated with the basis functions, we deduce

$$\frac{d}{dt} \int\limits_{M^{\mathrm{cell}}} u_h \, \varphi_{m,h}^{x_h} \, \mathrm{d}A = - \int\limits_{M^{\mathrm{cell}}} D_m(x) \nabla_\Gamma u_h \cdot \nabla_\Gamma \varphi_{m,h}^{x_h} \, \mathrm{d}A + \int\limits_{M^{\mathrm{cell}}} f(u_h, v_h|_{M^{\mathrm{cell}}}) \, \varphi_{m,h}^{x_h} \, \mathrm{d}A$$
$$\text{for all } x_h \in \mathcal{X}_h^{\mathrm{sur}}, \tag{7.53}$$

$$\frac{d}{dt} \int\limits_{V^{\mathrm{cyt}}} v_h \, \varphi_{c,h}^{x_h} \, \mathrm{d}V = - \int\limits_{V^{\mathrm{cyt}}} D_c(x) \nabla v_h \cdot \nabla \varphi_{c,h}^{x_h} \, \mathrm{d}V - \int\limits_{M^{\mathrm{cell}}} f(u_h, v_h|_{M^{\mathrm{cell}}}) \, \varphi_{c,h}^{x_h} \, \mathrm{d}A$$
$$\text{for all } x_h \in \mathcal{X}_h^{\mathrm{bulk}}. \tag{7.54}$$

The semidiscrete solution (u_h, v_h) can be represented as

$$u_h = \sum_{\tilde{x}_h \in \mathcal{X}_h^{\mathrm{sur}}} b_m^{\tilde{x}_h}(t) \, \varphi_{m,h}^{\tilde{x}_h} \quad \text{and} \quad v_h = \sum_{\tilde{x}_h \in \mathcal{X}_h^{\mathrm{bulk}}} b_c^{\tilde{x}_h}(t) \, \varphi_{c,h}^{\tilde{x}_h} \tag{7.55}$$

by time-dependent coefficient vectors $\mathbf{b_m}(t) = \left(b_m^{\tilde{x}_h}(t)\right)_{\tilde{x}_h \in \mathcal{X}_h^{\mathrm{sur}}}$ and $\mathbf{b_c}(t) = \left(b_c^{\tilde{x}_h}(t)\right)_{\tilde{x}_h \in \mathcal{X}_h^{\mathrm{bulk}}}$. Therefore, we get a system of ordinary differential equations

$$\left.\begin{aligned} \mathcal{M}_m \cdot \mathbf{b_m}'(t) + \mathcal{S}_m \cdot \mathbf{b_m}(t) &= \mathbf{f_m}\big(\mathbf{b_m}(t), \mathbf{b_c}(t)\big) \\ \mathcal{M}_c \cdot \mathbf{b_c}'(t) + \mathcal{S}_c \cdot \mathbf{b_c}(t) &= -\mathbf{f_c}\big(\mathbf{b_m}(t), \mathbf{b_c}(t)\big) \end{aligned}\right\} \quad \text{on} \quad [0,T], \tag{7.56}$$

with mass and stiffness matrices

$$\mathcal{M}_m := \left(\int_{M^{\mathrm{cell}}} \varphi_{m,h}^{\tilde{x}_h} \, \varphi_{m,h}^{x_h} \, \mathrm{d}A\right)_{x_h \in \mathcal{X}_h^{\mathrm{sur}}, \tilde{x}_h \in \mathcal{X}_h^{\mathrm{sur}}}, \tag{7.57}$$

$$\mathcal{S}_m := \left(\int_{M^{\mathrm{cell}}} D_m(x) \nabla_\Gamma \varphi_{m,h}^{\tilde{x}_h} \cdot \nabla_\Gamma \varphi_{m,h}^{x_h} \, \mathrm{d}A\right)_{x_h \in \mathcal{X}_h^{\mathrm{sur}}, \tilde{x}_h \in \mathcal{X}_h^{\mathrm{sur}}}, \tag{7.58}$$

$$\mathcal{M}_c := \left(\int_{V^{\mathrm{cyt}}} \varphi_{c,h}^{\tilde{x}_h} \, \varphi_{c,h}^{x_h} \, \mathrm{d}A\right)_{x_h \in \mathcal{X}_h^{\mathrm{bulk}}, \tilde{x}_h \in \mathcal{X}_h^{\mathrm{bulk}}}, \tag{7.59}$$

$$\mathcal{S}_c := \left(\int_{V^{\mathrm{cyt}}} D_c(x) \nabla \varphi_{c,h}^{\tilde{x}_h} \cdot \nabla \varphi_{c,h}^{x_h} \, \mathrm{d}A\right)_{x_h \in \mathcal{X}_h^{\mathrm{bulk}}, \tilde{x}_h \in \mathcal{X}_h^{\mathrm{bulk}}}, \tag{7.60}$$

and vector valued right hand side functions $\mathbf{f_m}$, $\mathbf{f_c}$,

$$\mathbf{f_m}\big(\mathbf{b_m}(t),\mathbf{b_c}(t)\big) := \Big(\int_{M^{\mathrm{cell}}} f\left(\sum_{\tilde{x}_h\in\mathcal{X}_h^{\mathrm{sur}}} b_m^{\tilde{x}_h}(t)\,\varphi_{m,h}^{\tilde{x}_h}, \sum_{\tilde{x}_h\in\mathcal{X}_h^{\mathrm{bulk}}} b_c^{\tilde{x}_h}(t)\,\varphi_{c,h}^{\tilde{x}_h}|_{M^{\mathrm{cell}}}\right)\varphi_{m,h}^{x_h}\,\mathrm{d}A\Big)_{x_h\in\mathcal{X}_h^{\mathrm{sur}}}, \tag{7.61}$$

$$\mathbf{f_c}\big(\mathbf{b_m}(t),\mathbf{b_c}(t)\big) := \Big(\int_{M^{\mathrm{cell}}} f\left(\sum_{\tilde{x}_h\in\mathcal{X}_h^{\mathrm{sur}}} b_m^{\tilde{x}_h}(t)\,\varphi_{m,h}^{\tilde{x}_h}, \sum_{\tilde{x}_h\in\mathcal{X}_h^{\mathrm{bulk}}} b_c^{\tilde{x}_h}(t)\,\varphi_{c,h}^{\tilde{x}_h}|_{M^{\mathrm{cell}}}\right)\varphi_{c,h}^{x_h}\,\mathrm{d}A\Big)_{x_h\in\mathcal{X}_h^{\mathrm{bulk}}}. \tag{7.62}$$

SFEM matrix/vector assembly via volumetric FEM basis functions

As we use node-based Lagrange spaces of the same polynomial degree based on the same triangular mesh, the set of Lagrange nodes of $\mathcal{V}_h^{\mathrm{sur}}$ can be described as $\mathcal{X}_h^{\mathrm{sur}} = \{x_h \in \mathcal{X}_h^{\mathrm{bulk}} \mid x_h \in M^{\mathrm{cell}}\} \subset \mathcal{X}_h^{\mathrm{bulk}}$. Moreover, the employed Lagrange basis functions have the property, that

$$\varphi_{m,h}^{x_h} = \varphi_{c,h}^{x_h}|_{M^{\mathrm{cell}}} \ \forall x_h \in \mathcal{X}_h^{\mathrm{sur}}. \tag{7.63}$$

Thus, instead of directly implementing the SFEM ansatz space $\mathcal{V}_h^{\mathrm{sur}}$, the constrained function space

$$\partial\mathcal{V}_h^{\mathrm{bulk}} := \{v \in \mathcal{V}_h^{\mathrm{bulk}} \mid v(x_h) = 0 \text{ for } x_h \in \mathcal{X}_h^{\mathrm{bulk}} \setminus \mathcal{X}_h^{\mathrm{sur}}\} \subset \mathcal{V}_h^{\mathrm{bulk}} \tag{7.64}$$

can be utilized to perform the assembly of $\mathcal{M}_m$, $\mathcal{S}_m$, $\mathbf{f_m}$ and $\mathbf{f_c}$. In particular, the restriction of its basis $\left\{\varphi_{c,h}^{x_h}\right\}_{x_h\in\mathcal{X}_h^{\mathrm{sur}}}$ to the set M^{cell} equals the Lagrange basis $\left\{\varphi_{m,h}^{x_h}\right\}_{x_h\in\mathcal{X}_h^{\mathrm{sur}}}$ of $\mathcal{V}_h^{\mathrm{sur}}$.

Note that $\partial\mathcal{V}_h^{\mathrm{bulk}} \not\subset \mathcal{V}_h^{\mathrm{sur}}$. Hence, the surface component of the numerical solution can not be directly represented in the space $\partial\mathcal{V}_h^{\mathrm{bulk}}$. Nevertheless, using the identity $\partial\mathcal{V}_h^{\mathrm{bulk}}|_{M^{\mathrm{cell}}} = \mathcal{V}_h^{\mathrm{sur}}$, the semidiscrete solution $(u_h, v_h) \in L^2([0,T],\mathcal{V}_h^{\mathrm{sur}}) \times L^2([0,T],\mathcal{V}_h^{\mathrm{bulk}})$ can be calculated as

$$u_h = \sum_{\tilde{x}_h\in\mathcal{X}_h^{\mathrm{sur}}} b_m^{\tilde{x}_h}(t)\,\varphi_{c,h}^{\tilde{x}_h}|_{M^{\mathrm{cell}}} \quad \text{and} \quad v_h = \sum_{\tilde{x}_h\in\mathcal{X}_h^{\mathrm{bulk}}} b_c^{\tilde{x}_h}(t)\,\varphi_{c,h}^{\tilde{x}_h}. \tag{7.65}$$

Fully discretized systems

System (7.56) can be equivalently written as

$$\mathbf{b_m}'(t) = -\mathcal{M}_m^{-1}\mathcal{S}_m \cdot \mathbf{b_m}(t) + \mathcal{M}_m^{-1} \cdot \mathbf{f_m}\big(\mathbf{b_m}(t),\mathbf{b_c}(t)\big), \tag{7.66}$$

$$\mathbf{b_c}'(t) = -\mathcal{M}_c^{-1}\mathcal{S}_c \cdot \mathbf{b_c}(t) - \mathcal{M}_c^{-1} \cdot \mathbf{f_c}\big(\mathbf{b_m}(t),\mathbf{b_c}(t)\big), \tag{7.67}$$

or as

$$\mathbf{b}'(t) = -\mathcal{M}^{-1}\mathcal{S} \cdot \mathbf{b}(t) + \mathcal{M}^{-1} \cdot \mathbf{f}\big(\mathbf{b}(t)\big) \qquad \text{on} \quad [0,T], \tag{7.68}$$

using the notation

$$\mathcal{M} := \begin{pmatrix} \mathcal{M}_m & 0 \\ 0 & \mathcal{M}_c \end{pmatrix}, \quad \mathcal{S} := \begin{pmatrix} \mathcal{S}_m & 0 \\ 0 & \mathcal{S}_c \end{pmatrix}, \quad \mathbf{b}(t) := \begin{pmatrix} \mathbf{b_m}(t) \\ \mathbf{b_c}(t) \end{pmatrix} \tag{7.69}$$

$$\text{and} \quad \mathbf{f}\big(\mathbf{b}(t)\big) := \begin{pmatrix} \mathbf{f_m}\big(\mathbf{b}(t)\big) \\ \mathbf{f_c}\big(\mathbf{b}(t)\big) \end{pmatrix}. \tag{7.70}$$

For discretization in time, the interval $[0, T]$ is split into sub-intervals $[t_k, t_{k-1}]$ of length $\tau_k := t_k - t_{k-1}$, $k = 1 \ldots, K$, with $0 = t_0 < t_1 < \ldots < t_k < \ldots < t_{K-1} < t_K = T$. By $\mathbf{b^k}$ we denote a time-dependent coefficient vector $\mathbf{b}$ evaluated at t_k. Employing the backward Euler method in (7.68), we end up with a system of nonlinear algebraic equations

$$\mathbf{b^k} = \mathbf{b^{k-1}} - \tau \mathcal{M}^{-1} \mathcal{S} \cdot \mathbf{b^k} + \tau \mathcal{M}^{-1} \cdot \mathbf{f}\big(\mathbf{b^k}\big), \qquad k \in \{1, \ldots, K\}, \tag{7.71}$$

which can be solved e.g. using a multidimensional Newton's method. However, solving this fully discretized system can get very time-consuming, especially when a fine finite element mesh is used, as this results in high-dimensional coefficient vectors. For this reason, we employ a semi-implicit scheme for temporal discretization which decouples equations (7.66) and (7.67). In particular, we use the backward Euler method separately for each equation, while treating the unknowns of the other equation explicitly. In contrast to the IMEX Euler method (see e.g. (Koto, 2008)), the unknowns of each separate equation are thus treated fully implicit. The fully discretized system then reads

$$\left.\begin{aligned} \mathbf{b_m^k} &= \mathbf{b_m^{k-1}} - \tau \mathcal{M}_m^{-1} \mathcal{S}_m \cdot \mathbf{b_m^k} + \tau \mathcal{M}_m^{-1} \cdot \mathbf{f_m}\big(\mathbf{b_m^k}, \mathbf{b_c^{k-1}}\big) \\ \mathbf{b_c^k} &= \mathbf{b_c^{k-1}} - \tau \mathcal{M}_c^{-1} \mathcal{S}_c \cdot \mathbf{b_c^k} + \tau \mathcal{M}_c^{-1} \cdot \mathbf{f_c}\big(\mathbf{b_m^{k-1}}, \mathbf{b_c^k}\big) \end{aligned}\right\} \qquad k \in \{1, \ldots, K\} \tag{7.72}$$

and can be solved e.g. using a multidimensional Newton's method for both equations in parallel.

Our experiments have shown no obvious qualitative differences between the solutions computed with both schemes (7.71) and (7.72).

Simulation framework

The presented numerical approach can be implemented with tools provided by standard PDE software frameworks. For the assembly of the required matrices, the framework has to provide the space of simplicial Lagrange finite elements of order one on a triangular mesh. Furthermore, it either has to provide the space of simplicial Lagrange finite elements of order one on the boundary of the same mesh or a mechanism for constraining the degrees of freedom of the volumetric Lagrange space which do not lie on the boundary of the mesh. The latter mechanism usually is available in those frameworks, since constrained degrees of freedom are frequently used to implement Dirichlet boundary conditions.

All of our simulations were performed using the Distributed and Unified Numerics Environment (DUNE) (Bastian et al., 2008b,a). The numerical discretization schemes were implemented using the discretization module DUNE-PDELab which is based on DUNE. It provides the volumetric finite element space $\mathcal{V}_h^{\text{bulk}}$ which in addition can be constrained for SFEM matrix/vector assembly using the space $\partial\mathcal{V}_h^{\text{bulk}}$. Furthermore, it features an easy to use assembly infrastructure, as well as the linear solver, nonlinear solver and time-stepping schemes that were used.

Finite element meshes were generated with Gmsh (Geuzaine and Remacle, 2009). An example of the 3D mesh used in Chapter3, Section 3.3 is shown in Figure 7.1.

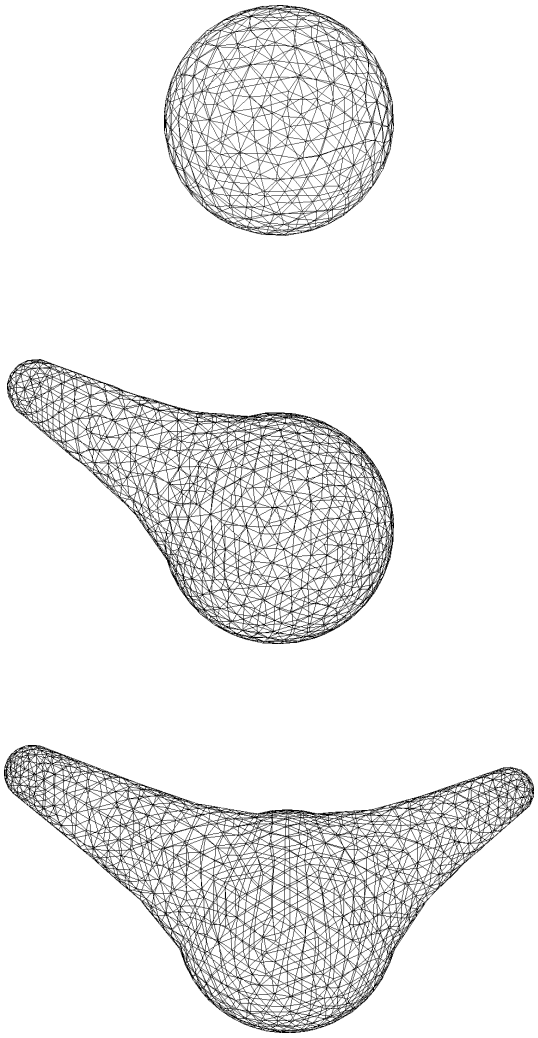

Figure 7.1: 3D meshes as used in Chapter 3, Section 3.3.

Appendix C

Computation of the von Mises Stress for a Single Triangle

The linear stress tensor $\mathcal{S}$, as defined in Chapter 4, Section 4.4.1, has the form:

$$\mathcal{S} = \lambda \cdot \mathrm{tr}(\mathcal{E})I + \mu \cdot \mathcal{E}. \tag{7.73}$$

We compute the principal stresses σ_1 and σ_2, which are given by the eigenvalues of $\mathcal{S}$. The trace and the determinant of $\mathcal{S}$ can be computed from

$$\begin{aligned} \mathrm{tr}(\mathcal{S}) &= \mathrm{tr}\left(\lambda \mathrm{tr}(\mathcal{E})I + \mu\mathcal{E}\right) \\ &= 2\lambda \mathrm{tr}(E) + \mu \mathrm{tr}(\mathcal{E}), \end{aligned} \tag{7.74}$$

and

$$\begin{aligned}
\det(\mathcal{S}) &= \det\left(\lambda \mathrm{tr}(\mathcal{E}) I + \mu \mathcal{E}\right) \\
&= \det \begin{pmatrix} \lambda \mathrm{tr}(\mathcal{E}) + \mu\varepsilon_{11} & \mu\varepsilon_{12} \\ \mu\varepsilon_{21} & \lambda \mathrm{tr}(E) + \mu\varepsilon_{22} \end{pmatrix} \\
&= (\lambda \mathrm{tr}(\mathcal{E}) + \mu\epsilon_{11})(\lambda \mathrm{tr}(\mathcal{E}) + \mu\epsilon_{22}) - \mu^2\epsilon_{12}\epsilon_{21} \\
&= \lambda^2 \mathrm{tr}(\mathcal{E})^2 + \lambda\mu \mathrm{tr}(\mathcal{E})(\epsilon_{11} + \epsilon_{22}) + \mu^2\epsilon_{11}\epsilon_{22} - \mu^2\epsilon_{12}\epsilon_{21} \\
&= \lambda^2 \mathrm{tr}(\mathcal{E})^2 + \lambda\mu \mathrm{tr}(\mathcal{E})^2 + \mu^2 \det(\mathcal{E}) \\
&= \lambda^2 \mathrm{tr}(\mathcal{E})^2 + \lambda\mu \mathrm{tr}(\mathcal{E})^2 + \mu^2 \det(\frac{1}{2}(\mathcal{C} - I)) \\
&= (\lambda^2 + \lambda\mu)\mathrm{tr}(\mathcal{E})^2 + \frac{\mu^2}{4}(\det(\mathcal{C}) - \mathrm{tr}(\mathcal{C}) + 1). \qquad (7.75)
\end{aligned}$$

Using these quantities von Mises stress can be computed from

$$\begin{aligned}
\sigma^{VM} &= \sqrt{\sigma_1^2 + \sigma_2^2 - \sigma_1\sigma_2} \\
&= \sqrt{(\sigma_1 + \sigma_1)^2 - 3\sigma_1\sigma_2} \\
&= \sqrt{\mathrm{tr}(\mathcal{S})^2 - 3\det(\mathcal{S})}. \qquad (7.76)
\end{aligned}$$

Refinement Employed for the Triangular Surface Mesh

Due to local growth of the cell wall, the computational representation, which is a triangular surface mesh has to extend. In this process triangular elements become very large and the desired accuracy can not be achieved anymore. Therefore, we employ local refinement strategies, e.g. large elements are divided into smaller elements. Here we show certain properties of this refinement. The elastic energy is conserved upon refinement. Assume a triangle T which is split into four similar triangles T^a,T^b, T^c and T^d as shown in Figure 7.2. Recall that the energy of the triangle T is calculated from:

$$\begin{aligned}
W(T) &= \frac{\lambda}{2} tr(E)^2 + \frac{\mu}{2} tr(E^2) \qquad (7.77) \\
&= \sum_{i=1}^{3} \frac{k_i^T}{4}(l_i^2 - L_i^2)^2 + \sum_{i \neq j}^{3} \frac{c_k^T}{2}(l_i^2 - L_i^2)(l_j^2 - L_j^2), \qquad (7.78)
\end{aligned}$$

with coefficients

$$k_i^T = E \cdot d \cdot \frac{2\cot^2\alpha_i + 1 - \nu}{16(1-\nu^2)A_P}, \qquad (7.79)$$

$$c_k^T = E \cdot d \cdot \frac{2\cot\alpha_i \cot\alpha_j - 1 + \nu}{16(1-\nu^2)A_P}. \qquad (7.80)$$

For each triangle we have $|A_P^a| = |A_P^b| = |A_P^c| = |A_P^d| = \frac{1}{4}|A_P|$, while the angles are conserved. Therfore, we have $k_i^{T^a} = k_i^{T^b} = k_i^{T^c} = k_i^{T^d} = 4k_i^T$. The length of the triangle sides are split into halfs and, therefore, $l_{a,i} = l_{b,i} = l_{c,i} = l_{d,i} = \frac{1}{2}l_i$

and $L_{a,i} = L_{b,i} = L_{c,i} = L_{d,i} = \frac{1}{2}L_i$. Therefore, we get for the energy of each of the four single triangles

$$W(T^a) = \sum_{i=1}^{3} \frac{k_i^{T^a}}{4}(l_{a,i}^2 - L_{a,i}^2)^2 + \sum_{i\neq j}^{3} \frac{c_k^{T^a}}{2}(l_{a,i}^2 - L_{a,i}^2)(l_{a,j}^2 - L_{a,j}^2) \tag{7.81}$$

$$= \sum_{i=1}^{3} \frac{k_i^{T}}{16}(l_i^2 - L_i^2)^2 + \sum_{i\neq j}^{3} \frac{c_k^{T}}{8}(l_i^2 - L_i^2)(l_j^2 - L_j^2) \tag{7.82}$$

$$= \frac{1}{4}W(T). \tag{7.83}$$

The same holds for the other triangles T^b,T^c and T^d. Hence, $W(T^a)+W(T^b)+W(T^c)+W(T^d)$ and, therefore, the elastic enrgy is conserved upon refinement.

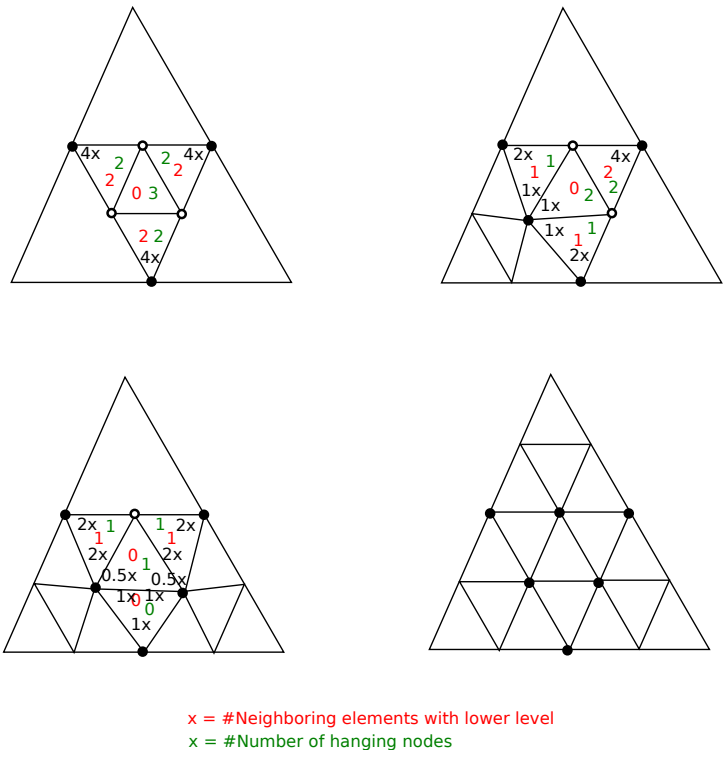

Figure 7.2: Illustration of four cases that can occur upon refinement.

Calculation of tr($\mathcal{E}$)

In the original work from Delingette (2008), the following relations were given

$$\mathrm{tr}(\mathcal{C}) = \frac{1}{2A_P}(l_1^2 \cot\alpha_1 + l_2^2 \cot\alpha_2 + l_3^2 \cot\alpha_3), \tag{7.84}$$

$$\mathrm{tr}(\mathcal{E}) = \frac{1}{2A_P}((l_1^2 - L_1^2) \cot\alpha_1 + (l_2^2 - L_2^2) \cot\alpha_2 + (l_3^2 - L_3^2) \cot\alpha_3), \tag{7.85}$$

While I checked the first term tr($\mathcal{C}$), which was calculated correct, the factor 1/2 seems to be missing in the second expression for tr($\mathcal{E}$). The term tr($\mathcal{E}$) is instead given by

$$\begin{aligned}
\mathrm{tr}(\mathcal{E}) &= \frac{1}{2}(\mathrm{tr}(\mathcal{C}) - 2) \\
&= \frac{1}{2}\left(\frac{1}{2A_P}(l_1^2 \cot\alpha_1 + l_2^2 \cot\alpha_2 + l_3^2 \cot\alpha_3) - 2\right) \\
&= \frac{1}{4A_P}(l_1^2 \cot\alpha_1 + l_2^2 \cot\alpha_2 + l_3^2 \cot\alpha_3) - 1 \\
&= \frac{1}{4A_P}((l_1^2 - L_1^2) \cot\alpha_1 + (l_2^2 - L_2^2) \cot\alpha_2 + (l_3^2 - L_3^2) \cot\alpha_3).
\end{aligned}$$

Methods

The steady state model was implemented in Python using the *NumPy* (Van Der Walt et al., 2011) and *SciPy* (Jones et al., 2001) packages as well as Matplotlib (Hunter et al., 2007). For the shape description of the axisymmetric shape parametric splines of 4th order were used, which allow for the computation of the first and second derivatives. The derivatives were used to calculated the curvatures, stresses, strains and elasticities on the basis of the equations described in Chapter 4, Section 4.2. The equation of motion based on the equations developed in Section 4.4 were solved numerically with the open source framework DUNE (Bastian et al., 2008a).

8 Acknowledgements

Collaborative Work

The work that I present in this thesis was performed in the collaborative research center SFB 740: "From molecules to modules". I was supervised by Edda Klipp and worked together with my colleague Björn Goldenbogen on the project "Spatial modeling of gradient sensing exemplified for the yeast pheromone response".

This project resulted in a number of manuscripts and puplications that I also refer to in my thesis. Chapter 2 is related to the publication (Diener et al., 2014). I contributed in writing the manuscript, building the model, implementing the FEM method in DUNE as well as analysis and interpretation of the data. Chapter 3 is related to the publication (Giese et al., 2015) and the WIAS preprint (Giese et al., 2014). Chapter 4 is related to the manuscript (Goldenbogen et al., 2016). The model was derived and AFM data interpreted toghether with Björn Goldenbogen. The data for the model was acquired by Björn Goldenbogen, while I did the model implementation in the computational framework. In all of the mentioned manuscripts I contributed as shared first author.

Acknowledgements

First of all I would like to thank my supervisor **Edda Klipp** for her support of my research and freedom to develop my research interests and thoughts. I also like to thank **Andreas Schröder** who motivated and supported me to enter the field of systems biology but not to loose the contacts to the mathematics.

I also think back of the great time that I spend with my colleagues at the Humboldt-Universität during my PhD studies. The yeast did not only manifest in science, but also in amazing cakes that where baked frequently and eaten in short time scales in the TBP kitchen. Occasionally, also the liquid yeast led to scientific insights in the heating, cooking and brewing of barley, hopes and the like.

For my academic exchange at the University of Californinia Irvine I thank **Qing Nie**. Also I enjoyed the work on fish data with my colleagues **Max Flöttmann** and **Jannis Uhlendorf**. Here, special thank to **Robert Arlinghaus** and the support to take part in the Humboldt-Princeton exchange.

I also like to thank **Martin Eigel** and my colleagues **Sebastian Westerheide** and **Christian Engwer** in Münster, who supported me in my adventures with cell compasses and programming in C++ and the **DUNE framework**.

I also thank my friends, colleagues and office mates **Björn Goldenbogen**, **Christian Heinemann**, **Christoph Wollstein**, **Friedemann Uschner**, **Gabriele Schreiber**, **Gregor Milicic**, **Katja Tummler**, **Marcus Krantz**, **Matthias Reis**, **Michael Gareis**, **Sebastian Thieme**, **Severin Ehret**, **Sora Lee** and **Ulrike Münzner** for moral support, advice and helpful discussions.

My thoughts are also with my mother who is always with me but left far too early. I thank **Dieter Strickrodt** and **Christel Luther** for their constant support. My partner **Franziska Mühleis** supported me through my work and took me out of the science world from time to time.

List of Publications

Christian Diener*, Gabriele Schreiber*, Wolfgang Giese*, Gabriel del Rio, Andreas Schröder, and Edda Klipp. Yeast mating and image-based quantification of spatial pattern formation. *PLoS Comput. Biol.*, 10(6):e1003690, June 2014. 10.1371/journal.pcbi.1003690.

Wolfgang Giese*, Martin Eigel*, Sebastian Westerheide, Christian Engwer, and Edda Klipp. Influence of cell shape, inhomogeneities and diffusion barriers in cell polarization models. *WIAS Preprint*, 1(1959), 2014.

Wolfgang Giese*, Martin Eigel*, Sebastian Westerheide, Christian Engwer, and Edda Klipp. Influence of cell shape, inhomogeneities and diffusion barriers in cell polarization models. *Physical biology*, 12(6):066014, 2015.

Björn Goldenbogen*, Wolfgang Giese*, Marie Hemmen, Jannis Uhlendorf, Andreas Herrmann, and Edda Klipp. Dynamics of cell wall elasticity pattern shapes the cell during yeast mating morphogenesis. *Open Biology*, 6(9): 160136, 2016.

* These authors contributed equally.

Selbständigkeitserklärung

Ich erkläre hiermit, dass ich die vorliegende Arbeit selbständig verfasst und noch nicht für andere Prüfungen eingereicht habe. Sämtliche Quellen einschließlich Internetquellen, die unverändert oder abgewandelt wiedergegeben werden, insbesondere Quellen für Texte, Grafiken, Tabellen und Bilder, sind als solche kenntlich gemacht. Mir ist bekannt, dass bei Verstößen gegen diese Grundsätze ein Verfahren wegen Täuschungsversuchs bzw. Täuschung eingeleitet wird.

Wolfgang Giese